Investigating the formation and properties of multiple star systems using Monte Carlo models

Rebecca J. Houghton

Department of Physics and Astronomy
The University of Sheffield

A dissertation submitted in candidature for the degree of Doctor of Philosophy at the University of Sheffield

October 2023

> “While I’m still confused and uncertain,
> it’s on a much higher plane, d’you see,
> and at least I know I’m bewildered about
> the really fundamental and important facts
> of the universe.”
>
> — Terry Pratchett, *Equal Rites*

Declaration

I declare that, unless otherwise stated, the work presented in this thesis is my own. No part of this thesis has been accepted or is currently being submitted for any other qualification at the University of Sheffield or elsewhere.

The work presented in Chapter 4 has already been published and can be found in Houghton & Goodwin (2022). The work in Chapter 2 has been submitted for publication. The methods presented in Chapter 5 will be submitted for publication as part of Shenton et al. (in prep).

Acknowledgments

First of all, a massive thank you to Simon Goodwin for being an incredible supervisor. I wouldn't have made it through the chaos of the last four years without your constant support, kindness, and scientific guidance. I'd also like to thank Richard Parker, for telling me I was good enough to be here every time I convinced myself I wasn't.

I'm incredibly grateful to the rest of the astro group for making my time here so wonderful. Thank you to Vik and Pablo for encouraging me to go on the 3rd year field trip - it helped me decide to do a PhD and allowed me to start building up my self confidence to get where I am today. Extra thanks to Pablo for all the tech support over the years. Thank you to Clive, for letting a theorist come on your observing run.

Thank you to all the postdocs and PhD students that have been around during my time here. In particular, Alex, Summer, Martin, Mark, George, Luke, James W, Umar, Emma, Joe, Adam, Dustin, James G and Thaer. Big thanks to Martin for teaching me almost everything I know about Git and proper python coding, and to Mark for letting me take advantage of your unhealthy knowledge of statistics. Another massive thank you to Alex, for letting me talk through my research whenever I needed to (and always coming up with helpful suggestions), and for all of the care and support over the past years that I've been extremely lucky to have.

To my uni mates, thank you for getting me through lockdown and the difficult times with online chats, movies, and games. To Alana and Joe, thanks for letting me be your lockdown bubble and to Owen and Leila, thank you for several years of wonderful Tuesday/Thursday night dinners.

Finally, and most importantly, thank you to my mum, my dad, and my brother for supporting me every single step of the way. I could never have made it this far without you. Thanks to my granddad, for the years of chats about space and science fiction which led me to astronomy, and to my nana and grandma, for making sure every taxi driver, carer, and hairdresser in all of Merseyside knew I was doing a PhD.

Summary

Stellar multiplicity has been extensively studied over the past few decades. It is believed that most stars form in multiple systems, meaning that understanding multiplicity is crucial for understanding star formation as a whole. Studying binary systems can tell us about their formation histories and orbital properties.

In this thesis, I investigate the properties of multiple systems using three different methods. Firstly, I tested various simple rules for ‘universal’ star formation using a toy Monte Carlo model. These rules define how protostellar cores fragment into multiple systems and how these systems then decay (through secular processes or encounters). I found that the number of stars formed in each core must be a weak function of core mass in order to produce the canonical IMF and multiplicity fractions that increase with primary mass. However, it is difficult to match the multiplicity fractions exactly without a more detailed model for dynamical and secular decay.

I then present a summary of `FOBOS` - an orbit fitting algorithm designed to estimate the orbital parameters of binaries, triple systems, or directly imaged exoplanets from as few as two astrometric observations. `FOBOS` uses a brute force Monte Carlo method to sample parameter space using uniform priors. I tested the code on a large sample of fake systems, as well as two real systems with brown dwarf companions, showing that it is a reliable method of estimating the semi-major axis, inclination, and eccentricity of a system.

Finally, I created a binary population synthesis model. I used this model to estimate the selection effects present in samples of visual binaries, by first performing some general tests and then applying it to a sample of binary YSOs, taken from archival data. I found that the majority of the YSOs in the sample had a significantly larger semi-major axis than was first expected, implying that the sample included only (a) ultrawide binaries or (b) tertiary companions that were too close for the survey to resolve.

Contents

1 Introduction 1

1.1 Foreword . . . 1
1.2 Molecular clouds and star-forming regions . . . 2
  1.2.1 Molecular clouds and the interstellar medium . . . 3
  1.2.2 Filaments and dense cores . . . 4
  1.2.3 The core mass function . . . 5
1.3 Star formation . . . 7
  1.3.1 Core collapse . . . 7
  1.3.2 Low mass star formation . . . 8
  1.3.3 Brown dwarf formation . . . 12
  1.3.4 High-mass star formation . . . 13
  1.3.5 Planet formation . . . 14
1.4 Initial mass function . . . 15
  1.4.1 Single-star vs. system IMF . . . 17
  1.4.2 Universal IMF . . . 17
  1.4.3 Mapping from the CMF to the IMF . . . 19
1.5 Multiple formation . . . 20
1.6 Multiple system decay and dynamical destruction . . . 23
1.7 Multiplicity . . . 24
  1.7.1 Multiplicity statistics . . . 24
  1.7.2 Incompleteness and uncertainties . . . 28
  1.7.3 Nearby star-forming regions vs the field . . . 29
1.8 Observing binaries and multiple systems . . . 29
1.9 Summary . . . 30
1.10 Work in this thesis . . . 31

2 Multiplicity of stellar systems in the field from simulations 33

2.1 Introduction . . . 33
2.2 Methods . . . 34
  2.2.1 Simulations . . . 34
  2.2.2 Output . . . 37
2.3 Results . . . 37
  2.3.1 Self-similar model . . . 38
  2.3.2 Strongly mass dependent model . . . 42

2.3.3 Hybrid model 47
2.3.4 Optimised decay model 55
2.4 Discussion 57
2.5 Conclusions 60

3 Celestial mechanics and binary modelling 61

3.1 A brief history of celestial mechanics 61
3.2 Generating a binary 64
3.2.1 Orbital properties 64
3.2.2 Solving Kepler's equation 64
3.3 Triples 67
3.3.1 Stability 67

4 Orbit fitting with FOBOS 71
4.1 Introduction 71
4.2 Methods 72
4.2.1 Parameter constraints 75
4.2.2 Orbital Parameter Generation 76
4.2.3 A note on degeneracies 77
4.2.4 Errors on observed quantities 77
4.2.5 Selection effects 78
4.3 Testing on binary systems 78
4.3.1 General performance 79
4.4 Triples 86
4.4.1 Results 87
4.5 Timing 96
4.6 Multi-Epoch Observations 96
4.7 Comparisons 99
4.8 Summary 105

5 A binary population synthesis model and its applications 107
5.1 Summary 107
5.2 Orbital selection effects 108
5.3 Estimating the binary fraction of YSOs 113
5.3.1 Sample characteristics 113
5.3.2 My contribution 114
5.3.3 The model 115
5.3.4 Selection effects 115
5.3.5 Comparing data sets using a Binary Search Tree 116
5.3.6 Binary search trees in this work 119
5.3.7 Measuring Goodness of Fit 121
5.4 Results 122
5.4.1 Model parameters and assumptions 122
5.4.2 Monte Carlo modelling 123

5.4.3 Discussion 126
5.5 Summary 129

6 Conclusions and future work 131
6.1 Multiplicity of stellar systems in the field from simulations 131
6.1.1 Future work 132
6.2 FOBOS 134
6.2.1 Future work 134
6.3 Binarity of YSOs 135
6.3.1 Future work 135

A Multiplicity of stellar systems 149

B Additional FOBOS corner plots and simulation data tables 155
B.1 Simulation data tables 158

List of Figures

1.1 The Big Dipper/Ursa Major. Credit: ESA/Hubble, A. Fujii 2

1.2 Young star-forming region NGC 346 in the Small Magellanic Cloud, taken with the NIRcam instrument on JWST. NASA's 'Astronomy Picture Of the Day' 13/01/2023. Image credit: NASA, ESA, CSA. 3

1.3 Prestellar core mass function (blue histograms) in the Aquila rift cloud. The red solid line shows a lognormal fit to the data, which peaks at $\sim 0.6\ M_\odot$. The solid black line shows a power-law slope of -1.5 ± 0.2. The Kroupa (2001) and Chabrier (2005) IMFs are shown for reference. The region to the left of the vertical dashed line suffers from incomplete sampling. Figure from André et al. (2010). 6

1.4 The stages of star formation. The top left panel shows the scale of the prestellar core, spanning ∼30 000 au in radius. Following the arrows to the right, the middle panel shows a class 0 protostar where the dense core is collapsing and forming a small accreting protostar. When the object reaches class I, the surrounding envelope has collapsed into a disc of radius ∼100 au. Image credit: Persson (2014a). 9

1.5 SEDs of YSOs in Classes 0, I, II, and III. In Class 0, the protostar is embedded in a dense envelope of material and is visible as a black body at far-IR wavelengths due to dust radiation. During Class I, the protostar has IR emission due to the remaining envelope and an IR excess indicating the presence of a disc. During the Class II phase, the remaining envelope has dissipated enough for the pre-MS star to be visible as a BB at optical wavelengths with a disc indicated by IR emission. Finally, in the Class III phase, the stellar BB is observed with a small contribution to the SED from a debris disc/planets. Image credit: Persson (2014b) 10

1.6 Probability density function from Maschberger (2013) of the system IMF (top plot, solid black line) and the single-star IMF (bottom plot, solid black line). The solid red lines on the top plot represent the power law segments of the solid black line. On both plots, the green dashed line shows the Chabrier (2003a) IMFs. In the bottom plot, the Kroupa (2001) is shown by the blue dashed line. See (Maschberger, 2013) for definitions of symbols. 18

1.7 Left: the multiplicity fractions (thick lines) and triple/high-order fractions (thin lines) for different primary mass ranges. Right: The companion star fractions for different primary mass ranges. The different colours represent different spectral types, which are indicated on the top axis of each plot. The x error bars represent the total mass range sampled for which the MF/THF/CSF is calculated. The figure is from Offner et al. (2022) and the data points correspond to values from their Table 1, all of which were corrected for incompleteness. 25

2.1 The system (top) and single star (bottom) IMFs for the self-similar model. On both plots, the Salpeter (orange), Chabrier (blue) and Maschberger (pink) IMFs are shown by the solid lines. The core mass function used in our simulations is shown by the solid black line. The IMFs are plotted for several values of the star formation efficiency: $\eta = 0.3$ (densely dashed), $\eta = 0.5$ (dotted), $\eta = 0.9$ (dashed), and $\eta = U[0, 1]$ (dash-dotted). The grey shaded region on the left of both plots shows the brown dwarf regime. The functional forms of the Salpeter and Chabrier IMFs were generated using `https://github.com/keflavich/imf`. 39

2.2 Top: Observed multiplicity fractions (blue squares) and triple high order fractions (red circles) from various sources listed in table 1 of Offner et al. (2022). The blue lines and red lines show the multiplicity fractions and triple higher order fractions (respectively) from my model using self-similar fragmentation and ejection rules from section 2.2.1. The values for the MFs and THFs are plotted for several values of the star formation efficiency: $\eta = 0.3$ (densely dashed), $\eta = 0.5$ (dotted), $\eta = 0.9$ (dashed), and $\eta = U[0, 1]$ (dash-dotted). Bottom: Companion star fractions following the same rules as the top plot. 40

2.3 Multiplicity fractions, triple/higher-order fractions (left) and companion star fractions (right) for four self-similar model simulations. From top to bottom, N_* is selected randomly for each core from a uniform distribution in the range $1-6$, $2-6$, $3-7$, and $4-8$. 43

2.4 IMFs from the Bonnor-Ebert mass dependent model. See caption of Figure 2.1 for more details. 45

2.5 Multiplicities from the Bonnor-Ebert mass dependent model. See the caption of Figure 2.2 for more details. 46

2.6 Conditions for fragmentation in the hybrid model. The histogram shows the core mass distribution in log space. The vertical dashed lines show the different mass ranges with the text above each section stating the possible values of N_* (uniformly weighted) for a core in the corresponding mass range. 48

2.7 IMFs from the hybrid fragmentation model. See the caption of Figure 2.1 for more details. 49

2.8 Multiplicities from the hybrid fragmentation model. See the caption of Figure 2.1 for more details. 50

2.9 IMFs from the semi-random fragmentation model where low mass stars are ejected from multiple systems following the Sterzik & Durisen (1998) decay rules. See the caption of Figure 2.1 for more details. 52

2.10 Multiplicities from the semi-random fragmentation model where low mass stars are ejected from multiple systems following the Sterzik & Durisen (1998) decay rules. See the caption of Figure 2.2 for more details. 53

2.11 Multiplicities from the hybrid fragmentation model where there are strict rules on system decay, which are tailored to replicate the observed MFs, THFs, and CSFs. The densely dashed line shows the multiplicity values for various mass ranges when the star formation efficiency is set to $\eta = 0.6$. 56

3.1 Diagram of an elliptical orbit. 63

3.2 Diagram of an elliptical orbit inclined and rotated relative to an observer. The orbit of the companion is inclined at an angle i from the $x - y$ plane and rotated through an angle ϕ around the z-axis. The true anomaly (ν) of the companion is shown measured relative to periastron. 65

4.1 Diagram of a triple system. The diagram depicts the orbit of secondary and tertiary stars around a primary star. Each orbit is inclined with an inclination i relative to an observer and rotated through an angle ϕ about an axis perpendicular to the line of sight. The true anomaly of each star is measured from periastron, assuming periastron is coincident with the line of sight for $\phi = 0°$. 74

4.2 On sky projection of system B17 at two epochs. The position of the companion star at the first and second epochs of observation are marked as 1 and 2 respectively, with the direction of the star's on sky motion shown by the arrow. The primary star is located at (0,0) in both observations. The axes are in au. 80

4.3 The final probability density functions for system B17 show as a histogram (top) and a cumulative distribution function (bottom) for the semi-major axis (left), eccentricity (middle), and inclination (right). The true parameters for the semi-major axis, eccentricity, and inclination are shown as the magenta dashed lines on each plot, and the minimum projected separation of the two stars (in au) is shown by the black dotted lines on the semi-major axis plots. The shaded regions represent the 68 per cent confidence intervals on each of the orbital parameters. 81

4.4 Corner plot of parameters a, e, i, ϕ, and M for system B17, with solid blue lines representing the true values and the shaded blue regions showing the `FOBOS` 68 per cent confidence intervals. The panels at the top of each column show the probability density functions for each orbital parameter individually and all other panels show two dimensional covariance of each combination of parameters. 83

4.5 On sky projection of system B4 at two epochs. Annotations and axis units are as in Figure 4.2. 84

4.6 Probability density functions for system B4. Legend as in Figure 4.3. . . 85

4.7 Histograms and cumulative distribution functions for semi-major axis, eccentricity, and inclination for the inner orbit in the system T19. The grey shaded regions show the 68 per cent confidence interval for each parameter. The magenta dashed lines represent the true value of each orbital parameter and the black dotted line shows the maximum projected separation of the primary and secondary star out of the two observations. 88

4.8 Histograms and cumulative distribution functions for semi-major axis, eccentricity, and inclination for the outer orbit in the system T19. The grey shaded regions show the 68 per cent confidence interval for each parameter. The magenta dashed lines represent the true value of each orbital parameter and the black dotted line shows the maximum projected separation of the primary and secondary star out of the two observations. 89

4.9 Corner plot for triple system 19, with solid blue lines representing the true orbital parameters (available in online data) and the blue shaded regions showing the `FOBOS` 68 per cent confidence intervals. Sample size of 1000 matches. 92

4.10 Histograms and cumulative distribution functions for semi-major axis, eccentricity, and inclination for the inner orbit of system T25. Legend as in previous figure. 93

4.11 Histograms and cumulative distribution functions for semi-major axis, eccentricity, and inclination for the outer orbit of system T25. Legend as in previous figure. 94

4.12 Zoom in of corner plot of the semi-major axis vs eccentricity solutions for system T25. The blue points on the bottom left plot represent all systems for which the mean anomaly is $M < 90°$ or $M > 270°$ (i.e. the star is closer to periastron) and the red points for $90° < M < 270°$ (the star is closer to apastron). 95

4.13 On sky projection of a binary system with three epochs of observation. The position of the star at the first, second and third epoch is marked by the numbers 1, 2 and 3 respectively. The primary star is centred on (0,0) for all observations and the axes given in au. 97

4.14 Cumulative distribution for a binary system with 3 epochs of observation. The top three plots show the PDFs using all three epochs together. The bottom plots show the PDFs from each possible pair of observations (blue: epochs 1 and 2, orange: epochs 2 and 3, and red: epochs 1 and 3). The grey shaded regions represent the 68 per cent confidence interval for each CDF. 98

4.15 Corner plot of the semi-major axis, eccentricity and inclination for the system shown in Figure 4.13. The true value of each parameter is indicated by the solid vertical blue line. 99

4.16 Corner plot for the orbit of 2M 0103-55 (AB) b with respect to 2M 0103-55 (AB). The top panels of each column show the `FOBOS` probability distribution functions for semi-major axis (left), eccentricity (middle), and inclination (right). The green solid lines on these panels show the OFTI median values and the green shades regions show their 68 per cent confidence intervals (Blunt et al., 2017, Table 20). The grey shaded regions are the `FOBOS` 68 per cent confidence intervals. 101

4.17 Corner plot showing the probability density functions for semi-major axis (top left), eccentricity (top middle), and inclination (right) for the low mass companion HD 206893 B. The other panels in the figure show the covariances of each of these parameters. The solid green lines show the most probable values for each orbital parameter obtained by Ward-Duong et al. (2021) and the green shaded regions represent their 1σ error ranges. The grey shaded regions are the `FOBOS` 68 per cent confidence intervals. . 103

4.18 Subsample of 200 randomly selected orbital fits for HD 206893 B using the four epochs of VLT/SPHERE astrometric observations (black circles). The observational errors on the measurements are plotted as error bars on the black points, but are too small to be noticeable on this scale. The lighter/yellower orbits correspond to systems with inclinations closer to face-on (90°) and the darker/bluer orbits closer to edge-on (0°). The primary star is located at (0,0). 104

5.1 The effects of different physical/orbital parameters of binary systems on the observed separation distribution. The red histogram shows the semi-major axis distribution of the sample and the grey histogram shows the separation distribution in au. All binaries in the sample have a semi-major axes drawn from a uniform distribution in the range 700-100 000 au. Each subplot shows results for when all orbital conditions are fixed except from one (the variable parameter is stated in the top right corner of each panel).110

5.2 Histogram showing the projected separation of binaries with semi-major axes drawn from a uniform distribution in the range 0-100 000 au. The plot shows the effects of the orbital parameters only, with the distance being fixed at 1kpc. 111

5.3 CDF with the same values as Figure 5.2 111

5.4 Diagram depicting the structure of a binary search tree of height $h = 3$ for a 1-D data set. The example data is shown by the values in boxes at the top of the diagram. The root node (level 1) bisects the data. Two child nodes are added on either side of the root node in the second level, bisecting each data subset. On the final level, there are four 'leaf' nodes added, one to the left and one to the right of each of the nodes from level 2.117

5.5 Graphical representation of the binary tree algorithm. The 64 black circles are randomly generated data points from uniform distributions. The points are first divided into two groups along the x-axis (1, pink) by adding a node. Each of these subsets is split again on the y-axis (2, purple) and two additional nodes added. The pattern continues, with 4 nodes added along the x-axis in the next level (3, orange) followed by 8 on the y-axis (4, blue). This represents a binary tree with a height (h) of 4. 118

5.6 Grid of binary tree tests on randomly generated datasets from a multivariate Gaussian distribution. On each plot there are two datasets; red points and orange points. The black dashed lines show the binary tree cells for the red points, and the blue dashed lines show the cells for the orange points. Each dataset in the left column is divided into 32 cells and the right column is divided into 64 cells. The number of points in each data set is $N = 1000$ (top row), $N = 5000$ (middle row), and $N = 9000$ (bottom row). 120

5.7 Best fit simulation for a binary population with a lognormal semi-major axis distribution, with parameters $\mu_a = 10.99$, $\sigma_a = 0.19$, $\mu_{\delta\mathrm{mag}} = 2.76$ and $\sigma_{\delta\mathrm{mag}} = 2.65$. The fraction of cases detected from an initial binary sample of 1×10^6 objects was 3.45%. 124

5.8 Semi-major axis distribution for the fit above. 125

5.9 Distance distribution for the best fitting model after the selection effects have been applied (grey) compared to the true distances distribution of the observed binaries (red). 126

5.10 Best fit model, with parameters $\mu_a = 2.12 \times 10^4$, $\sigma_a = 2.85$, $\mu_{\mathrm{dmag}} = 2.89$ and $\sigma_{\mathrm{dmag}} = 3.19$. The number of systems detected from an initial binary sample of 50 000 objects was 2.05% and the Goodness of fit was -1243.61 (compared to the 'best fit' value of -1170.54). 127

5.11 Semi-major axis distribution for the fit above. 127

A.1 The system (top) and single star (bottom) IMFs for the self-similar model. On both plots, the Salpeter (orange), Chabrier (blue) and Maschberger (pink) IMFs are shown by the solid lines. The core mass function used in our simulations is shown by the solid black line. The IMFs are plotted for several values of the star formation efficiency: $\eta = 0.3$ (densely dashed), $\eta = 0.5$ (dotted), $\eta = 0.9$ (dashed), and $\eta = U[0, 1]$ (dash-dotted). The grey shaded region on the left of both plots shows the brown dwarf regime. 150

A.2 Top: Observed multiplicity fractions (blue squares) and triple high order fractions (red circles) from various sources listed in table 1 of Offner et al. (2022). The blue lines and red lines show the multiplicity fractions and triple higher order fractions (respectively) from my model using random fragmentation and Sterzik & Durisen (1998) **secular decay** rules. The values for the MFs and THFs are plotted for several values of the star formation efficiency: $\eta = 0.3$ (densely dashed), $\eta = 0.5$ (dotted), $\eta = 0.9$ (dashed), and $\eta = U[0, 1]$ (dash-dotted). Bottom: Companion star fractions following the same rules as the top plot. 151
A.3 IMFs from the Bonnor-Ebert mass dependent model. These results are from a model that uses the Sterzik & Durisen (1998) **secular decay** rules for dynamical processing. See caption of Figure A.1 for more details. . . 152
A.4 Multiplicities from the Bonnor-Ebert mass dependent model. These results are from a model that uses the Sterzik & Durisen (1998) **secular decay** rules for dynamical processing. See the caption of Figure A.2 for more details. 153

B.1 Corner plot showing orbital parameter covariances for test system B4. See Fig. 4.4. 156
B.2 Corner plot for triple system 25. Sample size of 1011 matches. See Fig. 4.9. 157

List of Tables

2.1 Parameters used to generate the core mass function for random sampling. 35

2.2 The decay probabilities for $N = 2 - 7$ systems. The column headings show the different decay channels defined according to Sterzik & Durisen (1998), where BS: binary system and $N - 2$ singles, TS: triple system and $N - 3$ singles, QS: quadruple system and $N - 4$ singles, BBS: two binary systems and $N - 4$ singles, and TB: one triple system and one binary system and $N - 5$ singles. The $N = 3, 4$ and 5 rows contain the values from Sterzik & Durisen (1998) (for a clump mass spectrum), and the other rows (in bold) contain the extrapolated values for lower/higher order systems based on these probabilities. 54

4.1 Definitions of the physical and instantaneous orbital parameters along with their allowed ranges. 76

5.1 Ranges for each of the orbital parameters (and distances). 108

5.2 The average separation of binary stars as a fraction of their semi-major axis, for different eccentricity ranges. 112

5.3 The first 10 rows of YSO data from the Shenton et al. sample. SOURCEID: ID of companion star, CENTREID: ID of the primary star, d: distance, M_p: primary mass, s: separation, BSD: background star density, P_{chance}: probability that the companion is a chance alignment, δmag: magnitude difference between the primary and the companion. Note that a single primary can have multiple companions attributed to it, and each companion has no impact on any other companions detected around the same primary. Omitted from this table are the RA and dec of each star. The full data set has 842 rows. 114

5.4 Parameter ranges sampled using the Monte Carlo method to find the best fit values. Note that these values are *not* for the semi-major axis parameters because of the use of a lognormal distribution. 123

B.1 The orbital parameters, masses, and the time between observations for each of the test binary systems. The leftmost column shows the index used to refer to each system in the text. From left to right, the columns contain the semi-major axes (in au), eccentricities, inclinations (in degrees), orientations (in degrees), mean anomalies (in degrees), the masses of the primary and secondary stars (in solar masses), and the time between observations (in years). All values quoted to 2 d.p. (excluding eccentricity, which is quoted to 3 d.p.). Any values with fewer significant figures are followed by a 0. 159
B.2 The true orbital parameters a, e, and i for each system compared to the 68% and 95% confidence intervals obtained from simulations. 162
B.3 The orbital parameters, masses, and the time between observations for each of the test triple systems. 165
B.4 Confidence intervals for all secondary stars obtained from each of the 60 test simulations. The leftmost column shows the index used to refer to each system in the text. Column 2 shows the true values of the semi-major axis for each system, followed by the 68% and 95% confidence intervals for a in columns 3 and 4 respectively. The eccentricity values and confidence intervals are stated in columns 5, 6, and 7, and this is repeated for inclination in the final three columns. The inclination confidence ranges quoted in columns 9 and 10 represent the positive component of the bimodal inclination PDF, which is mirrored for negative values. 168
B.5 Confidence intervals for all tertiary stars obtained from each of the 60 test simulations. See table B.4. 171

Chapter 1

Introduction

1.1 Foreword

One of the first constellations that my dad pointed out to me when I was a child was the Ursa Major (the Big Dipper). It is one of the most famous constellations in the sky and many people in the northern hemisphere, whether they have any interest in astronomy or not, can recognise it. Out of the seven stars in the Big Dipper asterism, one is a quadruple system (Mizar), one is a triple system (Megrez) and several are believed to be binaries (Dubhe, and potentially Phecda) (Shaya & Olling, 2011). Observational surveys searching for multiple star systems show that this is typical for high-mass stars, as $\sim 50\%$ of Sun-like stars have companion(s) and $\sim 80 - 100\%$ of massive stars have companions (Offner et al., 2022, and references therein).

With the ongoing advancements in astronomical instrumentation, observations of multiple systems are yielding a wealth of information regarding their formation histories, orbital properties, and stellar evolution. Observing binary stars can give us unique information that single stars cannot provide, such as direct determination of the masses of the stars. Additionally, the remarkable spatial resolution of the James Webb Space Telescope (JWST) allows for unparalleled precision in observing binary protostars, granting us fresh perspectives and invaluable insights into the earliest stages of multiple system formation and the star formation process. The separation distributions of these protostars can tell us the fraction of systems that formed through core fragmentation vs disc fragmentation or dynamical capture.

Alongside observations, theoretical models are invaluable when studying multiple systems, as they provide a framework to understand the observed properties and behaviours of these systems. By comparing the results of theoretical models with multiple system

Figure 1.1: The Big Dipper/Ursa Major. Credit: ESA/Hubble, A. Fujii

characteristics (such as the orbital parameters, mass estimates, and formation histories), we can investigate complex phenomena and gain insights into the underlying physical processes occurring within binary star systems. Simulations can predict how and why stellar multiplicity changes depending on the environment, along with which multiplicity properties are a result of the star formation process and which are due to occurrences later in the system's evolution.

1.2 Molecular clouds and star-forming regions

The term 'star-forming region' is a general term referring to any environment where star formation takes place. Most stars form in dense environments and are dispersed into lower density environments, such as the Galactic field, which has a stellar density of ~ 0.1 stars pc^{-3} (Binney & Tremaine, 2008). They are dispersed either because they form unbound from the host environment or due to dynamical interactions and relaxation. It is generally accepted that most stars form in associations (loosely bound or unbound groups of stars with a density of ~ 6 stars pc^{-3}) rather than dense open clusters (~ 5000 stars pc^{-3}) (Lada & Lada, 2003; King et al., 2012a; Wright et al., 2022).

Figure 1.2: Young star-forming region NGC 346 in the Small Magellanic Cloud, taken with the NIRcam instrument on JWST. NASA's 'Astronomy Picture Of the Day' 13/01/2023. Image credit: NASA, ESA, CSA.

1.2.1 Molecular clouds and the interstellar medium

Molecular clouds are over-dense regions of the interstellar medium (ISM), consisting primarily of molecular hydrogen, H_2. They typically have densities of $n_{\mathrm{H}_2} \sim 100\ \mathrm{cm}^{-3}$, Which is significantly higher than the ISM (typically $n_{H_2} \sim 0.1 - 1\ \mathrm{cm}^{-3}$). Supersonic turbulence plays a crucial role in shaping the structures of molecular clouds. It occurs when the velocity of the moving gas within a region exceeds the speed of sound, generating shock waves that cause over-densities within the medium. This can be induced by stellar feedback, supernova shock fronts, gravitational instabilities, or passage through dense regions of the galaxy, such as the spiral arms (McKee & Ostriker, 2007; Krumholz et al., 2014). As such, molecular clouds are inhomogeneous and have a clumpy structure (Ward-Thompson & Whitworth, 2011).

In recent years, radio, sub-mm, and far-infrared (IR) observations have allowed us to build up a clear picture of the hierarchical structure of GMCs and their life cycles in different environments (i.e. Temi et al., 2018; Chevance et al., 2020; Muraoka et al., 2020). Observationally, they are characterised by large amounts of CO emission, and many studies have determined that GMCs typically have masses of $\sim 10^4 - 10^6\ \mathrm{M}_\odot$, temperatures of $\sim$ 10K, mean densities $n_{H_2} \sim 100$ cm^{-3} (e.g. Solomon et al., 1987; Scoville et al., 1987; Dame et al., 2001; Ward-Thompson & Whitworth, 2011), and sizes of $10 - 100$pc. Both local and extragalactic GMCs have been observed and linked with areas of high and low levels of star formation.

Theoretical models of star formation from GMCs initially predicted that it was a slow and quasi-static process that occurred as a result of magnetic fields (e.g. Shu et al., 1987) or purely gravitational free-fall collapse (e.g. Zinnecker, 1984). These models predicted a star formation timescale of $\sim$ 100 Myr, which exceeds the typical observed lifetime of a molecular cloud ($\sim 10 - 30$ Myr, depending on the rate of accretion, McKee & Ostriker, 2007; Chevance et al., 2020). However, subsequent simulations found that turbulence and gravitational instability contribute to cloud fragmentation, filament production, and star formation (Bate et al., 2003; Seifried & Walch, 2015; Federrath, 2016).

1.2.2 Filaments and dense cores

Molecular clouds are threaded with a network of filaments. Large scale filaments typically have lengths of $\sim$1 pc and widths of $\sim$0.1 pc (Arzoumanian et al., 2011), but within large filaments are smaller levels of filamentary substructure, as can be seen in Figure 1.2. It is believed that magnetic fields, photo evaporation, stellar feedback, differential rotation and gravitational collapse all result in filamentary structures (Hacar et al., 2022; Pineda et al., 2022), which explains why this structure is observed in so many different environments and on such a range of scales. Gas flows along the length of the filament, directed by magnetic fields, and accumulates in over-dense regions that eventually fragment to form cores (Könyves et al., 2015; Lee et al., 2017; Hacar et al., 2018; André et al., 2019; Motte et al., 2022).

The Jeans criterion

Fragmentation occurs when internal pressure is unable to support the core against gravitational collapse. This is known as the Jeans instability, and was first quantified by Jeans (1902). By considering small deviations from hydrostatic equilibrium (the scenario in which pressure and gravity are balanced), Jeans derived equations for the Jeans mass,

$$M_J \simeq \left(\frac{5kT}{G\mu m_H}\right)^{\frac{3}{2}} \left(\frac{3}{4\pi\rho_0}\right)^{\frac{1}{2}} = \frac{4\pi c_s^3}{3G^{3/2}\rho^{1/2}}, \tag{1.1}$$

and the Jeans length,

$$R_J \simeq \left(\frac{15kT}{4\pi G\mu m_H \rho_0}\right)^{\frac{1}{2}} = \sqrt{\frac{c_s^2}{G\rho}}, \tag{1.2}$$

where k is the Boltzmann constant, T is the temperature, μ is the mean molecular weight, m_H is the mass of hydrogen, ρ_0 is the initial density, and c_s is the speed of sound in the medium. According to the Jeans criteria, a core will collapse if it has a mass greater than the Jeans mass or a length greater than the Jeans length.

Bonnor-Ebert mass

The stability of a core can also be quantified using the Bonnor-Ebert mass (Bonnor, 1956; Ebert, 1955). Much like the Jeans instability, the Bonnor-Ebert mass has a critical value ($M_{\mathrm{BE,crit}}$) above which the core will collapse. This critical value is the maximum mass of an isothermal gas cloud can have whilst remaining in hydrostatic equilibrium. The Bonnor-Ebert mass derivation accounts for the presence of external pressure on the gas cloud, unlike the Jeans mass. In general, M_{BE} is given by

$$M_{\mathrm{BE}} = 1.82 \left(\frac{\bar{n}}{10^4\ \mathrm{cm}^{-3}}\right)^{-0.5} \left(\frac{T}{10\ \mathrm{K}}\right)^{1.5} M_{\odot}, \tag{1.3}$$

where $\bar{n}$ is the volume density of the core and T is the temperature. The equation for M_{BE} can be expressed in many forms, and is often represented in terms of parameters such as the external pressure, density, or speed of sound in the medium (the version in Equation 1.3 is from Lada et al., 2008). Due to its dependence on the properties of the host cloud, the critical Bonnor-Ebert mass can vary depending on the host environment. For low-mass star-forming regions, the value is typically on the order of $\sim 1M_{\odot}$ (McKee & Ostriker, 2007), but it can vary from $\sim 0.6M_{\odot}$ in the Aquila cloud (Könyves et al., 2015) up to $\sim 2M_{\odot}$ in the Pipe nebula (Lada et al., 2008).

1.2.3 The core mass function

The dense cores that form from filaments are the birth environment of stars (di Francesco et al., 2007; André et al., 2014), and typically cores are defined as the precursors of either single stars or gravitationally bound binaries/multiple systems. Observationally, cores without clear indicators of a protostar are classified as ‘starless’, but may also be counted as ‘prestellar’ (i.e. go on to form cores later) if the mass is $> 2M_{\mathrm{BE,crit}}$ or it appears gravitationally bound (e.g. Könyves et al., 2010).

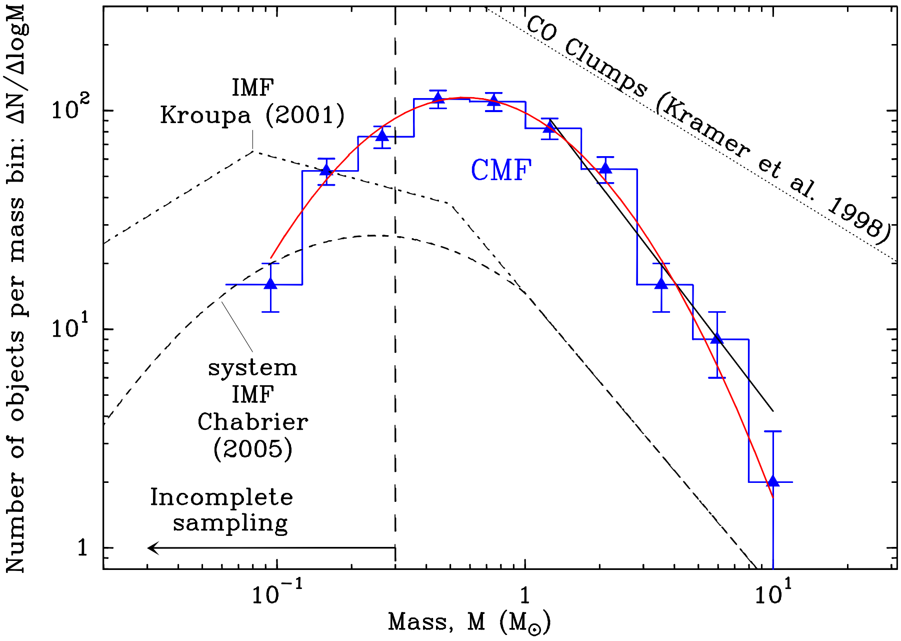

Figure 1.3: Prestellar core mass function (blue histograms) in the Aquila rift cloud. The red solid line shows a lognormal fit to the data, which peaks at $\sim 0.6\ M_{\odot}$. The solid black line shows a power-law slope of -1.5 ± 0.2. The Kroupa (2001) and Chabrier (2005) IMFs are shown for reference. The region to the left of the vertical dashed line suffers from incomplete sampling. Figure from André et al. (2010).

Filaments and cores have been extensively mapped in recent years, using two main methods; mapping using molecular tracers (e.g Benson & Myers, 1989; Scibelli & Shirley, 2020) and dust continuum mapping (e.g. Motte et al., 1998; André et al., 2010; Könyves et al., 2010; Massi et al., 2019; Marsh et al., 2016; Di Francesco et al., 2020).

A key program in dust continuum mapping is the *Herschel* Gould Belt Survey (HGBS, André et al., 2010), which observed molecular clouds within 500pc at infrared and sub-mm wavelengths. In the initial results released from this survey, they detected 500 prestellar and protostellar cores in the Aquila rift cloud, which were used to generate a dense core mass spectrum. The core mass function (CMF) (shown in Figure 1.3) has an approximately lognormal shape, with a high mass slope with an exponent of $\Gamma = -2.35$ and a peak mass of around $\sim 1 M_{\odot}$. Due to incomplete sampling, the low mass end of the CMF is not well defined, but seems to have a lognormal shape (André et al., 2010).

Similarly, Di Francesco et al. (2020) utilized the *HGBS* data for the Cepheus Cloud by extracting 832 dense cores from the data to generate a CMF. Their CMF is comparable to the CMF for the Aquila rift cloud; it peaks at $\sim 0.56 M_{\odot}$ and has a power law slope at the high mass end. It also suffers from incomplete sampling at low masses, but when the population of 'candidate' cores are included rather than just 'robust' cores, the low mass slope becomes significantly shallower. This implies that there are probably many more low mass cores than it is currently possible to confirm with current observations and core finding algorithms.

A key feature in the majority of dense core surveys is the lognormal/power-law functional form of the CMF, which appears to represent the shape of the CMF in most regions (André et al., 2014) (i.e. it is 'universal'). The relation between the CMF and the stellar initial mass function (IMF) are discussed in Section 1.4.3.

1.3 Star formation

The initial phase of core formation is the fragmentation of filaments into smaller, dense regions, which collapse gravitationally and isothermally to form a dense core. Cores can either form individual stars or fragment to form multiple systems. In this section, I will discuss the collapse of a prestellar core to form a single star, and move on to discussing core fragmentation and multiple system formation in Section 1.5.

The star formation process can be described using four different classes/phases; Class 0, I, II, and III (Lada, 1987; Andre et al., 1993), which are defined by the shapes of their spectral energy distributions (SEDs). In all phases, we refer to the newly forming star as a young stellar object (YSO). Classes 0 and I represent the protostellar phase of formation and classes II and III represent the pre-main sequence (pre-MS) phase.

1.3.1 Core collapse

The initial phase of star formation is the isothermal collapse of the protostellar core, which will occur if the core mass exceeds the Bonnor-Ebert mass. In this phase, the temperature of the core is only ~10 K (di Francesco et al., 2007; Launhardt et al., 2013) and the opacity is low enough that the energy released through the gravitational collapse is radiated away from the core, maintaining the low temperature (Larson, 1969). The collapsing core can only be observed through it's far IR/sub-mm thermal radiation. The isothermal collapse occurs on the free-fall timescale of the core,

$$t_{\rm ff} = \left(\frac{3\pi}{32G\rho}\right)^{1/2}, \tag{1.4}$$

where ρ is the density of the core.

As the density of the core increases due to collapse, the optical depth also increases to the point where energy can no longer be radiated away from the core. This occurs at $\rho \sim 10^{-13}$ g cm^{-3} (Larson, 1969). This causes the core to enter an adiabatic phase, in which all thermal energy released in contraction stays within the core. As a result, the pressure within the core builds up until it is enough to stop the contraction. When this occurs, the core is in hydrostatic equilibrium and is classed as a protostar (Ward-Thompson & Whitworth, 2011).

The star formation process differs depending on the mass of the star; in particular the contraction timescales, the development of radiative/convective zones, and the time taken to reach the hydrogen burning stage. In Section 1.3.2, the process for forming Sun-like stars is described, with sections 1.3.3 and 1.3.4 focusing on brown dwarfs and high-mass stars respectively.

1.3.2 Low mass star formation

The youngest protostars are classified as Class 0 objects. They are characterised observationally by a black body (BB) SED caused from radiation from the dust in the envelope and a deeply embedded hydrostatic object. The SED peaks at far-infrared and sub-mm wavelengths, as shown in the top left plot in Figure 1.5.

Initially, the protostar is significantly smaller than the envelope (which extends out to $\sim 10,000$ au). The protostar accretes approximately $\sim 50\%$ of it's mass from the envelope over a timescale of $\sim 0.1 - 0.3$ Myr (Andre et al., 2000; André et al., 2007; Ward-Thompson & Whitworth, 2011; Dunham et al., 2015). This accretion begins to produce weak bipolar outflows and begins flattening some of the material in the envelope into a disc (illustrated in panel (b) of Figure 1.4).

Many Class 0 protostars are believed to be in multiple systems, formed by fragmentation of the core during the isothermal phase (Ward-Thompson & Whitworth, 2011; Tobin et al., 2022).

Class I

In the Class I phase, the SED is still dominated by mid-IR to far-IR emission, due to dust remaining in the envelope. However, as shown in the top right panel in Figure 1.5, there is also a significant IR excess indicating the presence of the disc. The typical timescale of the Class I phase is $\sim 0.1 - 0.5$ Myr (André et al., 2007; Ward-Thompson & Whitworth, 2011; Dunham et al., 2015) and the bolometric temperature increases from $T_{\mathrm{bol}} \sim 70$ K to ~ 650 K (Chen et al., 1995).

At the start of this phase, the envelope has collapsed to a region of ~ 300 au and approximately half of the material in the envelope has been accreted onto the protostar.

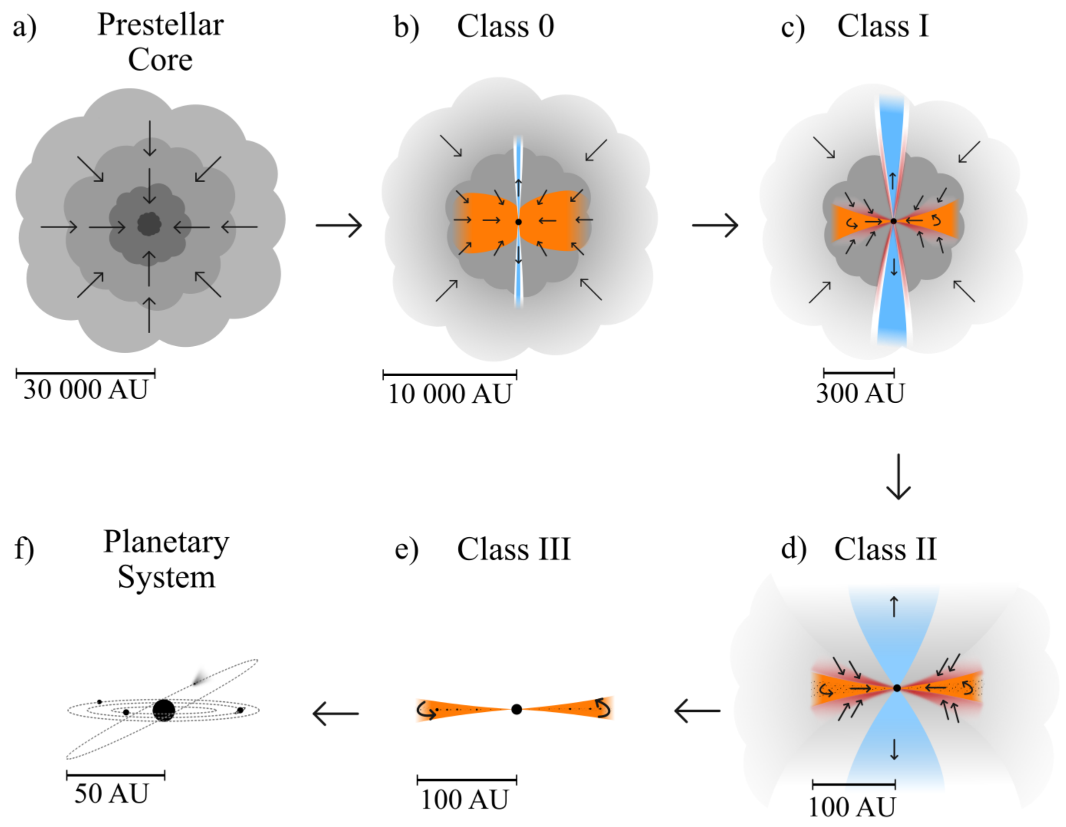
a) Prestellar Core
30 000 AU
b) Class 0
10 000 AU
c) Class I
300 AU
d) Class II
100 AU
e) Class III
100 AU
f) Planetary System
50 AU

Figure 1.4: The stages of star formation. The top left panel shows the scale of the prestellar core, spanning ~30 000 au in radius. Following the arrows to the right, the middle panel shows a class 0 protostar where the dense core is collapsing and forming a small accreting protostar. When the object reaches class I, the surrounding envelope has collapsed into a disc of radius ~100 au. Image credit: Persson (2014a).

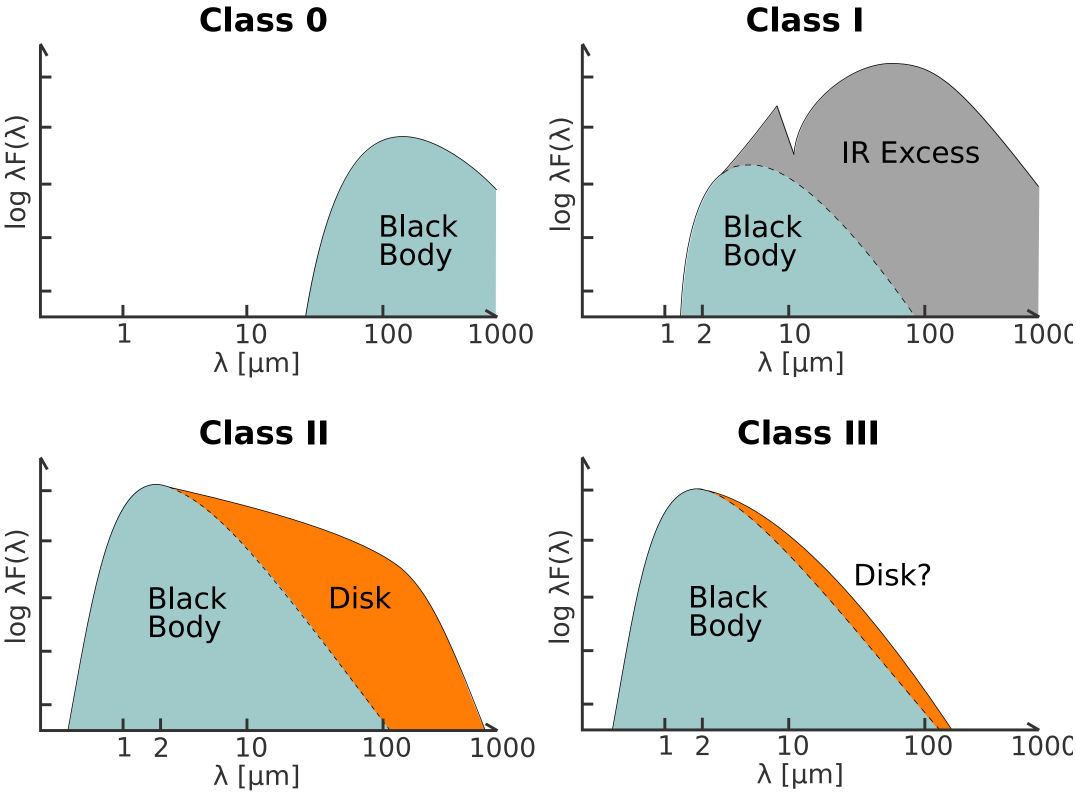

Figure 1.5: SEDs of YSOs in Classes 0, I, II, and III. In Class 0, the protostar is embedded in a dense envelope of material and is visible as a black body at far-IR wavelengths due to dust radiation. During Class I, the protostar has IR emission due to the remaining envelope and an IR excess indicating the presence of a disc. During the Class II phase, the remaining envelope has dissipated enough for the pre-MS star to be visible as a BB at optical wavelengths with a disc indicated by IR emission. Finally, in the Class III phase, the stellar BB is observed with a small contribution to the SED from a debris disc/planets. Image credit: Persson (2014b)

The material at the poles falls onto the protostar from an angle close to perpendicular, and when the infalling material collides with material in the envelope of the protostar, it creates hot, high-density regions. This produces strong bipolar outflows, which clear away some of the surrounding envelope (Carroll & Ostlie, 2017).

Class II

The Class II phase marks the beginning of the pre-main-sequence stage of star formation. Class II objects have a black body SED peaking at optical wavelengths, with an IR excess indicating the presence of a (possibly protoplanetary) disc. In this phase, the star becomes visible at optical wavelengths because most of the gaseous envelope has dissipated. The disc is thinner and may be more sub-structured than in the previous phase, extending from $\sim$ 10s-100s au and containing $\sim 1\%$ of the mass of the pre-MS star (Ward-Thompson & Whitworth, 2011).

Class II stars are also known as Classical T Tauri stars (CTTS) (if they are $<2\ M_\odot$) or Herbig Ae/Be stars (if they are $>2\ M_\odot$). T Tauri stars are defined by their variability (Joy, 1945), which is caused by accretion from the disc onto the star (Hartmann et al., 2016).

Also in this phase, the contraction of the pre-MS star increases the temperature to the point where hydrogen burning can begin ($T \geq 10^6$ K).

Class III

The Class III phase is the final pre-main sequence phase. The SED shows a similar BB spectrum to the Class II objects, but the pre-MS star is no longer accreting and the outflows have ceased. The star is surrounded by a much smaller, gas-free debris disc, which appears in the SED as a much smaller millimetre contribution on top of the BB spectrum (Hartmann et al., 2016). The pre-MS star may also be orbited by planets that formed during the Class II phase.

Stars in this phase are classified as Weak-lined T Tauri stars (WTTS) due to the relatively low intensity of emission lines compared with Classical T Tauri stars. They continue to contract and increase their temperature until hydrogen burning can begin. This is the longest of the protostellar/pre-MS phases, with the exact timescale depending strongly on the mass of the star.

During the star formation process, $\sim 1-10\%$ of the material in the host molecular cloud will be converted into star(s) (Murray, 2011; Kim et al., 2021; Chevance et al., 2022). The amount of gas in the core that is converted into stars varies (but could be as low as 20% or as high as 80%), with the remainder of the material dispersed due to accretion outbursts (Fischer et al., 2022), stellar winds, protoplanetary disc/planet formation, etc.

1.3.3 Brown dwarf formation

Brown dwarfs are the ‘missing link’ between stars and planets and are some of the most numerous objects in the universe (Luhman et al., 2007, and references therein). Their masses range from $\sim 0.012 M_{\odot}$ (the upper limit on planetary masses) to $0.075 M_{\odot}$ (the lower limit on stellar masses). Brown dwarfs never get massive enough to begin hydrogen burning, but they can fuse deuterium in their core (Ward-Thompson & Whitworth, 2011).

Brown dwarfs were first proposed theoretically in the 60s and observed unambiguously in the late 90s. Initially, there was significant debate as to whether they formed like planets (through pebble accretion) or like stars (through gravitational instability). Today, is it widely believed that most BDs form via the same mechanisms as low-mass stars, as their multiplicities, initial mass function, velocities, and spatial distribution follow the same trends as main-sequence stars at birth (Whitworth et al., 2007; Luhman, 2012).

There are many theories as to why brown dwarfs have such low masses. One theory suggests that they form from the turbulent fragmentation from the lowest mass prestellar cores (Padoan & Nordlund, 2004), meaning that they have a smaller gas reservoir to accrete from. Due to incomplete sampling at the low mass end of the CMF, it is unclear whether there are a sufficient number of low mass cores to produce the correct amount of brown dwarfs (Stamatellos & Whitworth, 2009). Secondly, the accretion of protostars in higher-mass cores (i.e. solar-type progenitor cores) could be reduced or interrupted due to photo-evaporation of the envelope from nearby high mass-stars (Whitworth & Zinnecker, 2004) or dynamical interactions with close neighbours in the star-forming region (Reipurth & Clarke, 2001; Bate et al., 2002).

Other theories suggest that most brown dwarfs form from gravitational instabilities in accretion discs around higher mass stars (i.e. Stamatellos et al., 2007, 2011); a mechanism that is discussed further in Section 1.5.

1.3.4 High-mass star formation

High-mass star formation differs from low-mass star formation in several ways. In general, high-mass stars are defined as having masses of $> 8M_\odot$. The most massive O type stars ($\geq 16M_\odot$) have some of the most drastically different star formation properties to low-mass stars.

The core accretion model of star formation (described in Section 1.3.2) begins with the collapse of the core and proceeds through the protostar (Class 0/I) and pre-MS (Class II/III) stages of star formation. However, the density of the high-mass core needed to form a high-mass star facilitates rapid gravitational collapse and accretion onto the protostar. Due to the high rate of accretion, high mass stars reach the hydrogen burning stage after only $\sim 10^5$ years (Mottram et al., 2011).

At the end of the protostellar phase, the massive star will have very strong outflows and stellar winds. These outflows/winds have a significant impact on the surrounding environment, creating cavities in the surrounding molecular cloud (known as HII regions, e.g. Churchwell, 2002).

Formation mechanisms

Competitive accretion (Bonnell et al., 2001; Bonnell & Bate, 2006) may also be an important factor in the formation of massive stars. In the competitive accretion model, the massive protostar accretes from a wider region of gas outside the dense core. This process ‘steals’ gas from lower mass cores, which often results in high-mass stars being surrounded by several lower mass stars. Bonnell et al. (2001, 2007) and Bate (2012) proposed that the competitive accretion model successfully accounts for the shape of the IMF for high masses, and can reproduce the observed multiplicity statistics of stellar systems.

Massive stars can also form through monolithic collapse. This process involves the direct collapse of a subvirial massive core to form a massive protostar, which evolves to become a high-mass star (Krumholz et al., 2005; Zinnecker & Yorke, 2007; Rosen et al., 2019). The gravitational forces within the core dominate any internal turbulence or magnetic fields, suppressing high levels of fragmentation.

In reality, both mechanisms probably produce a fraction of high-mass stars, but there is still debate as to which mechanism is dominant.

1.3.5 Planet formation

Most YSOs are surrounded by a disc during the Class I & II stages of formation. These protoplanetary discs typically extend to 10s-100s au around YSOs (Williams & Cieza, 2011). Approximately 1% of the material contained within the disc is micron-sized rocky or icy dust (Drazkowska et al., 2022), with the rest being hydrogen-helium gas.

Planet formation begins when the YSO is still an embedded Class 0 object and the disc has just begun to form. During the earliest stages of planet formation, the dusty and icy grains in the disc coalesce due to turbulence and drag forces, forming pebbles with sizes of $\gtrsim 1$ cm. These pebbles continue to grow in size through aerodynamic interactions until they reach sizes of $\sim 1 - 100$km[1]. These bodies (called 'planetesimals') are then massive enough to experience gravitational interactions with the surrounding dust/pebbles (typically ~few m to km in size, Drazkowska et al., 2022). Once gravitational interactions can occur, the planetesimal accretes much more rapidly and experiences 'runaway growth' (Greenberg et al., 1978; Raymond et al., 2014; Raymond & Morbidelli, 2022) for $\sim 10^5$ years. This stage is followed by 'oligarchic' growth, where a small number of the most massive planetesimals continue to grow, sweeping up smaller planetesimals to form a few hundred planetary embryos in < 1 Myr. The collisions that follow between these embryos build up rocky protoplanets.

However, there is a key issue with the planetary embryo model; in the inner disc, the Raymond et al. (2014) model builds up protoplanets to approximately Mars masses, and in the outer disc, Earth mass planetary embryos begin to repel small particles and suppress growth. This led to the development of the pebble accretion model, in which protoplanets accrete pebbles rather than colliding with other planetesimals (Raymond & Morbidelli, 2022; Drazkowska et al., 2022).

The most massive rocky protoplanets (≥ 10 Earth masses) in the outer disc are massive enough to attract a gaseous envelope, forming gas giants. It is also possible for very high mass planets to occasionally form through disc instability (i.e. Helled et al., 2014), in a similar way to low mass stars (see Section 1.5).

Direct imaging of exoplanets

Planets can be observed using a variety of different techniques, including radial velocity, transits, microlensing, and direct imaging, each of which probe different semi-major axis and mass ranges (Fischer et al., 2014). Direct imaging is the only exoplanet observation method that is relevant to this thesis (see work in Chapter 4). In this method, a coronagraph is used to obscure the light from the host star so that any planets can be observed directly (Currie et al., 2022). It preferentially detects planets with large masses and separations. Since both the planet and host star can be resolved, astrometric data can be obtained for the planet. Multiple epochs of astrometry for directly imaged exoplanets allow their orbital properties to be constrained.

---

[1] There are still many different theories of how pebbles grow to planetesimals, summarized in Drazkowska et al. (2022), but the details of these models and the planet formation process are outside the scope of this thesis.

1.4 Initial mass function

The initial mass function (IMF) describes the mass distribution of a group of stars at the time of their formation. It has been determined for various environments such as stellar clusters, associations, star-forming regions, the Galactic field, and other galaxies. It is calculated using stellar evolution models and mass-age-luminosity relations to convert between the observed luminosity function (LF) and the mass function (MF), and is typically defined as the number of stars (N) per unit volume (V) and per logarithmic mass interval ($d\log m$),

$$\xi(\log m) = \frac{\mathrm{d}(N/V)}{\mathrm{d}\log m} = \frac{\mathrm{d}n}{\mathrm{d}\log m}. \tag{1.5}$$

Extensive studies have shown that the IMF appears to be universal in the local universe; i.e. it is constant across all regions of space and at all times (i.e. Bastian et al., 2010; Offner et al., 2014; Clark & Whitworth, 2021). The universality of the IMF suggests that star formation itself is also the same across all times and locations. As such, it has been studied in a lot of detail and has been quantified by several empirical relationships.

The first of such relationships was determined by Salpeter (1955), and is still often used to represent star formation relations in the local universe (e.g Kroupa, 2001; Chabrier, 2003a,b). Salpeter determined that a power-law with a slope of -2.35 (-1.35 in the logarithmic form) describes the shape of the IMF for masses $\sim 1 - 10\ M_{\odot}$. This power law slope also fits the high mass slope of the CMF.

Whilst the Salpeter slope fits the IMF at high masses, more complex models are required to reproduce the distribution at lower masses. Miller & Scalo (1979) initially proposed a lognormal form of the IMF, but this under predicted the number of stars $>$20 $M_{\odot}$. Two decades later, Kroupa (2001, 2002) used a broken power-law function to model the full range of the IMF, with different indices used in different mass ranges,

$$\xi(m) \propto \begin{cases} m^{-\alpha_0} & \alpha_0 = 0.3 \pm 0.7 \quad 0.01 \geq m/M_{\odot} < 0.08 \\ m^{-\alpha_1} & \alpha_1 = 1.3 \pm 0.5 \quad 0.08 \geq m/M_{\odot} < 0.50 \\ m^{-\alpha_2} & \alpha_2 = 2.3 \pm 0.3 \quad 0.50 \geq m/M_{\odot} < 1.00 \\ m^{-\alpha_3} & \alpha_3 = 2.3 \pm 0.7 \quad 1.00 \geq m/M_{\odot}. \end{cases} \tag{1.6}$$

Whilst this is a good approximation of the shape of the IMF, and is often still used to illustrate the difference in the IMF at different masses, it might imply that there are distinct regimes in which different physical processes occur. Bonnell & Bate (2006) proposed that a segmented IMF could be caused by the effects of competitive accretion; if there is a common reservoir of gas from which multiple protostars can accrete, then the stars with the highest initial mass will accrete more readily than lower mass stars within the same reservoir. They conclude that the low mass section of the IMF results from gravitational fragmentation, whilst the higher mass slope is modified by competitive accretion. This is just one potential scenario - the exact mechanisms affecting star formation at different masses, and how this translates onto the IMF, is still highly debated.

Following Kroupa's work in developing a segmented form of the IMF, Chabrier (2003a,b, 2005) approximated the IMF by combining the lognormal distribution of Miller & Scalo (1979) with a power-law tail above $\gtrsim 1\ M_{\odot}$.

A more recent paper by Maschberger (2013) fits the IMF using a single log-logistic function, which is a 'heavy tailed' extension to a log-normal (shown in Figure 1.6). They discuss two functional forms within the paper; the L_3 IMF and the B_4 IMF. The L_3 IMF is the primary result of the paper and has a probability distribution function given by

$$p_{L^3}(m) \propto \frac{\left(\frac{m}{\mu}\right)^{-\alpha}}{\left(1 + \left(\frac{m}{\mu}\right)^{1-\alpha}\right)^{\beta}}. \tag{1.7}$$

Masses can be sampled from the Maschberger IMF very easily, using the quantile function

$$M_c = \mu\left(\left[u\left(G(m_u) - G(m_l)\right) + G(m_l)\right]^{\frac{1}{1-\beta}} - 1\right)^{\frac{1}{1-\alpha}}, \tag{1.8}$$

where μ is the scale parameter, $u \in [0, 1]$, $G(m_l)$ and $G(m_u)$ is the auxiliary function (equation 1.9) associated with the Maschberger IMF evaluated at the lower and upper mass limits respectively, β is the low-mass exponent and α is the high mass exponent.

$$G(m) = \left(1 + \left(\frac{m}{\mu}\right)^{1-\alpha}\right)^{1-\beta}. \tag{1.9}$$

As it is so easy to draw masses randomly using the quantile function, the Maschberger IMF is used for all simulations in Chapter 2.

1.4.1 Single-star vs. system IMF

Early work modelling the form of the IMF (such as Salpeter, 1955; Miller & Scalo, 1979; Kroupa, 2001) does not account for the presence of multiple systems. As stated in the introduction of this chapter, and expanded on in Section 1.7, most stars are in multiple systems. This has major implications for the form of the IMF.

If all stars in multiple systems could be resolved perfectly, then the observed IMF would be the single-star IMF. However, as many stars are in multiples which cannot be resolved, there is also the system IMF (the IMF of the combined mass of all stars in a bound stellar system).

Both the system and single star IMFs have been parameterised by Chabrier (2003a,b) and Maschberger (2013). Figure 1.6 shows the functional forms of the system IMF (top plot) and single-star IMF (bottom plot). In both plots, the Maschberger IMF is shown in black and the Chabrier IMF shown in green. The bottom plot also shows the Kroupa segmented IMF for reference. There are two clear differences between the two functions; the single-star IMF has (a) a much shallower low-mass slope and (b) a peak value of $\sim 0.1 M_\odot$ as opposed to $\sim 0.2 M_\odot$ for the system IMF. This is because in the system IMF, an unresolved binary appears as a single star, with a mass equal to the sum of the component masses. Furthermore, low-mass stars are disproportionately missed in multiplicity surveys due to their comparatively lower brightness, making the low mass tail of the IMF most heavily affected.

1.4.2 Universal IMF

As mentioned previously, the IMF appears to be universal in the local universe, across a range of environments (including most clusters, associations, and the galactic field). The IMF in neighbouring galaxies also appears to match the shape of the IMF in the local universe.

There is still some debate about the level of variation between IMFs in different regions. For example, Taurus is one of the most highly studied nearby star-forming

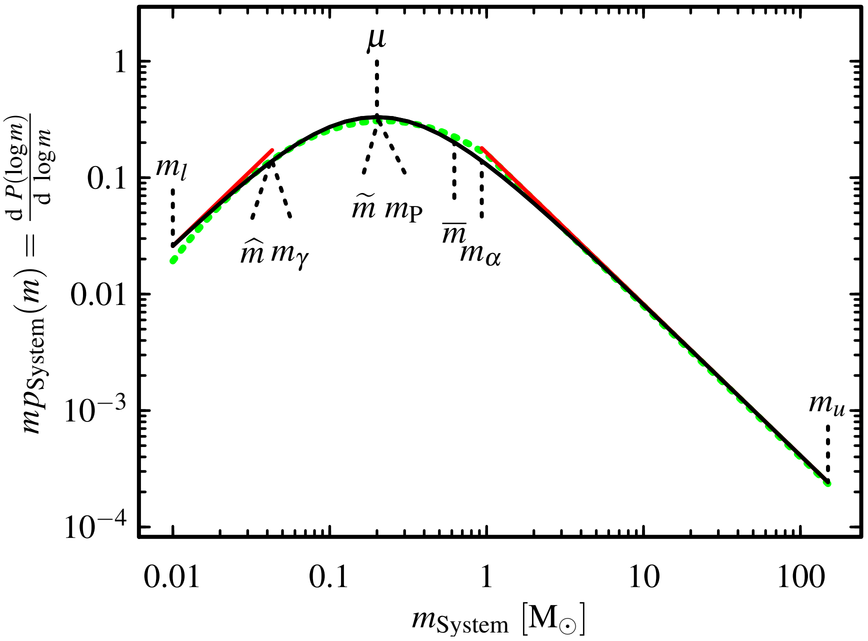

(a) System IMF

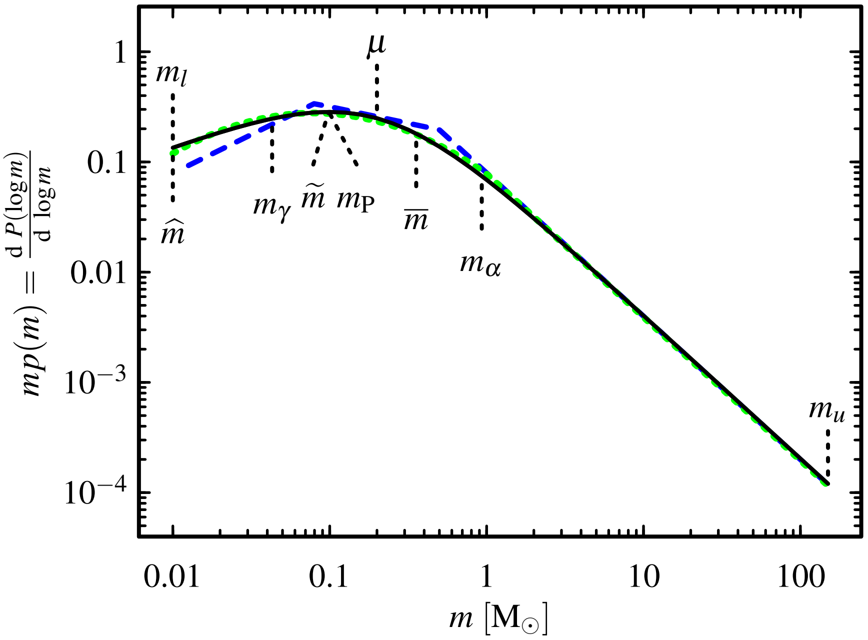

(b) Single star IMF

Figure 1.6: Probability density function from Maschberger (2013) of the system IMF (top plot, solid black line) and the single-star IMF (bottom plot, solid black line). The solid red lines on the top plot represent the power law segments of the solid black line. On both plots, the green dashed line shows the Chabrier (2003a) IMFs. In the bottom plot, the Kroupa (2001) is shown by the blue dashed line. See (Maschberger, 2013) for definitions of symbols.

regions, and the IMF for Taurus shows a definite excess of pre-MS K type stars compared to other star-forming regions (Luhman, 2012; Dib, 2014). Observations of the Orion Nebula Cluster show that there is a significant deficit of sub-stellar objects compared to both the Kroupa and Chabrier IMFs (Da Rio et al., 2012; Dib, 2014). Da Rio et al. (2012) stress that this is not an observational bias, as the data has been corrected for incompleteness. The 30 Doradus star-forming region in the Large Magellanic Cloud (LMC) appears to contain an overabundance of high-mass stars, with the best fit power law slope having in index of -1.90 rather than the Salpeter power law of -2.35 (Schneider et al., 2018).

The reasons for these variations of the IMF in particular environments is still unknown, as there is also strong evidence that the form of the IMF is mostly unaffected by environmental factors (Damian et al., 2021; Guszejnov et al., 2022). In spite of the variation between some star-forming regions, most environments have an IMF that is approximated by the canonical forms of the IMF discussed in Section 1.4, and the assumption that the IMF is universal is still a good approximation for most environments.

1.4.3 Mapping from the CMF to the IMF

The reason behind the relationship between the CMF and the IMF is still heavily debated. The similarities between the CMF and the IMF are often taken to imply a direct and self-similar mapping between the two functions, where the IMF is shifted to lower masses by a factor of ~3-5 (Motte et al., 1998; Padoan & Nordlund, 2002; Alves et al., 2007; Nutter & Ward-Thompson, 2007; Könyves et al., 2010; Guszejnov & Hopkins, 2015). This implies that the average star formation efficiency (η) of dense cores is $\sim 30\%$. Both observations and theoretical models usually agree on this value, with results from Alves et al. (2007); Goodwin et al. (2008); Könyves et al. (2015); Marsh et al. (2016) presenting values of $\sim 20 - 40\%$.

However, several models now propose that core growth via accretion from the surrounding molecular cloud is a more viable model than stars being purely fed through the material contained in a prestellar core in virial equilibrium (i.e. Bonnell & Bate, 2006; Vázquez-Semadeni et al., 2019). A recent paper by Nony et al. (2023) showed a overabundance of high mass cores in the Westerhout 43 (W43) star-forming region, implying that high-mass cores may grow more efficiently than low-mass cores. Results such as these suggest that the relation between the CMF and the IMF may not be a simple mapping.

1.5 Multiple formation

So far, I have discussed the star formation process for individual stars. However, a large fraction of stars form in binaries or higher-order multiple systems. It is believed that most binaries and higher order multiple systems form during the earliest stages of star formation. It was initially debated whether binary formation occurred due to core fragmentation during the star formation process or capture of main-sequence stars. However, Tohline (2002) determined that 'capture' is an inefficient method of forming binaries in large enough numbers to match observations in the field. Therefore, the majority of binary formation must take place during the star formation process. This theory has been supported by observations (Haisch et al., 2004; Tobin et al., 2016; Sadavoy & Stahler, 2017).

There are three main methods of multiple system formation; core fragmentation, disc fragmentation, and capture. All of these processes occur on timescales of <1 Myr and produce binaries with different separation distributions. It is generally accepted that fragmentation of cores and discs are the dominant methods of binary production (Kroupa, 1995a; Tohline, 2002; Offner et al., 2010; Moe & Di Stefano, 2017). Capture can also produce binaries, but nowhere near as frequently as the two fragmentation mechanisms.

Core fragmentation

As described in Section 1.2.2, dense cores form due to over-densities within the host filament. These cores can then fragment to form multiple gravitationally bound protostars.

Various studies have been carried out to determine which mechanisms induce core fragmentation. Both Murillo et al. (2018) and Palau et al. (2021) investigated the relationship between envelope gas temperature and multiplicity using molecular tracers in dense cores, but find that core mass and density are more highly correlated with with multiplicity than temperature. Palau et al. (2021) also showed that multiplicity is related to core density as part of their study using polarization data to study the effect of magnetic fields on fragmentation. Their results indicate that magnetic fields suppress fragmentation of both cores and discs, agreeing with simulation data (i.e. Commerçon et al., 2011; Hennebelle et al., 2011; Mignon-Risse et al., 2021).

Simulations also show that turbulence and radiative feedback can induce fragmentation, with larger amounts of turbulence potentially leading to more fragmentation and higher order multiple systems (Goodwin et al., 2004; Attwood et al., 2009; Bate, 2012;

Lomax et al., 2015; Chen et al., 2020).

Due to the nature of turbulent core fragmentation, there are some characteristic signatures that can be searched for to confirm whether a multiple system formed through fragmentation. Models such as Guszejnov et al. (2017); Haugbølle et al. (2018), and Guszejnov et al. (2020) combine turbulence, angular momentum, magnetic fields, and tidal interactions within their simulations, and determine that binaries produced via core fragmentation cannot form with separations $\lesssim$100 au. However, it is possible for a binary to migrate to smaller separations on timescales of $\sim 10^5$ years (Lee et al., 2019). Similarly, fragments separated by $\gtrsim$ 0.1 pc will either form as unbound objects or very easily become unbound due to interactions with the surrounding medium.

Disc fragmentation

In Section 1.3.2, I discussed how a natural part of the star formation process is forming a protostellar disc during the Class I-II stages. These discs are thought to be the precursors to protoplanetary discs and a site for planet formation, but it is also possible for the disc to fragment due to gravitational instabilities during the early stages of star formation and form a stellar companion (Bonnell, 1994; Stamatellos & Whitworth, 2009). Disc fragmentation is a particularly important mechanism for the formation of brown dwarfs (Whitworth & Stamatellos, 2006; Stamatellos et al., 2007).

There are two main conditions define whether a disc will fragment. The first depends on whether the disc is massive enough to be gravitationally unstable. This can be quantified using the Toomre parameter (Toomre, 1964),

$$Q = \frac{c_s \Omega}{\pi G \Sigma} = f \frac{M_*}{M_d} \frac{H}{r}. \tag{1.10}$$

Where c_s is the sound speed in the disc, Ω is the epicyclic frequency (comparable to the angular frequency for Keplerian discs), and Σ is the surface density of the disc. The disc is likely to be gravitationally unstable if the Toomre parameter is less than the critical value, $Q \leq Q_{\rm crit} \sim 0.7 - 1$. The value of $Q_{\rm crit}$ is lower for an model of a 1-D isothermal disc, and closer to 1 for a 2-D disc (Goldreich & Lynden-Bell, 1965). Therefore, for more massive discs, $Q_{\rm crit}$ is likely to be significantly lower than 1. All of the variable parameters in Equation 1.10 are a function of the disc radius, meaning that the value of Q decreases as the radius increases. As a result, fragmentation is more likely to occur in the outer disc.

Also noted in Equation 1.10 is a different form of the Toomre stability condition. In this version, H is the scale height of the disc ($\approx c_s/\Omega$), r is the radius, and M_*/M_d is the ratio of stellar mass to the disk mass. There is also commonly a scale factor (f) based on the assumed surface density profile.

The second condition is that the disc cooling time (t_{cool}) must be comparable to, or less than, the orbital timescale,

$$t_{\mathrm{cool}} = \beta\Omega^{-1}. \tag{1.11}$$

This was first shown by Gammie (2001) and confirmed through additional simulations (Johnson & Gammie, 2003; Stamatellos et al., 2007). The condition for fragmentation is that $\beta \lesssim \beta_{\mathrm{crit}}$, with values of β_{crit} ranging from ~ 3 (from 2D simulations with a specific heat value of $\gamma = 2$ by Gammie, 2001) to ~ 30 (determined from SPH simulations by Meru & Bate, 2012) for different initial conditions.

Companions formed within the disc will typically experience inward migration due to interactions with the disc. As the companion migrates through the disc, mass is preferentially accreted onto the companion. The combined effects of migration and this preferential accretion results in a population of close binaries with approximately equal masses (Tokovinin & Moe, 2020).

Capture

Dynamical capture is another method of multiple system formation, occurring when stars that were initially not bound to one another become part of a gravitationally bound system (Parker et al., 2014). There are two main capture scenarios that can occur; N-body capture (Fabian et al., 1975; Hills & Day, 1976) and gas-mediated capture (Clarke & Pringle, 1991; Bate, 2012; Cournoyer-Cloutier et al., 2021). N-body encounters can occur between stars in dense environments, and include processes such as a close encounter of two unbound stars to form a binary, an interaction between an unbound star and a binary, or binary-binary encounters. Gas-mediated capture occurs in the early stages of star formation, as protostars interact dynamically with the host star-forming cloud and circumstellar discs of neighbouring stars to form multiple systems. The orbital evolution of multiple systems is an efficient and often chaotic process, with companions in higher-order systems being frequently ejected from their birth system and very young protostars often undergoing ‘companion exchange’, where they become bound and unbound several times during formation (Offner et al., 2022, and references therein).

Two-body capture is likely to produce close and circular binaries (i.e. Moe & Kratter, 2018, and references therein) whereas three-body may be a viable method of producing very wide binaries (i.e. Kouwenhoven et al., 2010; Moeckel & Bate, 2010; Griffiths et al., 2018). Therefore, observational techniques which probe different separations ranges can also provide insight into the formation mechanisms.

In dense star-forming regions where single stars may have close encounters with one another, they may become gravitationally bound in a multiple system (Parker & Meyer, 2014). The rate of capture in different environments is affected by the stellar density and velocity dispersion (Parker & Meyer, 2014). N-body dynamical capture cannot produce binaries as efficiently as core or disc fragmentation, due to the low frequency of dynamically favourably encounters (Tohline, 2002). However, recent work by Kuruwita & Haugbølle (2022) determined that the ratio of *close young* multiples formed by capture compared to core fragmentation is 40% to 60% respectively, indicating a higher rate of favourable gas-mediated encounters than N-body encounters.

1.6 Multiple system decay and dynamical destruction

Multiplicity fractions in young star-forming regions are typically higher than the field (Kraus et al., 2011; King et al., 2012a,b; Duchêne et al., 2018). Furthermore, observations of T Tauri stars show higher multiplicities than the field in the intermediate separation range ($\sim 10 - 300$ au), field-like multiplicities in the close separation range ($<$10 au) (i.e. Kounkel et al., 2019; Tokovinin & Briceño, 2020). This indicates that stars frequently form in multiples and are then 'processed' to make the field population.

The two methods of processing binaries are secular decay and dynamical destruction. Secular decay occurs in triple or higher-order multiple systems as a result of inherent instabilities in the system. It is independent of the environment and usually results in the lowest mass object being ejected from a triple system after several orbits (Anosova, 1986; Sterzik & Durisen, 1998; Reipurth & Mikkola, 2012). Higher-order systems can decay through a variety of channels; for example, a quadruple system may decay into two binaries, a triple and a single, or a binary and two singles (Sterzik & Durisen, 1998).

Dynamical destruction occurs due to close encounters between existing multiple systems and single stars (Heggie, 1975; Hills, 1975; Parker & Goodwin, 2012; Parker & Meyer, 2014). It can affect binaries as well as triple and higher-order systems. The rate of destruction depends on the density of the environment (Bressert et al., 2010) along with the separations, primary masses, and mass ratios of the stars (Parker & Meyer, 2014).

1.7 Multiplicity

Various multiplicity surveys have been carried out to study binaries and higher order multiple systems, characterising the relative number of stars in multiples using the multiplicity fraction (Reipurth & Zinnecker, 1993), MF,

$$\mathrm{MF} = \frac{B + T + Q + ...}{S + B + T + Q + ...}, \tag{1.12}$$

where S, B, T, and Q are the number of single, binary, triple and quadruple systems of a given spectral type. The ellipses in this equation indicate the inclusion of even higher order systems (such as quintuples and sextuples), although these systems are rare and do not change the multiplicity fraction significantly. The multiplicity fraction is also often referred to as the 'binary fraction' in the literature.

The fraction of triple or higher-order systems is given by the triple/higher-order fraction, THF,

$$\mathrm{THF} = \frac{T + Q + ...}{S + B + T + Q + ...}, \tag{1.13}$$

and the average number of companions per primary star is given by the companion star fraction, CSF,

$$\mathrm{CSF} = \frac{B + 2T + 3Q + ...}{S + B + T + Q + ...}. \tag{1.14}$$

1.7.1 Multiplicity statistics

Multiplicity is a strong function of primary mass. Figure 1.7 (from Offner et al., 2022) shows that the MF increases from a value of $\sim 20\%$ for M-dwarfs all the way up to $\sim 100\%$ for the highest mass O type stars. Additionally, the CSFs in the right hand panel show that the average number of companions per primary for massive stars is ~ 2 i.e. most massive stars are in triples or higher-order multiples.

Multiplicity surveys also often study the mass ratio distribution of binaries in the sample. The mass ratio of a system (q), is

$$q = \frac{m_2}{m_1}, \tag{1.15}$$

for a binary. For triple systems, q is given by

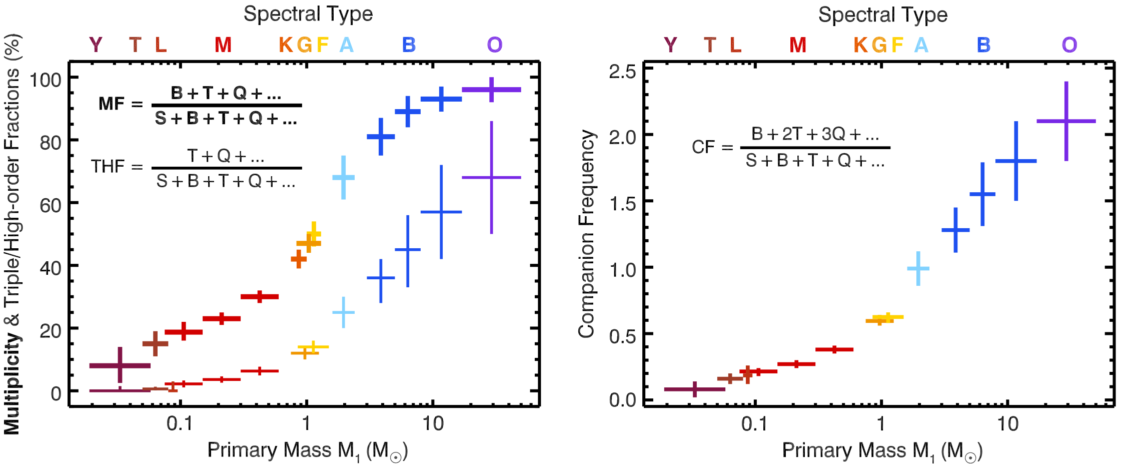

Figure 1.7: Left: the multiplicity fractions (thick lines) and triple/high-order fractions (thin lines) for different primary mass ranges. Right: The companion star fractions for different primary mass ranges. The different colours represent different spectral types, which are indicated on the top axis of each plot. The x error bars represent the total mass range sampled for which the MF/THF/CSF is calculated. The figure is from Offner et al. (2022) and the data points correspond to values from their Table 1, all of which were corrected for incompleteness.

$$q = \frac{m_3}{m_1 + m_2}, \tag{1.16}$$

where m_1, m_2, and m_3 in both equations are the masses of the primary, secondary, and tertiary stars respectively.

As well as varying with primary mass, the multiplicity statistics also depend on the separation range that is being sampled over. For example, the MF of solar type binaries with close/intermediate separations is larger than for wide separations (Deacon & Kraus, 2020; Torres et al., 2021). Whilst the definitions of ‘close’, ‘intermediate’, and ‘wide’ vary between different studies, the Offner et al. (2022) review paper uses $\lesssim$10 AU, $\sim$10-300 AU, and $\gtrsim$300 AU for each category respectively, which is adopted as the convention for this thesis.

The separation distribution for a binary sample is also dependent on the mass of the primary. Typically, the semi-major axis/separation distribution is approximated by either Öpik’s law (a distribution flat in log-space) or a log-normal distribution.

Solar type stars

Solar-type stars have most often been the focus of multiplicity surveys for the past several decades, starting with the pioneering study of Duquennoy & Mayor (1991). Duquennoy & Mayor (1991) calculate a value of MF = 58% and find a period distribution peaking at 180 yr. Subsequent work by Raghavan et al. (2010) studied a 25 pc volume limited sample of FGK dwarfs (with masses in the range of 0.75-1.25$M_{\odot}$), finding values of MF $= 46 \pm 3\%$ and CSF $= 60 \pm 4\%$. This result was supported by Tokovinin (2014), who obtained MF $= 44 \pm 3\%$ and CSF $= 62 \pm 4\%$ 67 pc volume limited sample over the $0.85 - 1.5 M_{\odot}$ range. Qualitatively, this means that slightly less than half of solar-type stars have a companion and $\sim 12\%$ are in triple or higher-order systems.

Solar-type binaries appear to have an approximately uniform mass-ratio distribution throughout the entire separation range (Duquennoy & Mayor, 1991; Raghavan et al., 2010), with a small excess of 'twins' ($q = m_2/m_1 > 0.95$, Tokovinin, 2000; Moe & Di Stefano, 2017). A uniform mass-ratio distribution means that there is an equal likelihood for the companion star to possess a mass anywhere within the $\sim 0.012\ M_{\odot} - M_p\ M_{\odot}$ range.

The overall semi-major axis distribution of the sample from Raghavan et al. (2010) is best fit with a lognormal distribution peaking at $a \approx 45$ AU (Duchêne & Kraus, 2013). The close binary fraction is consistent between measurements of the field and young open clusters (Torres et al., 2021), but there is a deficit of solar-type wide binaries in denser stellar environments (i.e. Scally et al., 1999; Deacon & Kraus, 2020). This is expected, as wide binaries have a lower binding energy and can be more easily dynamically disrupted by close encounters (Parker et al., 2011; Deacon & Kraus, 2020; Offner et al., 2022).

M-dwarfs and brown dwarfs

The multiplicity of M-dwarfs was first studied by (Fischer & Marcy, 1992). They found a multiplicity fraction of $42 \pm 9\%$, which is lower than the multiplicity of G-type stars determined by Duquennoy & Mayor (1991); one of the first indicators of how multiplicity scales with primary mass. They also found a separation distribution peaking in the range of $3 - 30$ AU. Two pivotal volume-limited surveys from Ward-Duong et al. (2015) and Winters et al. (2019) found much lower stellar multiplicity fractions of $23.5 \pm 3.2\%$ and $26.8 \pm 1.4\%$ respectively, with the latter finding a peak separation around 4-20 AU.

The mass-ratio distribution trend of M-dwarf binaries follows the same trend as for solar-type binaries (Ward-Duong et al., 2015). Brown dwarf binaries, however, have a strong preference for being in equal mass systems (Burgasser et al., 2003; Fontanive et al., 2018).

M-dwarf surveys observe a sufficient number of targets with appropriate resolution to have robust completeness limits on their observations. However, as the primary mass decreases down into the brown dwarf regime, completeness becomes much harder to estimate due to small number statistics and the close separation distribution of the systems. However, a survey by Fontanive et al. (2018) found a value of MF $= 8 \pm 6\%$ (CSF $= 8 \pm 6\%$) in 47 objects in the mass range 0.019-0.058$M_{\odot}$. Similarly, Burgasser (2007) found MF $= 15 \pm 4\%$ (CSF $= 16 \pm 4\%$) for 162 objects of 0.05-0.08$M_{\odot}$. In spite of their larger uncertainties, these two studies make it clear that the trend of increasing MF and CSF with primary mass continues into the brown dwarf regime.

Intermediate and high mass stars

The dependence of multiplicity on primary mass becomes even more evident when we consider the transition from solar-type stars up through intermediate masses ($\sim 1.5 - 8M_{\odot}$) to high masses ($\geq 8M_{\odot}$). Moe & Kratter (2021) found that moving from solar-type masses to a mass range of $1.6 - 2.4M_{\odot}$ increases the MF to $68 \pm 7\%$, and studies by Moe & Di Stefano (2017) determined MFs of $81 \pm 6\%$, $89 \pm 5\%$, and $93 \pm 4\%$ for mass ranges of $3 - 5M_{\odot}$, $5 - 8M_{\odot}$, and $7 - 18M_{\odot}$ respectively. Furthermore, Sana et al. (2012, 2014) calculated that almost all very massive stars (17-50$M_{\odot}$) are in multiple systems, presenting a MF of $96 \pm 4\%$.

In addition to high multiplicity fractions, there is also a lot of evidence from these same studies that a large fraction of intermediate and high mass stars are in triples or higher-order systems. The CSF follows the same trend as the MF, with Moe & Di Stefano (2017) finding CSFs of $128 \pm 17\%$, $155 \pm 24\%$, and 180 ± 30 for mass ranges of $3 - 5M_{\odot}$, $5 - 8M_{\odot}$, and $7 - 18M_{\odot}$. For stars above $17M_{\odot}$, the companion star fraction exceeds 2 (Sana et al., 2012, 2014).

De Rosa et al. (2014) and Moe & Di Stefano (2017) find that the mass-ratio distribution for A-type and B-type binaries across all separations are skewed towards unequal mass ratios (with a peak of $q \sim 0.3$). This same skew to low mass-ratios is observed for wide O-type binaries (Sana et al., 2012), but the mass-ratio distribution is approximately uniform (with a small twin excess) for close and intermediate O-type binaries (Moe & Di Stefano, 2017).

Pre-main-sequence stars

Obtaining accurate multiplicity statistics for protostars/pre-MS stars is a difficult task, due to the high level of obscuration from the gaseous envelope or disc.

Spectroscopy of Class II and III T Tauri stars by Kounkel et al. (2019) find close binary fractions for FGK stars that match very closely with observations of MS stars in the field. However, imaging studies in a range of different environments show an excess of companions to pre-MS stars. This excess is even more pronounced for studies of Class 0/I protostars across large separations (Tobin et al., 2022), showing that multiplicity decreases with age (from protostar formation until the star reaches the main sequence).

The separation distributions determined by Tobin et al. (2016) and Tobin et al. (2022) show bimodal distributions for both the Perseus and Orion star-forming regions, with one peak at ~ 75 au and the other at ~ 3000 au. One explanation for this is that the close binaries (around ~ 75 au) formed through disc fragmentation, whilst the wider binaries formed via core fragmentation.

1.7.2 Incompleteness and uncertainties

Incompleteness refers to the phenomenon where some objects of a particular characteristic are not included in a observational survey. For multiplicity studies, the main sources of incompleteness are detection limits meaning that faint companions are missed, the resolution of the telescope meaning that systems with a small separation cannot be resolved, or the survey strategy.

Using a volume limited sample is one way of correcting for incompleteness. Volume limited surveys mean that a set detection limit can be used for all objects in the sample, and meaningful comparisons can be made across different regions of the sky. They also mean that the incompleteness can be computed statistically and more accurate corrections can be applied to the data, based on their estimates of what kind of object might be missed in their sample. The majority of M-dwarf, Solar-type and A-type multiplicity surveys presented in this introduction are volume limited and have been corrected for incompleteness to the best of the author's ability. The exact method by which this is done is outside the scope of this thesis, but incompleteness corrected values provide a more meaningful comparisons for simulation results.

1.7.3 Nearby star-forming regions vs the field

Observations of nearby star-forming associations show a significantly higher number of multiples compared to the field (Leinert et al., 1993; Duchêne, 1999; Haisch et al., 2004; Duchêne & Kraus, 2013), whereas dense clusters typically have similar multiplicities to the field (Patience et al., 2002; Duchêne et al., 2018; Deacon & Kraus, 2020; Torres et al., 2021). More specifically, denser environments show a dearth of wide binaries (Torres et al., 2021) in comparison to close binaries, across a variety of masses.

This could be explained if the majority of stars form in multiple systems (Goodwin & Kroupa, 2005) and then undergo significant post-formation processing due to a combination of both secular (from inherent instabilities and without external perturbations) and dynamical (from encounters with other stars in dense environments and star-forming regions) decay. This lowers the multiplicity fractions and results in the field population (Goodwin et al., 2007).

In dense environments, dynamical interactions between stars are much more frequent, and both observations and theory show that the binary fractions in these regions can be lowered by up to a factor of two (Kroupa, 1995a,b; Parker et al., 2011; Duchêne & Kraus, 2013). Dynamical destruction preferentially affects loosely gravitationally bound stars (i.e. systems with large separations, larger number of companions, and potentially smaller masses).

1.8 Observing binaries and multiple systems

Binary systems can be observed in a variety of different way, and are often classified based on their detection method. These classifications include:

- **Visual binaries**: Both stars in the system can be independently resolved.
- **Eclipsing binaries**: The companion periodically passes in front of the primary star, decreasing the system luminosity.
- **Spectroscopic binaries**: Detected due to doppler shifts in a star's spectral lines due to a companion.
- **Astrometric binaries**: Detected when a star appears to 'wobble' around a point in space, even though no companion is visible.

The observational characteristics of a binary system affect the method of determining its orbital properties. For example, the light curves that can be obtained through observations of eclipsing binaries can be used to determine the effective temperatures and radii of each star. Similarly, observations of spectra from spectroscopic binaries can be used to determine the orbital phase of the system.

Visual binaries

Visual binaries are binary systems that can be resolved into two stars. Visual binaries are typically nearby and have large physical separations, both of which make the companions easier to resolve. The resolution limit on visual binaries is dictated by the seeing conditions (typically on the order of ~1 arcsecond) and diffraction limit set by the Rayleigh criterion for resolution. The Rayleigh criterion depends on both the wavelength of the light and the diameter of the telescope aperture,

$$\Theta = 1.22\frac{\lambda}{D}. \tag{1.17}$$

Individual observations of visual binaries provide the position of the stars and their separation. The motion of the stars about their centre of mass can be observed through long term monitoring of the system, and this motion can be used to estimate the orbital period, semi-major axis, and the masses of the two stars.

1.9 Summary

In this chapter, I have summarised the star formation process, the initial mass function, and current measurements of the multiplicity statistics for stars in the field.

Star formation takes place mostly in giant molecular clouds, specifically within dense cores. Cores with masses that exceed a critical value (such as the Jeans mass, M_J, or the Bonnor-Ebert mass, $M_{\rm BE}$) will gravitationally collapse to form stars. In Section 1.3.2, I described how stars are formed, and outlined the differences between low and high-mass star formation in Section 1.3.4. Dense cores may form either a single star or a multiple system.

The multiplicity of the field population of stars has been extensively studied over the past several decades. The multiplicity of field stars increases significantly with primary mass, and local star-forming regions have higher multiplicities than the field. In Section 1.7, I discussed the multiplicity fractions observed for different stellar masses in the field. It is widely believed that the field acts as the sum of all star formation and evolution from different environments, although the exact processes responsible for producing the field binary population are not well understood.

I have discussed in detail the functional form of the initial mass function (IMF) in Section 1.4. Observations show that the stellar IMF seems to be universal (the same in all regions and at all times), particularly in local, resolved stellar populations. This might suggest that star formation is always similar in how it distributes mass between stars. Furthermore, the shape of the IMF is similar to that of the core mass function (CMF), but shifted to lower masses, implying self-similar mapping between the two.

1.10 Work in this thesis

This thesis contains three chapters studying the formation and properties of multiple systems.

Chapter 2 includes my work in developing a Monte Carlo model to test various simple universal rules for star formation. The aim of this work was to find a model that could produce the canonical form of the IMF as well as the multiplicity fractions, companion star fractions, and triple/higher-order fractions of stars in the field.

In Chapter 3, I discuss the properties of elliptical orbits, and include my method for generating a 'fake' observation of a binary system. Producing fake binaries in simulations is important for the work presented in chapters 4 and 5.

In Chapter 4, I describe the orbit fitting algorithm I developed (`FOBOS`: the 'Few Observation Binary Orbit Solver'). `FOBOS` is a brute force Monte Carlo code that can estimate the orbital parameters of a binary system or directly imaged brown dwarf/exoplanet using only two or three epochs of astrometric data. This chapter includes results of a comprehensive test of `FOBOS` on simulated data, along with results for two real systems.

In Chapter 5, I describe my work estimating the selection effects on observed binary samples. The sample was provided by collaborators at the University of Leeds, who wanted estimates on the biases present in their data, along with estimates on the semi-major axis distribution and multiplicity fraction of the sample. I did this my creating a 'fake' binary population, applying their observational selection effects to it, and comparing the simulation and observations using a binary search tree.

Finally, Chapter 6 summarises each of the previous chapters and discusses potential future work in each area.

Chapter 2

Multiplicity of stellar systems in the field from simulations

2.1 Introduction

As mentioned in Chapter 1 (particularly Section 1.2.3 and 1.4), star formation is often thought of as a universal process that is the same across all environments and at all times. In very simple terms, this process is (a) the formation of individual stars or multiple systems from dense cores within GMCs, then (b) the dynamical and secular evolution of multiple systems due to interactions with nearby stars or the cloud within which the system is embedded. The galactic field is then the sum of all star formation across different environments (Goodwin, 2010).

The multiplicity and IMF of stars in the field has been extensively studied, but its formation history is still not fully understood. There are two basic theories of how the field is produced; (a) that stars form with multiplicities similar to the field, or (b) stars form with much higher multiplicities and then decay to produce the field values (as proposed in Kroupa, 1995a,b; Kroupa & Bouvier, 2003). A spectroscopic study of pre-MS stars by Kounkel et al. (2019) found multiplicity fractions comparable to the field for close separation solar-type stars, whereas studies such as Tobin et al. (2022) found an excess of companions. Similarly to the result of Tobin et al. (2022), the high multiplicity of nearby star-forming regions implies most stars form in multiples and are dynamically processed to make the field. Therefore, there must be some disruption/decay of multiple systems between birth and dispersal into the field, but it is difficult to quantify the extent to which this occurs.

This chapter presents the results of my work using toy Monte Carlo models to model the conversion of cores into stars and the decay/destruction of multiple systems, in an attempt to match the observed IMF and multiplicity fractions in the field. In particular, I investigate three methods of core fragmentation; one in which the number of stars produced is completely random, one where it is a very strong function of mass, and one where it is a weak function of mass. Additionally, I apply the secular decay rules determined by (Sterzik & Durisen, 1998) to the primordial multiple system population, to see how much this modifies the frequency of multiple systems at birth. I compare the IMFs and mass dependent multiplicity fractions from my models to the functional form of the (Maschberger, 2013) IMF and the observed multiplicity fractions in the field (from several studies, collated in the review article by Offner et al., 2022).

This work has been submitted to MNRAS.

2.2 Methods

The main aim of this research was to see if I could find a simple set of rules that take us from a population of cores with masses drawn from the CMF, to a stellar population with the IMF and multiplicities of the field. To investigate this, I used toy Monte Carlo simulations; a statistical technique used to approximate complex problems by random sampling. I define a simple rule for the way cores are split into stars (representing the fragmentation process) and assign a probability that each system decays (an approach that builds on work such as Lada, 2006; Goodwin et al., 2008; Holman et al., 2013).

I performed several simulations using different conditions for the fragmentation of cores and ejection of stars (outlined in Section 2.2.1).

2.2.1 Simulations

Sampling the CMF

All simulations begin by drawing masses for n cores (with mass values M_c) from the Maschberger function (Maschberger, 2013, shown in Equation 1.8). Our CMF adopted the characteristic parameters of the L_3 system IMF, but with a scale parameter (i.e. peak value) of 1.0 $M_\odot$, a lower mass limit of $m_l = 0.1$ $M_\odot$, and an upper mass limit of 150 $M_\odot$. All parameters used are given in Table 2.1. For all simulations presented in Section 2.3, the number of cores sampled was set to $n = 1 \times 10^6$.

Parameter	Symbol	Value
High-mass exponent	α	2.3
Low-mass exponent	β	1.4
Scale parameter	μ	1.0 $M_\odot$
Lower mass limit	m_l	0.1 $M_\odot$
Upper mass limit	m_u	150 $M_\odot$

Table 2.1: Parameters used to generate the core mass function for random sampling.

Splitting the core into stars

Each core is then ‘fragmented’ into N_* stars, where N_* varies according to the fragmentation conditions stated above. The total stellar mass ($M_{\rm sys}$) is calculated as

$$M_{\rm sys} = \sum_{i=1}^{N_*} m_i = \eta M_c, \tag{2.1}$$

where η is the star formation efficiency of the core (i.e. the fraction of material within the core that is converted into stars) and $m_{\rm i}$ is the mass of each star.

$M_{\rm sys}$ is then divided up between the stars, in such a way that the overall mass ratio distribution is flat for all primary masses. The total stellar mass is divided up between the stars by randomly selecting $N_* - 1$ mass ratio values q from a uniform distribution in the range 0.2-1. For binary systems, I select a single value of q_1 and assign masses such that $m_2 = q_1 m_1$. For triple systems, m_3 will have the value $q_2(m_1 + m_2)$. This pattern is continued for higher order systems. This gives mass ratio distributions similar to those of the field (cf. Goodwin, 2013).

I tested two models for the star formation efficiency; one where η is assumed to be constant and one where η varies randomly between 0 and 1 for each core. In reality, the SFE may depend on the mass of an embedded star (Matzner & McKee, 2000). However, it is not clear whether this would increase (due to more gas contained within the larger potential well of the core/star), or decrease (due to stellar feedback) the SFE with increasing core mass (Goodwin et al., 2008). Since I am aiming to find an overall rule for explaining the origin of the field population, a constant value of the SFE should represent an average of the SFE across all cores.

Secular decay and dynamical destruction

The steps above produce an initial system, containing either a single or multiple stars. However, if the system is a multiple then there is a possibility that the system won't enter the field in its initial state. This could be either due to the secular effects in the system or dynamical destruction due to an encounter. Binaries can only be destroyed by external perturbations, whereas higher order systems can also decay due to their own inherent instabilities as a relaxation process.

As mentioned in Section 1.6, the physical properties that affect the probability of a system decaying or being destroyed are the separations of the stars, the configuration of the system (i.e. hierarchical vs. non-hierarchical) and the number of stars in the system. Secular decay is environmentally independent whereas dynamical destruction is strongly environmentally dependent.

The field represents the sum of star formation across all environments. If star formation is indeed a universal process with a 'typical outcome' then it should be possible to use a single probability distribution to represent the combined effects of both dynamic and secular decay. The results presented in Section 2.3 show that a rule such as this struggles to match observations.

For the simplest combined model, each channel of decay for a system of N_* stars is mass-independent and has an equal probability. This leads to a scenario where 50 per cent of binaries are destroyed to form two singles and 50 per cent remain stable. For triples, one third of systems will eject 2 stars, one third will eject 1 star, and the rest will remain stable. Similarly, for quadruples, one quarter of systems will eject 1 star, one third of systems will eject 2 stars, etc. This pattern continues for $N_* = 5$ and $N_* = 6$. Due to the high rate of decay of binaries, these probabilities are representative of population with a high rate of destruction due to interaction with other stars (Parker & Goodwin, 2012), making them a good starting point for testing the effect of different overall decay rates on multiplicity fractions.

In reality, it is extremely unlikely that all decay channels have equal probability. Sterzik & Durisen (1998) determined probabilities for different secular decay channels, including channels that our simple rules do not capture (such as the decay of a quadruple to a pair of binaries, see Table 2.2). However, this only accounts for secular decay, not dynamical destruction. This point is discussed in detail in Section 2.4.

As we expect the lowest mass objects to be preferentially lost as a result of secular decay (Anosova, 1986; Reipurth & Mikkola, 2012) stars are removed in order of increasing mass. Any stars that have been ejected from multiple systems are counted as single stars when calculating the multiplicity fractions.

Core fragmentation conditions

I tested three models for the core fragmentation:

1. N_* is generated from a random uniform distribution, with no dependence on core mass;
2. N_* depends strongly on the Bonnor-Ebert mass (explained further in section 2.3.2) and will be proportional to this value;
3. N_* has a weak dependence on the core mass, but still shows some random variation.

Each model is described in more detail in the subsections of Section 2.3.

2.2.2 Output

I used the stellar masses outputted from the simulations to calculate the IMF of the stars. I compared the simulated IMF with the canonical IMF, considering both the single-star IMF (counting all stars) and the system IMF (using the total mass of each system, M_{sys}). It's important to note that the goal was not to perfectly match the IMF, as observations of the IMF have associated errors, and any functional fits tend to smooth out small details[1]. Nevertheless, I considered good models to be ones that exhibited self-similar mapping between the CMF and the IMF, peaked at $\sim 0.2\ M_{\odot}$, and had an overall shape that did not not deviate significantly from the canonical IMF.

I also calculate the multiplicity statistics of our stellar population for different primary mass intervals. Due to the fact that all observed multiplicity values used for comparison are corrected for incompleteness, all companions with a mass greater than $0.012 M_{\odot}$ ($\sim$minimum brown dwarf mass) are included our statistics. This is discussed further in section 2.4.

2.3 Results

I want to show that (a) the IMF demonstrates self-similar mapping from the CMF and (b) the multiplicity fractions are consistent with observations. As mentioned in section 2.2, I consider three cases for the fragmentation; a) a self-similar model (2.3.1), b) a

---

[1] For more detailed information about variations in the IMF, refer to Section 1.4

Bonnor-Ebert mass dependent model (2.3.2), and c) a hybrid model with both random and core mass dependent elements (2.3.3).

The four model simulations presented in this section are a subset of the simulations that were performed, and are representative of a much wider range of test conditions.

2.3.1 Self-similar model

I started with a simulation in which all cores fragment into a random number of stars between $N_{\rm min}$ and $N_{\rm max}$, with no dependence on the initial core mass (as used as the basis for simulations such as Goodwin et al., 2008; Holman et al., 2013). The reason that this model has been used as a basis for previous simulations is because it preserves the mapping from the CMF to the IMF, with the location of the peak being defined by the star formation efficiency. Stars are then 'ejected' from the system following the simplest (and potentially naive) conditions where 50% of binaries decay, one third of triples eject one star, etc (as described in Section 2.2.1). Whilst this is not necessarily a realistic model of decay, it provides a good starting point to test the model, before applying a more realistic set of decay rules in a later model.

For this simulation, it is assumed that *all* stars form in multiple systems ($N_{\rm min}$=2) and that the maximum possible multiplicity is $N_{\rm max}$=6. The number of stars has no dependence on core mass. The minimum and maximum values for the number of stars formed are variable parameters and their effect on our results are discussed in section 2.3.1.

The simulation is repeated with three different fixed values of the star formation efficiency, and one scenario where η is allowed to vary randomly.

Figure 2.1 and 2.2 show the system and stellar IMFs and multiplicity properties respectively of simulations using the self-similar model. These results are reflective of the common problems in self-similar models, which I will explain.

Figure 2.1 shows the resulting IMFs from my simulations in comparison to the normalised Salpeter (Salpeter, 1955) (in orange), Chabrier (Chabrier, 2003a, 2005) (in blue), and Maschberger (Maschberger, 2013) (in pink) forms of the IMF. The top plot of Figure 2.1 shows the system IMF and the bottom plot shows the single star IMF (after processing). The system IMF is expected to match the observations more closely, but the single star IMF to be a more appropriate comparison for the results of our simulations, due to the fact that we can 'resolve' all multiples perfectly in a numerical simulation. The prior distribution of core masses is shown by the solid black line and the resulting IMFs for different values of η are shown by the grey dashed/dotted lines.

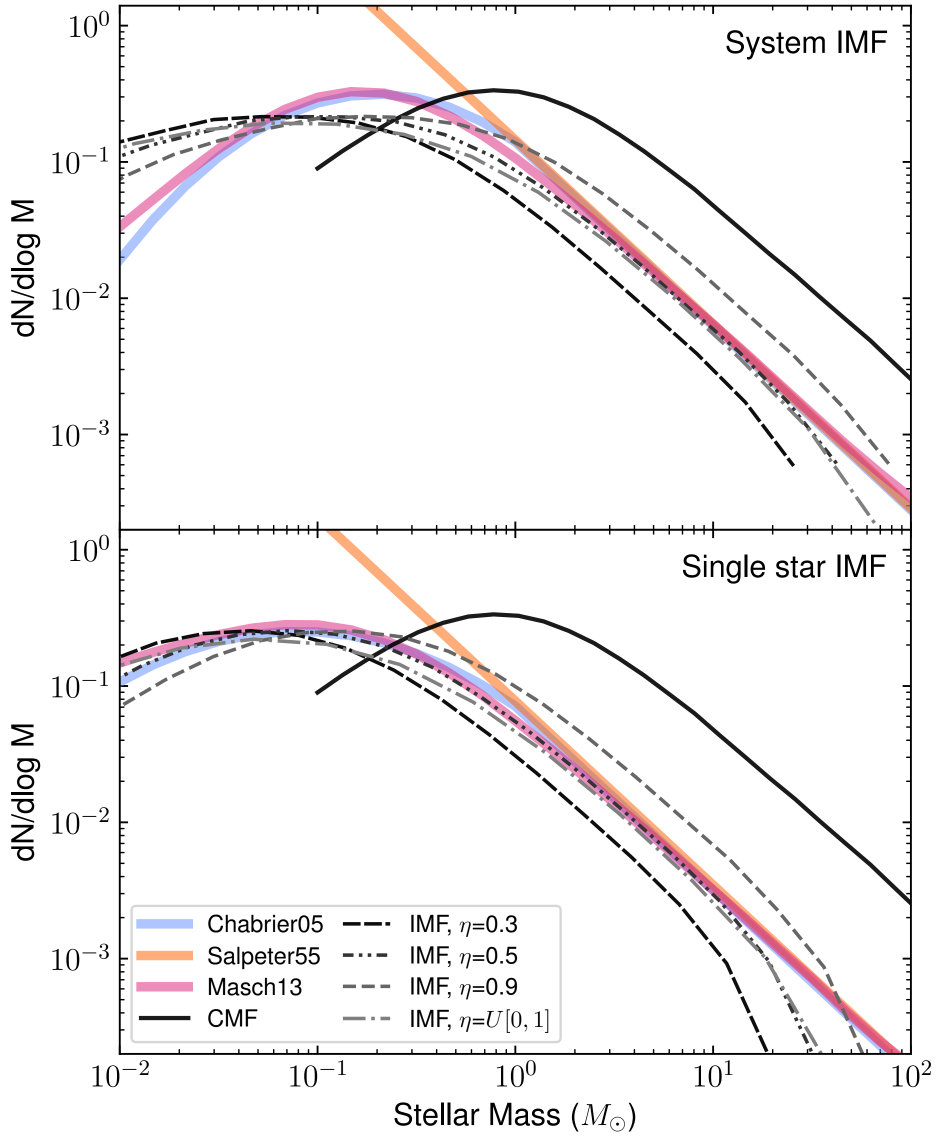

Figure 2.1: The system (top) and single star (bottom) IMFs for the self-similar model. On both plots, the Salpeter (orange), Chabrier (blue) and Maschberger (pink) IMFs are shown by the solid lines. The core mass function used in our simulations is shown by the solid black line. The IMFs are plotted for several values of the star formation efficiency: $\eta = 0.3$ (densely dashed), $\eta = 0.5$ (dotted), $\eta = 0.9$ (dashed), and $\eta = U[0,1]$ (dash-dotted). The grey shaded region on the left of both plots shows the brown dwarf regime. The functional forms of the Salpeter and Chabrier IMFs were generated using `https://github.com/keflavich/imf`.

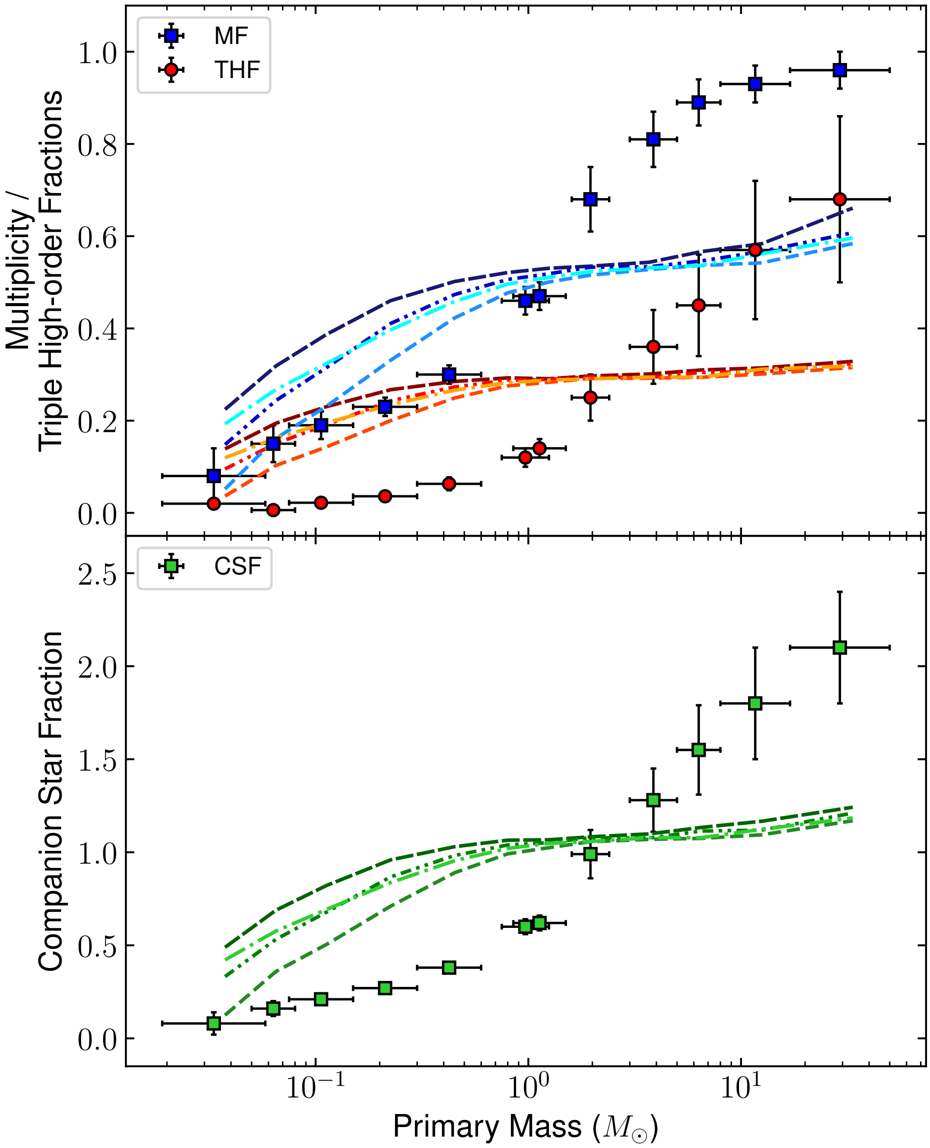

Figure 2.2: Top: Observed multiplicity fractions (blue squares) and triple high order fractions (red circles) from various sources listed in table 1 of Offner et al. (2022). The blue lines and red lines show the multiplicity fractions and triple higher order fractions (respectively) from my model using self-similar fragmentation and ejection rules from Section 2.2.1. The values for the MFs and THFs are plotted for several values of the star formation efficiency: $\eta = 0.3$ (densely dashed), $\eta = 0.5$ (dotted), $\eta = 0.9$ (dashed), and $\eta = U[0, 1]$ (dash-dotted). Bottom: Companion star fractions following the same rules as the top plot.

The single star IMFs are a very good fit to the canonical IMFs. This is unsurprising as this model was designed to produce this match by preserving the shape of the CMF. The best fit value of η in this model is 0.5. The system IMFs are significantly wider than the canonical system IMFs; while this could possibly be fixed by adjusting how masses are distributed between stars within a core, this is not worthwhile due to the poor fit of the multiplicity fractions.

Figure 2.2 shows the multiplicity statistics from my simulations compared to their observed values. The blue points and red points on the top plot show the observed multiplicity fractions and triple/high-order fractions respectively, and the green points on the bottom plot show the observed companion star fractions (from table 1 of Offner et al., 2022). The horizontal error bars show the primary mass interval covered by each data point. The blue, red/orange, and green lines on each plot represent my MFs, THFs, and CSFs respectively for the same discrete mass ranges as the Offner et al. (2022) values, but shown as a continuous line to guide the eye.

It is immediately clear from looking at Figure 2.2 that this model is a very poor fit to the data. The multiplicities increase with mass very slowly from low mass objects to objects with $M_\mathrm{p} \sim 0.5 M_\odot$, and then plateau at $\sim 1\ M_\odot$.

The exact characteristics of the IMF and multiplicities are due to the details of my chosen model (in particular, the decay probabilities), but they are all indicative of using a self-similar model. I concluded this by testing a variety of different decay rules, plus different limits on N_min and N_max, all of which failed to fit the multiplicity statistics.

If all cores produce multiple systems, and N_* is independent of core mass, then the initial multiplicity statistics will be the same for *all* masses (i.e. MF $= 1$, THF ~ 1, and a CSF > 1). As higher order systems decay by ejecting the lowest mass stars, the multiplicity fractions for low-mass bins will decrease. Therefore, using a self-similar fragmentation model with mass/multiplicity-independent decay probabilities leads to a roughly flat multiplicity-mass dependency, which completely fails to match the observations. This issue is present regardless of the values used for N_min and N_max (and the multiplicity-mass dependence actually flattens further if cores are allowed to form a single star).

Dynamical decay probabilities

In this model, I have applied a flat dynamical decay probability dependence with mass to systems which survive secular decay. To try and reduce the low-mass multiplicities to close to the observed values, this probability has to be extremely high, which in turn decreases the high-mass multiplicities to well below the observations (as can be seen in Figure 2.2).

It would be possible to follow up on this model by using a dynamical decay probability that depends on mass. There would be good reason to do this, as higher mass systems are likely to be more resistant to dynamical decay due to their increased binding energy, and more likely to reform binaries throughout their lifetimes due to capture (Parker & Meyer, 2014). However, any rule would need to be a *very* strong function of mass; all systems with $M_\mathrm{p} > 5M_\odot$ need to survive, while almost all systems $M_\mathrm{p} < 0.5M_\odot$ need to be destroyed, with a 'tipping point' at $\sim 1M_\odot$ where there is a 50% survival chance. This model seems quite fined tuned, and determining whether it is a 'realistic' model of multiple system decay, it would require a much more in depth study including the separation and mass ratio distributions of each system. Whilst this would be a worthwhile study, it goes against the purpose of this work, which was to see if there is a set of *simple* rules to take us from the CMF to the IMF and replicate the field multiplicity properties.

N_min and N_max

As mentioned in the previous section, N_min and N_max are variable parameters. For the results shown above, I assumed that all stars form in binary or higher order systems (as was the basis for work such as Kroupa, 1995a, 2008) and the highest order multiple that can be formed from a single bound core is $N = 6$. A variety of models using higher and lower values of N_min and N_max were also tested, the results of which are shown in Figure 2.3.

In all cases, the gradient of the MFs, THFs, and CSFs with respect to mass is far too shallow to match the observations. If cores are allowed to form a single star, there is almost no variation in MF, THF, or CSF with increasing mass. If all cores form a very high number of stars ($N_* = 4 - 8$) then the multiplicity properties do start to vary as a function of mass, but not enough to match the observations. Observations of protostars such as Kounkel et al. (2019) and Tobin et al. (2022), along with our own intuition, suggest that it is unlikely that this could be the case.

2.3.2 Strongly mass dependent model

I showed above that splitting all cores into a random number of stars produces multiplicities that are much too flat with respect to mass. Therefore, it stands to reason that having N_* increase with M_c should better match the multiplicity observations.

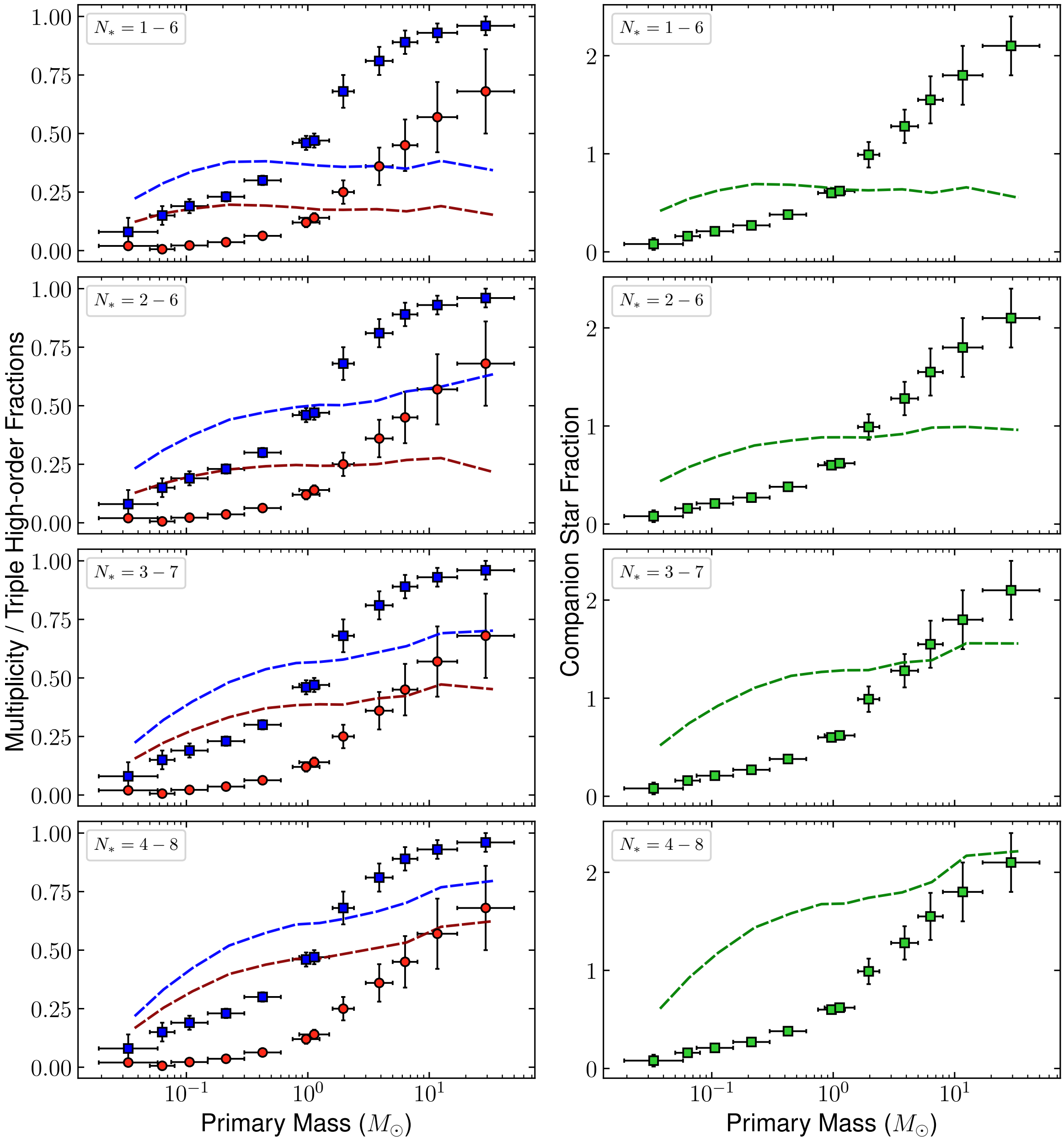

Figure 2.3: Multiplicity fractions, triple/higher-order fractions (left) and companion star fractions (right) for four self-similar model simulations. From top to bottom, N_* is selected randomly for each core from a uniform distribution in the range $1-6$, $2-6$, $3-7$, and $4-8$.

Some theories suggest that the number of stars formed from a collapsing core may be proportional to the ratio of the core mass to the critical Bonnor-Ebert mass $M_{\rm BE}$ (such as Lada, 2006), which is the maximum mass that can be contained within an isothermal Bonnor-Ebert sphere while remaining in hydrostatic equilibrium (Bonnor, 1956; Ebert, 1955, equations and more detail described in Section 1.2.2). In these theories, each Bonnor-Ebert sphere within a core with a mass $\geq 1 M_{\rm BE}$ collapses to form a single star, gravitationally bound to any other objects which form within the same core.

I consider the case in which multiplicity of the final system is a strong function of the initial core mass, with each core fragmenting such that $N_* = M_c/M_{\rm BE}$. For the results presented in this section, a random value of the critical Bonnor-Ebert mass is selected from a uniform distribution between $0.5 M_\odot$ and $2.5 M_\odot$. The decay/ejection conditions are kept the same as in Section 2.3.1.

Figures 2.4 and 2.5 show the IMFs and multiplicities from this model (cf. Figures 2.1 and 2.2).

As expected, the multiplicities from this model show a strong dependence on primary mass. The THFs show a reasonable fit to the observations, and although the MFs and CSFs are far from a perfect fit, they fit the trend of the observations well. However, there is a significant flaw in this model when it comes to multiplicities: due to the condition that all cores below the Bonnor-Ebert mass do not form stars, and cores below $2 M_{\rm BE}$ form only 1 star, multiple systems with a total mass of $2 \eta M_{\rm BE}$ cannot form. As soon as the core mass exceeds $M_{\rm BE}$, there is a huge jump in the multiplicity as suddenly cores start forming two or more stars. As N_* increases with $M_{\rm c}$, the MF, THF and CSF all continue to increase rapidly as the core mass exceeds a couple of Bonnor-Ebert masses.

One option for increasing the MFs for low-mass stars would be if low-mass binaries are formed via capture. However, it is highly unlikely that binaries with $M_p < 1 M_\odot$ (particularly M dwarfs) would form via this method, especially in significant enough numbers to increase the MFs. Multiple system decay via different channels, such as the decay of a quadruple system to two binaries, could also increase the low mass multiplicity fractions, but as I will explain, there is little point doing this due to the issues with the shape of the IMF.

The IMFs shown in Figure 2.4 are vastly different from the canonical IMFs and do not show self-similar mapping from the CMF. There is a strong overabundance of stars around the average Bonnor-Ebert mass, appearing as a very large "bump" at the peak of the IMF. This bump is extremely pronounced for all fixed values of the star formation efficiency, and is only slightly less pronounced if η is allowed to vary. The shape of the

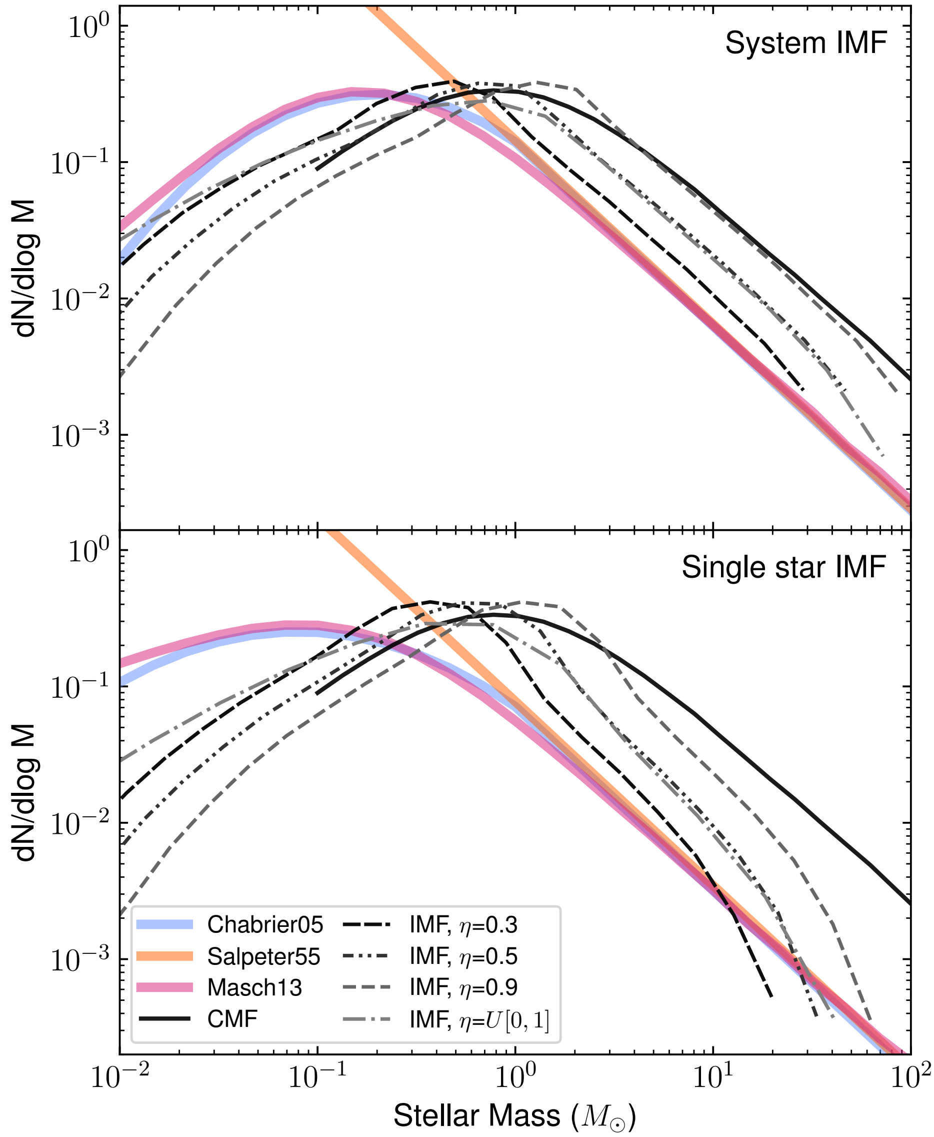

Figure 2.4: IMFs from the Bonnor-Ebert mass dependent model. See caption of Figure 2.1 for more details.

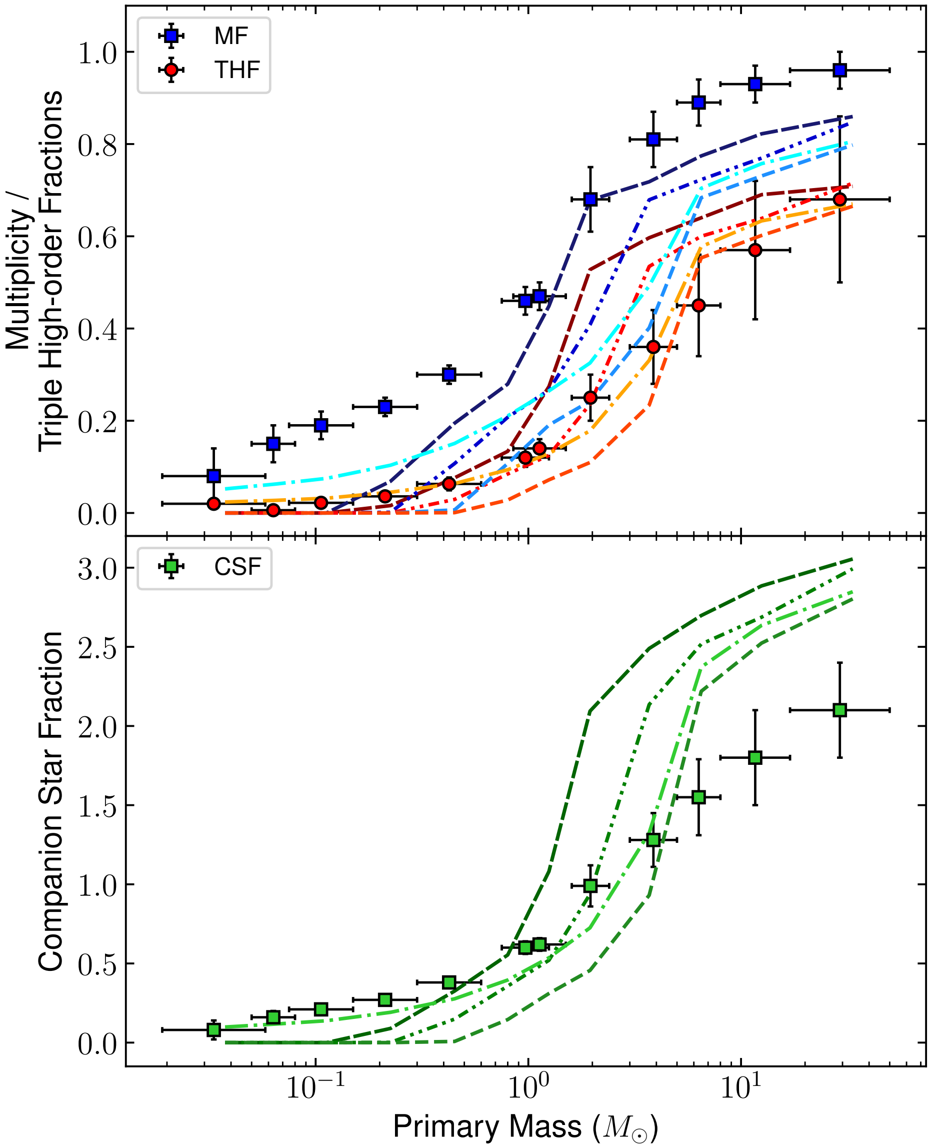

Figure 2.5: Multiplicities from the Bonnor-Ebert mass dependent model. See the caption of Figure 2.2 for more details.

IMF is fundamentally wrong (something that was noted briefly by Goodwin et al., 2008).

These models are for a range of BE masses chosen core by core. In a scenario for star formation within a single star forming region, one would expect the BE to be roughly fixed. For a fixed BE mass, the bump is even sharper and more pronounced due to the much stronger mass dependence, and peaks at the value of the BE mass used. This would suggest that the IMF should vary strongly from region to region depending on the local BE mass, which is at odds with the apparent universality of the IMF.

I can conclude that if fragmentation was a strong function of the core mass, the IMF would have a very different shape to the canonical IMF and would vary from region to region. This implies that a much weaker relation between N_* and M_c is needed.

2.3.3 Hybrid model

I have shown in Section 2.3.1 and Section 2.3.2 that simulations struggle to match the observations if the core fragmentation model is either self-similar or a strong function of core mass. The former cannot reproduce the observed multiplicity fractions and the latter breaks self-similar mapping between the CMF and the IMF.

I next considered a hybrid with elements of both the self-similar model and the strongly core mass dependent model, to test whether combining the two elements would produce a reasonable fit to both the IMF and the multiplicities. I therefore consider a model where N_* depends loosely on the core mass. I start by splitting the masses from the CMF uniformly in log space, resulting in a mass range corresponding to each value of N_*. Rather than forcing cores of a given mass to only fragment into N_* stars, a random value is selected surrounding the corresponding value of N_*. The mass ranges and their corresponding possible N_* values are shown in Figure 2.6.

Slight variations to the conditions used do not change the results presented below, and any significant variations lead to the same problems as already outlined in Section 2.3.1 and Section 2.3.2. This specific set of conditions shown in Figure 2.6 were chosen to present here because they provide the best match to the multiplicity fractions.

For our initial test of this model, stars are ejected from systems using the simple secular plus dynamical model as in Section 2.3.1 and Section 2.3.2.

This hybrid model provides a better fit to the observations than the previous models. In Figure 2.7, the shape of the system and single-star IMFs matches that of the canonical IMF, with the best fit for the system IMF occurring when $\eta \sim 0.5$. In the case of the single star IMF, the best fit value of η is ~ 0.3. One could argue that an efficiency of $\eta \sim 0.4$ could fit both within the observational errors.

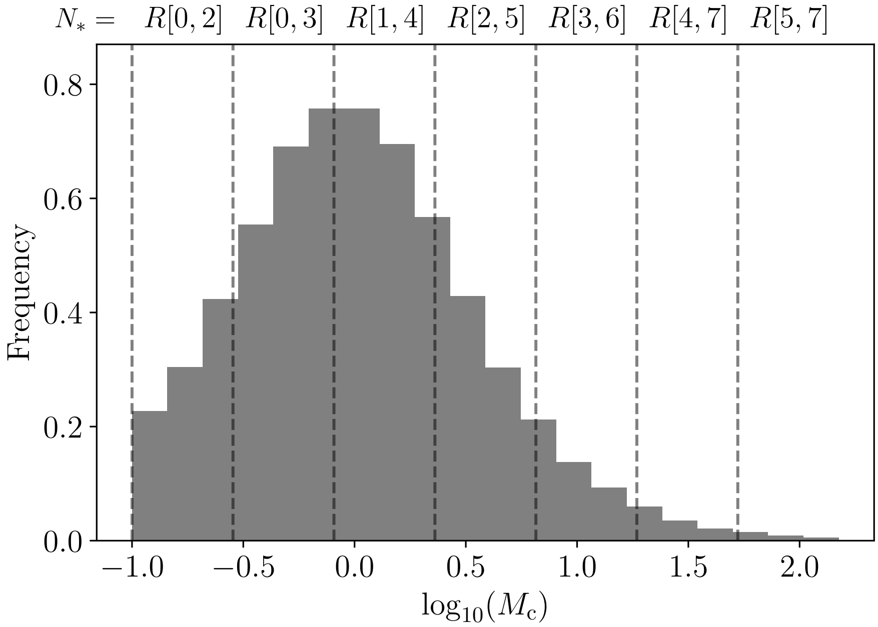

Figure 2.6: Conditions for fragmentation in the hybrid model. The histogram shows the core mass distribution in log space. The vertical dashed lines show the different mass ranges with the text above each section stating the possible values of N_* (uniformly weighted) for a core in the corresponding mass range.

The single star IMF has a small bump at the peak, but due to the uncertainties associated with the IMF, the chances of seeing this feature in observations (if it did exist) are extremely slim; the real data does exhibit some variation and has error bars, but it tends to be fitted with a smooth function. Furthermore, the high mass tail of the IMF deviates from the Salpeter slope when $M_p > 20 M_\odot$, but here we are in the low-N tail of our distribution and it is not at all clear if a universal model would extend to extremely high-mass systems.

Figure 2.8 shows that the hybrid model does a good job of fitting the CSF (green) and THF (red), but is poor at fitting the high-mass end of the MF (blue).

The balance of increasing the number of stars formed with core mass, but not fragmenting into so many objects that high mass stars are under-produced, means that the THFs and CSFs start to resemble the observations very closely. However, the multiplicity fractions for primary stars with masses $> 1 M_\odot$ are far lower than their observed counterparts; in the highest mass bin, approximately 60 per cent of stars are in multiples and 50 per cent are in high order systems, meaning that only 10 per cent of O stars are in binaries, meaning that there are far too many single high mass stars (compared to the expected number of binaries) in this simulation.

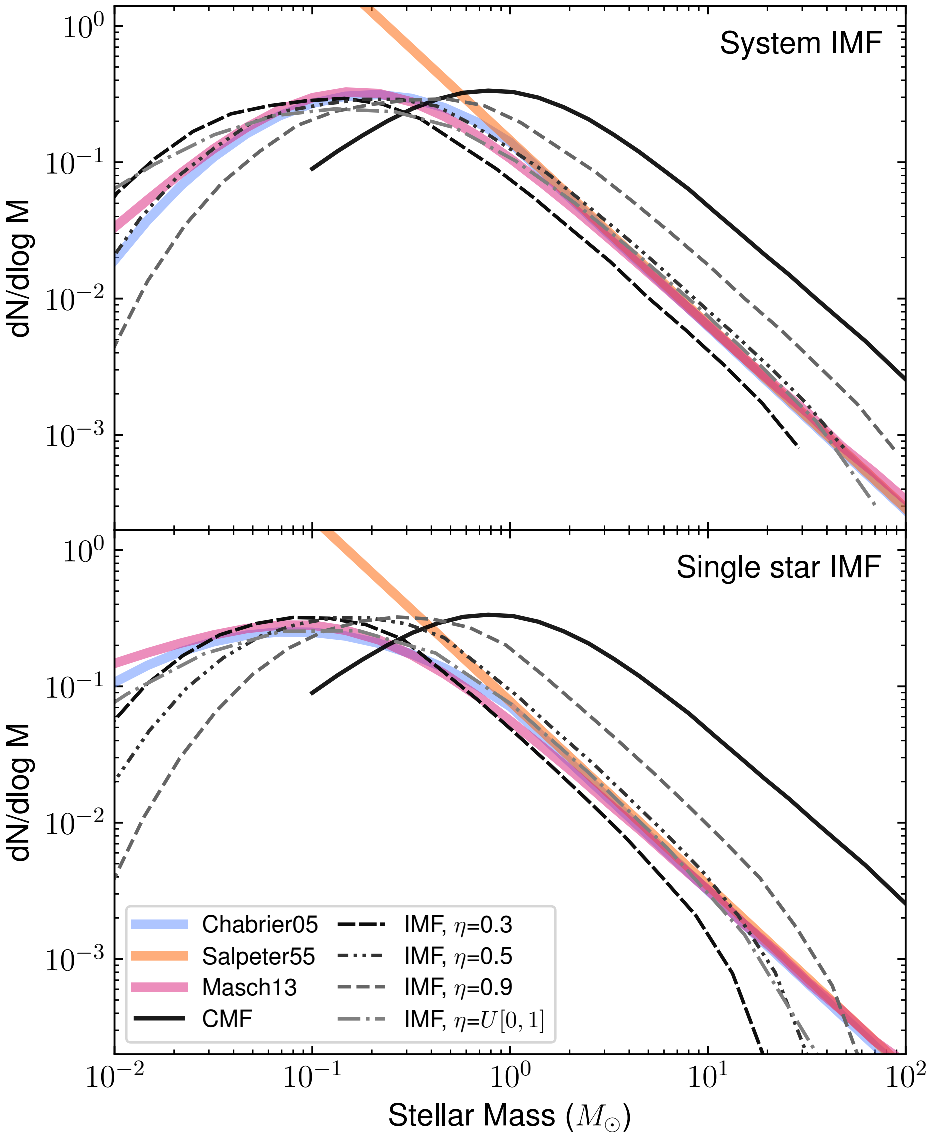

Figure 2.7: IMFs from the hybrid fragmentation model. See the caption of Figure 2.1 for more details.

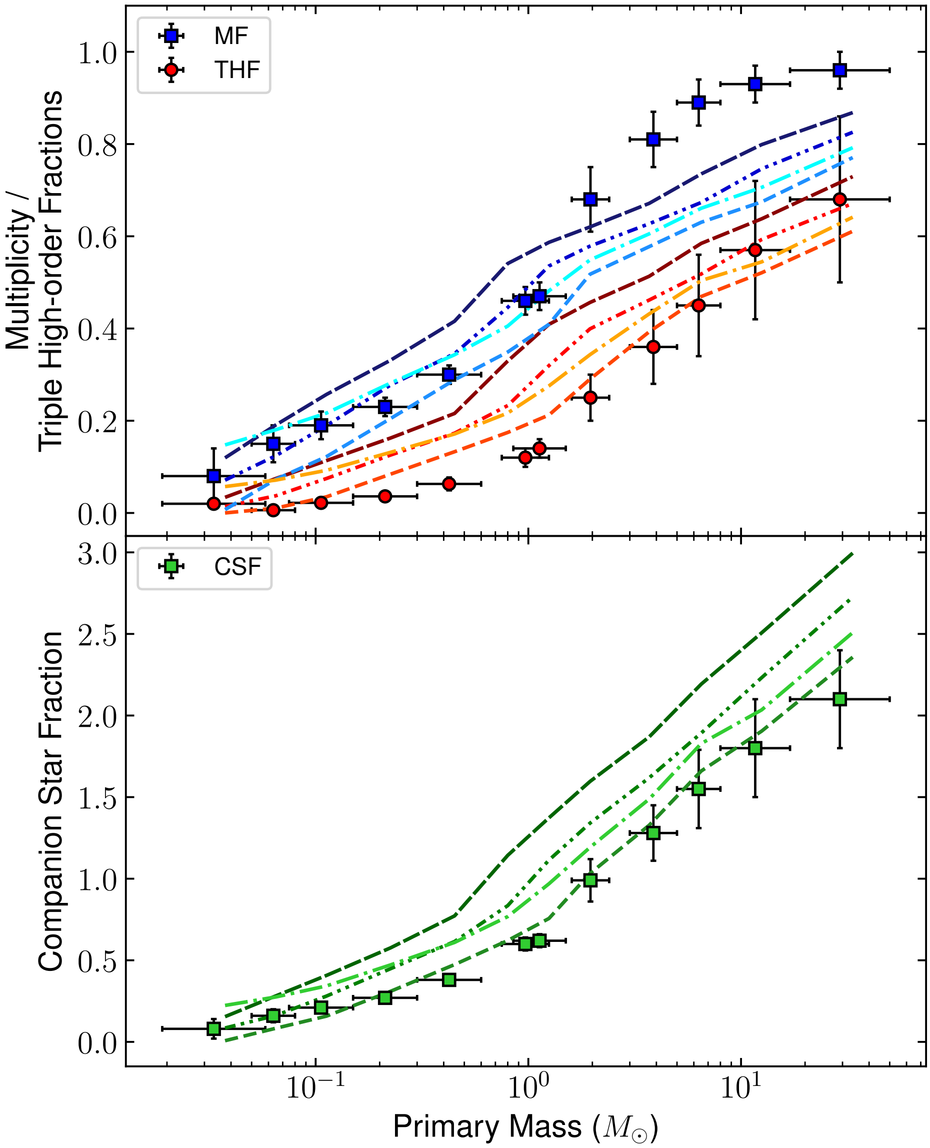

Figure 2.8: Multiplicities from the hybrid fragmentation model. See the caption of Figure 2.1 for more details.

This is due to the large number of binary systems which decay due to the random ejection rules in our simulations; most cores massive enough to form stars $\geq$ a few solar masses will form a larger number of stars, as in the BE mass dependent model. The majority of these very high order systems ($N_* = 5 - 7$) will eject a few stars, diluting the multiplicity fraction whilst keeping the THF and CSF high.

Modelling secular decay only

The hybrid model for fragmentation presented above does a reasonable job in fitting various aspects of the IMFs and multiplicities. However, there are some major issues with the multiplicity fractions, which are likely due to the self-similar model for system decay and dynamical destruction. Therefore, I applied a more 'realistic' set of decay probabilities taken from Sterzik & Durisen (1998). These conditions were also applied to the self-similar and Bonnor-Ebert mass dependent models, but they did not significantly improve the fit to the observations.

Sterzik & Durisen (1998) used numerical and analytical modelling of 1000 non-hierarchical $N = 3, 4,$ and 5 systems to evaluate the likelihood that a system will decay due to secular processes. Their findings are shown for various initial mass ratio distributions in their table 1. Their orbit integration approach mimics the effect of secular decay *only* in high order systems.

As well as considering cases where the multiple system ejects single stars, they also include the various decay channels that produce two lower order systems (i.e. an $N = 5$ system may decay to a binary and a triple system). They do not include any decay statistics for $N = 6$ or $N = 7$ systems, so I extrapolated from the data presented in their paper to estimate the probabilities of high-order systems decaying through each channel (shown in Table 2.2). I assume that all binaries in this model are stable, as they can only be destroyed due to dynamical interactions, which is not included in the modelling in Sterzik & Durisen (1998).

The IMF and multiplicity fractions determined using the Sterzik & Durisen (1998) decay rules are shown in Figure 2.9 and Figure 2.10. The shape of the single star IMF is the same as in Figure 2.7, and the system IMFs are extremely similar as one would expect.

The multiplicity statistics change now that only the secular decay processes are included. The THFs fit the observations very well and the CSFs are somewhat flatter than the observations. The MFs match the observed values for masses $\geq 2M_\odot$ (which is an improvement on the results for high mass stars from the previous model), but are a

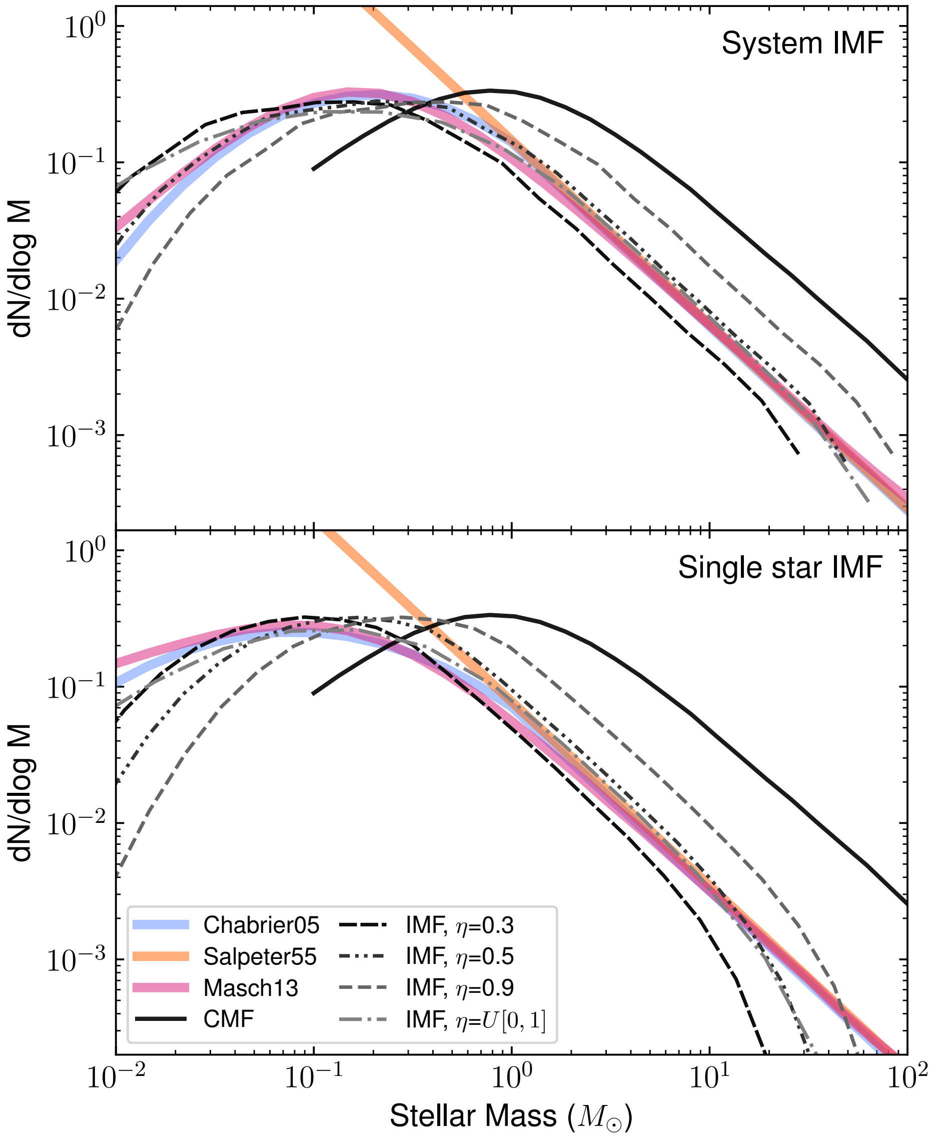

Figure 2.9: IMFs from the semi-random fragmentation model where low mass stars are ejected from multiple systems following the Sterzik & Durisen (1998) decay rules. See the caption of Figure 2.1 for more details.

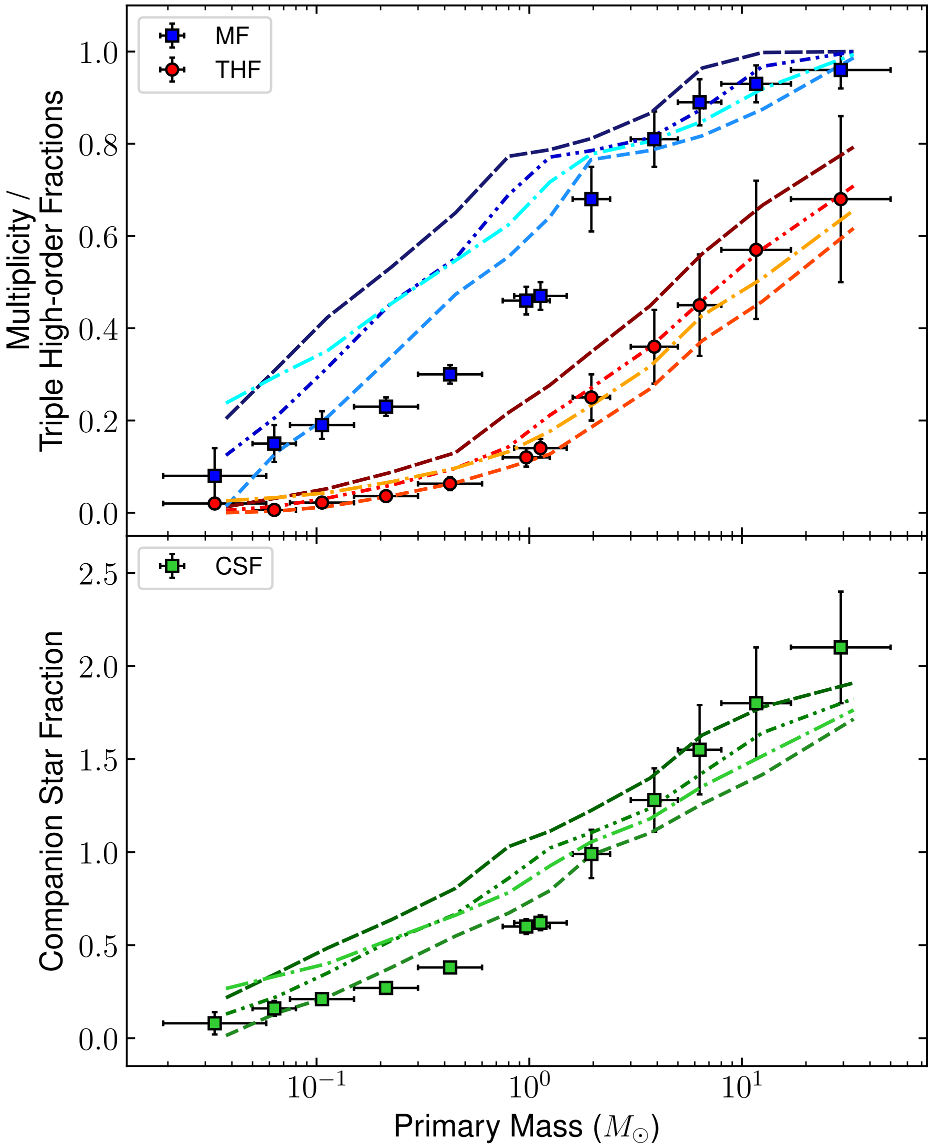

Figure 2.10: Multiplicities from the semi-random fragmentation model where low mass stars are ejected from multiple systems following the Sterzik & Durisen (1998) decay rules. See the caption of Figure 2.2 for more details.

N	BS	TS	QS	BBS	TB	Other
2	**1000**	-	-	-	-	-
3	874	118	-	-	-	8
4	751	181	37	12	-	19
5	532	340	62	41	8	17
6	**313**	**499**	**87**	**70**	**31**	-
7	**94**	**658**	**112**	**99**	**37**	-

Table 2.2: The decay probabilities for $N = 2 - 7$ systems. The column headings show the different decay channels defined according to Sterzik & Durisen (1998), where BS: binary system and $N-2$ singles, TS: triple system and $N-3$ singles, QS: quadruple system and $N-4$ singles, BBS: two binary systems and $N-4$ singles, and TB: one triple system and one binary system and $N-5$ singles. The $N = 3, 4$ and 5 rows contain the values from Sterzik & Durisen (1998) (for a clump mass spectrum), and the other rows (in bold) contain the extrapolated values for lower/higher order systems based on these probabilities.

factor of $\sim 1.5-2$ times too high for primaries with masses $\leq 2M_{\odot}$. It is worth exploring the reasoning for this to determine if the inclusion of dynamical destruction could solve any of these problems.

With secular decay only, all binaries survive. At $< 1M_{\odot}$ there are only singles, binaries and triples initially (see Figure 2.6). Most triples will secularly decay to a binary and a single, ejecting the lowest mass member. This reduces the MF, and significantly lowers the THF and CSF as there are so many low-mass single stars and only binaries to counter these. For primaries $> 1M_{\odot}$, the initial population contains many triples, quadruples, and even higher-order systems. These eject low-mass members (further diluting the multiplicities at lower masses), but retain the highest mass members in binaries and triples resulting in high THFs and CSFs.

The main failing of the secular decay only model is the over-production of binaries at lower masses. A down turn appears in the MF at $0.5-1M_{\odot}$ (depending on the SFE). For the best fit SFE of 0.3-0.5 the down turn occurs for primaries less massive than about $\sim 0.7M_{\odot}$. The reason for this feature is that systems that form from cores around the peak of the CMF ($\sim 1M_{\odot}$) will usually form stars of $0.1 - 0.5M_{\odot}$ (1 to 3 stars of total system mass $0.3-0.5M_{\odot}$). Therefore by far the most common triple systems around the peak of the IMF will eject stars of typically $0.1 - 0.2M_{\odot}$ which significantly dilutes the lowest mass bins. To dilute mass bins greater than about $0.8M_{\odot}$ requires ejections of stars of that mass from what must be initially much higher mass cores, which are much rarer (c.f Goodwin, 2013).

Essentially, there are very few systems in which the lowest mass component is about

$0.5 - 1 M_\odot$ and so it is impossible to significantly dilute the MF above that mass. As the system IMF drops to higher masses there are fewer and fewer increasingly high mass stars ejected to dilute the high mass MF. Changing the fragmentation rules cannot fix this issue without introducing discrepancies in either the shape of the IMF or the THF/CSFs. Therefore, dynamical destruction needs to occur on top of the secular decay to alter this.

I also tested models where the secular decay probabilities were used with the self-similar and strongly core mass dependent fragmentation models. The results of this testing are shown in Appendix A. I do not discuss these results in detail, as they suffer from the same issues as the models in Section 2.3.1 and Section 2.3.2.

2.3.4 Optimised decay model

The final model presented in this thesis aimed to reproduce the field multiplicities *without* considering the physicality of the constraints; I force the statistics to match observations by using arbitrary conditions. The core fragmentation conditions are the same as those in section Section 2.3.3, so that the shape of the IMF and self-similar mapping are maintained. The IMF is therefore the same as Figure 2.7 so an additional figure is not included.

I implemented strict rules on the number of systems that decay, which were dependent only on the initial multiplicity of the system. The rules were as follows:

If the system has $N_* = 6$ or $N_* = 7$, it ejects either two ($N_* = 6$) or three ($N_* = 7$) stars to form a quadruple system. If $N_* = 5$, the system ejects two stars to form a triple system. If $N_* = 4$, the system has a 70 per cent chance of ejecting one star and forming a triple system, and a 30 per cent chance of ejecting two stars to become a binary. If $N_* = 2$ or $N_* = 3$, then one star is ejected to form a single, or a binary system (respectively). These values were chosen because their match to the observed multiplicities, after iterative sampling of a variety of different conditions.

The multiplicity fractions, triple high-order and companion star fractions from this simulation all match extremely closely with the observations, by design. The best fit value of the star formation efficiency for both the multiplicities and the IMF for this model was $\eta = 0.6$.

Whilst at a glance this appears to be a promising result, the decay conditions required to produce these values are very unphysical and I do not consider this to be an accurate representation of the star formation process. This is because to achieve these multiplicities, *all* primordial binaries and triples need to decay, but studies of local star formation indicate that this does not occur (either through dynamical or secular processes).

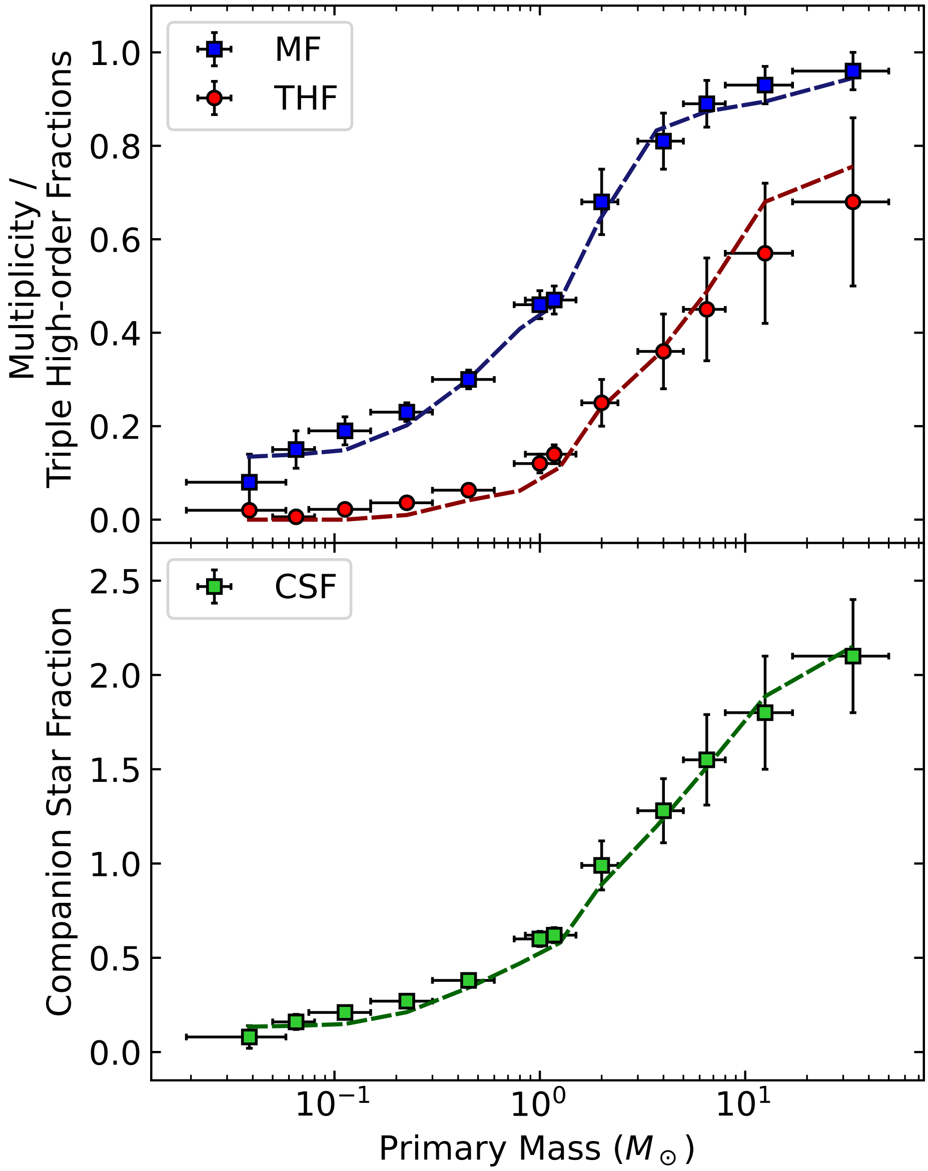

Figure 2.11: Multiplicities from the hybrid fragmentation model where there are strict rules on system decay, which are tailored to replicate the observed MFs, THFs, and CSFs. The densely dashed line shows the multiplicity values for various mass ranges when the star formation efficiency is set to $\eta = 0.6$.

The exact parameters defining the decay of higher-order systems can vary somewhat while still giving fairly consistent results, but they all require a huge over processing of low-order systems to strongly resemble the observations.

2.4 Discussion

Comparing the IMFs and multiplicities generated from our Monte Carlo simulations to observations allows us to eliminate some universal star formation models.

Firstly, self-similar fragmentation cannot replicate the rapid increase of multiplicity with primary mass. This is because if all cores fragment in the same way (independently of mass) then the initial multiplicities will be the same at all masses. The only factors which can then decrease the multiplicity factors are the effects of secular decay and dynamical destruction. Secular decay only has a very slight mass dependence, in that the lowest mass objects from a system will be preferentially ejected, decreasing the low-mass multiplicity fractions only. The only solution to this problem would be to have an extremely mass dependent dynamical decay that has little effect on moderate to high-mass multiples.

Secondly, having a strict rule where the number of stars formed is directly proportional to the core mass significantly changes the shape of the IMF. When splitting cores based on a rigorous condition, the resulting IMF is a convolution of the CMF and the function defining how N_* depends on M_c, making self-similar mapping impossible.

Given these problems, I tried a hybrid model for fragmentation that was between the two extremes. This model provide the best fit to the system IMF, as the gentle dependence of N_* on M_c solves the problem of initial multiplicity having no mass dependence (from the self-similar model) without introducing harsh features in the IMF (like from the strongly core mass dependent model).

The universal IMF

Throughout, I have assumed that the IMF is universal, and have judged the quality of fit of the simulations similarities to IMF models. Whilst this is widely accepted (and therefore a reasonable assumption), there is still some debate about the level of variation between IMFs in different regions. Observations of young clusters by Dib (2014) suggest that the IMF may not be universal, but there is also strong evidence that the form of the IMF is mostly unaffected by environmental factors (Damian et al., 2021; Guszejnov et al., 2022). Interestingly, the strongly peaked IMF as seen in our mass dependent model shows some similarities to the unusual IMF in Taurus (Luhman et al., 2003; Dib, 2014), which has a strong peak at $\sim 0.8 M_\odot$. A detailed comparison between our simulated IMF and the observed IMF in Taurus is outside the scope of this paper, but similarities are intriguing (cf. Goodwin et al., 2004).

Secular vs. dynamical decay

The Sterzik & Durisen (1998) decay probabilities were used to test the effects of a more 'realistic' model of secular decay. The results fit the multiplicity properties for primaries greater than $2 M_\odot$ quite well, but results in too many binaries for primaries of 0.1 to $2 M_\odot$. The MF does decline with primary mass in this range, but is consistently roughly double the field values for all primary masses.

There are two interesting things to say about this result.

Firstly, as mentioned above, in order to fit the field multiplicities, some of these binaries would need to be dynamically processed into two singles. In order to reduce the MF by a factor of two, we need to dynamically destroy about a third of the systems. For example, for an MF of 0.6, ie. 60/100, to become an MF of 0.3 if 20 of the 60 binaries are processed into 40 singles the MF is now 40/120 (lowering the number of binaries from 60 to 40, and in the process producing 20 new single systems). This would only need to be weakly mass-dependent: not effective for systems with primaries over a few $M_\odot$, and equally effective for all low mass systems. This seems rather more physical than a strongly mass-dependent dynamical process which would seem to require a fine tuning of encounter energies.

However, it is still quite a significant level of processing that requires one third of systems to spend enough time in an environment with high enough density and encounter energy to have an unbinding encounter. But, one third of systems spending time in such an environment (e.g. a fairly dense cluster) is not implausible, and such environments are effective at processing binaries (e.g. Parker et al., 2009).

Secondly, an overabundance of binaries by a factor of about two is what is observed in local star forming regions. King et al. (2012a,b) found that local low density star forming regions all show a similar over abundance of multiples by a factor of roughly two when compared to the field, and Duchêne et al. (2018) find the same over abundance in the Orion Nebula Cluster. Therefore, for at least roughly $1 M_\odot$ primaries local star forming regions possibly match the too high MFs only found with secular decay in the hybrid model. This suggests that the hybrid model is an acceptable model of how cores produce stellar systems, and then how those systems secularly decay.

A problem here is that the observed local over abundance contains too many hard binaries below 100 au separation to be dynamically processed by any of the environments in which they are found (King et al., 2012a,b; Duchêne et al., 2018).

Therefore, only around one third of stars need to be formed at much higher densities than are observe locally in order to process them. This could cause problems to the universal model I are trying to make work in this model, as then it is arguable that they do not form in the same way as stars locally. In particular, at high densities cores will not be isolated while forming stars and they will interact (Goodwin et al., 2007), and I have implicitly assumed cores are isolated objects so that there can be a mapping from the CMF to IMF. Since locally we observe cores to be quite separate, isolated objects, this could suggest a different 'mode' of forming stars in much denser environments.

Inclusion of brown dwarf companions

As mentioned in section 2.2, I include all companions with a mass $>0.012M_{\odot}$(the minimum brown dwarf mass) in our multiplicity statistics. The observed values from Offner et al. (2022) have been corrected for incompleteness. The solar type MFs are calculated by counting all stellar and brown dwarf companions (Raghavan et al., 2010), but the original M dwarf statistics from Winters et al. (2019) do not include brown dwarf companions; in a discussion of results, however, they state that the inclusion of BD companions only increases the multiplicity fractions by ∼1 per cent.

For intermediate/higher mass stars, the surveys by De Rosa et al. (2014) (1.6-2.4 $M_{\odot}$), Moe & Kratter (2021) (1.6-2.4 $M_{\odot}$), and Moe & Di Stefano (2017) (3-17 $M_{\odot}$) identified companions down to 0.08 $M_{\odot}$, and only corrected for completeness down to this limit. I account for this in my simulations by not including any brown dwarf companions in the multiplicity statistics for intermediate and high-mass stars.

Since my simulations include *all* companions, they should never be lower than the observations.

Separation distributions

There are several additional factors which could be taken into account in order to make this model more detailed. Applying a mask of different separations to the multiple systems would allow me to study the variability of the MFs with separation. The separation distribution could also be used to estimate which systems would be detected in observational surveys, which would then allow us to introduce a new model for the dynamic and secular decay of systems depending on the separations. Incorporating these parameters into our model is outside the scope of this paper but would provide interesting opportunities for follow up research.

2.5 Conclusions

I have tested several simple scenarios which attempt to replicate both the initial mass function and the multiplicity/companion fractions of stars in the field using toy statistical models. Neither a self-similar model for core fragmentation or a strongly core mass dependent model can reproduce the observations in their entirety. In our simulations with parameters tailored specifically to demonstrate both self-similar mapping of the IMF and multiplicity fractions, binary systems need to decay at a rate much higher than is expected in reality.

The number of stars formed in a molecular core must be some function of core mass in order for the multiplicity fractions to increase with mass, but if the dependence on mass is too strong then self-similar mapping from the CMF to the IMF is compromised.

As is the case for many toy models, there is a vast number of additional parameters that could be included in the simulations to model the effects of more complex physics. However, the purpose of this work was to determine if a set of simple rules could explain the universality of the IMF and the multiplicity statistics in the field.

Chapter 3

Celestial mechanics and binary modelling

3.1 A brief history of celestial mechanics

Celestial mechanics is the branch of astronomy that mathematically explains the orbital motion of objects due to their gravitational interactions. Whilst the key developments in the field were initial made to explain the orbits of the planets in our own solar system, the same mathematical principles can be applied to binary stars and higher order multiple systems, to understand their orbits. The history included in this section can be found in Gribbin (2002).

The development of the modern field of celestial mechanics began with the observations of Tycho Brahe in the late 1500s. Brahe made meticulous measurements of the positions of the 'wandering stars' (now known to be planets) in an attempt to disprove the Copernican heliocentric model of the Solar System. Whilst his conclusions (that the Earth shows no detectable motion throughout the heavens) were ultimately false, the measurements he made were at the highest level of precision possible at the time, an achievement for which he is often credited as one of the greatest astronomers who ever lived.

Brahe invited German mathematician Johannes Kepler to work on his observational data with him. After Brahe's death in 1601, Kepler meticulously studied the data, hoping it would support the heliocentric model of the Solar System. His truly revolutionary scientific achievement came when he disregarded one of the key assumptions of the Ptolometic/geocentric model - that orbits are circular - and instead considered the possibility that they may be elliptical. This finally reconciled Brahe's observations with the heliocentric model and allowed Kepler to develop his three pivotal laws of planetary motion.

Since these laws are based on the mathematical properties of an ellipse and the gravitational forces acting between any two bodies, they hold true for binary systems as well as a planet orbiting a star.

Kepler's First Law: Elliptical orbits

> 'A planet orbits the Sun in an ellipse, with the Sun at one of the foci of the ellipse.'

A diagram of an elliptical orbit is shown in Figure 3.1. The two most important quantities in characterising an elliptical orbit are the semi-major axis and the eccentricity. The semi-major axis (a) is the distance from the centre of the ellipse to the furthest part of the orbit. The semi-major axis is constant for a given orbit and is a key quantity in the definition of an ellipse; something can only be classified as 'elliptical' if at every point in the orbit (Prussing & Conway, 1993).

$$, r + r' = 2a \tag{3.1}$$

where r and r' represent the distances from each focal point to *any* point around the edge of the ellipse.

The eccentricity (e) is a measure of how elliptical the orbit is, ranging from 0 if the orbit is perfectly circular to close to 1 if the orbit is extremely elliptical. If $e = 1$ then the companion object is unbound and on a parabolic orbit and if $e > 1$ then the companion is on an unbound, hyperbolic orbit.

Marked on the diagram are the two foci (F_1 and F_2) which are equidistant from the centre of the ellipse and located at a distance of ae, which is the semi-major axis multiplied by the eccentricity. The primary star is located at F_1 and the planet (or secondary star, in the case of a binary) orbits in an ellipse.

Kepler's Second Law:

> 'The imaginary line which joins a planet and the Sun sweeps out equal areas of space in equal time intervals.'

This means that the velocity of the planet changes throughout its orbit based on the distance from the star, reaching it's fastest velocity at periastron (closest approach to the star) and slowest at apastron (furthest distance from the star).

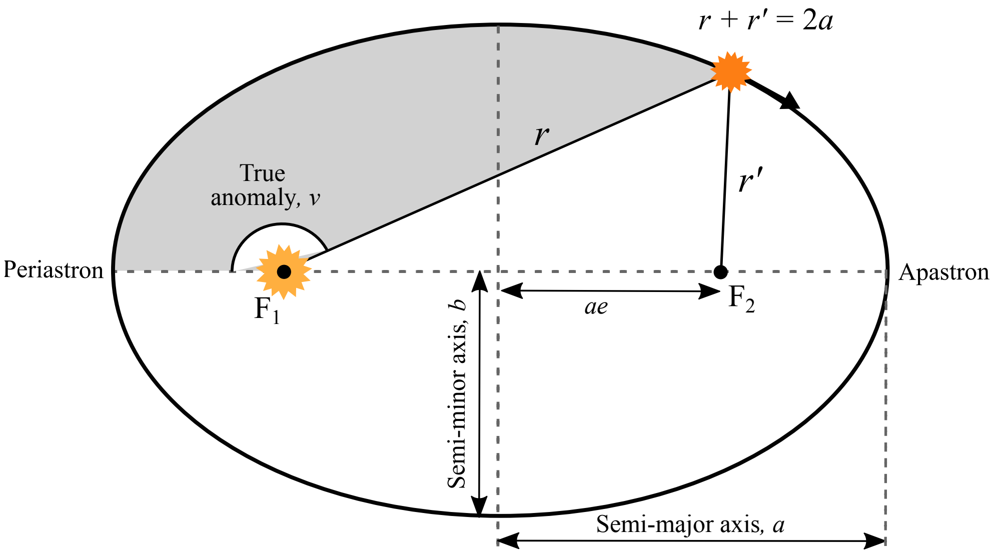

Figure 3.1: Diagram of an elliptical orbit.

Kepler also proposed an equation which relates the position of a planet within its orbit to the time elapsed since a reference point within its orbit. Today, this is simply referred to as 'Kepler's equation', and is given by

$$M = E - e\sin(E), \tag{3.2}$$

where M is the mean anomaly, E is the eccentric anomaly, and e is the eccentricity of the orbit (Prussing & Conway, 1993). All of these quantities, plus an explanation of how to solve Kepler's equation, is given in section Section 3.2.2.

Kepler's Third Law

> 'The square of the orbital period of the planet is directly proportional to the cube of the planet's semi-major axis, i.e. $P^2 \propto a^3$.'

The original version of Kepler's third law for planets orbiting the Sun was $P^2 = a^3$, which is only true for planets orbiting the Sun (or a star of 1 $M_\odot$) when the period P is measured in years and the semi-major axis a is measured in astronomical units (au). The full version of Kepler's third law, applicable to any two gravitationally bound objects

(Prussing & Conway, 1993), is

$$P^2 = \frac{4\pi^2}{G(m_1 + m_2)} a^3. \tag{3.3}$$

3.2 Generating a binary

For the work presented in Chapter 4 and Chapter 5, I had to produce fake "observations" of binary systems by creating a fake binary system, assigning some instantaneous orbital parameters to it, and making a projection of the two stars on a 2D plane. The method for doing this, using the theory described in Section 3.1, is described below.

3.2.1 Orbital properties

An orbit is characterised by three physical parameters: the semi-major axis a, eccentricity e, and the inclination of the system relative to the observer i. There are also two 'instantaneous' orbital properties: the orientation of the system ϕ and the phase at the orbit (the true anomaly) ν. The orientation of the system will be subject to precession over long timescales (~10s-100s of Myrs, depending on the period of the orbit) and as shown in figure 4.1, $\phi = 0°$ is defined such that the semi-major axis of the system coincides with the line of sight from Earth.

The true anomaly (also known as the flight path angle in both orbital mechanics and aeronautics) is a function of time $\nu(t)$, and is an angular representation of the position of the companion within it's orbit at time t (Prussing & Conway, 1993). It is defined such that when $\nu = 0°$, the companion star is at periastron (i.e. at closest approach to the primary). For circular orbits, ν is uniformly distributed in time. However, in an elliptical orbit, it is not. This is because while the orbiting body is nearer apastron than periastron, it's velocity is lower (in accordance with Kepler's second law).

3.2.2 Solving Kepler's equation

The true anomaly is calculated using a random variable called the mean anomaly, M, which *is* uniformly distributed in time, by definition (such that $M(t) = U[0, 2\pi]$). To calculate the true anomaly from the mean anomaly, we need to numerically solve Kepler's equation (Equation 3.2).

Due to the form of Kepler's equation (specifically the fact that the eccentric anomaly (E) appears both on its own and in the sin function) it is not possible to solve analytically.

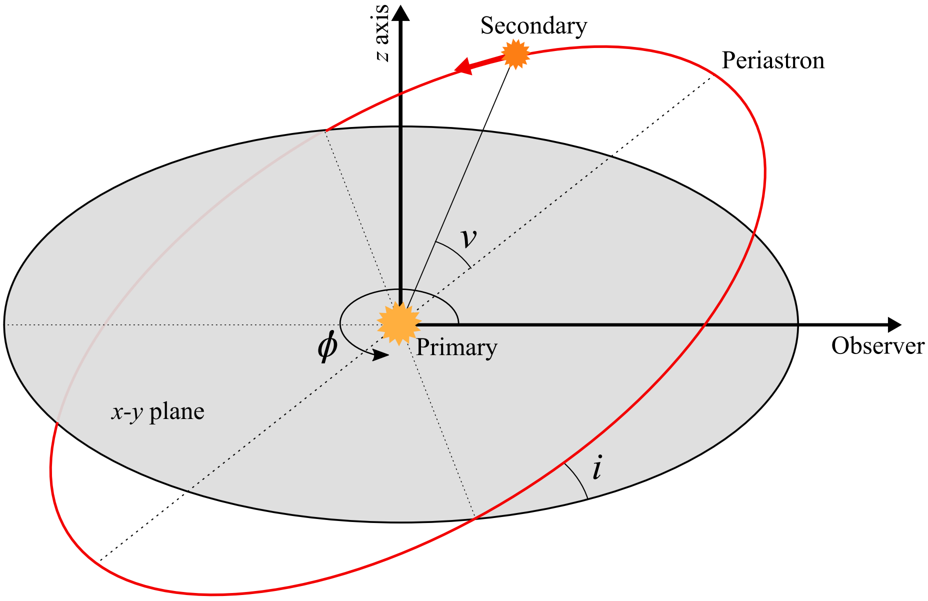

Figure 3.2: Diagram of an elliptical orbit inclined and rotated relative to an observer. The orbit of the companion is inclined at an angle i from the $x - y$ plane and rotated through an angle ϕ around the z-axis. The true anomaly (ν) of the companion is shown measured relative to periastron.

The most common way of doing this is using the Newton-Raphson method; an iterative process which gradually finds the root of the function by trying different values in place of the eccentric anomaly. This numerical approach was used throughout this work.

Once a value for E has been found, it can be used to calculate the true anomaly using

$$\tan\left(\frac{\nu}{2}\right) = \sqrt{\frac{1+e}{1-e}}\tan\left(\frac{E}{2}\right). \tag{3.4}$$

The true distance between the stars as a function of the true anomaly is given by

$$r = \frac{a(1-e^2)}{1+e\cos\nu}, \tag{3.5}$$

(see Prussing & Conway, 1993).

Orientation

When we initialise the binary system, the semi-major axis is along the x-axis (perpendicular to our line of sight). There is no reason that this would be favoured over any other orientation when we observe a binary, so we need to spin the system around the z-axis to randomise the orientation. We call the orientation angle ϕ and it is uniformly distributed between 0 and 2π.

$$\begin{aligned} x' &= x\cos\phi - y\sin\phi, \\ y' &= x\sin\phi + y\cos\phi, \\ v'_x &= v_x\cos\phi - v_y\sin\phi, \\ v'_y &= v_x\sin\phi + v_y\cos\phi. \end{aligned} \tag{3.6}$$

Inclination

After applying the transformations in Equation 3.6, we have a binary system orbiting in the $x - y$ plane, with the semi-major axis at a random orientation within that plane. We now need to incline the system in the z-direction by an inclination angle i.

$$\begin{aligned} x'' &= x', \\ y'' &= y'\cos i, \\ z'' &= y'\sin i, \\ v''_x &= v'_x, \\ v''_y &= v'_y\cos i, \\ v''_z &= v'_y\sin i. \end{aligned} \tag{3.7}$$

For initial conditions in a simulation, the inclination angle should be randomly selected from a distribution that is uniform in $\sin i$, between 0 and 2π (i.e.$U[\sin i]$), because there is no preferred inclination from the reference frame of the binary. However, as we are generating fake observations of a binary, it needs to be done a little differently. This is because it is more likely that a system will be observed closer to edge-on than face-on, due to the fraction of solid angle that will result in an edge on system rather than a face-on one.

On sky separation

The results of Equation 3.7 are the 3D spatial coordinates of the companion (x,y, and z) and the 3D velocity components (v_x,v_y, and v_z). Astrometric observations of a visual binary will give the coordinates of the companion in the image, which correspond to (x,z) from Equation 3.7. The separation can be calculated very simply as

$$s = \sqrt{(x^2 + z^2)}. \tag{3.8}$$

The 'observed' separation can also be calculated in a single step using the true distance and the angles θ, ϕ, and i,

$$s = \sqrt{r(1 - \sin^2(\phi + \theta)\sin^2 i)}. \tag{3.9}$$

3.3 Triples

In Chapter 4, I also need to generate fake triple systems. The majority of triple systems are in a hierarchical configuration, meaning that the primary and secondary star orbit closely while the tertiary orbits at a much larger distance. This is a much more stable configuration of stars than a non-hierarchical orbit. Due to the distance between the primary/secondary orbit and the tertiary, we can consider a triple system as being composed of two independent orbits: the secondary star around the primary (the inner orbit) and the tertiary around the primary (outer orbit).

For a hierarchical triple to be stable, the tertiary needs to be orbiting at a much larger distance than the secondary, so that the stars do not pass closely enough to perturb one another's orbits. There are many different methods of quantifying the stability of triple systems, which are outlined below.

3.3.1 Stability

Many triple and higher-order systems are not stable over long timescales. Triple systems typically decay with a half life of

$$t_{\text{decay}} = 14 \left(\frac{R}{\text{au}}\right)^{3/2} \left(\frac{M_{\text{stars}}}{M_\odot}\right)^{-1/2} \quad \text{years}, \tag{3.10}$$

where R is the separation of the stars and M_{stars} is the combined mass of the components (Anosova, 1986). This form of Equation 3.10 is from Goodwin & Whitworth (2007).

Using typical values of $R = 250$ AU and $M_{\text{stars}} = 1M_{\odot}$, this gives a timescale of ~ 55 kyr, which is well within the Class 0 stage of the object.

The stability of a triple system is determined by the semi-major axes, eccentricities, and the relative inclinations of the secondary and tertiary.

There is no single empirical stability equation for hierarchical triple systems, although there are several widely used models including Harrington (1972); Eggleton & Kiseleva (1995); Valtonen et al. (2008); Reipurth & Mikkola (2012). One of the most commonly used stability equations is the criteria of Mardling & Aarseth (1999), shown in Equation 3.11, derived based on the chaotic energy and angular momentum interactions between the orbits of the two stars.

$$\frac{a_{\text{out}}}{a_{\text{in}}}\Big|_{\text{crit}} = \frac{2.8}{1-e_{\text{out}}}\left(1-\frac{0.3 i_{\text{rel}}}{\pi}\right)\left(\frac{(1.0+q_{\text{out}})(1+e_{\text{out}})}{\sqrt{1-e_{\text{out}}}}\right)^{\frac{2}{5}}, \tag{3.11}$$

where e_{out} is the eccentricity of the outer star, and i_{rel}, is the relative inclination between the inner and outer orbits, and

$$q_{\text{out}} = \frac{m_3}{m_1+m_2}, \tag{3.12}$$

where m_1, m_2 and m_3 are the masses of the primary, secondary, and tertiary stars respectively. A system is unstable if

$$\frac{a_{\text{out}}}{a_{\text{in}}} > \frac{a_{\text{out}}}{a_{\text{in}}}\Bigg|_{\text{crit}}, \tag{3.13}$$

i.e. the ratio of the outer semi-major axis to the inner semi-major axis must be greater than the critical value given by Equation 3.11.

This stability condition is valid for stellar mass objects, and for prograde orbits. It also ignores a small dependence on the inner mass ratio and inner eccentricity. However, it provides a conservative estimate of the stability of an orbit, occasionally rejecting stable orbits in order to ensure no unstable orbits are accepted.

Valtonen et al. (2008) also developed a stability condition for triple systems, using the energy change in an encounter between a binary and a single star to determine that

$$Q_{\text{st}} = 3\left(1+\frac{m_3}{M_{12}}\right)^{\frac{1}{3}}(1-e)^{-\frac{1}{6}}\left(\frac{7}{4}+\frac{1}{2}\cos i-\cos^2 i\right)^{\frac{1}{3}}, \tag{3.14}$$

where Q_{st} is the stability limit of a single encounter, and the stability parameter $Q = q/a_i$ (where a_i is the semi-major axis of the inner binary and q is the pericentre distance of a third body orbiting relative to the barycentre of the binary). M_{12} is the combined mass of the primary and secondary, m_3 is the mass of the tertiary, and e is the eccentricity of the tertiary.

Chapter 4

Orbit fitting with FOBOS

4.1 Introduction

As discussed in chapters 1 and 2, most stars appear to form in multiple systems (Duchêne & Kraus, 2013; Reipurth et al., 2014), and over half of all solar-type and high-mass stars remain in multiple systems when they reach the main sequence. In Chapter 2, I presented the results of my Monte Carlo simulations that model simple rules of star formation from dense cores to bound systems. As well as understanding the formation mechanisms behind multiple system formation, it is also important to be able to determine the orbital properties of main-sequence multiple systems (such as the semi-major axis distribution of binaries or the relative inclinations of triple systems).

Binary orbital parameters can be estimated in different ways depending on the method of observation. Several orbital fitting tools have been developed recently, including `BATMAN` (Kreidberg, 2015) (which uses transit light curves), `RadVel` (Fulton et al., 2018) and `The Joker` (Price-Whelan et al., 2017) (radial velocity measurements), as well as `orbitize!` (Blunt et al., 2020), `ExoSOFT` (Mede & Brandt, 2017), and `orvara` (Brandt et al., 2021) (which use radial velocity measurements and/or astrometry). The majority of these tools have been developed with the intent of fitting the orbits of exoplanets rather than stellar systems, and obtain better fits when there are 10s of epochs of orbital data available. Only `The Joker` is designed to use sparse observations, providing fits to as few as three epochs of data, using radial velocity measurements only.

Unfortunately, the majority of data on multiple systems (obtained for multiplicity surveys, such as those referenced in Section 1.7) only contains a single epoch of relative astrometry. In some cases, there is a second or third epoch available from follow-up observations.

I have developed a new orbital parameter finder - `FOBOS` (Few Observation Binary Orbit Solver). `FOBOS` is designed to find confidence limits for orbital parameters with only two epochs of observation. This chapter describes the development of the `FOBOS` algorithm and shows the results of testing on a large sample of fake binary and triple systems. In Section 4.7, I show the results of using the `FOBOS` algorithm on some observed systems with brown dwarf companions, and compare my results to orbital fits from the literature.

`FOBOS` was developed to constrain the orbital parameters of binary or triple systems with only two or three epochs of relative astrometry. As such, it may act as an incentive to obtain a second epoch on what are currently single-epoch observations. During the development of this algorithm, I realised that it has applications to directly imaged exoplanets that have been very recently discovered, as a way to determine priors on the orbital parameters that can inform follow-up observations.

4.2 Methods

`FOBOS` is a flat-prior brute force Monte Carlo method. A Monte Carlo method is a mathematical technique in which parameter space is randomly sampled to find the probability of certain outcomes. In practice, the algorithm works by producing a very large number of fake systems with a random set of orbital parameters, projecting them into 2D, and comparing the positions of the companion star(s) at the different epochs to establish whether the orbital parameters of the fake system match the observations (to within the observational errors).

For any two epochs of observations at times t_1 and t_2, the companion star is separated by a distance s_1 and s_2 from the primary, with (arbitrary) position angles θ_1 and θ_2, differing by an angle $\Delta\theta$. Note that s_1, s_2, and $\Delta\theta$ will have some observational uncertainty associated with them, and s_1 and s_2 in au depend on the distance and the uncertainty associated with it.

The steps outlined in Section 3.2 are followed to make a fake observation of a system. It starts by generating a fake observation for the first epoch of observation (t_1), with random values of the semi-major axis (a), eccentricity (e), inclination (i), orientation (ϕ), and mean anomaly (M). The limits on these parameters are discussed in section Section 4.2.1. The ability of `FOBOS` to fit the orbit of a system requires at least one more observation at a time t_2.

Assuming that the precession of an orbit can be ignored, so the only parameter which is a function of time is the true anomaly, $\nu(t)$. The true 3D separation at a time t, $r(t)$, for a system with parameters a, e, and $\nu(t)$ is given by

$$r(t) = \frac{a(1-e^2)}{1+e\cos\nu(t)}. \tag{4.1}$$

The on-sky separation at a given time, $s(t)$, is related to the true 3D separation, $r(t)$, and instantaneous angles $\nu(t)$, ϕ, and i via

$$s(t) = r(t)\ (1-\sin^2(\phi+\nu(t))\sin^2 i)^{1/2}. \tag{4.2}$$

The orbital period (P) is also needed, to calculate the fraction of the orbit through which the companion will have moved between the two epochs of observation,

$$P = \sqrt{\frac{a^3}{m_1+m_2}}, \tag{4.3}$$

where m_1 and m_2 are the masses of the primary star and the companion respectively. Note that to calculate the orbital period of the system, we also need to know the masses, which may have significant observational uncertainties, particularly for lower mass companions. The masses of the stars can be determined through the Monte Carlo method, but this significantly increases the computational overheads of the fit.

In the simplest case of two epochs of observations, there is a known time difference $\Delta t = t_2 - t_1$, a change of on-sky angle $\Delta\theta$, and two separations, s_1 and s_2. These are related to the change in ν and s between observations which depend on P, a, e, ϕ, and i.

Triple systems

If the orbit of a triple is being fitted, then it is treated as two separate binaries; one consisting of the primary and secondary, and the other the primary/secondary (pretending they act as a single star) and tertiary. In both cases, the primary star is located at (0,0) in the frame of our coordinates. This is a valid way of treating hierarchical triples, in which the tertiary is orbiting sufficiently far from the primary and secondary for them to act as a point source.

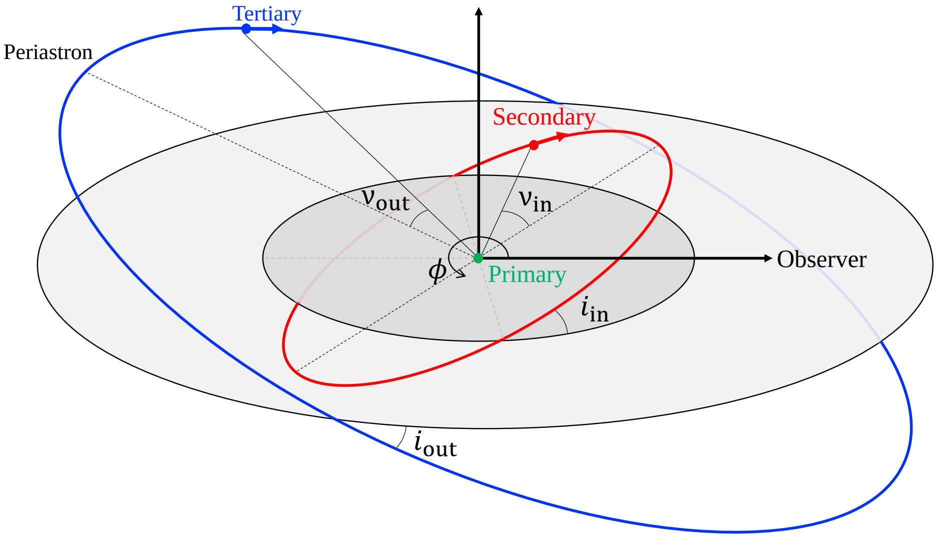
Tertiary
Periastron
Secondary
$\nu_{\rm out}$
$\nu_{\rm in}$
ϕ
Primary
Observer
$i_{\rm in}$
$i_{\rm out}$

Figure 4.1: Diagram of a triple system. The diagram depicts the orbit of secondary and tertiary stars around a primary star. Each orbit is inclined with an inclination i relative to an observer and rotated through an angle ϕ about an axis perpendicular to the line of sight. The true anomaly of each star is measured from periastron, assuming periastron is coincident with the line of sight for $\phi = 0°$.

4.2.1 Parameter constraints

`FOBOS` samples from uniform distributions of parameters without any other prior assumptions on the form of the semi-major axis or eccentricity distributions.

An absolute lower limit on the semi-major axis a_{min} is given by half of the projected on sky separation of the primary and companion star. This is because the true distance of the star has a maximum in a highly eccentric ($e \sim 1$) system, such that $r_{\text{max}} \sim 2a$. If the system is inclined, the observed projected separation s is almost always smaller than the true distance. Therefore, $a_{\text{min}} = s/2$. As this method requires at least two observations that will usually have different separations, a_{min} is calculated using the largest value.

Another highly constraining feature of this method involves the on-sky velocity of the star, v_{obs}. This is how fast the secondary star has moved with respect to the primary. It contains a large contribution from the tangential velocity of the star but no contribution from the radial velocity. The on-sky velocity is therefore a lower limit on the star's true orbital velocity.

The companion star reaches it's maximum orbital velocity, v_{max}, at periastron, so for an orbit with parameters a and e

$$v_{\text{max}} = \sqrt{\frac{G(m_1 + m_2)}{a} \frac{(1+e)}{(1-e)}}. \tag{4.4}$$

Due to the fact that v_{obs} is a lower limit on the speed of the companion star, it is only possible for it to have orbital parameters that satisfy

$$a < \frac{G(m_1 + m_2)}{v_{\text{obs}}^2} \frac{(1+e)}{(1-e)}. \tag{4.5}$$

By assuming that it is extremely unlikely for the observed system to have an eccentricity of $e \gtrsim 0.98$, Equation 4.5 can be used to give a probable upper limit on the semi-major axis of the companion

$$a_{\text{max}} = 100 \times \frac{G(m_1 + m_2)}{v_{\text{obs}}^2} \quad \text{for } e < 0.98. \tag{4.6}$$

For systems with very large on sky velocities, this can be highly constraining. This gives a useful upper limit on the semi-major axis, by reducing the possible range of parameter space to be sampled. In the event that the simulation manages to find no solutions, the limit on the semi-major axis can be removed to allow sampling of extremely

Parameter	Symbol	Range	Units
Semi-major axis	a	a_{min} - a_{max}	au
Eccentricity	e	0 - 1	-
Inclination	i	0 - 90	deg
Orientation	ϕ	0 - 360	deg
Mean anomaly	M	0 - 360	deg

Table 4.1: Definitions of the physical and instantaneous orbital parameters along with their allowed ranges.

high eccentricities at larger-a than previously allowed.

Note that Equation 4.5 also contains the masses of the stars. I used the upper limit on the masses to determine a_{max}, as these give the largest possible value of a_{max}.

4.2.2 Orbital Parameter Generation

At the beginning of each iteration of the Monte Carlo simulation, random values for each of the orbital parameters are selected from within the ranges shown in Table 4.1.

In order to avoid any biases in the posterior PDFs, this method assumes flat uniform priors when selecting the semi-major axis, eccentricity, orientation, and mean anomaly values, and inclination uniform in $\sin i$.

The true anomaly is generated from a distribution that is uniform in time. ν is calculated by first selecting a random value between 0 and 2π for the mean anomaly M of the companion. This is then converted to the true anomaly, ν, by solving Kepler's equation using the Newton-Raphson method (as in Section 3.2.2).

Once all 5 parameters have been selected/calculated for our test system, a 'fake' observation can be produced and $s(t_1)$ can be calculated. If the test separation $s(t_1)$ does not match the observed first separation to within the observational errors, the parameters are rejected as a possible match and the process is restarted.

If the test separation is a possible match to the observed system, we can then proceed to advance the system forward in time. This is done by calculating the period P of the orbit, then dividing the time between the epochs of observation by P to calculate the fraction of an orbit through which the secondary star will move in time Δt. Since M is uniformly distributed in time we can calculate M_2 at time t_2 from

$$M_2 = M_1 \pm \frac{2\pi\Delta t}{P}. \tag{4.7}$$

The companion could be moving in either direction around it's orbit, hence the ±, and in elliptical orbits an equal change in $\pm M$ will almost certainly not correspond to an equal change in $\pm\nu$. The companion is allowed to have multiple orbits in time Δt (which will occur if $\Delta t > P$).

The two new values of the mean anomaly are converted to true anomalies using the same process as outlined in Section 3.2.2. These two new sets of parameters are projected onto the sky to see if either of the sets of $s(t_1)$, $s(t_2)$, and $\Delta\theta$ match their observed counterparts within the observational errors.

This process is repeated n times, randomly sampling different orbital parameters from the whole of the parameter space given in Table 4.1. The final probability density function is calculated from all matches found for a particular set of observations (ideally at least 1 000 matches, and never less than 300 - this is discussed further in Section 4.4.1).

4.2.3 A note on degeneracies

As our observations are a projection onto the sky, the orientation and inclination are 'degenerate'. The inclination may be such that the secondary is either in front of or behind the primary and we would have no way of knowing which. Therefore, an inclination of 20° could correspond to either plus 20°, or minus 20°. Similarly, the orientation could be such that e.g. periastron was on the near side of the primary, or on the far side, and we would not be able to distinguish this. These degeneracies mean that it is often impossible to tell the direction of motion (e.g. clockwise vs. anticlockwise) of the orbit from only a two epochs (the exception would be an almost face-on orbit).

For binaries, the fact that orientation, inclination, and direction are degenerate does not matter at all. However, in triple systems the degeneracy in inclination and the direction of the orbit can be important and will be discussed in Section 4.4.1.

4.2.4 Errors on observed quantities

The code compares the separations and position angles of the fake system to an observation. When running the code, a match will be triggered if both separations and the angle match within the observational errors. For the example systems tested in this paper, I apply a blanket error of 5 per cent to each separation and angle. This value was chosen as it represents an upper limit of typical observational errors. Unsurprisingly, smaller errors in the observation tend to tighten the constraints on a system while increasing the time to find solutions.

I assume that the possible true values of the observations fall uniformly within the

the assigned observational errors. The observational errors could be incorporated more cleverly into the PDFs by weighting ‘hits’ by their closeness to the observed values - however, while the confidence ranges found for some systems can be really quite small, they are too large to justify the extra complexity of doing this.

I have assumed in these tests that observed systems will have a good *Gaia* distance available, or be within a cluster/star forming region with a good distance estimate. The distance can be included as an extra parameter to find the best fit for this as well. Whether this is worth doing depends on how large the uncertainty in the distance is compared to the uncertainty in the angular separations and angular shift.

In my tests, I also assume that the masses are known to a much greater accuracy than the uncertainty in the angular separations and angular shift, and so any error can be neglected. This will often not be the case and the masses of the primary and companion(s) can be included as extra parameters to be sampled. This will add computational expense as there are now two or three new parameters to include.

The impact of real observational errors (including the astrometric errors and errors on masses/distances) is discussed further in Section 4.7.

4.2.5 Selection effects

In order to estimate orbital parameters `FOBOS` requires an on-sky motion to be observed. Rather obviously, this means that if a system’s orbital parameters are such that the companion’s motion is too small to be observed, then it’s orbital parameters cannot be estimated (other than extremely weak constraints based on it not being observed to move).

This means `FOBOS` is only able to estimate the orbital parameters of a biased subset of systems with the ‘right’ orbital parameters. On a system-by-system basis this is not important - if a companion is observed to move we can obtain confidence limits on its orbital parameters. However, over a population of binary or triple systems, particular configurations of parameters will be missed. This is addressed in Chapter 5, in which I examine populations and biases.

4.3 Testing on binary systems

I tested `FOBOS` on 60 fake observations of binary stellar systems. I show that the correct values are found for parameters within the 68 per cent and 95 per cent confidence intervals as often as one would expect. I also show that sometimes `FOBOS` is surprisingly good at constraining orbital parameters (and when it cannot, it is statistically reliable in telling us so).

The orbital parameters, masses, and time between epochs for each of the synthetic binaries used to test our code are available online. The semi-major axis values are randomly distributed in the range 4-450 au and the other orbital parameters within the ranges shown in Table 4.1 for each system. The time between epochs for each of the systems is ∼2-12 yrs, and the masses of the primaries are $m_1 = 0.2 - 1.4\ M_\odot$ and of secondaries $m_2 = 0.016 - 0.7\ M_\odot$.

The only constraint that is applied on selecting binary systems to test is that the companion star must have moved a distance greater than 1 per cent of the initial separation s_1 between observations such that it's motion on the sky is clearly visible. While it is possible to constrain orbital parameters from an observation of no apparent motion, these constraints are *extremely* weak (the main constraint is that the on-sky velocity is too small to have been observed which rules-out some, usually close, orbital configurations).

Each of the test systems ran on a 6 core / 12 thread CPU and the simulation ended when the number of possible matches exceeded 50 000. The performance of the code is discussed in Section 4.5, but often solution PDFs can be found in minutes.

I found that 45/60 (75 per cent) simulations correctly identified the semi-major axis of the binary within the 68 per cent confidence range, and 58/60 (97 per cent) within the 95 per cent confidence range. Similarly, the true inclination of the system is within the 68 per cent range for 41/60 (68 per cent) of test systems and 95 per cent confidence range for 57/60 (95 per cent) of systems. The eccentricity has 35/60 (58 per cent) and 59/60 (98 per cent) within the 68 per cent and 95 per cent confidence intervals respectively.

The key point here is that `FOBOS` gets the 'wrong' answer as often as one would expect.

4.3.1 General performance

I find that `FOBOS` is often good at constraining orbital parameters, with the eccentricity being the most difficult parameter to constrain. Typically, `FOBOS` is able to indicate if the eccentricity is likely to be 'low', 'intermediate', or 'high'. This can be seen from the full table of 68 and 95 per cent confidence intervals (for all 60 test systems) that is available in Appendix B.

The 68 per cent confidence limits on the semi-major axis are often within a factor of < 3 (21/60 systems), mostly within a factor of 5 (40/60 systems), and in only 2 cases a

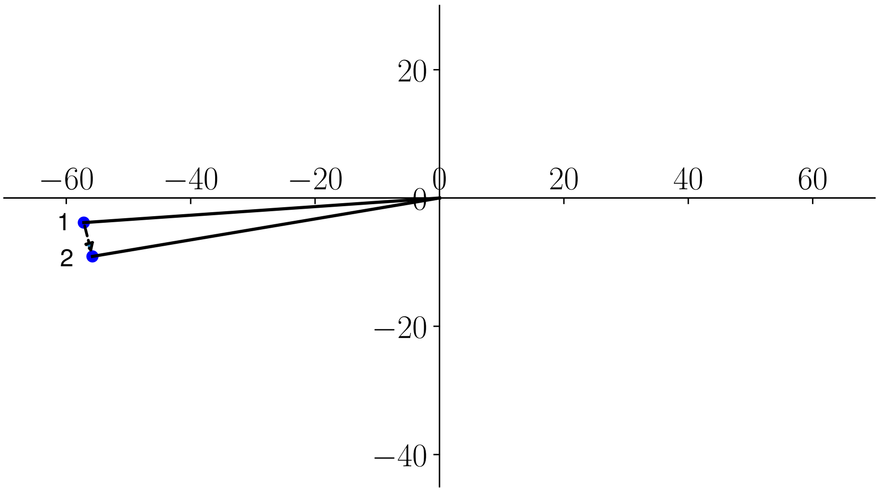

Figure 4.2: On sky projection of system B17 at two epochs. The position of the companion star at the first and second epochs of observation are marked as 1 and 2 respectively, with the direction of the star's on sky motion shown by the arrow. The primary star is located at (0,0) in both observations. The axes are in au.

factor of 10 or more. Given the difficulty in constraining eccentricity there is usually a 'floor' of a factor of 2 on constraining the semi-major axis.

`FOBOS` is often very good at constraining the inclination of the system - in 26/60 systems the 68 per cent confidence limits are less than 20°, and only 1/60 is beyond 40°.

System B17

An example of the ability of `FOBOS` to find tight constraints on orbital parameters is system B17. Figure 4.2 shows the on sky projection of system B17 at the two epochs. Note that the position angles are completely arbitrary - only the change in position angle, $\Delta\theta$, is important.

This binary system has a maximum projected separation of $s = 57.3$ au, meaning that the lower limit on the semi-major axis is $a_{\rm min} = 28.6$ au. The time between observations was 7.43 years, during which the star moved a distance of 5.45 au on the sky. Therefore, the observed on sky velocity of the star was 0.73 au yr^{-1}, or $v_{\rm obs} = 3.49\ {\rm km\,s^{-1}}$. The velocity gives an upper limit of $a_{\rm max} = 7\,930$ au to the semi-major axis using Equation 4.6. This upper limit is for the extreme case of the system being observed face-on while the companion is at periastron in a very highly eccentric orbit. (Note that the result is usually quoted to three significant figures, for real data this should obviously depend on the relative size of the errors on various quantities.)

Figure 4.3 shows the resulting probability density functions for semi-major axis (left),

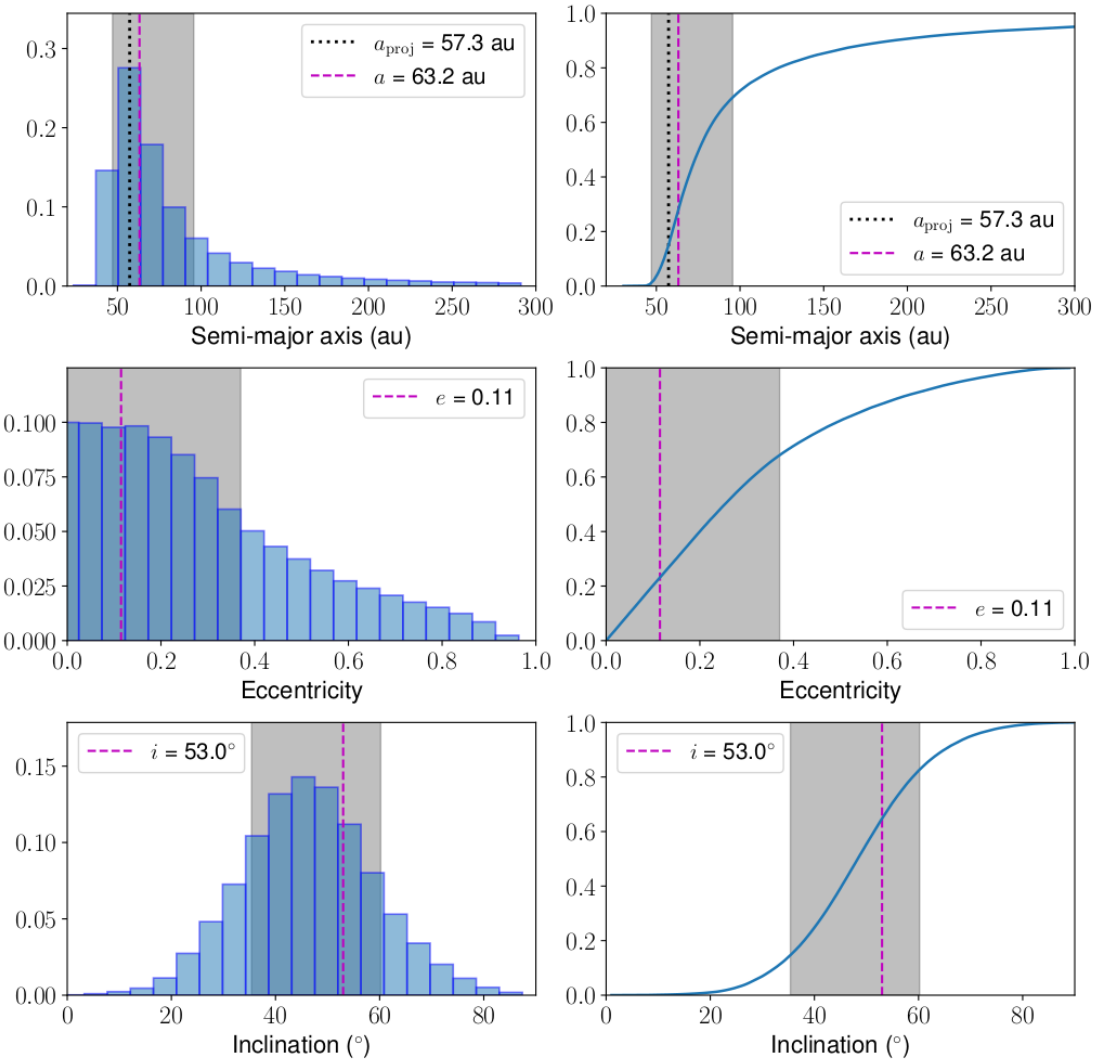

Figure 4.3: The final probability density functions for system B17 show as a histogram (top) and a cumulative distribution function (bottom) for the semi-major axis (left), eccentricity (middle), and inclination (right). The true parameters for the semi-major axis, eccentricity, and inclination are shown as the magenta dashed lines on each plot, and the minimum projected separation of the two stars (in au) is shown by the black dotted lines on the semi-major axis plots. The shaded regions represent the 68 per cent confidence intervals on each of the orbital parameters.

eccentricity (middle), and inclination (right) - as a histogram (top), and CDF (bottom). The 68 per cent confidence ranges are shown by the grey shaded regions and the true value of the semi-major axis, eccentricity, and inclination are shown by the purple dashed-lines in each panel. For the semi-major axis the black dotted line shows the maximum observed separation.

In this case, `FOBOS` has performed extremely well. The 68 per cent confidence limits for a are $47.0 - 95.6$ au (true value 63.2 au), for e, $0.00 - 0.37$ (true value 0.12), and for i, $35.4 - 60.2^\circ$ (true value 53.0°).

Corner plots are useful to examine the connection between different parameters. In Figure 4.4 I show the corner plot for system B17 - note that as well as a, e, and i, `FOBOS` can also estimate the instantaneous orbital parameters ϕ (orientation), and ν or M (phase).

Figure 4.4 shows slightly more subtle information than the individual PDFs in Figure 4.3. Semi-major axis and eccentricity are (unsurprisingly) related, and we can see that if a is high, then e must be high (far left, second panel down). The orientation (ϕ, fourth row) of the orbit shows a slight preference for being close to either $\phi = 0^\circ$ or $\phi = 180^\circ$, but could take any value in the $0 - 360^\circ$ range. The phase (M, bottom row), however, is well constrained to be probably very close to periastron ($M \sim 0^\circ$). Depending on what one is interested in in a particular system the instantaneous orbital parameters may be extremely interesting or of little use.

The information in the corner plot can allows us to rule-out particular combinations of parameters in a way that is not obvious from the individual PDFs. For example, if we were to have extra information that made us suspect that a was high (say, > 200 au) then that would constrain e to being high (> 0.4), and i to be quite low ($< 50^\circ$).

System B4

A much less well constrained system is system B4 whose observation is shown in Figure 4.5. It is worth comparing the observations of systems B17 and B4 in Figure 4.2 and Figure 4.5. System B4 has moved slightly further than system B17 and the two observations appear to the eye as if they are very similar and contain very similar information. However, as we will see, the data for system B4 is not particularly constraining. Additional corner plots for this system are shown in Appendix B.

System B4 has true values of $a = 190$ au, $e = 0.51$, and $i = 10.4^\circ$. The minimum semi-major axis was calculated as $a_{\rm min} = 12.1$ au from an on-sky separation of $s_{\rm proj} = 24.2$ au. The distance moved by the star in 10.6 yrs corresponds to an on sky velocity of

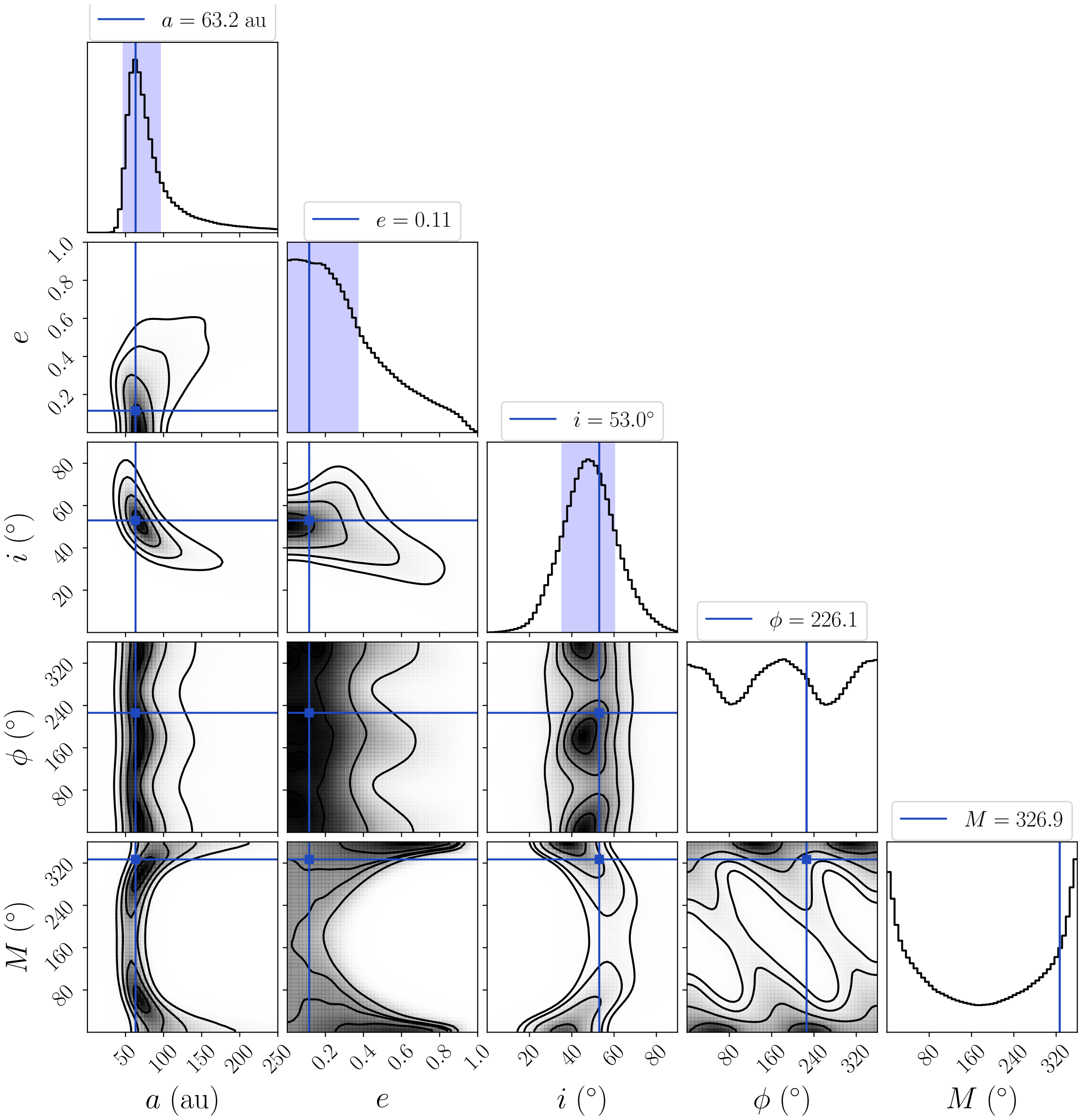

Figure 4.4: Corner plot of parameters a, e, i, ϕ, and M for system B17, with solid blue lines representing the true values and the shaded blue regions showing the `FOBOS` 68 per cent confidence intervals. The panels at the top of each column show the probability density functions for each orbital parameter individually and all other panels show two dimensional covariance of each combination of parameters.

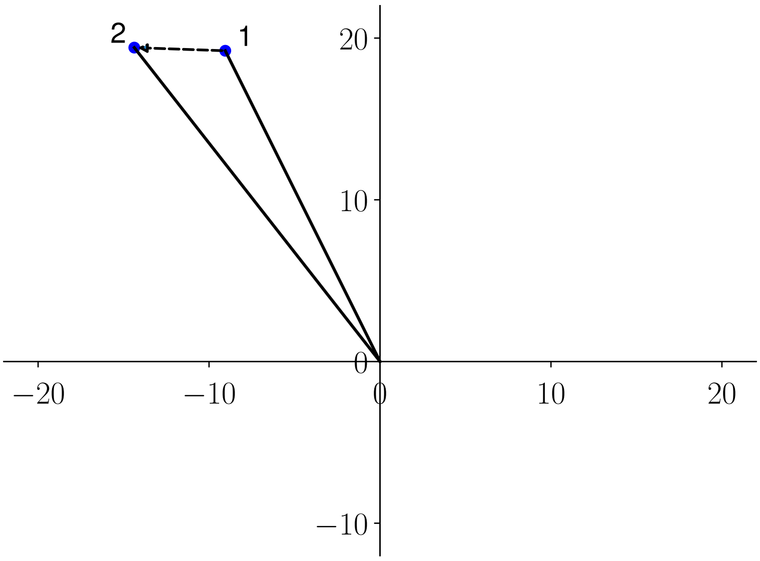

Figure 4.5: On sky projection of system B4 at two epochs. Annotations and axis units are as in Figure 4.2.

$v_{\rm obs} = 2.39\ {\rm km\,s^{-1}}$. These values do not appear to be dissimilar to other test systems.

The confidence limits for system B4 are shown in Figure 4.6. Starting with the middle and bottom panels: the eccentricity and inclination are almost in the 68 per cent confidence limits. The inclination is fairly well-constrained as probably $10 - 30°$. The eccentricity is probably less than 0.8, but the exact value would be difficult to estimate[1].

However, `FOBOS` fails to correctly find the true semi-major axis of 190 au with a 68 per cent confidence range of $14 - 56$ au. The true value is just outside the 95 per cent confidence range of $14 - 174$ au.

It should be noted that the code has not 'failed' - it is just that of all the orbital parameters that could have produced the observed movement on the sky within the assumed errors, there were many with much smaller semi-major axes than what we know to be the actual answer. The results are purely probabilistic and need to be treated as such: there is a higher probability that this particular projection of the motion of the binary on the sky corresponds to a system with a low eccentricity and small semi-major axis, rather than a relatively eccentric $e \sim 0.5$ system with instantaneous orbital parameters that cause the projected separation of the stars to be eight times lower than the semi-major axis.

---

[1] The confidence limits are found by finding the smallest range of parameter values containing 68 and 95 per cent of the PDFs. This fits peaks well, but in the case of the eccentricity distribution here, it doesn't quite map onto the almost flat PDF from 0 to 0.8. This illustrates the usefulness of 'eyeballing' PDFs.

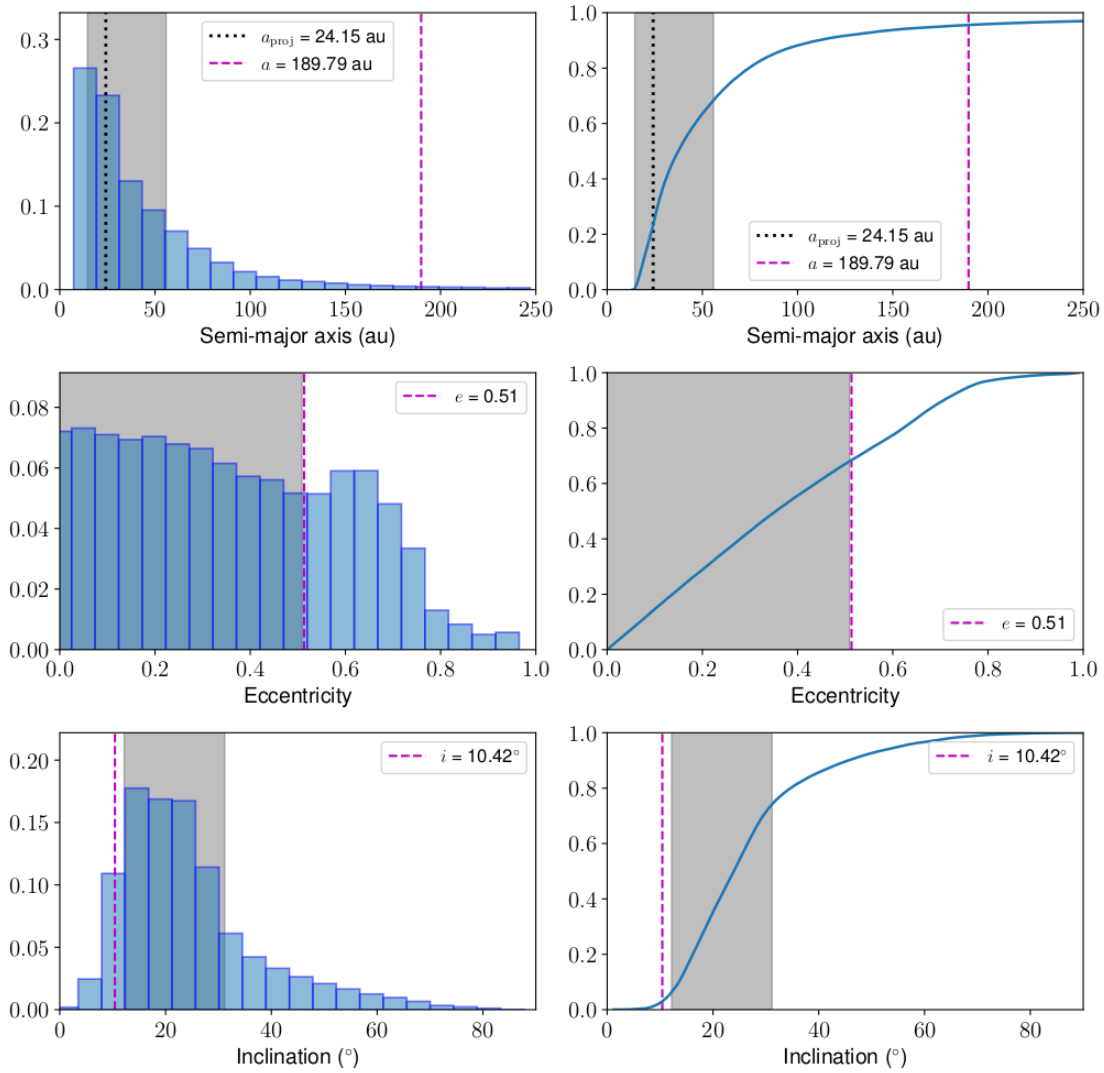

Figure 4.6: Probability density functions for system B4. Legend as in Figure 4.3.

4.4 Triples

The method outlined above can also be applied to hierarchical triple systems. Hierarchical triples are composed of an inner binary and a significantly more distant outer tertiary companion. Therefore, we can consider a system as being composed of two independent orbits - the secondary star around the primary (referred to as the inner orbit) and the tertiary around the primary (outer orbit). In hierarchical triples, there needs to be a significant separation between the inner and outer orbits for the system to be stable, which is a very useful constraint.

For triple systems, I first assume that the star closest to the primary on the sky is the secondary star and the star furthest from the primary on the sky is the tertiary star. This is true for the majority of observations, but in some cases the tertiary star may appear closer to the primary than the secondary[2]. In cases where no fits can be found assuming the most probable alignment, it is possible to relax this assumption.

Each orbit will have it's own set of parameters, defined in the same way as for a binary. I use a_{in}, e_{in}, i_{in}, ϕ_{in}, and M_{in} to denote the parameters of the inner orbit and a_{out}, e_{out}, i_{out}, ϕ_{out}, and M_{out} for the outer orbit. These orbital elements are shown on the diagram in Figure 4.1.

For systems with two companions, the inclination can vary from $-90°$ to $+90°$ as one orbit may be inclined above the plane on the side of the observer, and the other below.

Attempting to fit five additional orbital parameters means that simulations of triple systems are significantly more computationally expensive. However, parameter space can be significantly reduced by excluding all unstable systems.

Generating fake triples

The code treats a triple system as two individual orbits. In both cases, the primary star is at the centre of our co-ordinate system. Each orbit is modelled through the same process that is described in detail in Section 4.2, the first stage of which is generating and projecting the inner orbit for both epochs.

If both separations and the difference in position angle match the observation of the secondary star, then the simulation moves on to the outer orbit. I calculate a lower limit on a_{out} by evaluating Equation 3.11 for the selected values of a_{in} and e_{out}, this ensures that all fake systems would be (hypothetically) stable.

---

[2] Only in close-to edge-on systems for a small fraction of its orbit does the tertiary have the chance to be closer in the sky to the primary than the secondary. One interesting case where this may become moderately likely is a system with a close-to face-on secondary and a close-to edge-on tertiary near the stability limit.

The vast majority of iterations end without finding a match for the inner orbit (full details of the rejection rate for various test systems are explored in Section 4.5). When a match is found for the inner orbit, 1 000 orbital configurations for the outer orbit are sampled to look for possible matches.

4.4.1 Results

The code was tested on 60 fake triple systems. Each simulation ran until 1 000 matches had been found or the wall-clock time of the simulation exceeded 24 hours. The cutoff of 24 hours per simulation was an arbitrary time limit to ensure all simulations ran in a reasonable time frame, and should not be used for real systems.

Out of these 60 simulations, 4 of them (T14, T35, T44, T47) found between 300 and 1 000 matches, and a further 6 simulations (T5, T18, T42, T46, T50, T56) produced fewer than 300 matches. These last 6 systems are excluded from the following statistics, as there were too few solutions to generate reliable probability density functions.

In tests it was found that 300 is an absolute lower limit on the number of matches required to have a statistically reliable probability density function, and when analysing real systems we would ideally want 1 000 (or more) matches.

The true parameters for all of our triple systems are available in Appendix B. Note that the secondary and tertiary inclinations are both given relative to the plane of the sky - in triple systems a much more useful and interesting measure is the relative inclination of the two orbits.

The semi-major axis, eccentricity, and inclination of the inner orbit were all within the 68 per cent confidence interval for 44/54 (81 per cent), 35/54 (65 per cent) and 38/54 (70 per cent) of systems respectively. For the outer orbit these values are 36/50 (67 per cent), 32/54 (59 per cent) and 46/54 (85 per cent) respectively.

`FOBOS` is usually more effective at constraining the orbital parameters in triples compared to binaries due to the stability condition ruling-out many possible configurations which could otherwise fit the observations.

System T19

System T19 is an example of a well constrained triple system. The true parameters are $a_{\text{in}} = 24.5$ au, $e_{\text{in}} = 0.77$, and $i_{\text{in}} = -23.5°$, and $a_{\text{out}} = 504$ au, $e_{\text{out}} = 0.10$, and $i_{\text{out}} = -11.0°$. The relative inclination of the two orbits is 13.5°. The system was observed at two epochs which were 8.67 yrs apart.

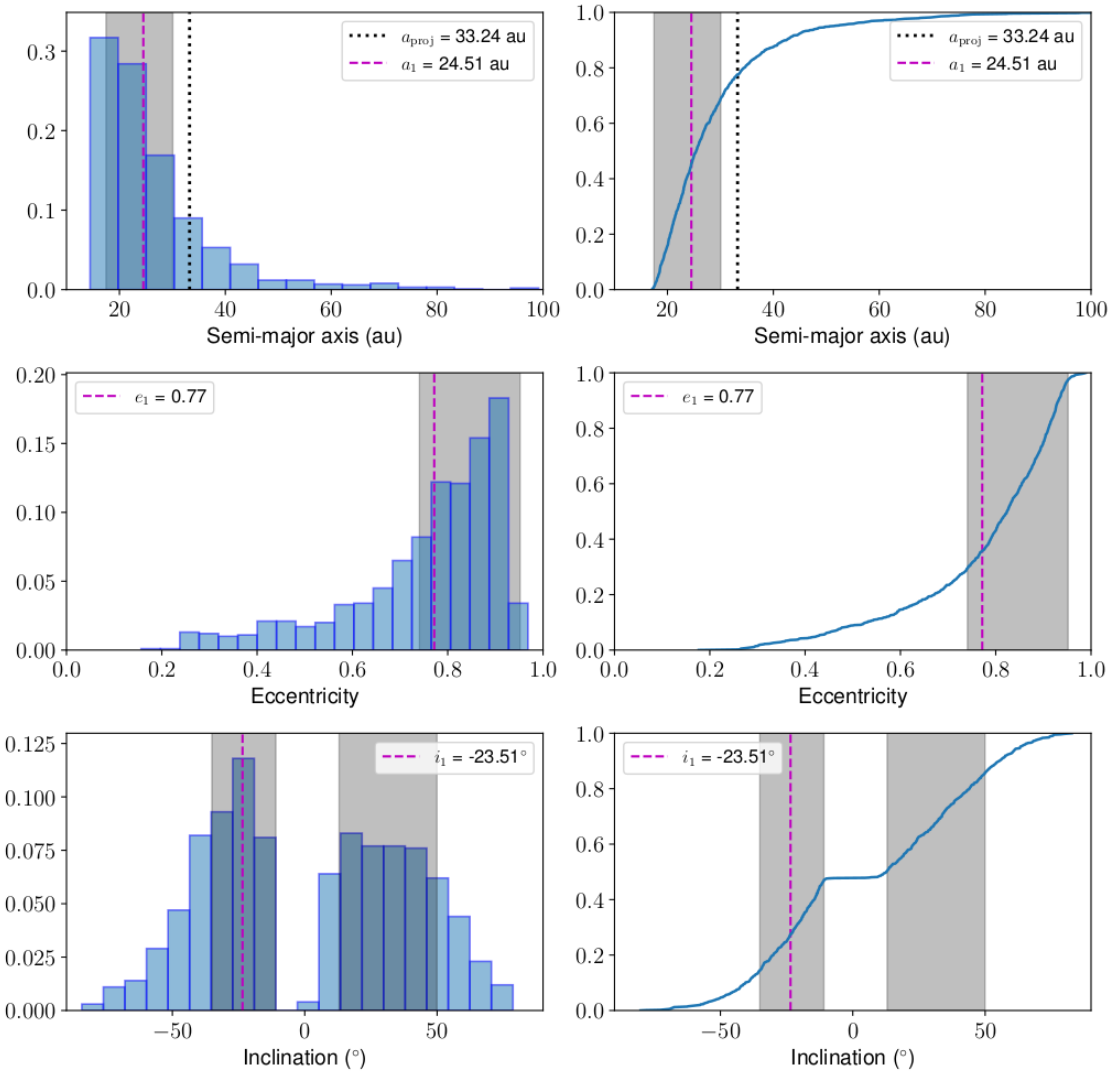

Figure 4.7: Histograms and cumulative distribution functions for semi-major axis, eccentricity, and inclination for the inner orbit in the system T19. The grey shaded regions show the 68 per cent confidence interval for each parameter. The magenta dashed lines represent the true value of each orbital parameter and the black dotted line shows the maximum projected separation of the primary and secondary star out of the two observations.

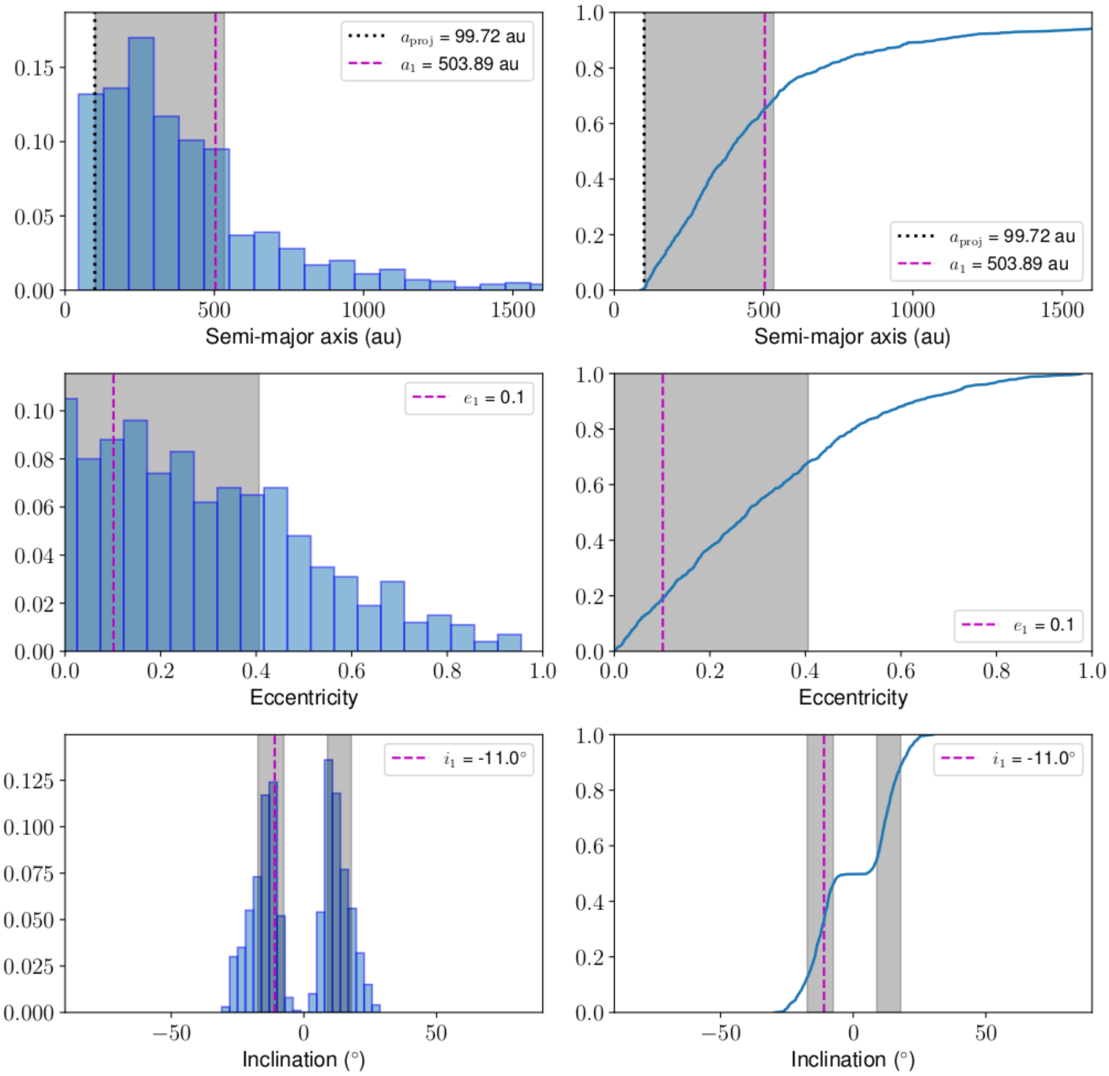

Figure 4.8: Histograms and cumulative distribution functions for semi-major axis, eccentricity, and inclination for the outer orbit in the system T19. The grey shaded regions show the 68 per cent confidence interval for each parameter. The magenta dashed lines represent the true value of each orbital parameter and the black dotted line shows the maximum projected separation of the primary and secondary star out of the two observations.

The maximum projected separations of the secondary and tertiary stars were 31.2 au and 99.0 au respectively, and they moved with on-sky velocities of 1.69 $\mathrm{km\,s^{-1}}$ and 1.73 $\mathrm{km\,s^{-1}}$.

Figure 4.7 and Figure 4.8 shows the PDFs of the secondary and tertiary for the semi-major axis (left), eccentricity (middle), and inclination (right). Again, the shaded regions are the 68 per cent confidence ranges, the purple dashed lines give the true value, and the green dotted line in the top panels the maximum observed separation. Note that the scales for semi-major axis and inclination are different for the secondary and tertiary.

The true semi-major axes of both the secondary and tertiary are within the 68 per cent confidence limits (left panels). Interestingly, the semi-major axis of the secondary is found to be almost certainly significantly smaller than its projected separation; and the semi-major axis of the tertiary as almost certainly much larger than its projected separation. Here the stability criterion is extremely powerful - if both the inner and outer semi-major axes of the components were close to their projected values the system would not be stable, hence the code has to move them in and out respectively to find mutually agreeable fits.

The eccentricities are fairly well constrained (middle panels). The secondary eccentricity must usually be high to see the observed velocity shift for a low semi-major axis. The tertiary eccentricity cannot be too high to fit the stability criteria (roughly speaking, the tertiary periastron needs to be at least about four times the secondary apastron), but is relatively weakly constrained as being probably less than 0.4.

Note that the inclinations in the right panels are different to those used for binary orbits. In binary orbits the inclination is given as a PDF between 0° and 90° as the degeneracy between e.g. $+45°$ and $-45°$ is unimportant. However, in triple systems this degeneracy can be extremely important as it reflects the relative inclination of the companion stars.

The inclination distributions (the right panels of Figure 4.7 and Figure 4.8) both show two peaks which are roughly symmetric around zero degrees. This is because it is roughly equally likely to find solutions at plus or minus a particular inclination (the only difference being if the companion is in front of or behind the primary). The slight discrepancy between the confidence intervals at positive and negative inclinations is due to Poisson noise. There is a relative inclination term in the stability condition (Equation 3.11) which makes a slight difference to the symmetry, but this term is only important if a system is very close to the stability limit.

In the right panels of Figure 4.7 and Figure 4.8 we can see that for the tertiary the inclination is well constrained at $\pm 8 - 18^\circ$, whilst the secondary is slightly less well constrained at $\pm 11 - 42^\circ$ (68 per cent confidence limits). The quoted confidence intervals are calculated assuming the inclinations are symmetric about zero (which is usually the case).

It is worth mentioning that the relative directions (prograde or retrograde) of the orbit could provide extra information if they were available. If the inclination is constrained to be close-to face-on then the direction of the orbit can be determined. However, in the much more common case of close-to edge-on orbits relative directions cannot be determined[3].

There are two possible relative inclinations: one in which the relative inclination is small ($0 - 20^\circ$ if both are positive or both negative), or quite large ($20 - 60^\circ$ if they have opposite signs). It is impossible to know which of these is true for an observed system (in system T19 we know that the correct answer is that the relative inclination is small).

There is potentially a prior expectation in real systems that the formation mechanism (e.g. disc fragmentation) should produce triples which have similar inclinations. With a population of real systems in which many have one possible configuration which is closely aligned in inclination, one could make statistical/physical arguments for one configuration being more likely than the other. However, in any single system considered in isolation it is impossible to distinguish.

I show the corner plot for system T19 in Figure 4.9. This is a much 'busier' plot than for a binary system as there are many more parameters all of which are related to each-other. Depending on what exactly one is interested in about a particular system, different parts of this plot will be more or less useful. For example, the orientation, $\phi_{\rm in}$, of the inner orbit is very well constrained to be around 70 or 290° (these are symmetric, the difference being if periastron is in front or behind the primary).

System T25

For system T25, the semi-major axis, eccentricity, and inclination PDFs for the secondary and tertiary are shown in Figure 4.10 and Figure 4.11. System T25 shows some interesting features. The semi-major axis histogram shows a sharp peak centred on the projected separation of the secondary, whilst the true value lies outside the 68 per cent

---

[3] If both stars move in the same direction on the sky (e.g. left to right) they may have prograde orbits if they are both on the same side of the primary relative to us, or retrograde orbits if they are on opposite sides. Unfortunately, from purely astrometric data we have no way of determining which side of the primary each companion is. Additional radial velocity data could break this degeneracy, but I assume all we have is astrometric data.

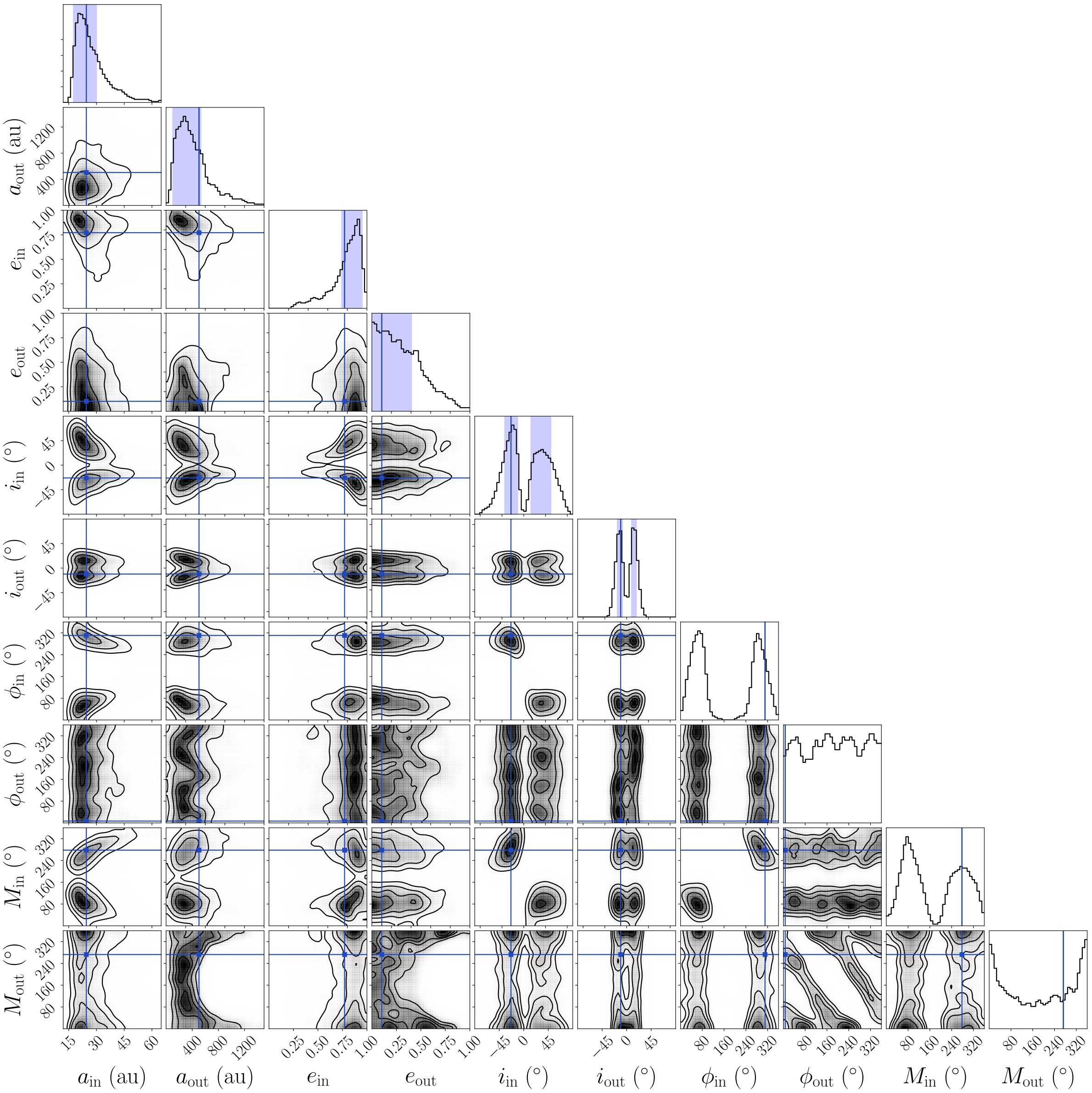

Figure 4.9: Corner plot for triple system 19, with solid blue lines representing the true orbital parameters (available in online data) and the blue shaded regions showing the `FOBOS` 68 per cent confidence intervals. Sample size of 1000 matches.

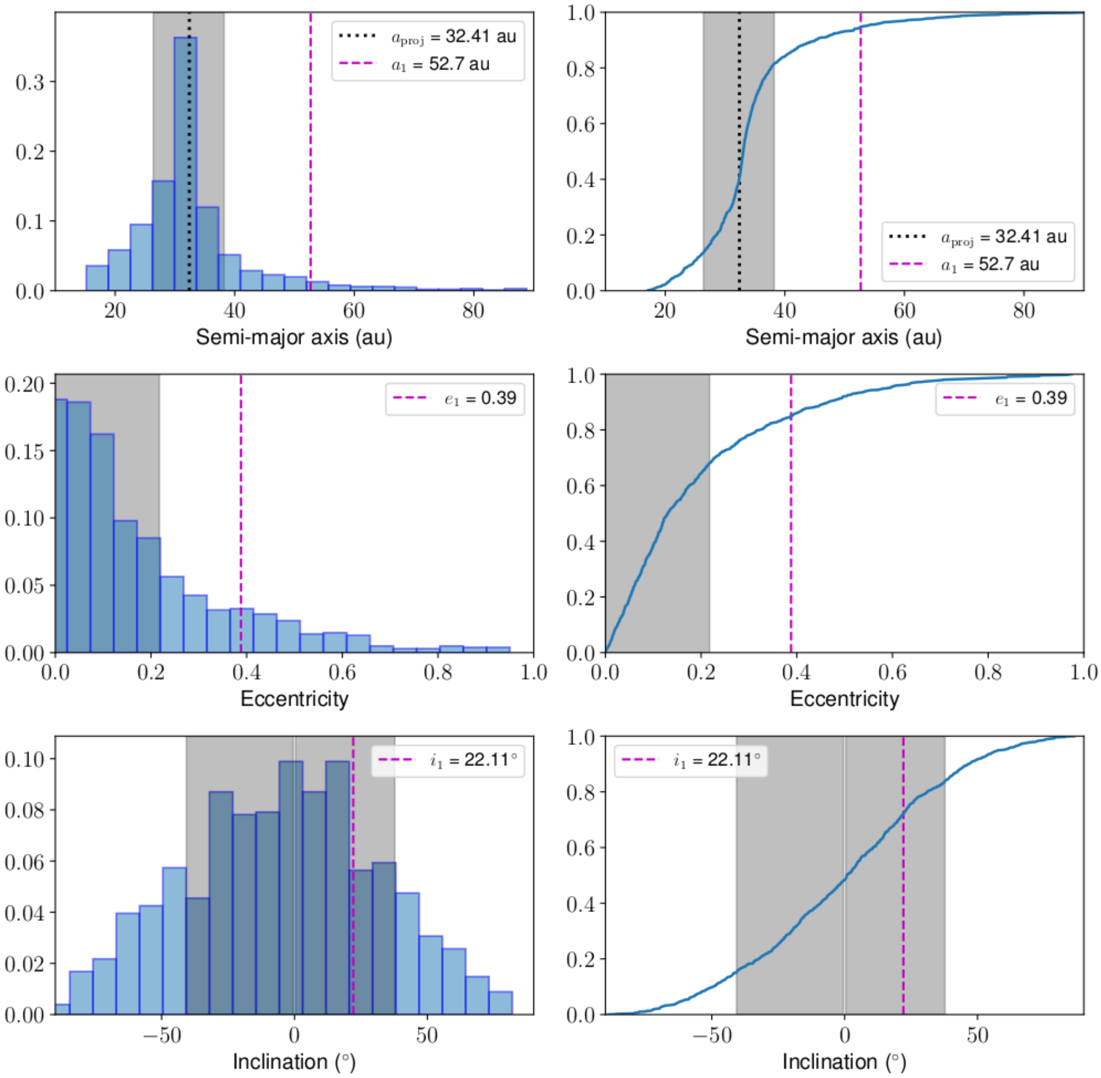

Figure 4.10: Histograms and cumulative distribution functions for semi-major axis, eccentricity, and inclination for the inner orbit of system T25. Legend as in previous figure.

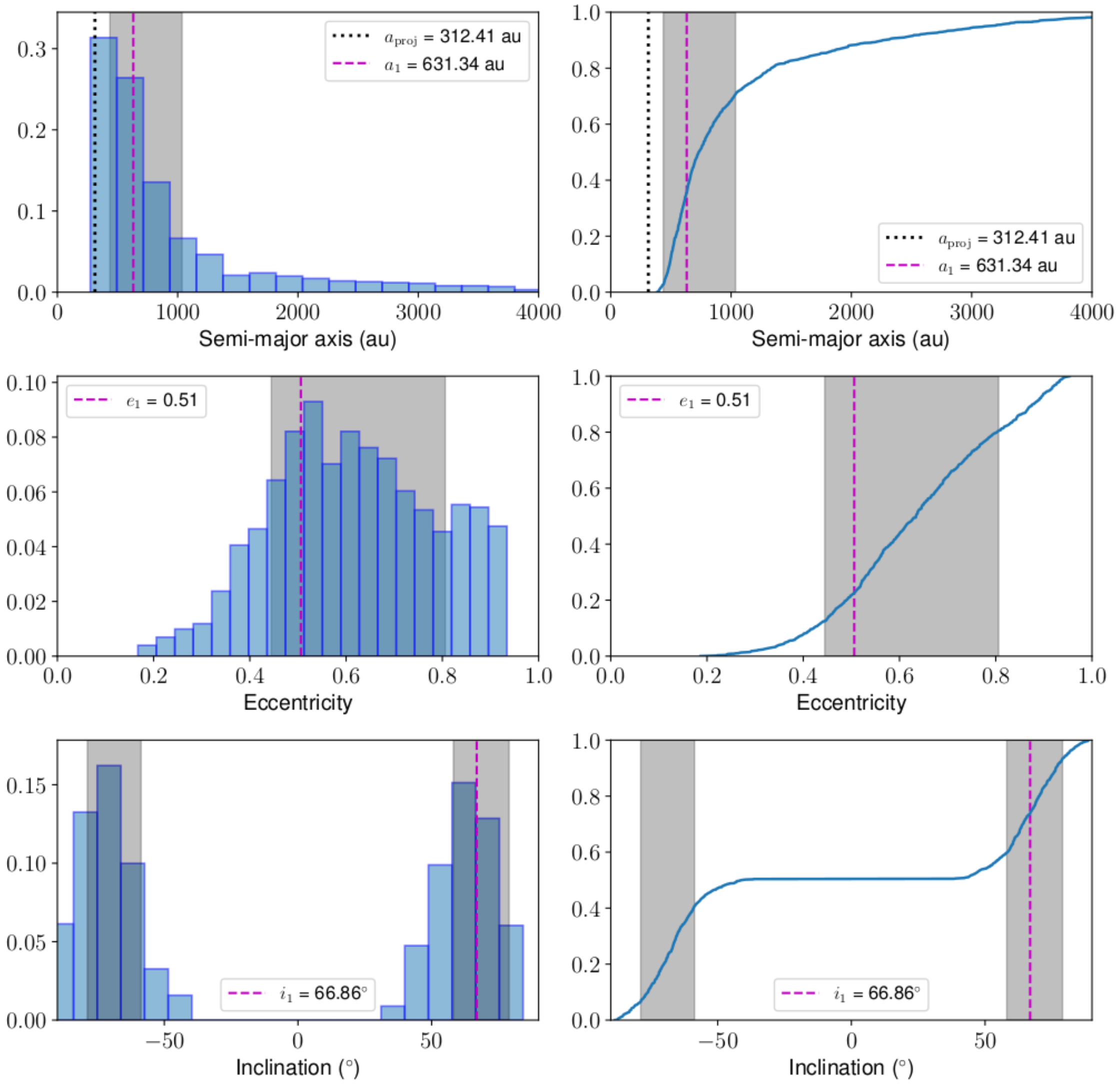

Figure 4.11: Histograms and cumulative distribution functions for semi-major axis, eccentricity, and inclination for the outer orbit of system T25. Legend as in previous figure.

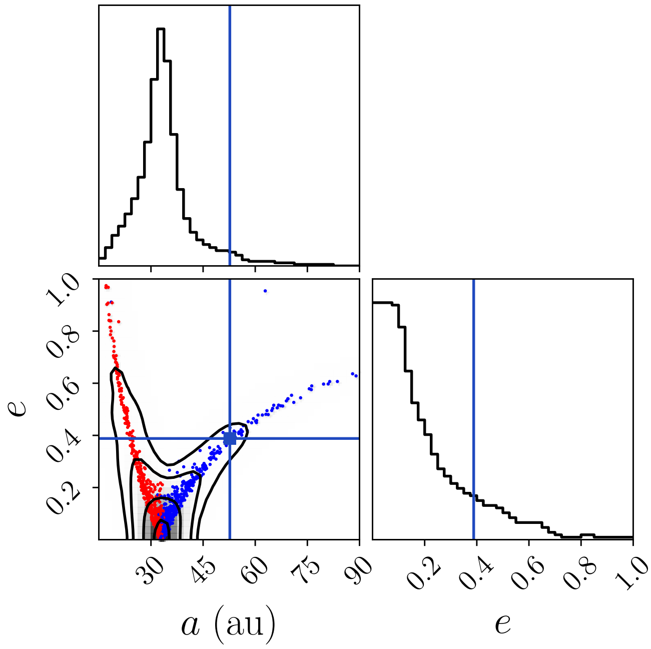

Figure 4.12: Zoom in of corner plot of the semi-major axis vs eccentricity solutions for system T25. The blue points on the bottom left plot represent all systems for which the mean anomaly is $M < 90°$ or $M > 270°$ (i.e. the star is closer to periastron) and the red points for $90° < M < 270°$ (the star is closer to apastron).

confidence interval and barely within the 95 per cent confidence interval. Also, the PDF for the inclination of the system does not show the same bimodality as the vast majority of the other systems, as we cannot constrain the values at all well, and the 68 per cent confidence interval is very large (essentially, the code cannot fit close-to face-on orbits, but anything less than about ±45° has a roughly equal probability). However, it does a remarkably good job of constraining the tertiary orbit.

Some of the more subtle interesting features of this system become apparent when the corner plot is examined. The PDF of $a_{\rm in}$ and $e_{\rm in}$ is shown in Figure 4.12 and has an unusual structure. There are many possible solutions for $a_{\rm in} \sim 20 - 50$au and low eccentricity, and then the possible solutions diverge into two distinct branches when $e_{\rm in} \gtrsim 0.2$ - with fits found at low-a and high-e, or high-a and intermediate-e. The possible fits have been coloured red when the system is close to apastron ($M \sim 180°$), and blue if the system is close to periastron ($M \sim 0/360°$). Which ‘branch’ is followed clearly depends on where in its orbit the system is placed.

This shows that despite the true value of the semi-major axis falling in the tail of the PDF of possible semi-major axes, it is still in a well-populated region of a-e parameter space. Again this shows the value of examining the corner plots rather than just relying on parameters reduced to a single dimension.

4.5 Timing

Our code uses a brute-force Monte Carlo method to randomly generate fake binary or triple systems, with parameters drawn from uniform distributions (for inclination this is uniform in sin i). This method samples the total available parameter space as comprehensively as possible, but due to the vastness of this parameter space, a huge number of iterations is required. Therefore, the code written is in `fortran90` and OMP parallelised to run on multiple cores.

The average CPU time per iteration over multiple simulations is ∼34 ns, and is very similar when testing on both binary and triple systems (a typical triple system is usually rejected after only modelling the inner binary making the time per iteration very similar).

The number of iterations required to find an appropriate number of matches varies significantly from system to system. For example, the simulation for system B38 ran for 11.2 min and found one match for every 42 000 fake systems tested (a match being found every 13 ms), but system B8 ran for 35.7 s and found one match every 4.47×10^6 iterations (a match was found every 0.12 ms).

The majority of binary simulations have a wall-time of ∼1-12 min, and run for $\sim 10 - 160$ CPU min. The simulation that produced the results in Figure 4.3 took 8 min 53 s to run, sampling a total of 1.9×10^{12} fake systems. From these, 51 293 matches were found with separations and position angles within the errors. This corresponds to a rejection rate of over 99.99999 per cent.

Due to the 5 additional orbital parameters that must be found to fit a triple system, the time taken to produce a sufficient number of matches for each triple simulation was significantly longer on average than for binaries. It also varied significantly from system to system, from a minimum of ∼2.22 minutes wall-time, to less than 300 matches being found in 24 hrs of wall-time.

4.6 Multi-Epoch Observations

I have concentrated above on estimating the orbital parameters from a bare minimum of data in just two epochs of observation. However, extra information from a third epoch can sometimes (unsurprisingly) significantly improve our estimates. With more than two

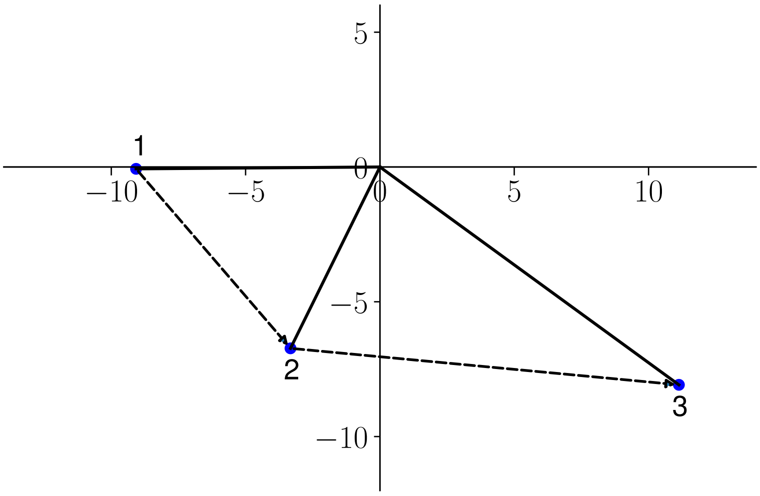

Figure 4.13: On sky projection of a binary system with three epochs of observation. The position of the star at the first, second and third epoch is marked by the numbers 1, 2 and 3 respectively. The primary star is centred on (0,0) for all observations and the axes given in au.

epochs of data, I go through the procedure outlined above to fit the first two epochs, and then repeat to fit any further epochs.

I tested the code on 20 additional fake systems with three epochs of observations each. This showed that an additional data point can sometimes be very constraining (not always, sometimes a third epoch makes very little difference). The observation of one such system is shown in Figure 4.13. The secondary has moved a significant distance between each observation suggesting we are seeing a reasonable fraction of its orbit (and that its period is not too many times greater than the time between epochs).

This system had a maximum projected separation of 13.8 au, from which the lower limit on the semi-major axis was calculated as $a_{\mathrm{min}} = 6.9$ au. The three epochs of observation were separated by 7.31 and 11.45 yrs (so it was observed over an 18.76 yr timescale), giving the companion star an observed on sky velocity of v_{obs} =1.20 au yr^{-1} (5.72 km s^{-1}) between the first and second epochs and v_{obs} =1.27 au yr^{-1} (6.03 km s^{-1}) between the second and third epochs. The upper limit on the semi-major axis for this system was therefore $a_{\mathrm{max}} = 3\,764$ au.

In Figure 4.14, I show the PDFs (as CDFs) for the semi-major axis, eccentricity, and inclinations of the system using all three epochs (top row), and using each pair of epochs (bottom row). The true values are given by the red dashed lines, and the 68 per cent confidence limits by the greyed regions. The projected separation is shown by the green dotted line for the semi-major axis.

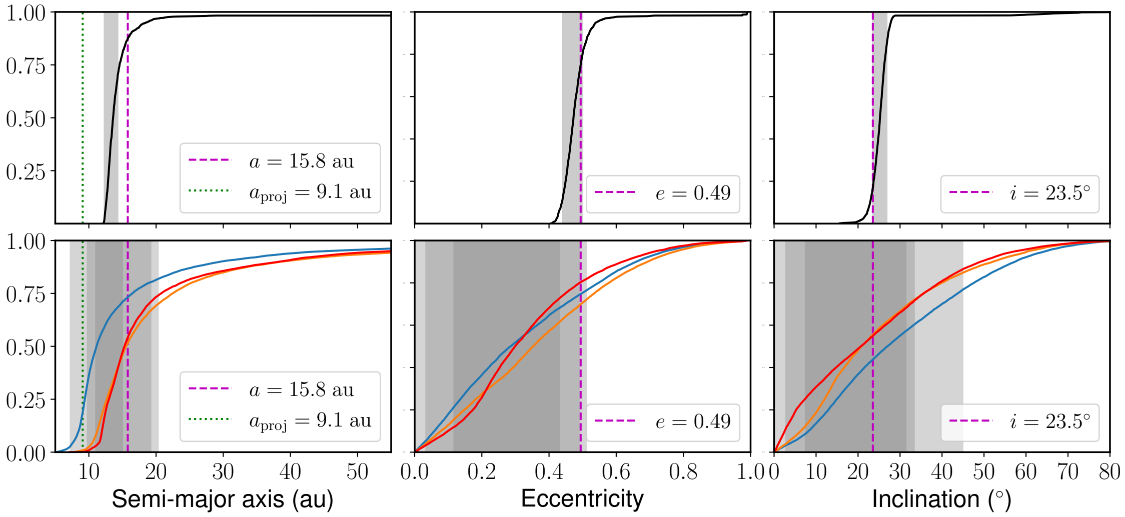

Figure 4.14: Cumulative distribution for a binary system with 3 epochs of observation. The top three plots show the PDFs using all three epochs together. The bottom plots show the PDFs from each possible pair of observations (blue: epochs 1 and 2, orange: epochs 2 and 3, and red: epochs 1 and 3). The grey shaded regions represent the 68 per cent confidence interval for each CDF.

The most striking feature of Figure 4.14 is how much a third epoch is able to constrain all three orbital parameters in this case. Figure 4.15 shows the corner plot of semi-major axis, eccentricity and inclination, with histograms featured in the top plot of each column and parameter covariances shown in the other panels. This highlights how tightly each parameter is constrained using the three epoch method when one sees how small the ranges of a, e, and i are.

The 68 per cent confidence limits on the semi-major axis have fallen from about $8 - 20$ au to $12.3 - 14.3$ au. The true value of the semi-major axis for this system is 15.8 au, falling outside the 68 per cent confidence interval but within the 95 per cent confidence interval of $12.1 - 18.6$ au.

Similarly, the inclination true inclination of 23.5° falls at the lower end of the 68 per cent confidence interval ($23.5 - 26.8°$) and comfortably within the 95 per cent limits of $21.0 - 28.3°$. The true eccentricity value of 0.49 falls within both the 68 per cent (0.44 - 0.50) and 95 per cent (0.41 - 0.54) confidence intervals.

The reason an extra epoch is so much more constraining for this system is that we have three epochs spanning ~ 19 yrs of a ~ 50 yr total period. Hence the third epoch requires a large on-sky motion in a very particular direction from any fits to the first two epochs which ‘pins down’ the orbit extremely well. When I test on systems where three epochs only cover a small fraction of an orbit and have large observational errors, I find

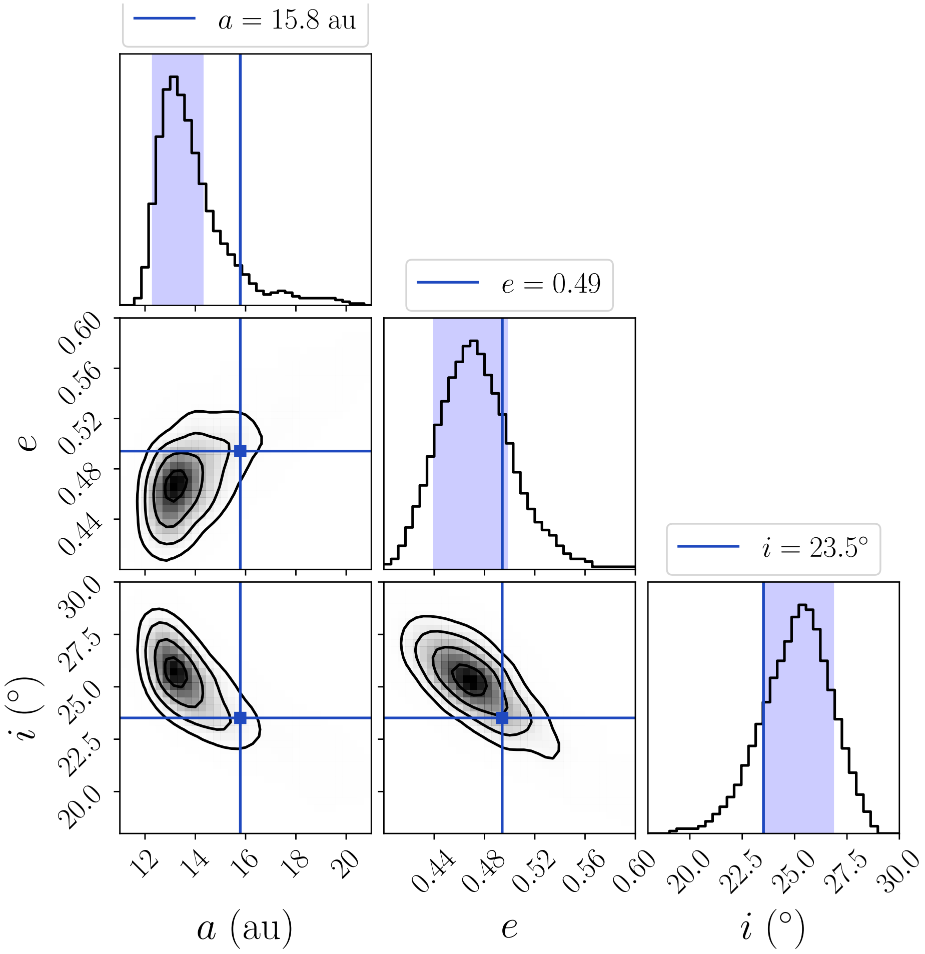

Figure 4.15: Corner plot of the semi-major axis, eccentricity and inclination for the system shown in Figure 4.13. The true value of each parameter is indicated by the solid vertical blue line.

that the third epoch can sometimes add very little to the constraints from just two.

4.7 Comparisons

It is worth comparing `FOBOS` to some other orbit-fitting codes. Note that `FOBOS` is deliberately designed to be used in situations where there is minimal astrometric data only. Other codes are often designed to use many more epochs with extra (e.g. velocity) information gained from a sustained and detailed observing program.

I used `FOBOS` to constrain the orbits of several observed binary systems and compared our results to various Bayesian Markov Chain Monte Carlo fitting methods. In this section, I present the results for the binary systems 2MASS J01033563-5515561 (Blunt et al.

(2017)) and HD 206893 B (Ward-Duong et al. (2021)), using two epochs of astrometric observations for the 2MASS binary and four epochs of astrometric observations for HD 206893 B.

The true observational errors on the separations, position angles, and distances were used to determine whether a particular set of orbital parameters is a match to the observations. The impact of the size of the observational errors is discussed later in this section.

2M 0103-55 (AB) b

2MASS J01033563-5515561 (AB) b (hereafter 2M 0103-55 (AB) b) is a 12-14 Jupiter mass companion orbiting the low mass binary system 2M 0103-55 (AB). The astrometric data for this system was acquired by Delorme et al. (2013) and analysed using the Orbits for the Impatient (OFTI) method (Blunt et al., 2017). Blunt et al. (2017) used two epoch of relative astrometry taken ∼10 years apart (see their Table 10) to generate the orbital parameter posteriors for 2M 0103-55 (AB) b. The same two astrometric data points were used as the input for `FOBOS`.

The separations quoted in this table are measured relative to the barycentre of the system 2M 0103-55 (AB). The errors on the position angles (PA) corresponds to the relative error on the observations between the two epochs, and both PA measurements have an additional error of ±0.4 milli arcseconds, dominated by systematic uncertainties. A distance of $d = 47.2 \pm 3.1$ pc (obtained using the parallax quoted in Blunt et al. (2017) Table 2) was used to convert the separations from milliarcseconds to au. The masses of the host binary system (treated as a single object) and the low mass companion were taken to be $M_{AB} = 0.36 \pm 0.04$ $\mathrm{M}_\odot$ and $M_b = 0.012 \pm 0.001$ $\mathrm{M}_\odot$ respectively.

Using the Orbits for the Impatient algorithm, Blunt et al. (2017) find median values for the semi-major axis, eccentricity, and inclination to be $a = 104.92$ au, $e = 0.1233$, and $i = 123.6°$, and 68 per cent confidence intervals of $79 - 149$ au, $0.09 - 0.59$, and $119 - 144°$, measured relative to the system being edge-on at 90°. As mentioned earlier, `FOBOS` defines edge-on as 0°, so this corresponds to an inclination range of $29 - 54°$ using the `FOBOS` frame of reference. These results are shown in Figure 4.16 by the green vertical lines and green shaded regions respectively.

`FOBOS` calculates the 68 per cent confidence intervals for the semi-major axis, eccentricity, inclination as $59.1 - 173.8$ au, $0.01 - 0.52$, and $19.9 - 44.7°$ respectively; these ranges are indicated on Figure 4.16 by the grey shaded regions. The median values for all three orbital parameters fall within the `FOBOS` 68 per cent confidence intervals and

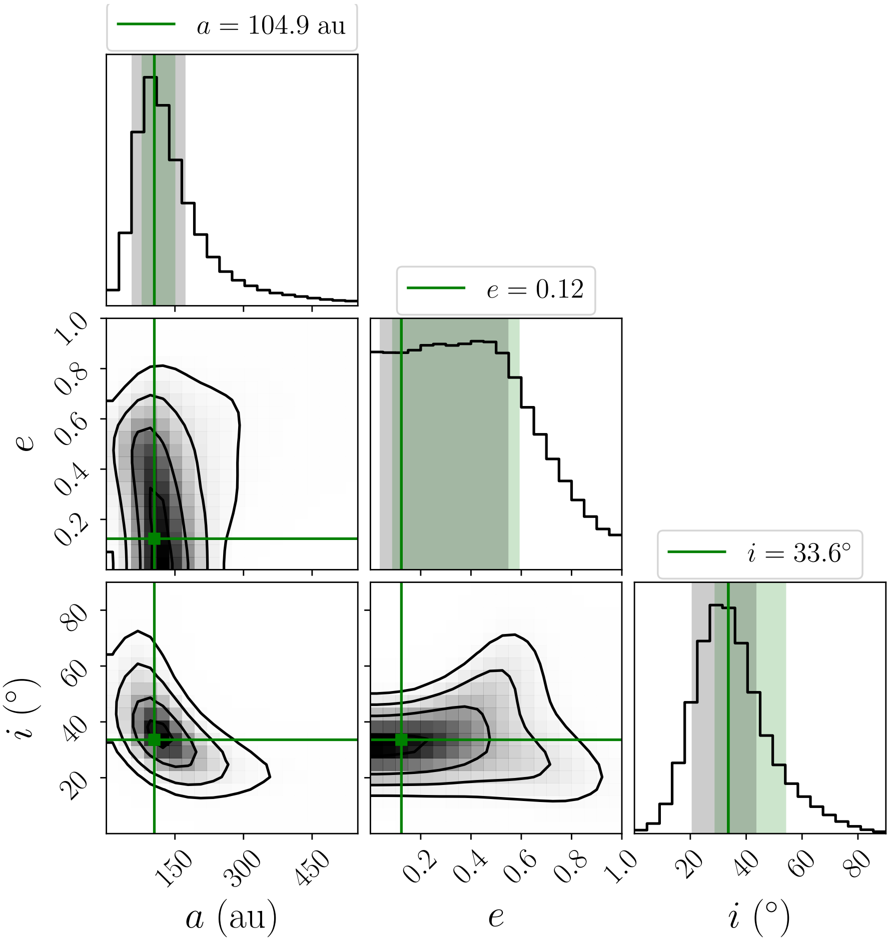

Figure 4.16: Corner plot for the orbit of 2M 0103-55 (AB) b with respect to 2M 0103-55 (AB). The top panels of each column show the `FOBOS` probability distribution functions for semi-major axis (left), eccentricity (middle), and inclination (right). The green solid lines on these panels show the OFTI median values and the green shades regions show their 68 per cent confidence intervals (Blunt et al., 2017, Table 20). The grey shaded regions are the `FOBOS` 68 per cent confidence intervals.

there is a significant overlap between all of the `FOBOS` and OFTI 68 per cent confidence intervals.

The widths of the confidence intervals for eccentricity (~ 0.5) and inclination ($\sim 25°$) calculated using `FOBOS` match those quoted by Blunt et al. (2017), but the `FOBOS` semi-major axis range is ~ 1.6 times larger than the OFTI range. For the inclination, the 68 per cent C. I. is a comparable width to that calculated by OFTI, but shifted to slightly lower values.

The `FOBOS` simulation of 2M 0103-55 produces over 50,000 solutions within the 1σ observational errors calculated by Delorme et al. (2013) in a wall-time of ~30 seconds. (Blunt et al., 2017) do not quote their wall or CPU time.

HD 206893 B

Further tests were carried out on HD 206893 B - a 12-40 Jupiter mass companion orbiting in the debris disk of its FV5 type host star. A detailed analysis of the physical and orbital properties of HD 206893 B was presented in Ward-Duong et al. (2021), using a total of nine astrometric observations from previous VLT/SPHERE, VLT/NaCo studies of the system (Milli et al., 2017; Delorme et al., 2017; Grandjean et al., 2019) and new Gemini Planet Imager (Macintosh et al., 2008) observations. These data points are given in Table 9 of Ward-Duong et al. (2021).

HD 206893 B has a Gaia distance of $d = 40.77 \pm 0.059$ pc and the host star and companion star have masses of $M_A = 1.31 \pm 0.01$ M$_\odot$ and $M_B = 0.11 \pm 0.01$ M$_\odot$ respectively.

Using a Bayesian MCMC method, Ward-Duong et al. (2021) find the semi-major axis of the system to be $10.4^{+1.8}_{-1.7}$ au and an eccentricity of $0.23^{+0.13}_{-0.16}$.

They also find a inclination of $145.6°^{+13.8°}_{-6.6°}$, corresponding to $55.6°^{+13.8°}_{-6.6°}$ using our definition. Their most probable values and 1σ ranges are shown on Figure 4.17 by the green vertical lines and shaded regions, with the inclination values being shifted down by 90° to match our definition of inclination. The corner plot showing their posterior distributions and covariances is shown in their Table 10.

I tested the `FOBOS` Multi-Epoch code on the four SPHERE/IRDIS observations. Using a 6 core/12 thread processor, ~1,000 matches to the observations for this system are found in a wall-time of ~ 60 minutes. These results were used to generate the probability distribution functions (top panels) and covariances (other panels) shown in Figure 4.17.

I calculated the 68 per cent confidence intervals for semi-major axis, eccentricity, and inclination as $8.8-11.9$ au, $0.02-0.34$, and $45.0-58.1°$. These ranges are represented by

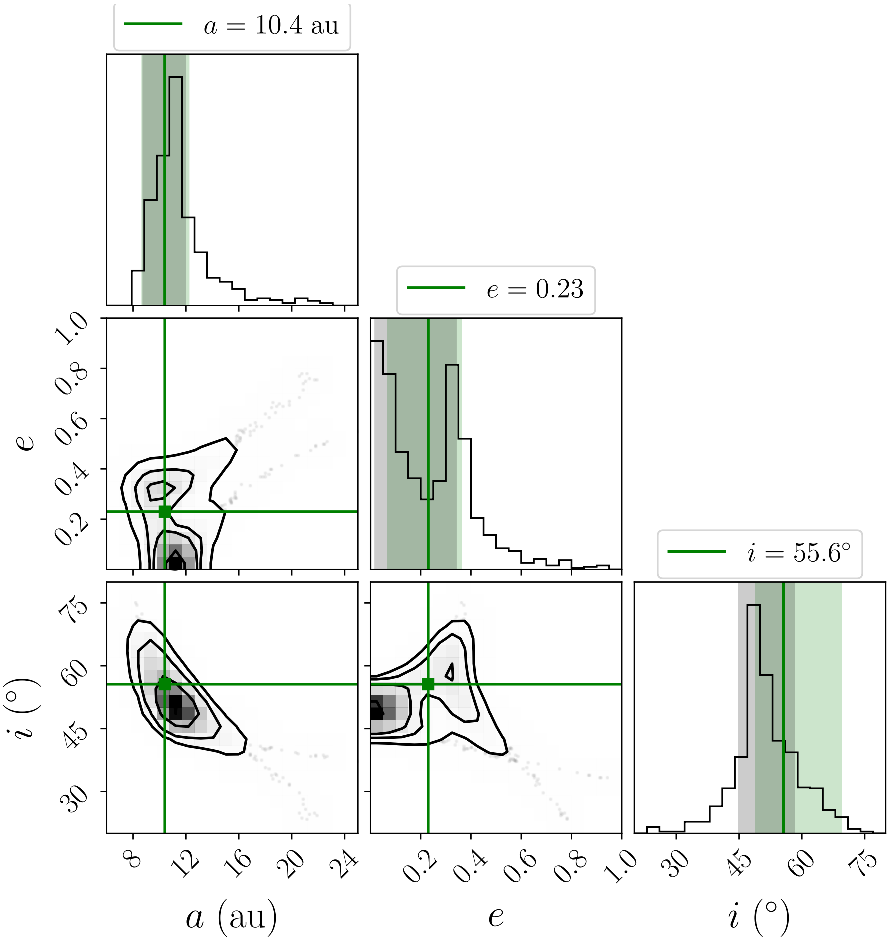

Figure 4.17: Corner plot showing the probability density functions for semi-major axis (top left), eccentricity (top middle), and inclination (right) for the low mass companion HD 206893 B. The other panels in the figure show the covariances of each of these parameters. The solid green lines show the most probable values for each orbital parameter obtained by Ward-Duong et al. (2021) and the green shaded regions represent their 1σ error ranges. The grey shaded regions are the `FOBOS` 68 per cent confidence intervals.

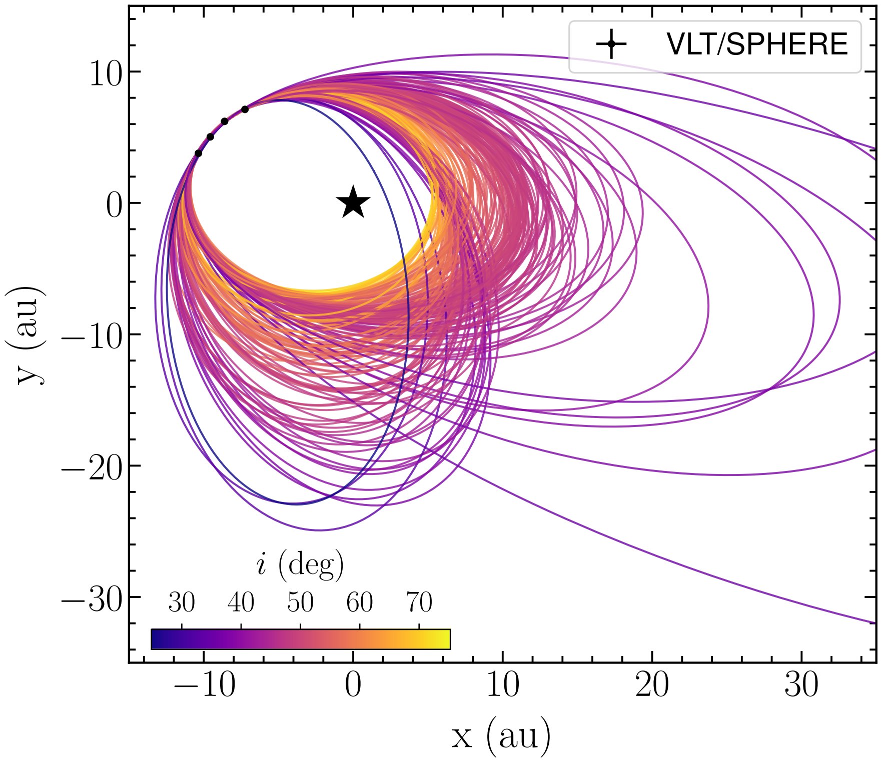

Figure 4.18: Subsample of 200 randomly selected orbital fits for HD 206893 B using the four epochs of VLT/SPHERE astrometric observations (black circles). The observational errors on the measurements are plotted as error bars on the black points, but are too small to be noticeable on this scale. The lighter/yellower orbits correspond to systems with inclinations closer to face-on (90°) and the darker/bluer orbits closer to edge-on (0°). The primary star is located at (0,0).

the grey shaded regions on the top panels of Figure 4.17. The top left panel of the plot shows that our confidence interval for a overlaps with the range from Ward-Duong et al. (2021) almost exactly. The `FOBOS` confidence interval extends to slightly lower values than the Ward-Duong CI and the PDF shows the same minimum at $\sim$0.2 followed by a peak at $\sim$0.3, before tailing off almost completely for values $\gtrsim$0.5. The `FOBOS` 68 per cent CI for inclination is 1.5 times smaller than the Ward-Duong et al. (2021) value and shifted to a slightly smaller inclination range, with the median value falling in the region where the two ranges overlap.

A sample of 200 orbits which fit the four VLT/SPHERE observations are shown in Figure 4.18. The colour of the orbit represents whether the inclination of HD 206893 B is closer to edge-on (0°, bluer orbits) or face-on (90°).

Observational errors

HD 206893 B is much more highly constrained than 2M 0103-55 (AB) b, due to the additional epochs of data available for HD 206893 B. However, I also found a difference in results depending on whether the four GPI observations or the four SPHERE observations were used. Fitting the GPI observations resulted in a semi-major axis confidence interval that was $\sim$2.5 times larger than the equivalent results using the SPHERE observations, and a $\sim$1.7 times increase in the inclination range.

There are two reasons why the VLT/SPHERE observations are much better at constraining the orbital parameters than the GPI observations. Firstly, two of the GPI observations were obtained within one month of each other and their 1σ error ranges overlap for both separation and position angle. Secondly, the fourth data point has 1σ errors that are $\sim$2 times larger than the errors for all other data points. This emphasises the importance of obtaining data points with small observational errors over a long enough timescale that the companion exhibits significant on sky motion.

4.8 Summary

I developed an orbit fitting algorithm (`FOBOS`) which can estimate the orbital parameters of binary and triple systems using as few as two epochs of relative astrometry. Originally, this was developed to fit the orbits of binary/triple systems that have been observed a couple of times during multiplicity surveys but have never had their individual properties studied. However, as the project developed, it became clear that `FOBOS` could be used on observations of directly imaged brown dwarfs and exoplanets.

To estimate the reliability of `FOBOS`, I tested the algorithm on 60 fake binary systems and 60 fake triples, each with two epochs of ‘observation’. The results of this testing are shown in Section 4.3. I found that the 68 and 95 per cent confidence limits are statistically reliable (and so tight constraints can be trusted). Smaller error bars on the observations and an extra epoch of data can be very constraining. Some fits contain very little information about the orbital parameters of the system, depending on the distance moved by the companion between observations, but others are highly constraining.

As well as testing `FOBOS` on fake data, I also applied it to two systems with low-mass brown-dwarf companions; HD 206893 B and 2M 0103-55 (AB) b. My fits agree well with published results from other sources, which use well-established orbital fitting codes.

Chapter 5

A binary population synthesis model and its applications

5.1 Summary

Introduction

The semi-major axis and eccentricity distributions of binary systems have been determined through various methods over the past decades (see Section 1.7 and Section 1.8 for more details). In particular, I showed in Chapter 4 that astrometry can be a useful tool, especially if there are enough epochs of observation to get a reliable fit to the orbit. However, many multiplicity surveys have single observations of binaries, and the observed separation distribution in au is often assumed to be the true distance between the two stars or the semi-major axis of the system.

Also in Chapter 4, I showed that the on-sky separation of two stars is affected by the eccentricity, inclination, orientation of the orbit, and the phase of the companion at the time of observation. The combination of these factors mean that the observed separation of the objects is always smaller than the true separation. When we only have data from a catalog of binaries, it can be difficult to work backwards to estimate how much the orbital properties impact the separation distribution of the stars. This is where binary population simulation are particularly useful.

The code written for the `FOBOS` algorithm produces projected separations of binary stars at a random point in it's orbit, the full details of which are explained in Chapter 3. For the work presented this chapter, I used this code as a basis to produce a binary population synthesis model; a program which generates a vast number of fake binary projections.

I will discuss the results of two applications of this model. Firstly, I quantify the difference between the observed separation and the true separation for a binary population, discussing how each of the orbital elements of a system affect its projection. Secondly, I use my binary population synthesis code to estimate the true semi-major axis distribution and multiplicity fraction of an observed sample of YSOs from the Leeds RMS catalog, provided by our collaborators Robert Shenton and René Oudmaijer at the Univeristy of Leeds. This work constitutes a subsection of their paper which in preparation for submission to MNRAS.

5.2 Orbital selection effects

The distribution of on-sky separations of binary systems does not necessarily reflect their semi-major axis distribution, because the inclination, system orientation and the orbital phase of the companion will also affect the instantaneous projection of a binary system on the sky. The projected separation of stars in a binary will *always* be smaller than their true separation.

I tested how varying the orbital parameters of a sample of binary systems affects their projected separation. For the initial test, I wanted to replicate the separation distribution of binaries on the sky without any observational selection effects (such as the stars being too close to resolve, or the companion too distant and faint to be attributed to it's primary star).

I created a sample of $2,000$ binaries, with semi-major axes a randomly selected from a uniform distribution between $700 - 100,000$ au. These values were chosen to correspond to the semi-major axis estimates for YSOs from the Shenton et al. sample, which forms the basis on this work and is discussed in detail in Section 5.3 and thereafter. The initial conditions for the eccentricity, inclination, orientation, phase, and distance are given in Table 5.1.

Parameter	Symbol	Range	Units
Semi-major axis	a	700 - $100,000$	au
Eccentricity	e	0 - 1	-
Inclination	i	0 - 90	°
Orientation	ϕ	0 - 360	°
Mean anomaly	M	0 - 360	°
Distance	d	1.4 - 11.2	kpc

Table 5.1: Ranges for each of the orbital parameters (and distances).

Figure 5.1 shows the frequency of systems with different semi-major axis values (red) and the separation of this same sample of binaries (grey) when the orbital properties or distances are varied. The variable parameter is stated in the top right corner of each of the sub-figures.

The orbital parameters of a system are not independent. For example, to examine how the eccentricity affects the separation (as shown in Figure 5.1), the mean anomaly is fixed at π radians (i.e. the companion is at apastron). If the mean anomaly was fixed at another value, then the eccentricity distribution would be different. Therefore the results in Figure 5.1 represent only a few finely tuned cases to help visualise how different orbital configurations can affect the separation.

In Figure 5.1(a), the eccentricity varied randomly in the range 0-1. The distance was fixed at 2,000 pc and the phase at π rad so that the only parameter impacting the separation was eccentricity. The separation distribution appears flat until a value of $\sim 100,000$ au and then falls off sharply. The tail of the separation values up to 200,000 au correspond to the highest eccentricity systems, which are more likely to be observed at very high separations due to their significantly slower velocity at this point in their orbit.

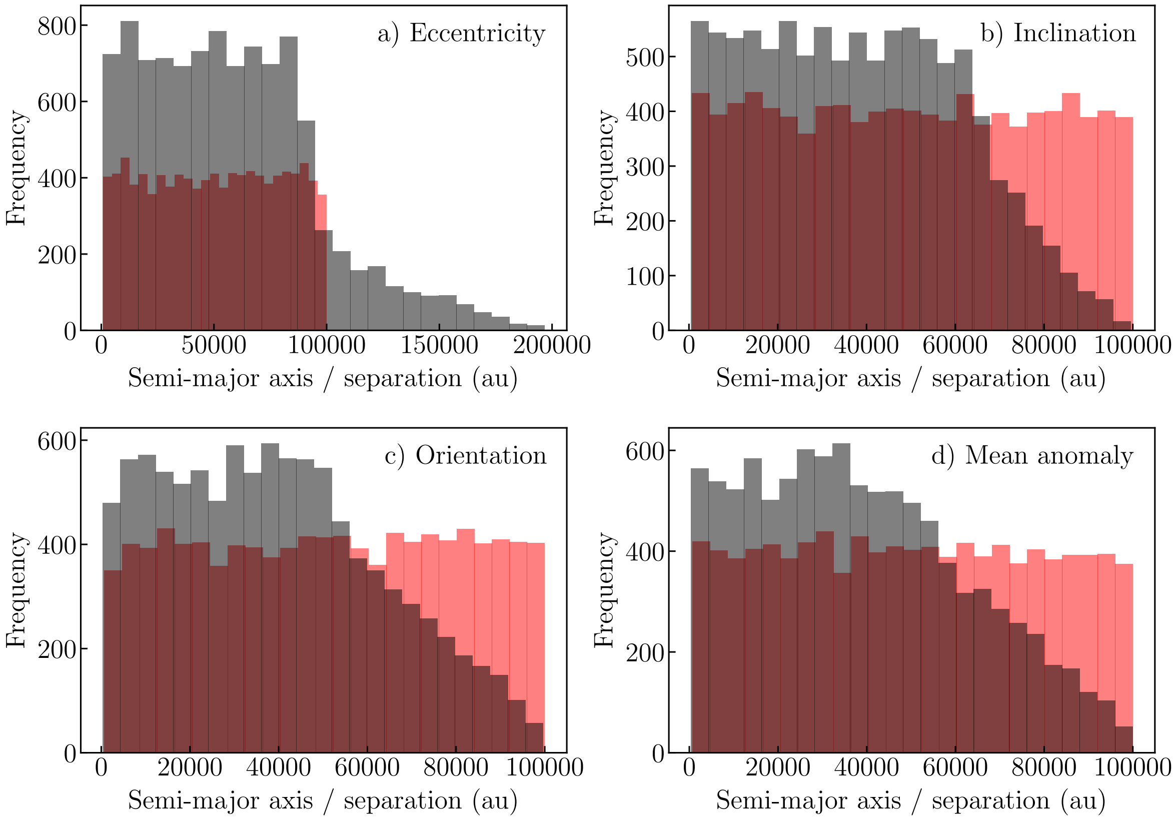

Figure 5.1: The effects of different physical/orbital parameters of binary systems on the observed separation distribution. The red histogram shows the semi-major axis distribution of the sample and the grey histogram shows the separation distribution in au. All binaries in the sample have a semi-major axes drawn from a uniform distribution in the range 700-100 000 au. Each subplot shows results for when all orbital conditions are fixed except from one (the variable parameter is stated in the top right corner of each panel).

Figure 5.1(b)-(d) all show very similar distributions to one another; they are approximately flat up to ~60,000 au and then drop off steeply. Whilst the eccentricity of the orbit can make the separation appear either larger or smaller than the semi-major axis, depending on the phase of the orbit, the inclination and orientation can only make the projection smaller.

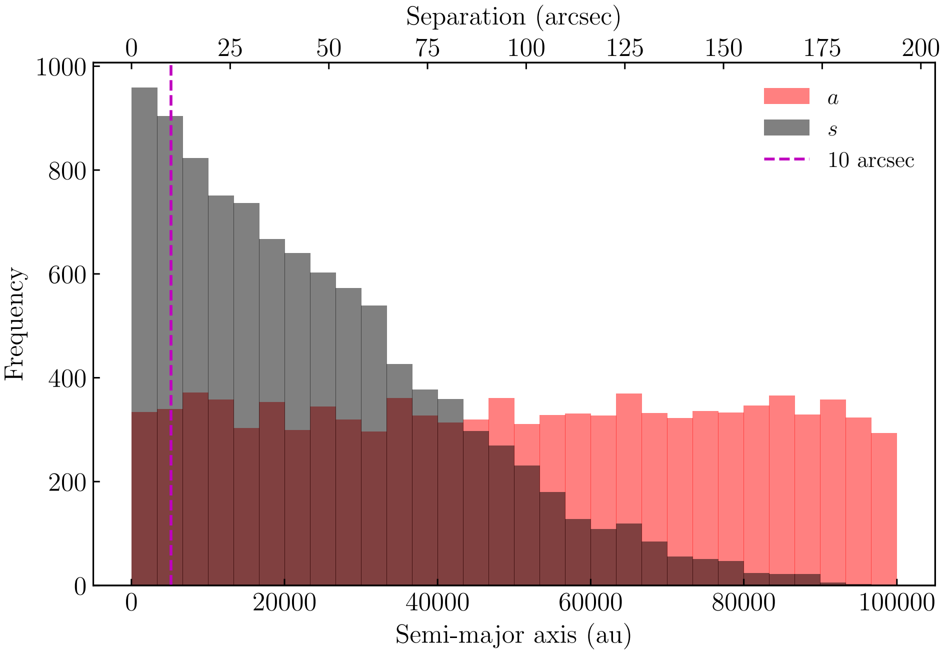

Figure 5.2: Histogram showing the projected separation of binaries with semi-major axes drawn from a uniform distribution in the range 0-100 000 au. The plot shows the effects of the orbital parameters only, with the distance being fixed at 1kpc.

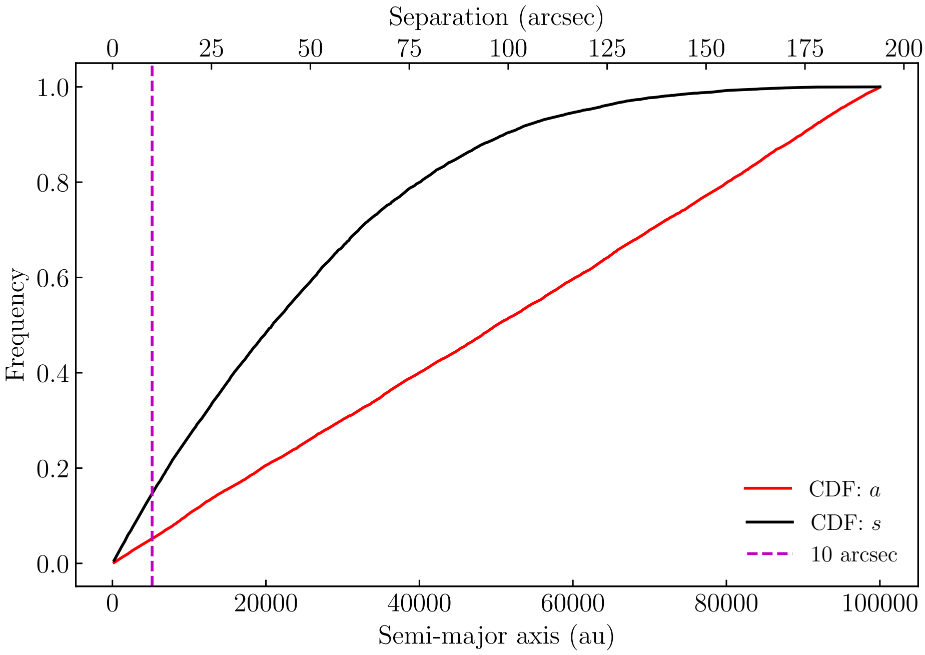

Figure 5.3: CDF with the same values as Figure 5.2

Eccentricity range	Mean s	Median s
0.0 - 0.2	0.81	0.79
0.2 - 0.4	0.82	0.77
0.4 - 0.6	0.92	0.94
0.6 - 0.8	1.11	1.18
0.8 - 1.0	1.34	1.45
0.0 - 1.0	1.01	0.96

Table 5.2: The average separation of binary stars as a fraction of their semi-major axis, for different eccentricity ranges.

The average impact of orbital parameters on separations

In the previous section, I discussed how individual orbital parameters affect the projected separation of a binary. Also as part of this work, I quantified the average difference between the separation and the semi-major axis of a system. I did this by sampling uniformly over the entire range of inclinations, orientations, and mean anomalies that a system can have, and taking the average overall separation. The semi-major axis was fixed at $a = 100$ au throughout.

Table 5.2 shows the results of these tests for various eccentricities. For example, for 50 systems with eccentricities in the range $0.0-0.2$, the separation will typically be ~80% of the semi-major axis, whereas for the most highly eccentric systems, it will be ~134% of a. Over the entire eccentricity range, we see that the two parameters (on average) will be approximately the same. Raghavan et al. (2010) found a uniform eccentricity distribution for solar-type stars, so this distribution is expected.

Summary

Population synthesis modes are an effective way of estimating the selection effects on an observed sample, and all of the factors evaluated in the section above will contribute to the ways in which observations differ from reality. For a sample of binaries with a uniform eccentricity distribution between 0 and 1, the separation will typically be comparable to the semi-major axis. However, for each individual observation, the separation can vary significantly depending on its instantaneous parameters.

5.3 Estimating the binary fraction of YSOs

This section focuses on the statistical analysis on the binary YSO/MYSO sample from Shenton et al. (in prep).

The term 'young stellar object' (YSO) refers to a star in the very early stages of formation. These objects are still embedded in their host clouds and often possess large accretion discs, making them bright primarily in the mid-IR. A full description of YSO formation is given in Section 1.3.2.

Shenton et al. (in prep) compiled a large sample of YSOs from 'The Red MSX Source survey' (RMS, Lumsden et al., 2013). This catalog contains sources from the UKIRT Infrared Deep Sky Survey Galactic Plane Survey (UKIDSS GPS, Lucas et al., 2008) and Vista Variables in the Via Lactea (VVV, Saito et al., 2012). UKIDSS focuses on targets in the Northern sky, whereas VVV is used for the Southern sky. The data was provided by Shenton and Oudmaijer in the format shown in Table 5.3.

The goal of their work was to calculate the multiplicity fraction of massive young stellar objects (MYSOs), which have $M \gtrsim 8M_{\odot}$. Part of calculating the multiplicity fractions involves estimating the incompleteness of the sample, to extrapolate from the observed number of multiple systems to the total value including those missed due to observational selection effects.

5.3.1 Sample characteristics

The master sample with which I was provided contains 842 'binary' YSOs, 513 of which are MYSOs (i.e. have a primary mass of $> 8M_{\odot}$). The most important characteristics of each binary are the separation (s, in arcseconds), the distance (d), and the magnitude difference of the two stars (δmag). All YSOs in the sample have separations in the range $0.5 - 10$ arcseconds, a distance between $1.4 - 11.2$ kpc, and δmag values between ~ -6 and ~ 8. Note that a negative δmag value can occur when the primary star suffers from a high level of extinction due to its debris disc, reducing its magnitude below that of the companion. The median separation of stars in this sample is 13 665 au (as determined by Shenton et al. in prep.).

Companions were selected from the sample by drawing a 1.5 arcminute radius surrounding the YSO, and evaluating all objects within this radius for the possibility of being a visual binary companion. In all cases, there is a probability that any star within the 1.5 arcmin radius is a chance alignment rather than a physically associated companion (Correia et al., 2006). This probability is quantified by

SOURCEID	CENTREID	d (pc)	M_p	s (arcsec)	BSD	P_{chance}	δmag
438306049182	G010.5067+02.2285	2900.0	6.960310	3.670980	0.001218	0.050268	-1.759306
438306049183	G010.5067+02.2285	2900.0	6.960310	4.687290	0.002161	0.138589	-0.939817
438466784310	G010.8856+00.1221	2700.0	8.807115	8.847030	0.000589	0.134930	1.160772
438466784296	G010.8856+00.1221	2700.0	8.807115	7.726310	0.000668	0.117757	1.244640
438466784158	G010.8856+00.1221	2700.0	8.807115	3.215360	0.004283	0.129880	3.180242
438402984624	G011.4201-01.6815	1500.0	10.957821	5.281270	0.000393	0.033848	0.935403
438144312770	G011.5001-01.4857	1700.0	10.633375	3.857130	0.000196	0.009142	0.832326
438144312771	G011.5001-01.4857	1700.0	10.633375	3.945420	0.001179	0.056023	2.114921
438635465594	G011.9019+00.7265	2900.0	7.181298	2.054140	0.005620	0.071786	2.299565
438635497754	G011.9019+00.7265	2900.0	7.181298	2.374360	0.011436	0.183343	3.168586
...	...	...	...	...	...	...	...

Table 5.3: The first 10 rows of YSO data from the Shenton et al. sample. SOURCEID: ID of companion star, CENTREID: ID of the primary star, d: distance, M_p: primary mass, s: separation, BSD: background star density, P_{chance}: probability that the companion is a chance alignment, δmag: magnitude difference between the primary and the companion. Note that a single primary can have multiple companions attributed to it, and each companion has no impact on any other companions detected around the same primary. Omitted from this table are the RA and dec of each star. The full data set has 842 rows.

$$P_{\text{chance}} = 1 - \exp\left(-\pi s^2 \rho\right), \tag{5.1}$$

where s is the distance between the primary and the potential companion in arcseconds and ρ is the background star density in that cell (also referred to as BSD). ρ is calculated using the full stellar catalogue data. If the value of P_{chance} was $< 20\%$ then the object was selected as a companion.

Due to the nature of the companion selection, there are some YSOs that appear to have a large number companions, as each potential companion is evaluated independently of whether any other companions have already been found. There are some YSOs with 6-10 companions noted in the sample. I will discuss how these systems are dealt with in Section 5.4.

They calculate multiplicity fractions of $64 \pm 4\%$ for the UKIDSS sample, $53 \pm 4\%$ for the VVV sample, and $49 \pm 8\%$ for the RMS imaging sample.

5.3.2 My contribution

My contribution to this work was to use a binary population synthesis model to (a) estimate the incompleteness of their sample, (b) calculate the completeness corrected MYSO multiplicity fraction, and (c) estimate the true semi-major axis distribution of the binaries in their sample.

This was done using a Monte Carlo method of sampling. The code generates 1×10^6 binary systems and calculates their projected separations (see Chapter 3) in arcseconds. Each binary is also assigned a magnitude difference δmag. A binary search tree algorithm (described in Section 5.3.5) is used to compare the 2-D separation vs δmag distribution of my population of binaries to the Shenton et al. sample.

5.3.3 The model

The simulation begins by drawing the orbital parameters for our test sample of binaries, using the same method as is described and used in Chapters 3 and 4. The semi-major axis distribution is one of the key variable parameters, as this is what we are hoping to obtain using this method. The code is set up to allow either a lognormal, log-flat (Öpik distribution), or flat distribution as defaults, but can take any distribution as an input.

The model also generates a value of δmag for each binary from a Gaussian distribution (which we are attempting to fit alongside the separation distribution in this model). The standard deviation of the δmag distribution is allowed to vary up to very high values, such that the distribution becomes approximately flat.

The binary projection code from Chapter 4 gives the separation values in au. This is converted to a value in arcseconds using Equation 5.2. The distance of each binary is selected from the same distance distribution as the objects in the Shenton et al. master sample (which contains all objects from the UKIDSS, VVV, and RMS catalogs, not just binaries).

$$s(\mathrm{arcsec}) = \frac{s(\mathrm{au})}{d(\mathrm{pc})}. \tag{5.2}$$

At this point, the selection effects are applied to the separation and δmag distributions. These are described in detail in Section 5.3.4.

5.3.4 Selection effects

Not every binary in the population synthesis model would be observed given the constraints on the Shenton et al. sample. To calculate the incompleteness of their sample, I apply the same selection effects that are present for their data to my fake binary population. Only the fake binaries that would be observed after these conditions are applied are included in the fit to the observed data, and the rest of the systems are rejected from the sample.

Firstly, their sample contains binaries with separations between ~ 0.8 and ~ 10 arcseconds. Any fake binaries with separations outside these ranges are disregarded. Similarly, they conclude that the probability of detecting a binary increases up to ~ 2 arcseconds, above which companions are reliably detected. I mimic this effect by applying a 'probability of detection' value to binaries below 2 arcseconds; the closer the separation is to the minimum value of ~ 0.8, the more likely the binary is to be rejected.

The observed separation vs. δmag distribution in the Shenton et al. sample data has two distinct regions at low separations and each end of the δmag scale (which can be seen in Figure 5.7), in which no binaries are detected. Any fake binaries in these regions are also rejected from my sample.

Finally, each fake binary has a value of P_{chance} which depends on the separation and the background star density (ρ). I was also supplied with the full YSO catalog from which the binaries where selected, and I used the ρ distribution of all YSOs to select values for each of the fake binaries. Any fake systems with $P_{\text{chance}} > 20\%$ were also rejected, to match with the selection criteria applied by Shenton & Oudmaijer to their observed sample.

The fraction of binaries which would still be observed after all of these selection effects had been applied was taken to be the multiplicity fraction.

5.3.5 Comparing data sets using a Binary Search Tree

After the selection effects have been applied to the fake binary population, we are left with simulated separation vs δmag distribution. The code cycles through a variety of parameters characterising the a and δmag distributions as part of the Monte Carlo method, so a statistically robust method of comparing the simulation results to the observations is required to find the best match. This was done using a binary search tree.

Binary search tree structures

A binary search tree (BST) is a tree-like data structure, like the one shown in the lower panel of Figure 5.4. The tree itself is made up of nodes (shown by circles), and each node has a maximum of two children; one to the left and one to right (in an ordered data set). The 'root' is the top node of the tree and the 'leaves' are nodes with no children.

Binary search trees offer a hierarchical data storage system, and are typically used as a data science technique for searching and sorting one-dimensional data. The tree

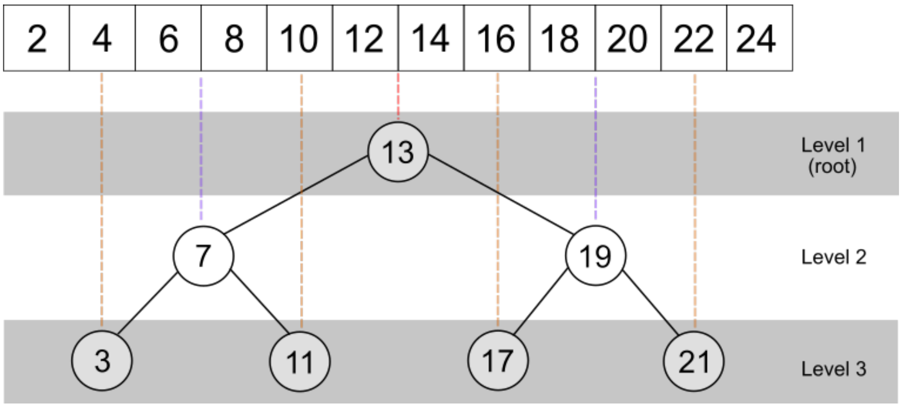

Figure 5.4: Diagram depicting the structure of a binary search tree of height $h = 3$ for a 1-D data set. The example data is shown by the values in boxes at the top of the diagram. The root node (level 1) bisects the data. Two child nodes are added on either side of the root node in the second level, bisecting each data subset. On the final level, there are four 'leaf' nodes added, one to the left and one to the right of each of the nodes from level 2.

starts with a root node, which bisects the data.[1] We consider this to be the first level of the tree. On the second level, two additional nodes are added; if the child node has a lower value than the root note then it is added as a left node, and if it is higher then it's added on the right. We then move to level 3, where four additional nodes are added. Each further level adds 2^{n-1} child nodes. This is illustrated by the tree diagram in 5.4, representing the binary tree nodes in a simple 1-D data set.

Two dimensional binary search trees

Our aim was to use a binary search tree to define the parameter space in our two dimensional data structure. Using a binary tree to map 2-D data is slightly more complex. The process begins in the same way; by adding a root node to bisect the data along the x-axis. On the second level, the additional nodes are added by splitting the two cells along the y-axis (as shown by the purple lines in Figure 5.5) so that each cell contains the same number of data points. For level 3, we then switch back to the x-axis to add 4 nodes (orange lines). This pattern of flipping the axis and adding 2^{n+1} nodes continues. The end result is a 2D grid of unequally sized cells, each of which contains approximately the same number of data points[2]. The idea for an k-dimensional binary search tree was first developed in Akter (2022) and has been refined for this work.

---

[1] For the cases mentioned in this work, we assume that the position of each node aims to split the data into two groups of equal size.

[2] If n is divisible by 2^{n+1}, then the cells will all contain exactly the same number of points.

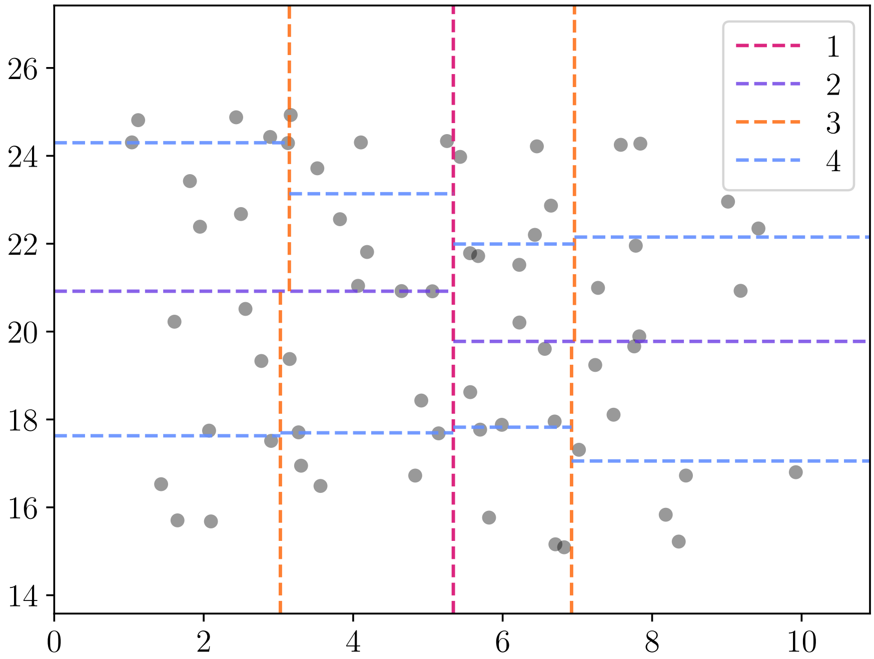

Figure 5.5: Graphical representation of the binary tree algorithm. The 64 black circles are randomly generated data points from uniform distributions. The points are first divided into two groups along the x-axis (1, pink) by adding a node. Each of these subsets is split again on the y-axis (2, purple) and two additional nodes added. The pattern continues, with 4 nodes added along the x-axis in the next level (3, orange) followed by 8 on the y-axis (4, blue). This represents a binary tree with a height (h) of 4.

5.3.6 Binary search trees in this work

I used a 2-D binary search tree to map the parameter space of the separation against δmag distribution, so that the simulation results and observations could be compared. This simulated data set is used to create a binary tree grid with 32 cells, mapping the s against δmag parameter space.

The root node is calculated by finding the median of the separation data. The data set is then split into two new data sets; one with separations less than the median value, and the other with separations greater than the median. At the second level, the nodes are the median δmag values of the two data subsets. The process continues, switching axis each time and adding 2^{n-1} nodes at each level, until the tree reaches the desired height (h). The height of binary tree is equivalent to the number of levels.

The nodes of the binary tree are used to determine the boundaries of each cell. The code cycles through each cell in turn and counts the number of observed points contained within that area. For a perfect match, all cells will have an equal number of points in all cells, but the majority of tests will produce binary trees with a highly uneven number of points in each cell. The distribution of data points and the quality of the fit is assessed using the 'Goodness of fit' measure, outlined in Section 5.3.7.

Creating an invariant grid

If the binary tree grid is generated for a small number of data points, then small random variations in the data points could have a significant effect on the positions of the nodes. This is illustrated in Figure 5.6, which shows binary trees produced for multivariate Gaussian distributions, for a variety of heights and containing different numbers of points (N). On each plot, there is a set of red points and a set of orange points, both drawn from the same distributions but with a different random number seed.

After conducting thorough testing, I determined that a minimum of 5000 data points for a binary tree with $h = 5$ (32 cells) is necessary to create an invariant binary tree grid, regardless of the random variation in a sample. For $h = 6$ (64 cells), more points are required to create a more consistent grid. For $N > 5,000$, the stability of the binary tree improves slightly, but not enough to justify the computational overheads of using a larger sample.

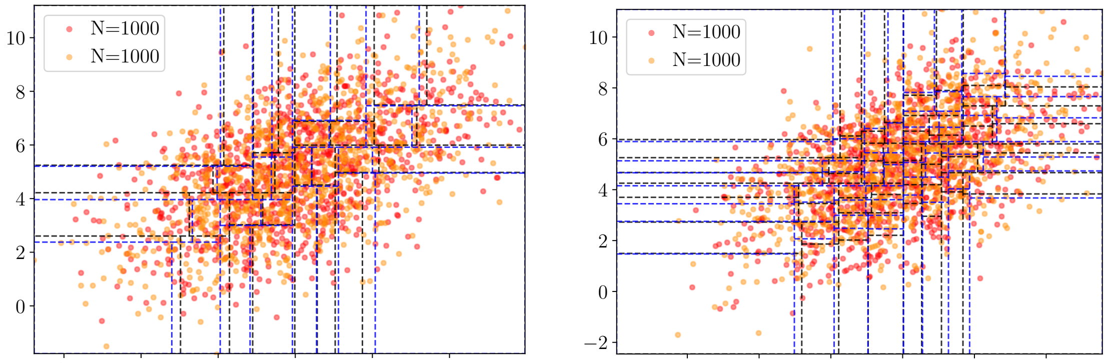

(a) $N = 1000$, $h = 5$ **(b)** $N = 1000$, $h = 6$

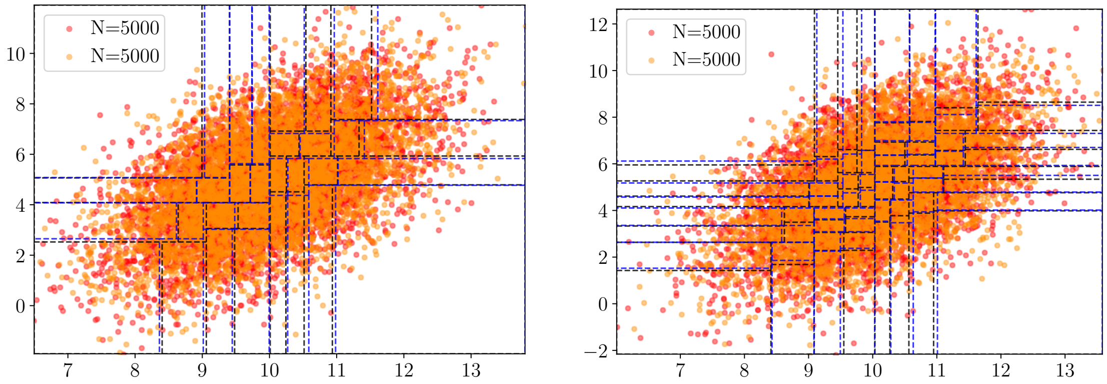

(c) $N = 5000$, $h = 5$ **(d)** $N = 5000$, $h = 6$

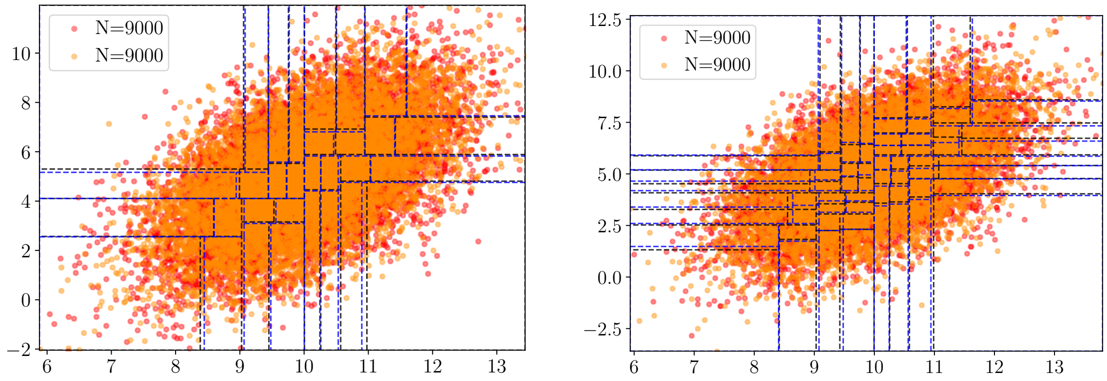

(e) $N = 9000$, $h = 5$ **(f)** $N = 9000$, $h = 6$

Figure 5.6: Grid of binary tree tests on randomly generated datasets from a multivariate Gaussian distribution. On each plot there are two datasets; red points and orange points. The black dashed lines show the binary tree cells for the red points, and the blue dashed lines show the cells for the orange points. Each dataset in the left column is divided into 32 cells and the right column is divided into 64 cells. The number of points in each data set is $N = 1000$ (top row), $N = 5000$ (middle row), and $N = 9000$ (bottom row).

5.3.7 Measuring Goodness of Fit

Once the binary tree has been generated, a statistical goodness of fit measure can be used to compare the results of various models to the observed data. Initially, I estimated the goodness of fit by calculating the variance of the number of points in each cell of the grid. Whilst this acted as a good preliminary test of the binary tree, a statistically robust goodness of fit measure is a better way of comparing the results of Monte Carlo simulation. This was done using a multinomial distribution.

The binary tree produces 2^h cells in a 2-D grid. As the binary tree uses the simulated data to find the nodes, we know that there will be an approximately equal number of fake data points in each of these cells. To compare the models, I superimpose this binary tree grid on top of the observed points. The number of observed data points in each cell is counted.

For a model to be a good fit to the data, it will also have an approximately equal number of data points in each of the cells. Furthermore, for each observation, there are 2^h defined outcomes (i.e. the point can fall within one of the 2^h cells).

The probability mass function of a multinomial distribution is

$$\mathrm{PMF} = \frac{n!}{k_1!...k_n!} p_1^{k_1}...p_n^{k_n}, \tag{5.3}$$

where k is an integer corresponding to one value in a discrete set of possible outcomes, and p is the probability of each outcome. In this case, p_i corresponds to the number of fake data points in cell i and k_i is the fraction of observed data points in cell i. To obtain the log-likelihood, we take the natural logarithm of this equation to obtain

$$\begin{aligned} \ln L &= \ln n! - \ln k_1! ... \ln k_n! + k_1 \ln p_1 ... k_n \ln p_n \\ &= \ln n! + \sum_i^n \{k_i \ln p_i - \ln(k_i!)\}. \end{aligned}$$

The binary tree is set up such that there is an equal number of fake data points in each cell, meaning that the probabilities for each cell p_i can also be approximated to being a constant P. This simplifies the equation further;

$$\ln L = \ln n! + n \ln P - \sum_i \{\ln k_i! \tag{5.4}$$

$$\ln L \propto \ln(n!) - \sum_i \{\ln(k_i!)\} \tag{5.5}$$

$\ln L$ is calculated for each of our different Monte Carlo models. If the number of fake data points in each cell are equal, this shows that they have the same distribution as the observations and we will get the maximum possible value of $\ln L$. Therefore, I select the model with the maximum log-likelihood parameter as the best fit model.

If a model is a particularly bad fit, then a single cell might have an extremely large number of fake data points within it. This can be an issue, as we can only take a factorial of a value ≤ 170 without the value becoming too large for the computer. To counteract this, I use the natural logarithm of the gamma function,

$$\Gamma(k) = (k-1)! \tag{5.6}$$

as the in-built Python `loggamma` function can compute the factorials of very high numbers.

5.4 Results

This section contains the preliminary results of my analysis. At the time of writing this thesis, the results are incomplete and there are several issues with how the simulations fit the observations, outlined in Section 5.4.3.

5.4.1 Model parameters and assumptions

I tested two functional forms for the semi-major axis distribution (a lognormal and an Öpik distribution), and used a Gaussian distribution for the δmag distribution (truncated such that it cannot generate values ≥ 8 and ≤ -6). I started with the lognormal model, which meant there were four parameters to fit; the mean and standard deviation of the semi-major axis distribution (μ_a and σ_a) and the mean and semi-major axis of the δmag distribution ($\mu_{\delta \mathrm{mag}}$ and $\sigma_{\delta \mathrm{mag}}$).

The parameters here are for the semi-major axis and δmag distribution *before* the selection effects have been applied (i.e. the true distribution rather than what is observed). It is for this reason that the δmag cannot simply be modelled by calculating the mean and standard deviation of the observed distribution.

As mentioned in Section 5.3.1, several of the YSOs in the sample have a large number of potential companions. I removed any YSOs with more than 6 companions from the

Symbol	Range
μ_a	0-30
σ_a	0-5
$\mu_{\delta\mathrm{mag}}$	0-4
$\sigma_{\delta\mathrm{mag}}$	0-8

Table 5.4: Parameter ranges sampled using the Monte Carlo method to find the best fit values. Note that these values are *not* for the semi-major axis parameters because of the use of a lognormal distribution.

data set before running my simulations, because it is unlikely that these are gravitationally bound multiple systems, and instead may be indicators of small clusters. This leaves 724 systems in the sample out of the original 842.

5.4.2 Monte Carlo modelling

The brute force Monte Carlo method varied the parameters for μ_a, σ_a, $\mu_{\delta\mathrm{mag}}$ and $\sigma_{\delta\mathrm{mag}}$ uniformly and did a random search of parameter space to find the best fit values. The parameter ranges used for the parameter space search are given in Table 5.4. The best fit results of this search are shown in Figure 5.7 and Figure 5.8.

These results are for the full sample of YSOs. The same method as described above was applied to the sub sample of MYSOs, and the results were extremely similar to the full sample. Therefore, results for the MYSOs only are not discussed here, but should be assumed to be more or less the same as the YSOs.

Figure 5.7 shows the separations against δmag for the best fit result of my simulations (grey circles) and the observations (red pluses). Above the scatter plot is a histogram of the separations and to the left is a histogram of δmags (grey for simulated data and red for observations). The black dashed lines on the scatter plot show the boundaries of the 64 binary search tree cells for the simulated data.

Figure 5.8 shows the semi-major axis distribution underlying the population of binaries for the best fit model (grey), compared with the separation distribution in au calculated by Shenton et al. (red). Note that the x-axis is slightly misleading, as the red data does *not* show the semi-major axis, but is a useful comparison for the simulation results.

As we can see from Figure 5.8, the fit required to match both the separation and δmag distributions of the observed sample comes from a model in which the semi-major axis distribution (Figure 5.8) is unphysical; all the binaries in this model have a semi-

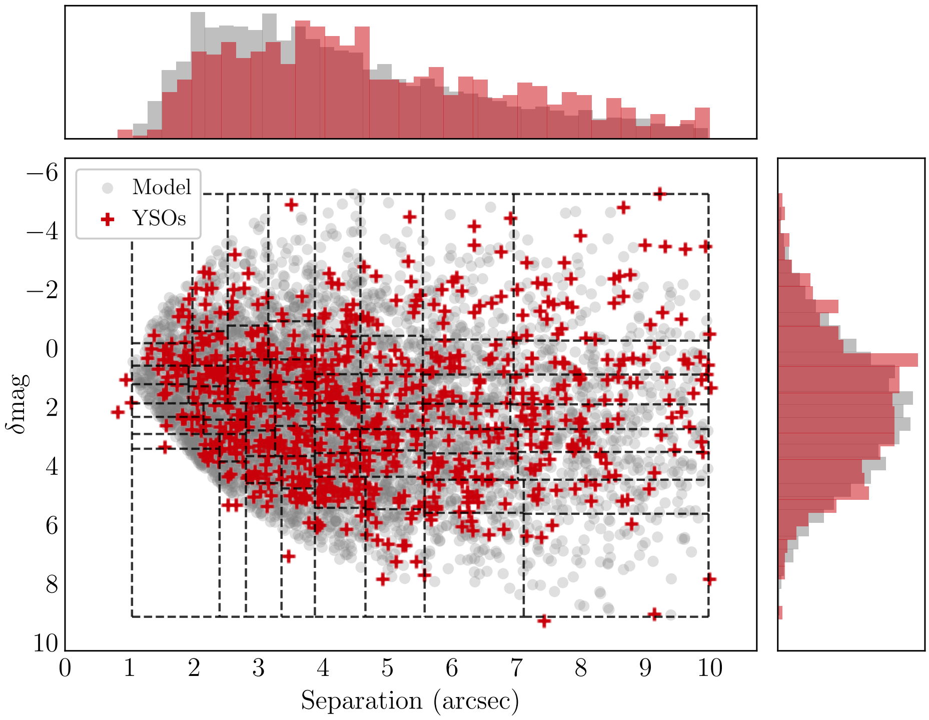

Figure 5.7: Best fit simulation for a binary population with a lognormal semi-major axis distribution, with parameters $\mu_a = 10.99$, $\sigma_a = 0.19$, $\mu_{\delta\mathrm{mag}} = 2.76$ and $\sigma_{\delta\mathrm{mag}} = 2.65$. The fraction of cases detected from an initial binary sample of 1×10^6 objects was 3.45%.

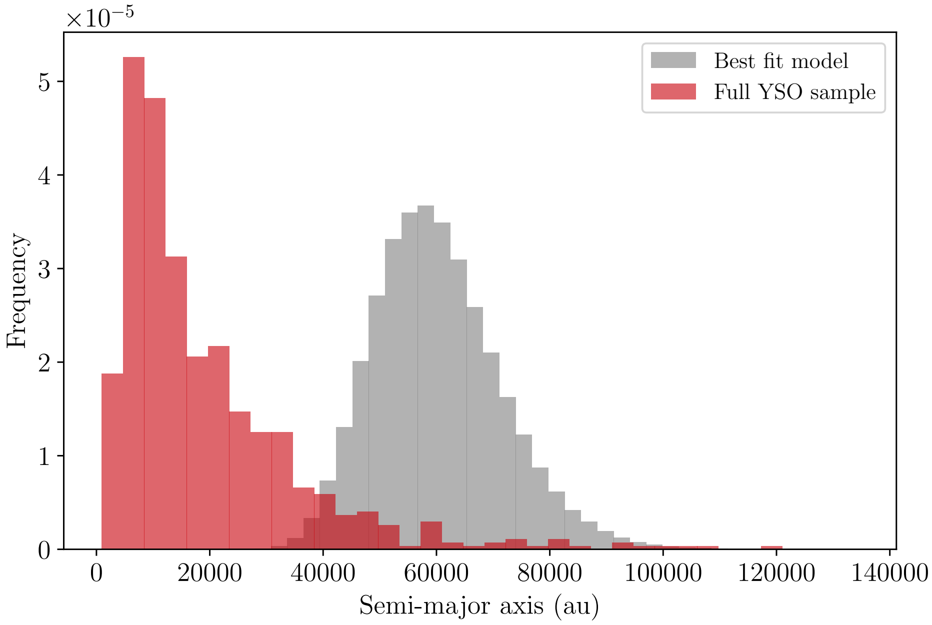

Figure 5.8: Semi-major axis distribution for the fit above.

major axis in the range 35,000−100,000 au, which corresponds to 0.17 − 0.48 pc. This is more comparable to the distances between stars in a relatively dense cluster than in binary systems. This is not simply an effect of projecting the true separations onto in image, because in Table 5.2 of Section 5.2, I showed that the typical on-sky separation of a binary is comparable to the semi-major axis of the system. The mean semi-major axis from my simulation results is 3.5 times higher than the projected separations in au from the Shenton et al. data.

Further issues with this result arise when we look at the multiplicity fraction and the distance distribution. In the simulation for Figure 5.7, only 3.45% of the binary population would be 'observed' after the selection effects are applied. This contradicts the multiplicity fractions of $64 \pm 4\%$ (UKIDSS only), $53 \pm 4\%$ (VVV only), and $49 \pm 8\%$ (RMS imaging sample) determined from observations only.

The most significant issue at this stage is how the selection effects impact the distance distribution at the end of the simulation. Initially, distances for each binary in the simulation are selected from the distances of all objects (not just binaries) in the UKIDSS, VVV, and RMS samples used for this work. We expected that the final distance distribution, after the selection effects are applied, to match the distribution for the binary sample. However, there is a huge disparity between the two distributions. Currently, the reason for this is not understood, but will be one of the first matters to

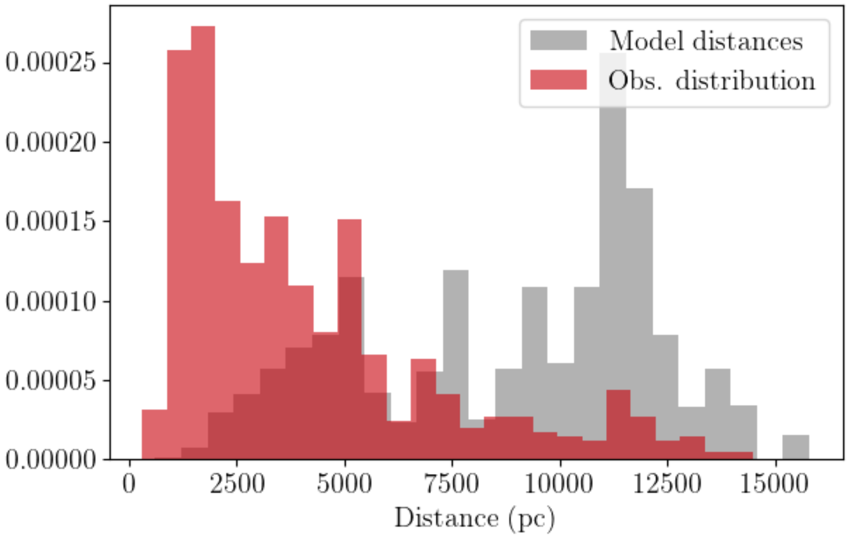

Figure 5.9: Distance distribution for the best fitting model after the selection effects have been applied (grey) compared to the true distances distribution of the observed binaries (red).

be addressed in the future work on this project.

Results using an Öpik distribution

The results of my model using an Öpik distribution are shown in Figure 5.10 and Figure 5.11. The shape of the Öpik semi-major axis distribution more closely matches the high separation tail of the observations than the lognormal shape. This fit also shows a semi-major axis distribution that peaks at much higher values than we would expect from a typical binary separation distribution.

5.4.3 Discussion

I have run several Monte Carlo simulations as part of this work, and all of them suffer from the same issues; (a) the semi-major axis distribution is extremely large, (b) the fraction of binaries 'observed' given the selection effects is extremely low, and (c) the distance distribution changes significantly after the selection effects are applied to the data. I will attempt to address the physical mechanisms that can explain each of these discrepancies, as well as considering any issues with the simulated/observed data that could affect my results.

The reason that a fit could not be found using a smaller semi-major axis distribution is the dearth of companions in the 1-2 arcsecond range; a binary population with a semi-

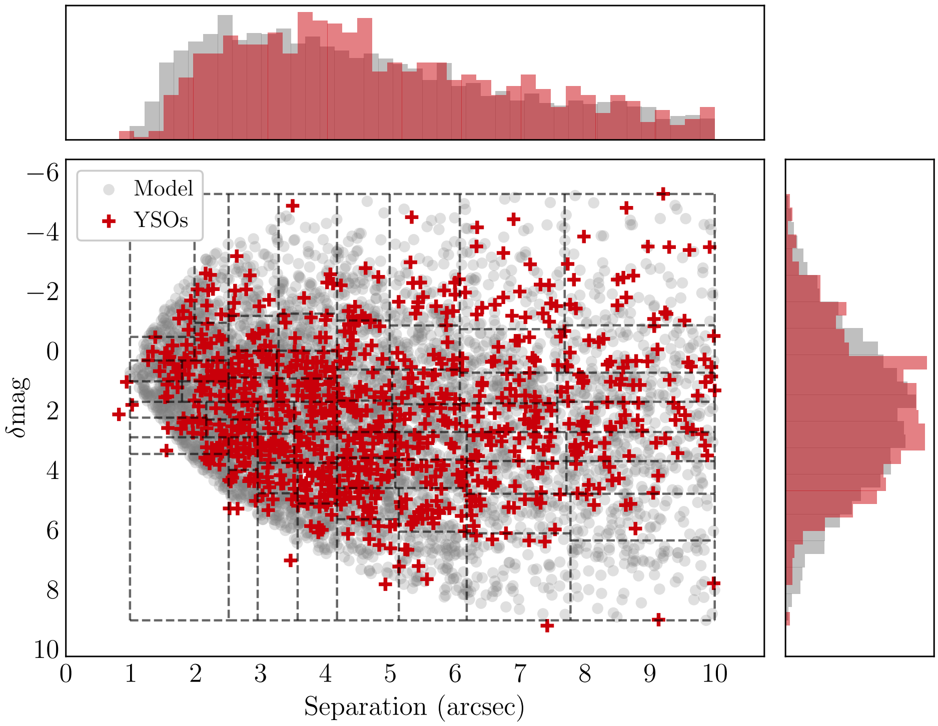

Figure 5.10: Best fit model, with parameters $\mu_a = 2.12 \times 10^4$, $\sigma_a = 2.85$, $\mu_{\mathrm{dmag}} = 2.89$ and $\sigma_{\mathrm{dmag}} = 3.19$. The number of systems detected from an initial binary sample of 50 000 objects was 2.05% and the Goodness of fit was -1243.61 (compared to the 'best fit' value of -1170.54).

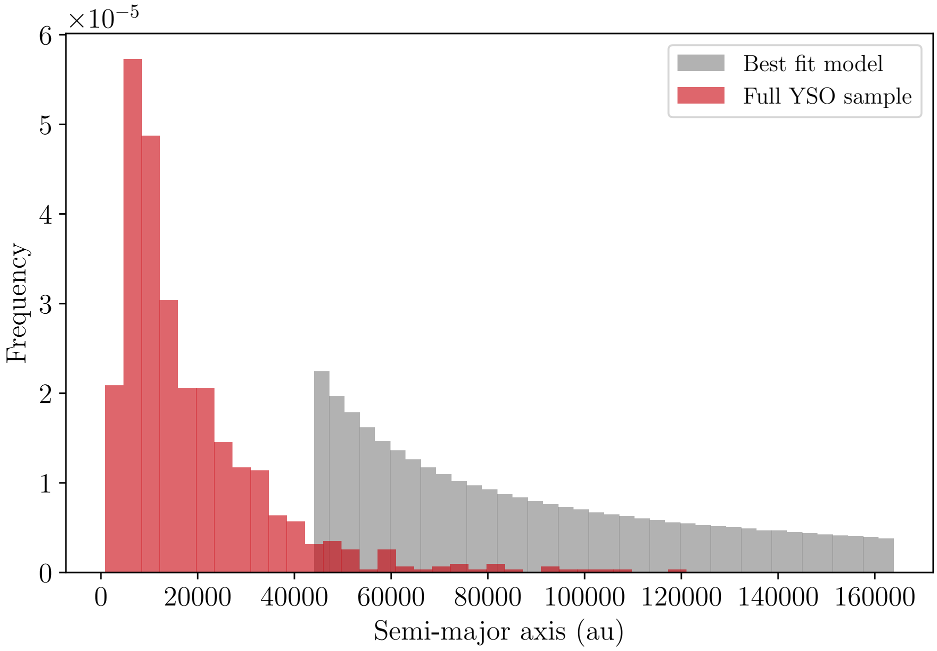

Figure 5.11: Semi-major axis distribution for the fit above.

major axis distribution only slightly higher than the separation distribution would be much more heavily weighted towards small separations than the observed sample. Whilst there are some selection effects meaning that companions in this separation might be missed, they should not impact the sample so heavily. Therefore, only a semi-major axis distribution peaking $\gtrsim 3$ times higher than the separation distribution can result in the observed separation distribution.

As companions are regularly found at 10-100s of au around YSOs, this result implies two things; firstly, it could be that this method is actually observing the extremely high separation tail of the binary distribution, because the limits on angular resolution mean that the majority of companions cannot be detected. If this is the extremely high separation tail of a typical separation distribution, then it will likely be better fit with an Öpik distribution than a lognormal. However, as we can see in Figure 5.10 and Figure 5.11, the simulation using the Öpik distribution suffers from all the same issues as the lognormal distribution.

Alternatively, this ‘binary’ sample could actually contain a large number of triple companions in systems where the secondary star is too close to the primary to be resolved. In this case, it’s possible that my ‘binary only’ population model is not the best way of fitting the observed data (see Chapter 6 for more details on how this could be corrected in the future).

Small number statistics

The models imply that only $\sim 1-3$ per cent of all binaries would be observed given the observational biases and selection effects present in this sample, providing further evidence that we may be observing the large separation tail of the binary/triple distribution; if $\sim$99 per cent of companions are much closer than our mean separation of 17900 au, which is likely, then they would not be detected through our methods.

Observational issues

The observed sample contains 842 YSOs, and my simulations used only 724 of these due to the presence of multiple companions for some objects. In Section 5.3.6, I showed that random noise could significantly alter the boundaries of cells in the binary tree for small sample sizes. I attempted to mitigate the effects of this by generating the binary tree grid for the much larger sample of fake data points. However, the small number of YSOs might be impacting the quality of the results using the binary tree method.

More issues might arise when we consider the way binaries are selected from the main observed sample. The observed separations of some of the binaries are comparable to distances between stars in a cluster rather than in binaries. This indicates that there could be a large number of 'companions' in the sample which are physically associated, but not in bound multiple systems. Since my model only includes binaries, it would be very difficult for it to fit the observations if this was the case, and might provide another explanation for the very large semi-major axis distributions.

Distance distribution after selection effects

The reason that the distance distribution appears so different after the selection effects have been applied to the binary sample is still not understood, but indicates that the results of this fit may be unreliable. This could be due to the issues listed above (about small number statistics, the presence of triple companions, etc.) meaning that this binary population model is not a good way of fitting these observations. This will be investigated very soon in future work.

5.5 Summary

I have presented the results of my study into the selection effects that impact the observations of binary stars. Orbital parameters such as the inclination, orientation, and phase of a system mean that the projected separation of a binary is not always the same as the semi-major axis or the true distance, even though on average the values are similar.

I also used my binary population model to attempt to find the true properties of an observed sample of YSO binaries. The aim was to estimate the number of binaries that would be missed due to observational biases, find the true semi-major axis distribution, and calculate the incompleteness corrected multiplicity fraction. This was done by generating a fake binary population, applying the observational selection effects (such as the minimum resolution of $\sim$1 arcsec and cutoff at $\sim$10 arcsecs) to this sample, and then comparing the results to the observational data through the use of a binary search tree.

The results of my preliminary testing indicate that this sample must be an extremely wide population of binaries (or perhaps dominated by the tertiary companions in hierarchical triple systems). The mean of the semi-major axis must be $\gtrsim 3$ times higher than the mean separation to fit the observations. If the semi-major axis distribution were lower, then we would expect an overabundance of binaries with small separations, which is not observed. This could be due to observational biases in the data that has not been accounted for, but at this point we have no evidence that any additional biases are present.

The results of this testing are by no means conclusive at this stage, and further work is needed to understand whether the simulations provide a good fit for the observations.

Chapter 6

Conclusions and future work

In this thesis, I have investigated whether a simple universal rule for star formation can be used to represent how multiplicity in prestellar cores evolves to produce the multiplicity fractions and initial mass function of the galactic field. I have also developed an orbit fitting algorithm for binary and triple stars with a small number of observations, which has applications to directly imaged brown dwarf and exoplanet systems. Finally, I have developed a binary population synthesis code that can be used to estimate the selection effects and biases on visual binary studies, through use of a binary search tree method. This method has been tested on a sample of YSO binaries. This work in this thesis has led to one publication (Houghton & Goodwin, 2022) and one submitted paper (Chapter 2).

6.1 Multiplicity of stellar systems in the field from simulations

Understanding the multiplicity properties of stars is essential for better models of stellar evolution, mass determination, orbital parameter estimates, and even galactic dynamics. Theoretical models that predict how multiple systems form are invaluable to the field of astronomy.

Many complex simulations (such as Bate, 2012) have aimed to incorporate magnetic fields, turbulence, and stellar feedback (amongst other microphysical mechanisms) into their models to determine how cores fragment and how multiple systems are formed. The method presented in this thesis used a toy Monte Carlo model to simulate the macrophysics of multiple system formation, in a effort to complement these existing models.

I considered three different scenarios for multiple system formation via fragmentation;

the self-similar model, the strongly mass-dependent model, and a hybrid fragmentation model (which depends on the core mass, but still has some random variance to the number of stars formed). Additionally, I considered one scenario in which stars are very frequently ejected from multiple systems, and another in which secular decay is the only form of post formation processing (using the probabilities determined by Sterzik & Durisen, 1998).

Using the stellar populations at the end of the simulation, I have compared the results to the observed initial mass function and multiplicity fractions of the field. This has not led to a model which perfectly fits both the IMFs and multiplicities, but some models have more success than others.

The key issue with self-similar fragmentation, in which all cores form a random number of stars irrespective of the initial core mass, is that it produces multiplicity fractions that do not have the strong primary mass dependence seen in the observations. If cores fragment with a strong dependence on their mass this breaks the self-similar mapping between the CMF and the IMF, and produce significant features in the IMF around the peak.

A hybrid model with a weak core mass-fragmentation dependence finds a good fit to the IMF, and a somewhat reasonable fit to the multiplicities. When the systems produced from this model are processed using the secular decay model only, the results seem to match the IMFs and multiplicities of loosely bound star-forming associations. This implies that a model in which the decay/dynamical destruction probabilities include contributions from both secular decay and dynamical destruction could reproduce the multiplicities of the field.

6.1.1 Future work

Developing a combined model of both secular decay and dynamical destruction is not trivial. The rate of dynamical destruction depends strongly on the properties of the star-forming regions, such as the velocity dispersions and density profile (e.g. Sollima, 2008; Parker & Goodwin, 2012; Parker & Meyer, 2014; Griffiths et al., 2018). As these properties differ significantly from region to region, an N-body model to determine an overall probability of dynamical destruction would need to include contributions from clusters of various environments. This work, whilst complex, would follow on nicely from the conclusions presented in Chapter 2.

A more complex toy model

The toy model that I developed considers a simple set of rules for star formation, without going into detail about different star formation mechanisms or the separation distributions. There are several ways to develop the complexity of my model now that we have established that it is difficult to produce the IMF and multiplicity properties of the field using a universal rule for star formation.

The first approach would be to consider how the star formation process differs for stars of different masses. In Section 1.3.4, I described how high-mass stars may form through 'competitive accretion', meaning that they accrete from the well of gas and dust outside the prestellar core to increase their mass at a very high rate. This often leads to lower mass companions being formed near the massive star. In my current model, the mass ratio distribution of systems has no dependence on the primary mass, but adding different mass ratio distributions that depend on primary mass into the initial conditions may produce interesting results.

Furthermore, since high mass stars are able to accrete additional material from the local gas reservoir, their star formation efficiency will be higher than for low mass stars (and in some cases, may be greater than 1). It is not clear whether the more powerful outflows and stellar winds would decrease the star formation efficiency of massive stars, which is why I have not included a mass dependence in the star formation efficiency so far. With more time, I would explore a variety of SFE distributions with different dependences on mass.

Previous work from Parker & Meyer (2014) shows that the multiplicity fraction over time depends on the primary mass. Current, more up to date work (Richard Parker, private communication) would provide robust limits on how the primary mass affects the multiplicity fraction and could be incorporated into my model.

The number of stars formed from each core in my simulations only depends on the mass of the core. (Murillo et al., 2018) used molecular tracers in star forming cores to calculate the cold gas mass present in each core, and determined that core mass is a primary factor in determining multiplicity (i.e. the mass affected fragmentation more than the temperature). It is therefore intuitive that the mass available for star formation combined with the critical mass for fragmentation (i.e. M_{BE}) affects the number of stars formed. The rules used in my simulations are all-encompassing of core fragmentation, disc fragmentation, and capture to create one overall universal rule. However, if one wanted to make these simulations more complex, it would be possible to include the individual contributions from each star formation mechanism in this simulation in detail.

This would allow more accurate separation distributions to be produced as a byproduct of the star formation process, which could in turn be used to construct a realistic model of how companions at different separations are disrupted due to encounters or decay through secular processes.

6.2 FOBOS

I developed an algorithm to estimate the orbital properties of visual binaries, triple systems, and directly imaged brown dwarfs/exoplanets. The algorithm (`FOBOS`) uses a brute force Monte Carlo method to randomly sample the full parameter space of orbital elements. This is a very computationally expensive method, but by writing the code in Fortran and parallelising it, I have managed to make it efficient enough to provide reliable confidence limits on the semi-major axis, eccentricity, and inclination of binary/triple systems within a few CPU minutes (binaries) or hours (triples).

`FOBOS` was tested on a large sample of fake binary and triple systems to test its reliability. I found that some pairs of observations can be very constraining whereas others are less constraining; for systems that can't be well constrained, the uncertainties are large rather than it narrowing in on the wrong area of parameter space, so it is simple to discount poorly fitting results.

By adding a third or fourth epoch of observation for a binary system, the uncertainties on the results are significantly decreased (as we would expect). If there are more observations available, a MCMC code such as `orbitize!` (Blunt et al., 2020) or `orvara` (Brandt et al., 2021) becomes much more efficient.

I tested `FOBOS` on two observed systems (2M 0103-55 (AB) b and HD 206893) both of which have low mass companions. The results I obtained matched very well with results in the literature by (Blunt et al., 2017) and (Ward-Duong et al., 2021).

6.2.1 Future work

As mentioned previously, `FOBOS` can be used to estimate orbital parameters for directly imaged exoplanets. Only a small number of exoplanets have been detected via direct imaging so far ($\sim 20 - 25$ out of > 5000, Currie et al., 2022). However, direct imaging allows exoplanet atmospheres to be studied, and there are many instruments dedicated to exoplanet imaging studies (not to mention the capabilities of JWST). There are likely to be many more directly imaged exoplanet discoveries over the coming years, and `FOBOS` provides a way of adding constraints to the orbital properties very soon after the initial detection.

6.3 Binarity of YSOs

Using the binary system projection code developed for the `FOBOS` algorithm, I developed a binary population synthesis code to estimate the selection effects present in surveys of visual binary systems. I determined that on average, a binary system will have a projected separation that comparable to its semi-major axis.

The inclination and orientation of the system both cause the projected separation of the two stars to appear smaller than the true distance between them. The eccentricity of a system means that the true distance between the two stars varies significantly over the course of the orbit, and as the companion star spends more time closer to apastron (where it is travelling more slowly), the projected separation often appears larger than the semi-major axis. These effects have been understood for decades, but in my work I have quantified the impact of these parameters and used it to estimate the selection effects on visual binary studies.

I have used a binary search tree algorithm based on the work of Akter (2022) to compare my binary population synthesis model to the separation and δmag distribution of a sample of binary stars collated by Shenton et al. (in preparation). Assuming that their sample is complete in the separation range of $1.5 - 10$ arcseconds, I found a semi-major axis distribution that was significantly larger than the separation distribution implied (if the separations were converted to au using the distances only) This indicates that either (a) they are looking at the tail end of a distribution of very wide binaries or (b) the majority of the 'binary' companions in their sample are actually the tertiary component of a hierarchical triple system.

6.3.1 Future work

This project has the most potential for future work. In the time following the submission of this thesis, I plan to make my code for producing a binary tree and comparing two data sets publicly available and pip installable.

The difference between the distance distribution of the YSOs before and after the selection effects have been applied is still a major issue with this model. Understanding the reasons behind this, and the extent to which it affects the reliability of my results, is the most important next step in this project.

Including triple companions

The results of my YSO analysis in Chapter 5 indicate that the separation range of the ‘binaries’ detected by Shenton et al. (in preparation) is extremely large, implying that they may be looking at a population of tertiary companions in triple systems rather than binaries. This is an interesting result, and could be followed up by including triple systems in my population synthesis model, to see if this better reproduces the separation and δmag distributions.

Inclination, debris disc extinction levels, and completeness

YSOs are surrounded by a debris disc. This disc obscures the host star, and in binary surveys this can often result in a primary that appears less bright than its companion. If there had been more time during then project, my intention was to study how the inclination of a debris disc affects the possibility of detecting a YSO, and how this would affect the Shenton et al. sample of YSOs.

The binary population synthesis code already generates the inclination of a binary system when forming a fake observation. Assuming that the companion is orbiting in the plane of the debris disc (which is more likely to be true for massive stars, where the companion may have formed through disc fragmentation), then systems with inclinations closer to edge on are more likely to have companions suffering from a higher level of debris disc extinction.

My plan was to use the inclination distribution of the fake binaries and the obscuration properties of the debris disc (provided by Shenton and Oudmaijer) to study how the inclination affects the δmag distribution. It could be that the YSO primaries are still consistently detected in the infrared, or it is possible that this work would show that edge on inclination YSOs are not often observed. I could use these results to estimate the total number of YSOs missed in observations due to disc extinction, allowing corrections to be applied to their results for an additional level of incompleteness.

Bibliography

Akter S., 2022, PhD thesis, University of Sheffield, UK

Alves J., Lombardi M., Lada C. J., 2007, A&A, 462, L17

Andre P., Ward-Thompson D., Barsony M., 1993, ApJ, 406, 122

Andre P., Ward-Thompson D., Barsony M., 2000, in Mannings V., Boss A. P., Russell S. S., eds, Protostars and Planets IV. p. 59 (`arXiv:astro-ph/9903284`), doi:10.48550/arXiv.astro-ph/9903284

André P., Belloche A., Motte F., Peretto N., 2007, A&A, 472, 519

André P., et al., 2010, A&A, 518, L102

André P., Di Francesco J., Ward-Thompson D., Inutsuka S. I., Pudritz R. E., Pineda J. E., 2014, in Beuther H., Klessen R. S., Dullemond C. P., Henning T., eds, Protostars and Planets VI. pp 27–51 (`arXiv:1312.6232`), doi:10.2458/azu_uapress_9780816531240-ch002

André P., Arzoumanian D., Könyves V., Shimajiri Y., Palmeirim P., 2019, A&A, 629, L4

Anosova J. P., 1986, Ap&SS, 124, 217

Arzoumanian D., et al., 2011, A&A, 529, L6

Attwood R. E., Goodwin S. P., Stamatellos D., Whitworth A. P., 2009, A&A, 495, 201

Bastian N., Covey K. R., Meyer M. R., 2010, ARA&A, 48, 339

Bate M. R., 2012, MNRAS, 419, 3115

Bate M. R., Bonnell I. A., Bromm V., 2002, MNRAS, 332, L65

Bate M. R., Bonnell I. A., Bromm V., 2003, MNRAS, 339, 577

Benson P. J., Myers P. C., 1989, ApJS, 71, 89

Binney J., Tremaine S., 2008, Galactic Dynamics: Second Edition. Oxford University Press

Blunt S., et al., 2017, AJ, 153, 229

Blunt S., et al., 2020, AJ, 159, 89

Bonnell I. A., 1994, MNRAS, 269, 837

Bonnell I. A., Bate M. R., 2006, MNRAS, 370, 488

Bonnell I. A., Bate M. R., Clarke C. J., Pringle J. E., 2001, MNRAS, 323, 785

Bonnell I. A., Larson R. B., Zinnecker H., 2007, in Reipurth B., Jewitt D., Keil K., eds, Protostars and Planets V. p. 149 (`arXiv:astro-ph/0603447`), doi:10.48550/arXiv.astro-ph/0603447

Bonnor W. B., 1956, MNRAS, 116, 351

Brandt T. D., Dupuy T. J., Li Y., Brandt G. M., Zeng Y., Michalik D., Bardalez Gagliuffi D. C., Raposo-Pulido V., 2021, AJ, 162, 186

Bressert E., et al., 2010, MNRAS, 409, L54

Burgasser A. J., 2007, ApJ, 659, 655

Burgasser A. J., Kirkpatrick J. D., Reid I. N., Brown M. E., Miskey C. L., Gizis J. E., 2003, ApJ, 586, 512

Carroll B. W., Ostlie D. A., 2017, An introduction to modern astrophysics, Second Edition. Pearson

Chabrier G., 2003a, PASP, 115, 763

Chabrier G., 2003b, ApJ, 586, L133

Chabrier G., 2005, in Corbelli E., Palla F., Zinnecker H., eds, Astrophysics and Space Science Library Vol. 327, The Initial Mass Function 50 Years Later. p. 41 (`arXiv:astro-ph/0409465`), doi:10.1007/978-1-4020-3407-7_5

Chen H., Myers P. C., Ladd E. F., Wood D. O. S., 1995, ApJ, 445, 377

Chen C.-Y., Mundy L. G., Ostriker E. C., Storm S., Dhabal A., 2020, MNRAS, 494, 3675

Chevance M., et al., 2020, MNRAS, 493, 2872

Chevance M., Krumholz M. R., McLeod A. F., Ostriker E. C., Rosolowsky E. W., Sternberg A., 2022, arXiv e-prints, p. arXiv:2203.09570

Churchwell E., 2002, ARA&A, 40, 27

Clark P. C., Whitworth A. P., 2021, MNRAS, 500, 1697

Clarke C. J., Pringle J. E., 1991, MNRAS, 249, 584

Commerçon B., Hennebelle P., Henning T., 2011, ApJ, 742, L9

Correia S., Zinnecker H., Ratzka T., Sterzik M. F., 2006, A&A, 459, 909

Cournoyer-Cloutier C., et al., 2021, MNRAS, 501, 4464

Currie T., Biller B., Lagrange A.-M., Marois C., Guyon O., Nielsen E., Bonnefoy M., De Rosa R., 2022, arXiv e-prints, p. arXiv:2205.05696

Da Rio N., Robberto M., Hillenbrand L. A., Henning T., Stassun K. G., 2012, ApJ, 748, 14

Dame T. M., Hartmann D., Thaddeus P., 2001, ApJ, 547, 792

Damian B., Jose J., Samal M. R., Moraux E., Das S. R., Patra S., 2021, MNRAS, 504, 2557

De Rosa R. J., et al., 2014, MNRAS, 437, 1216

Deacon N. R., Kraus A. L., 2020, MNRAS, 496, 5176

Delorme P., et al., 2013, A&A, 553, L5

Delorme P., et al., 2017, A&A, 608, A79

Di Francesco J., et al., 2020, ApJ, 904, 172

Dib S., 2014, MNRAS, 444, 1957

Drazkowska J., et al., 2022, arXiv e-prints, p. arXiv:2203.09759

Duchêne G., 1999, A&A, 341, 547

Duchêne G., Kraus A., 2013, ARA&A, 51, 269

Duchêne G., Lacour S., Moraux E., Goodwin S., Bouvier J., 2018, MNRAS, 478, 1825

Dunham M. M., et al., 2015, ApJS, 220, 11

Duquennoy A., Mayor M., 1991, A&A, 248, 485

Ebert R., 1955, Z. Astrophys., 37, 217

Eggleton P., Kiseleva L., 1995, ApJ, 455, 640

Fabian A. C., Pringle J. E., Rees M. J., 1975, MNRAS, 172, 15

Federrath C., 2016, MNRAS, 457, 375

Fischer D. A., Marcy G. W., 1992, ApJ, 396, 178

Fischer D. A., Howard A. W., Laughlin G. P., Macintosh B., Mahadevan S., Sahlmann J., Yee J. C., 2014, in Beuther H., Klessen R. S., Dullemond C. P., Henning T., eds, Protostars and Planets VI. pp 715–737 (`arXiv:1505.06869`), doi:10.2458/azu_uapress_9780816531240-ch031

Fischer W. J., Hillenbrand L. A., Herczeg G. J., Johnstone D., Kóspál Á., Dunham M. M., 2022, arXiv e-prints, p. arXiv:2203.11257

Fontanive C., Biller B., Bonavita M., Allers K., 2018, MNRAS, 479, 2702

Fulton B. J., Petigura E. A., Blunt S., Sinukoff E., 2018, PASP, 130, 044504

Gammie C. F., 2001, ApJ, 553, 174

Goldreich P., Lynden-Bell D., 1965, MNRAS, 130, 97

Goodwin S. P., 2010, Philosophical Transactions of the Royal Society of London Series A, 368, 851

Goodwin S. P., 2013, MNRAS, 430, L6

Goodwin S. P., Kroupa P., 2005, A&A, 439, 565

Goodwin S. P., Whitworth A., 2007, A&A, 466, 943

Goodwin S. P., Whitworth A. P., Ward-Thompson D., 2004, A&A, 419, 543

Goodwin S. P., Kroupa P., Goodman A., Burkert A., 2007, in Reipurth B., Jewitt D., Keil K., eds, Protostars and Planets V. p. 133 (`arXiv:astro-ph/0603233`)

Goodwin S. P., Nutter D., Kroupa P., Ward-Thompson D., Whitworth A. P., 2008, A&A, 477, 823

Grandjean A., et al., 2019, A&A, 627, L9

Greenberg R., Wacker J. F., Hartmann W. K., Chapman C. R., 1978, Icarus, 35, 1

Gribbin J., 2002, Science: A History 1543-2001. Penguin

Griffiths D. W., Goodwin S. P., Caballero-Nieves S. M., 2018, MNRAS, 476, 2493

Guszejnov D., Hopkins P. F., 2015, MNRAS, 450, 4137

Guszejnov D., Hopkins P. F., Krumholz M. R., 2017, MNRAS, 468, 4093

Guszejnov D., Grudić M. Y., Hopkins P. F., Offner S. S. R., Faucher-Giguère C.-A., 2020, MNRAS, 496, 5072

Guszejnov D., Grudić M. Y., Offner S. S. R., Faucher-Giguère C.-A., Hopkins P. F., Rosen A. L., 2022, MNRAS, 515, 4929

Hacar A., Tafalla M., Forbrich J., Alves J., Meingast S., Grossschedl J., Teixeira P. S., 2018, A&A, 610, A77

Hacar A., Clark S., Heitsch F., Kainulainen J., Panopoulou G., Seifried D., Smith R., 2022, arXiv e-prints, p. arXiv:2203.09562

Haisch Karl E. J., Greene T. P., Barsony M., Stahler S. W., 2004, AJ, 127, 1747

Harrington R. S., 1972, Celestial Mechanics, 6, 322

Hartmann L., Herczeg G., Calvet N., 2016, ARA&A, 54, 135

Haugbølle T., Padoan P., Nordlund Å., 2018, ApJ, 854, 35

Heggie D. C., 1975, MNRAS, 173, 729

Helled R., et al., 2014, in Beuther H., Klessen R. S., Dullemond C. P., Henning T., eds, Protostars and Planets VI. pp 643–665 (`arXiv:1311.1142`), doi:10.2458/azu_uapress_9780816531240-ch028

Hennebelle P., Commerçon B., Joos M., Klessen R. S., Krumholz M., Tan J. C., Teyssier R., 2011, A&A, 528, A72

Hills J. G., 1975, AJ, 80, 809

Hills J. G., Day C. A., 1976, ApJ, 17, 87

Holman K., Walch S. K., Goodwin S. P., Whitworth A. P., 2013, MNRAS, 432, 3534

Houghton R. J., Goodwin S. P., 2022, MNRAS, 513, 2635

Jeans J. H., 1902, Philosophical Transactions of the Royal Society of London Series A, 199, 1

Johnson B. M., Gammie C. F., 2003, ApJ, 597, 131

Joy A. H., 1945, ApJ, 102, 168

Kim J.-G., Ostriker E. C., Filippova N., 2021, ApJ, 911, 128

King R. R., Parker R. J., Patience J., Goodwin S. P., 2012a, MNRAS, 421, 2025

King R. R., Goodwin S. P., Parker R. J., Patience J., 2012b, MNRAS, 427, 2636

Könyves V., et al., 2010, A&A, 518, L106

Könyves V., et al., 2015, A&A, 584, A91

Kounkel M., et al., 2019, AJ, 157, 196

Kouwenhoven M. B. N., Goodwin S. P., Parker R. J., Davies M. B., Malmberg D., Kroupa P., 2010, MNRAS, 404, 1835

Kraus A. L., Ireland M. J., Martinache F., Hillenbrand L. A., 2011, ApJ, 731, 8

Kreidberg L., 2015, PASP, 127, 1161

Kroupa P., 1995a, MNRAS, 277, 1491

Kroupa P., 1995b, MNRAS, 277, 1522

Kroupa P., 2001, MNRAS, 322, 231

Kroupa P., 2002, Science, 295, 82

Kroupa P., 2008, in Knapen J. H., Mahoney T. J., Vazdekis A., eds, Astronomical Society of the Pacific Conference Series Vol. 390, Pathways Through an Eclectic Universe. p. 3 (`arXiv:0708.1164`), doi:10.48550/arXiv.0708.1164

Kroupa P., Bouvier J., 2003, MNRAS, 346, 343

Krumholz M. R., McKee C. F., Klein R. I., 2005, Nature, 438, 332

Krumholz M. R., et al., 2014, in Beuther H., Klessen R. S., Dullemond C. P., Henning T., eds, Protostars and Planets VI. pp 243–266 (`arXiv:1401.2473`), doi:10.2458/azu_uapress_9780816531240-ch011

Kuruwita R., Haugbølle T., 2022, arXiv e-prints, p. arXiv:2209.01909

Lada C. J., 1987, in Peimbert M., Jugaku J., eds, IAU Symposium Vol. 115, Star Forming Regions. p. 1

Lada C. J., 2006, ApJ, 640, L63

Lada C. J., Lada E. A., 2003, ARA&A, 41, 57

Lada C. J., Muench A. A., Rathborne J., Alves J. F., Lombardi M., 2008, ApJ, 672, 410

Larson R. B., 1969, MNRAS, 145, 271

Launhardt R., et al., 2013, A&A, 551, A98

Lee Y.-N., Hennebelle P., Chabrier G., 2017, ApJ, 847, 114

Lee A. T., Offner S. S. R., Kratter K. M., Smullen R. A., Li P. S., 2019, ApJ, 887, 232

Leinert C., Zinnecker H., Weitzel N., Christou J., Ridgway S. T., Jameson R., Haas M., Lenzen R., 1993, A&A, 278, 129

Lomax O., Whitworth A. P., Hubber D. A., Stamatellos D., Walch S., 2015, MNRAS, 447, 1550

Lucas P. W., et al., 2008, MNRAS, 391, 136

Luhman K. L., 2012, ARA&A, 50, 65

Luhman K. L., Briceño C., Stauffer J. R., Hartmann L., Barrado y Navascués D., Caldwell N., 2003, ApJ, 590, 348

Luhman K. L., Joergens V., Lada C., Muzerolle J., Pascucci I., White R., 2007, in Reipurth B., Jewitt D., Keil K., eds, Protostars and Planets V. p. 443 (`arXiv:astro-ph/0608546`), doi:10.48550/arXiv.astro-ph/0608546

Lumsden S. L., Hoare M. G., Urquhart J. S., Oudmaijer R. D., Davies B., Mottram J. C., Cooper H. D. B., Moore T. J. T., 2013, ApJS, 208, 11

Macintosh B. A., et al., 2008, in Hubin N., Max C. E., Wizinowich P. L., eds, Society of Photo-Optical Instrumentation Engineers (SPIE) Conference Series Vol. 7015, Adaptive Optics Systems. p. 701518, doi:10.1117/12.788083

Mardling R., Aarseth S., 1999, in Steves B. A., Roy A. E., eds, NATO Advanced Study Institute (ASI) Series C Vol. 522, The Dynamics of Small Bodies in the Solar System, A Major Key to Solar System Studies. p. 385

Marsh K. A., et al., 2016, MNRAS, 459, 342

Maschberger T., 2013, MNRAS, 429, 1725

Massi F., et al., 2019, A&A, 628, A110

Matzner C. D., McKee C. F., 2000, ApJ, 545, 364

McKee C. F., Ostriker E. C., 2007, ARA&A, 45, 565

Mede K., Brandt T. D., 2017, AJ, 153, 135

Meru F., Bate M. R., 2012, MNRAS, 427, 2022

Mignon-Risse R., González M., Commerçon B., Rosdahl J., 2021, A&A, 652, A69

Miller G. E., Scalo J. M., 1979, ApJS, 41, 513

Milli J., et al., 2017, A&A, 597, L2

Moe M., Di Stefano R., 2017, ApJS, 230, 15

Moe M., Kratter K. M., 2018, ApJ, 854, 44

Moe M., Kratter K. M., 2021, MNRAS, 507, 3593

Moeckel N., Bate M. R., 2010, MNRAS, 404, 721

Motte F., Andre P., Neri R., 1998, A&A, 336, 150

Motte F., et al., 2022, A&A, 662, A8

Mottram J. C., et al., 2011, ApJ, 730, L33

Muraoka K., et al., 2020, ApJ, 903, 94

Murillo N. M., van Dishoeck E. F., Tobin J. J., Mottram J. C., Karska A., 2018, A&A, 620, A30

Murray N., 2011, ApJ, 729, 133

Nony T., et al., 2023, arXiv e-prints, p. arXiv:2301.07238

Nutter D., Ward-Thompson D., 2007, MNRAS, 374, 1413

Offner S. S. R., Kratter K. M., Matzner C. D., Krumholz M. R., Klein R. I., 2010, ApJ, 725, 1485

Offner S. S. R., Clark P. C., Hennebelle P., Bastian N., Bate M. R., Hopkins P. F., Moraux E., Whitworth A. P., 2014, in Beuther H., Klessen R. S., Dullemond C. P., Henning T., eds, Protostars and Planets VI. p. 53 (`arXiv:1312.5326`), doi:10.2458/azu_uapress_9780816531240-ch003

Offner S. S. R., Moe M., Kratter K. M., Sadavoy S. I., Jensen E. L. N., Tobin J. J., 2022, arXiv e-prints, p. arXiv:2203.10066

Padoan P., Nordlund Å., 2002, ApJ, 576, 870

Padoan P., Nordlund Å., 2004, ApJ, 617, 559

Palau A., et al., 2021, ApJ, 912, 159

Parker R. J., Goodwin S. P., 2012, MNRAS, 424, 272

Parker R. J., Meyer M. R., 2014, MNRAS, 442, 3722

Parker R. J., Goodwin S. P., Kroupa P., Kouwenhoven M. B. N., 2009, MNRAS, 397, 1577

Parker R. J., Goodwin S. P., Allison R. J., 2011, MNRAS, 418, 2565

Parker R. J., Wright N. J., Goodwin S. P., Meyer M. R., 2014, MNRAS, 438, 620

Patience J., Ghez A. M., Reid I. N., Matthews K., 2002, AJ, 123, 1570

Persson M. V., 2014a, Current view of protostellar evolution (ENG), doi:10.6084/m9.figshare.654555.v7, `https://figshare.com/articles/figure/Current_view_of_protostellar_evolution/654555`

Persson M. V., 2014b, SEDs of the different protostellar evolutionary stages, doi:10.6084/m9.figshare.1121574.v2, `https://figshare.com/articles/figure/SEDs_of_the_different_protostellar_evolutionary_stages/1121574`

Pineda J. E., et al., 2022, arXiv e-prints, p. arXiv:2205.03935

Price-Whelan A. M., Hogg D. W., Foreman-Mackey D., Rix H.-W., 2017, The Joker: A custom Monte Carlo sampler for binary-star and exoplanet radial velocity data, Astrophysics Source Code Library, record ascl:1701.001 (ascl:1701.001)

Prussing J. E., Conway B. A., 1993, Orbital Mechanics. Oxford University Press

Raghavan D., et al., 2010, ApJS, 190, 1

Raymond S. N., Morbidelli A., 2022, in Biazzo K., Bozza V., Mancini L., Sozzetti A., eds, Astrophysics and Space Science Library Vol. 466, Demographics of Exoplanetary Systems, Lecture Notes of the 3rd Advanced School on Exoplanetary Science. pp 3–82 (`arXiv:2002.05756`), doi:10.1007/978-3-030-88124-5_1

Raymond S. N., Kokubo E., Morbidelli A., Morishima R., Walsh K. J., 2014, in Beuther H., Klessen R. S., Dullemond C. P., Henning T., eds, Protostars and Planets VI. pp 595–618 (`arXiv:1312.1689`), doi:10.2458/azu_uapress_9780816531240-ch026

Reipurth B., Clarke C., 2001, AJ, 122, 432

Reipurth B., Mikkola S., 2012, Nature, 492, 221

Reipurth B., Zinnecker H., 1993, A&A, 278, 81

Reipurth B., Clarke C. J., Boss A. P., Goodwin S. P., Rodríguez L. F., Stassun K. G., Tokovinin A., Zinnecker H., 2014, in Beuther H., Klessen R. S., Dullemond C. P., Henning T., eds, Protostars and Planets VI. p. 267 (`arXiv:1403.1907`), doi:10.2458/azu_uapress_9780816531240-ch012

Rosen A. L., Li P. S., Zhang Q., Burkhart B., 2019, ApJ, 887, 108

Sadavoy S. I., Stahler S. W., 2017, MNRAS, 469, 3881

Saito R. K., et al., 2012, A&A, 537, A107

Salpeter E. E., 1955, ApJ, 121, 161

Sana H., et al., 2012, Science, 337, 444

Sana H., et al., 2014, ApJS, 215, 15

Scally A., Clarke C., McCaughrean M. J., 1999, MNRAS, 306, 253

Schneider F. R. N., et al., 2018, Science, 359, 69

Scibelli S., Shirley Y., 2020, ApJ, 891, 73

Scoville N. Z., Yun M. S., Clemens D. P., Sanders D. B., Waller W. H., 1987, ApJS, 63, 821

Seifried D., Walch S., 2015, MNRAS, 452, 2410

Shaya E. J., Olling R. P., 2011, ApJS, 192, 2

Shu F. H., Adams F. C., Lizano S., 1987, ARA&A, 25, 23

Sollima A., 2008, MNRAS, 388, 307

Solomon P. M., Rivolo A. R., Barrett J., Yahil A., 1987, ApJ, 319, 730

Stamatellos D., Whitworth A. P., 2009, MNRAS, 392, 413

Stamatellos D., Hubber D. A., Whitworth A. P., 2007, MNRAS, 382, L30

Stamatellos D., Maury A., Whitworth A., André P., 2011, MNRAS, 413, 1787

Sterzik M. F., Durisen R. H., 1998, A&A, 339, 95

Temi P., Amblard A., Gitti M., Brighenti F., Gaspari M., Mathews W. G., David L., 2018, ApJ, 858, 17

Tobin J. J., et al., 2016, ApJ, 818, 73

Tobin J. J., et al., 2022, ApJ, 925, 39

Tohline J. E., 2002, ARA&A, 40, 349

Tokovinin A. A., 2000, A&A, 360, 997

Tokovinin A., 2014, AJ, 147, 87

Tokovinin A., Briceño C., 2020, AJ, 159, 15

Tokovinin A., Moe M., 2020, MNRAS, 491, 5158

Toomre A., 1964, ApJ, 139, 1217

Torres G., Latham D. W., Quinn S. N., 2021, ApJ, 921, 117

Valtonen M., Mylläri A., Orlov V., Rubinov A., 2008, in Vesperini E., Giersz M., Sills A., eds, IAU Symposium Vol. 246, Dynamical Evolution of Dense Stellar Systems. pp 209–217, doi:10.1017/S1743921308015627

Vázquez-Semadeni E., Palau A., Ballesteros-Paredes J., Gómez G. C., Zamora-Avilés M., 2019, MNRAS, 490, 3061

Ward-Duong K., et al., 2015, MNRAS, 449, 2618

Ward-Duong K., et al., 2021, AJ, 161, 5

Ward-Thompson D., Whitworth A. P., 2011, An Introduction to Star Formation. Cambridge University Press

Whitworth A. P., Stamatellos D., 2006, A&A, 458, 817

Whitworth A. P., Zinnecker H., 2004, A&A, 427, 299

Whitworth A., Bate M. R., Nordlund Å., Reipurth B., Zinnecker H., 2007, in Reipurth B., Jewitt D., Keil K., eds, Protostars and Planets V. p. 459

Williams J. P., Cieza L. A., 2011, ARA&A, 49, 67

Winters J. G., et al., 2019, AJ, 157, 216

Wright N. J., Goodwin S., Jeffries R. D., Kounkel M., Zari E., 2022, arXiv e-prints, p. arXiv:2203.10007

Zinnecker H., 1984, MNRAS, 210, 43

Zinnecker H., Yorke H. W., 2007, ARA&A, 45, 481

di Francesco J., Evans N. J. I., Caselli P., Myers P. C., Shirley Y., Aikawa Y., Tafalla M., 2007, in Reipurth B., Jewitt D., Keil K., eds, Protostars and Planets V. p. 17 (`arXiv:astro-ph/0602379`), doi:10.48550/arXiv.astro-ph/0602379

Appendix A

Multiplicity of stellar systems

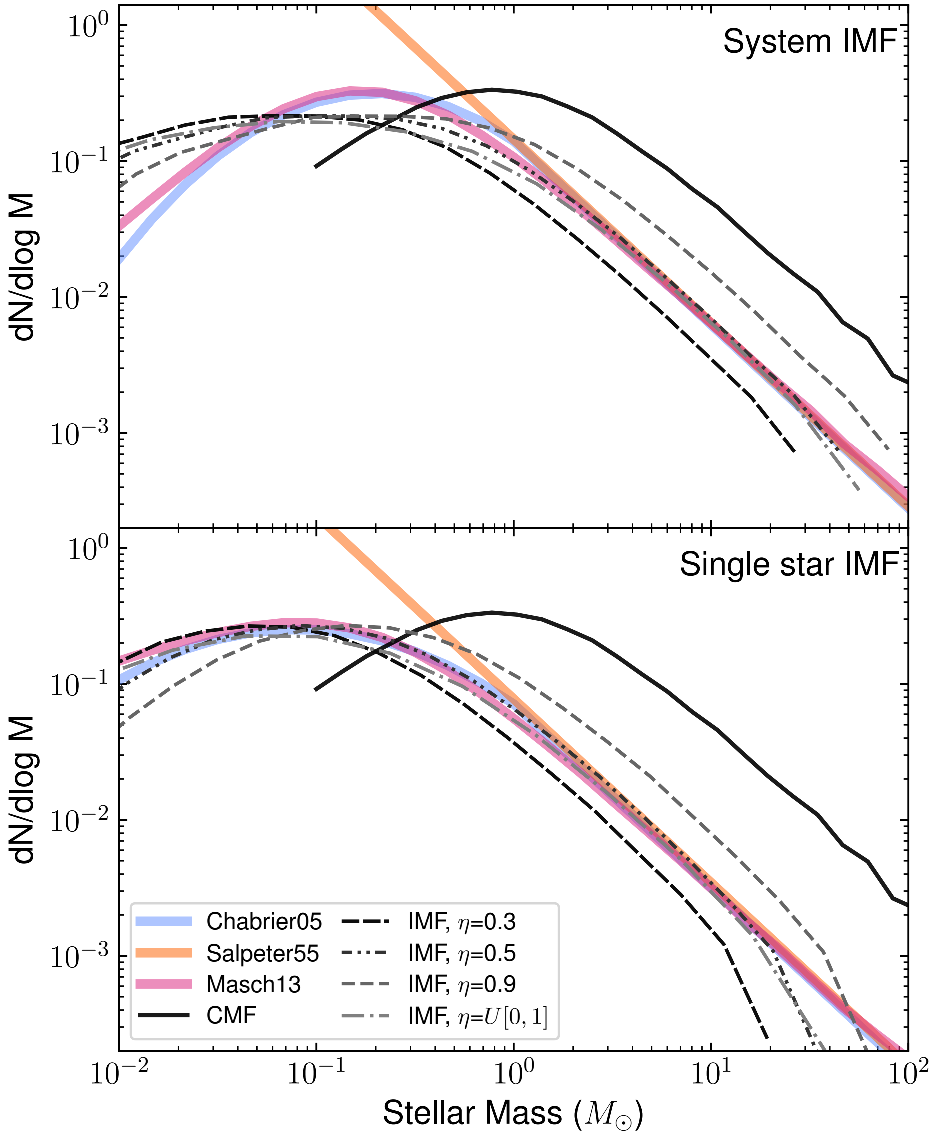

Figure A.1: The system (top) and single star (bottom) IMFs for the self-similar model. On both plots, the Salpeter (orange), Chabrier (blue) and Maschberger (pink) IMFs are shown by the solid lines. The core mass function used in our simulations is shown by the solid black line. The IMFs are plotted for several values of the star formation efficiency: $\eta = 0.3$ (densely dashed), $\eta = 0.5$ (dotted), $\eta = 0.9$ (dashed), and $\eta = U[0, 1]$ (dash-dotted). The grey shaded region on the left of both plots shows the brown dwarf regime.

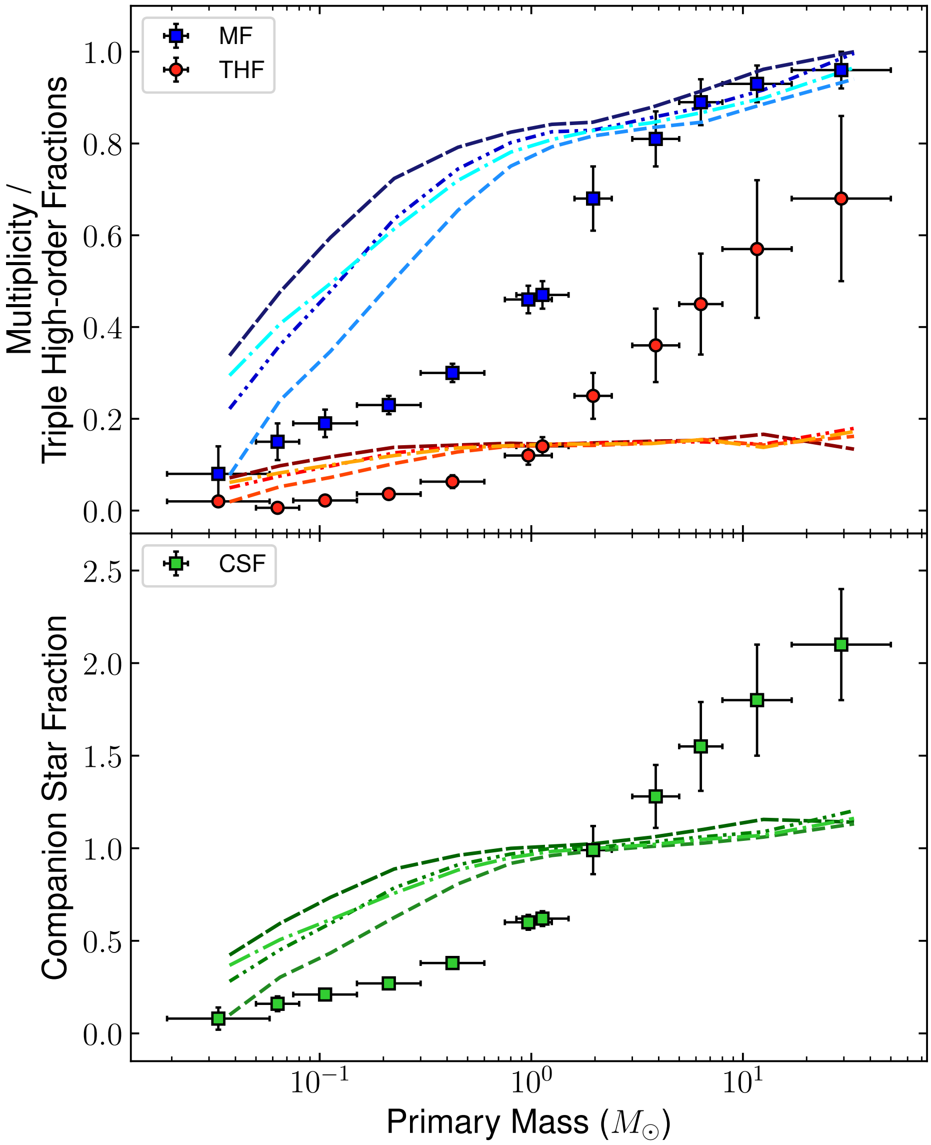

Figure A.2: Top: Observed multiplicity fractions (blue squares) and triple high order fractions (red circles) from various sources listed in table 1 of Offner et al. (2022). The blue lines and red lines show the multiplicity fractions and triple higher order fractions (respectively) from my model using random fragmentation and Sterzik & Durisen (1998) **secular decay** rules. The values for the MFs and THFs are plotted for several values of the star formation efficiency: $\eta = 0.3$ (densely dashed), $\eta = 0.5$ (dotted), $\eta = 0.9$ (dashed), and $\eta = U[0, 1]$ (dash-dotted). Bottom: Companion star fractions following the same rules as the top plot.

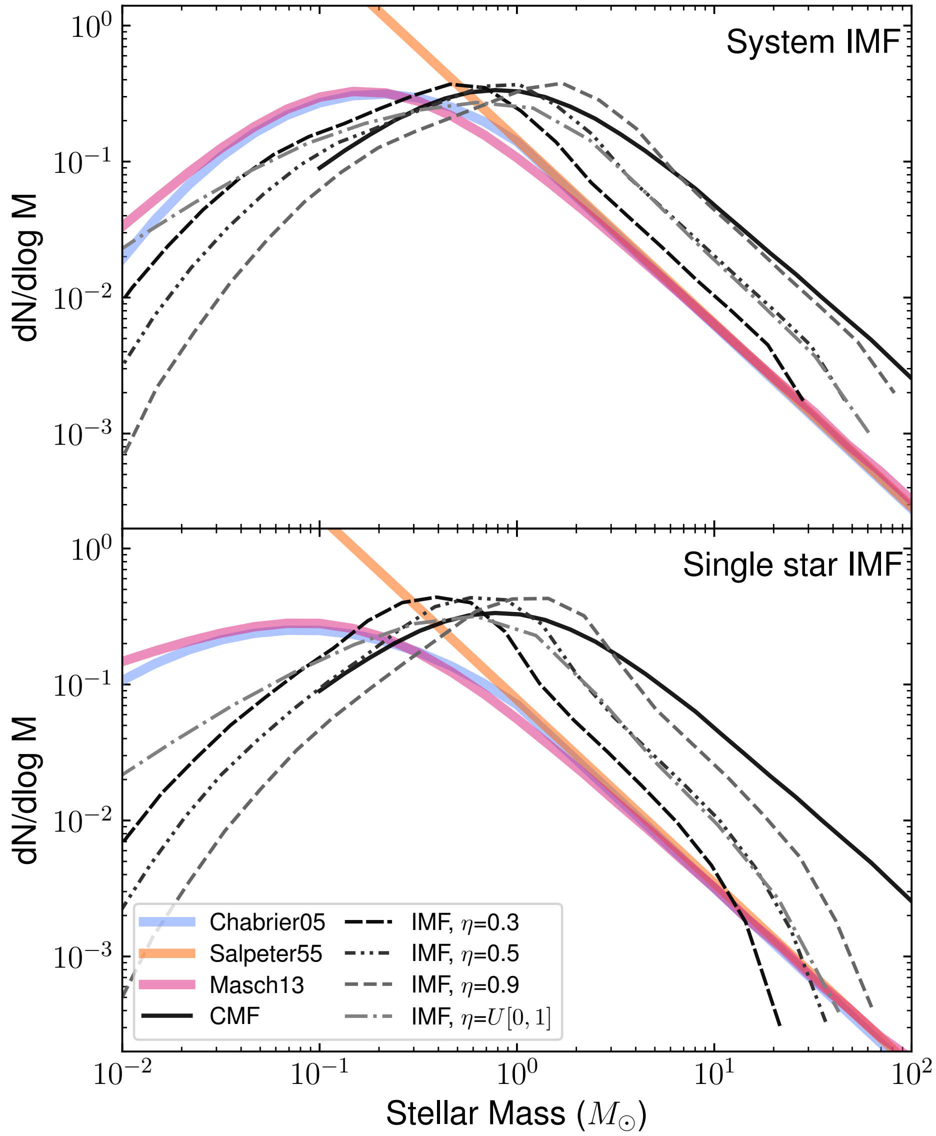

Figure A.3: IMFs from the Bonnor-Ebert mass dependent model. These results are from a model that uses the Sterzik & Durisen (1998) **secular decay** rules for dynamical processing. See caption of Figure A.1 for more details.

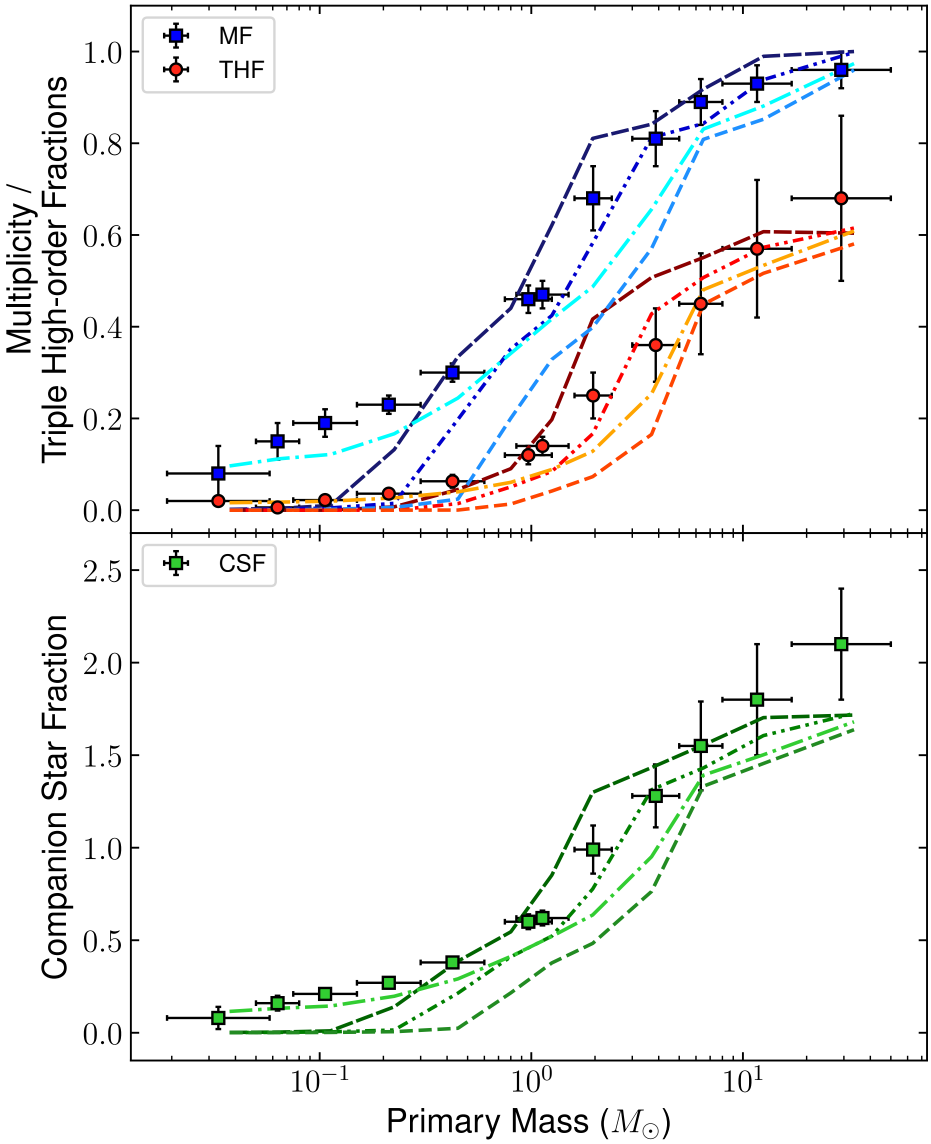

Figure A.4: Multiplicities from the Bonnor-Ebert mass dependent model. These results are from a model that uses the Sterzik & Durisen (1998) **secular decay** rules for dynamical processing. See the caption of Figure A.2 for more details.

Appendix B

Additional FOBOS corner plots and simulation data tables

Figure B.1 shows the probability distribution functions (top panels of each column) and parameter covariances for test system B4, and Figure B.2 shows these properties for system T25.

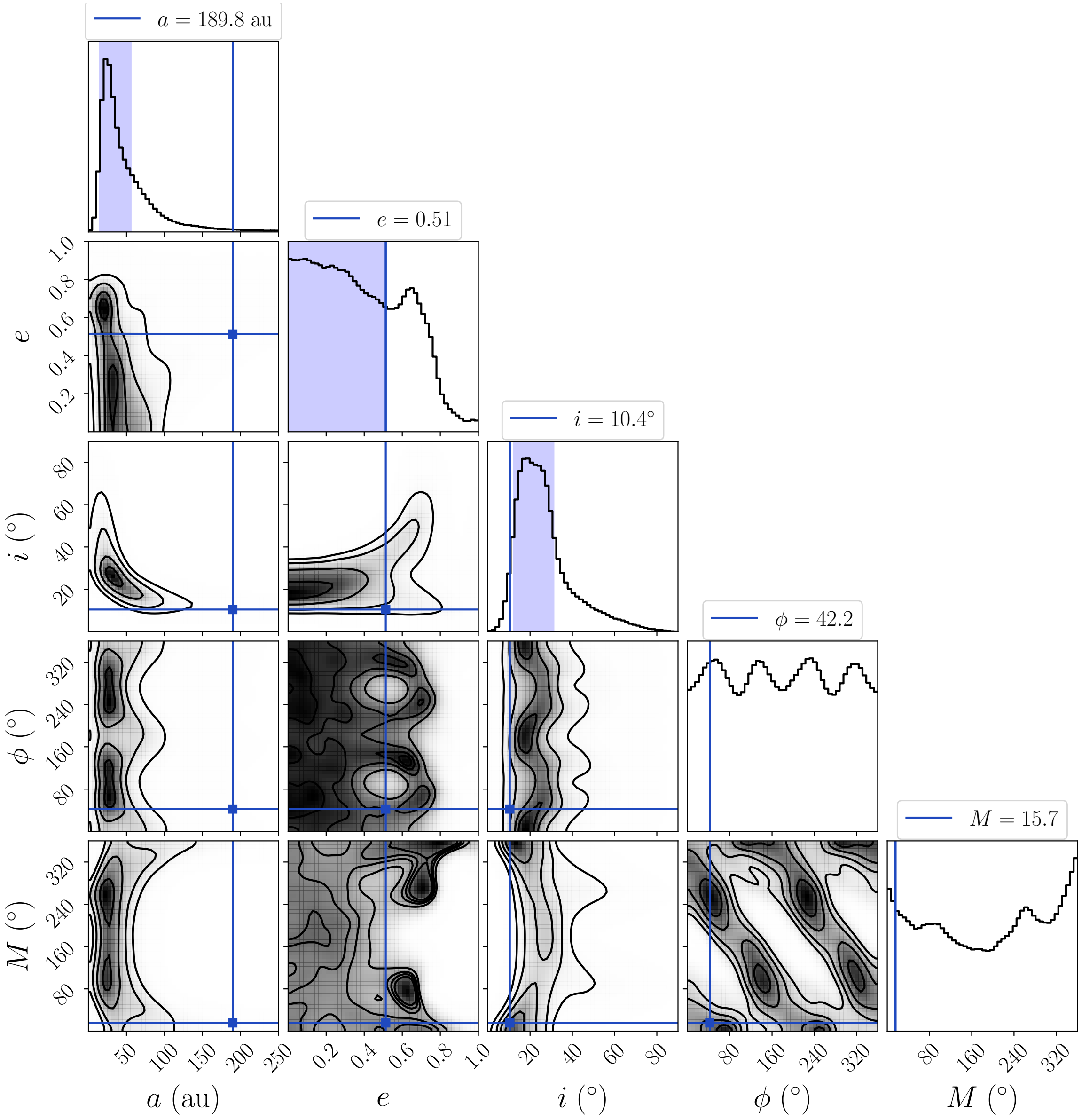

Figure B.1: Corner plot showing orbital parameter covariances for test system B4. See Fig. 4.4.

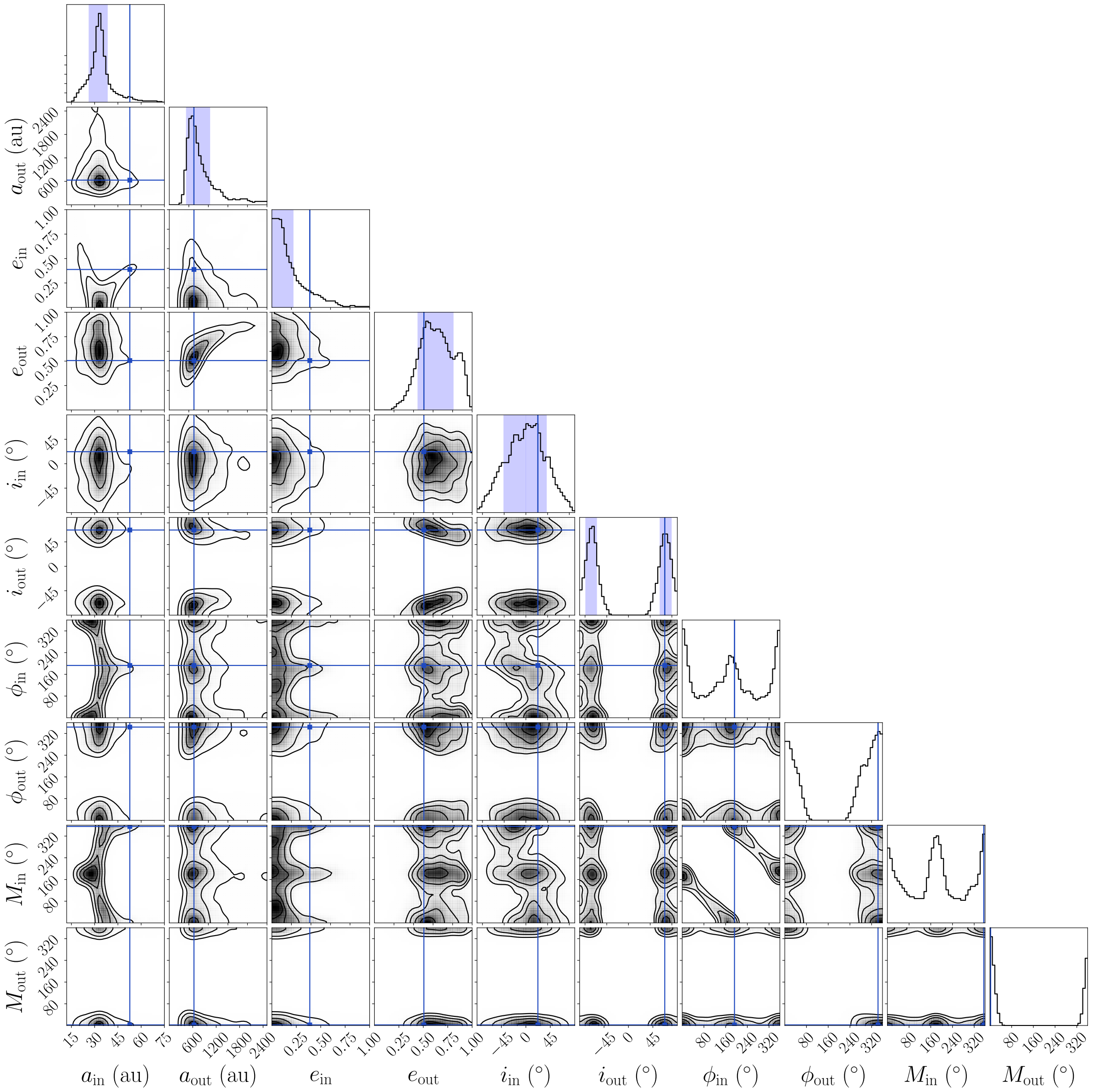

Figure B.2: Corner plot for triple system 25. Sample size of 1011 matches. See Fig. 4.9.

B.1 Simulation data tables

No.	a (au)	e	i ($^\circ$)	ϕ ($^\circ$)	M ($^\circ$)	m_1 ($M_\odot$)	m_2 ($M_\odot$)	Δt (years)
B1	54.72	0.388	20.45	-0.0	-0.0	0.66	0.19	8.7
B2	54.19	0.623	41.78	95.22	213.95	0.47	0.06	9.51
B3	18.83	0.864	27.77	191.37	340.05	0.6	0.24	10.07
B4	189.79	0.513	10.42	42.19	15.67	0.31	0.12	10.58
B5	107.06	0.442	64.59	223.1	236.32	0.27	0.13	11.3
B6	82.76	0.558	33.82	245.29	98.2	0.89	0.54	8.35
B7	87.46	0.02	38.93	116.94	249.37	0.65	0.22	2.39
B8	68.73	0.955	24.3	332.93	351.39	0.75	0.08	4.64
B9	64.6	0.235	43.6	317.48	294.6	0.59	0.07	9.21
B10	91.27	0.771	25.75	294.24	193.06	1.05	0.65	6.46
B11	68.21	0.316	82.61	140.72	343.86	0.9	0.28	7.25
B12	117.45	0.642	46.65	194.26	228.14	0.34	0.13	11.41
B13	183.5	0.682	6.7	345.97	36.91	0.42	0.38	3.94
B14	144.64	0.091	68.92	210.68	59.33	0.65	0.39	9.48
B15	150.02	0.04	8.9	100.34	168.31	0.68	0.39	6.65
B16	192.23	0.738	44.48	207.09	298.1	0.28	0.02	11.59
B17	63.17	0.115	52.99	226.07	326.87	0.8	0.29	7.43
B18	94.69	0.001	9.35	170.83	228.19	0.78	0.46	3.3
B19	70.63	0.171	26.09	147.25	71.14	0.74	0.1	2.02
B20	74.34	0.693	24.38	127.26	140.15	0.86	0.51	3.35
B21	249.98	0.014	39.47	46.63	206.75	0.83	0.15	11.7
B22	233.21	0.207	32.1	355.09	329.9	1.01	0.38	7.78
B23	256.99	0.44	45.75	346.35	334.58	1.01	0.66	9.57
B24	232.85	0.636	1.19	45.19	271.43	0.73	0.49	11.44
B25	322.94	0.833	20.52	63.08	358.55	0.7	0.27	11.77
B26	319.42	0.56	45.68	56.08	38.34	0.61	0.11	10.36
B27	206.5	0.067	26.47	210.47	210.5	0.6	0.02	11.15
B28	315.18	0.377	0.04	293.77	145.93	1.08	0.64	8.36
B29	383.72	0.355	9.86	95.3	148.65	0.67	0.52	7.63
B30	370.29	0.015	21.91	353.97	269.24	0.59	0.35	9.51
B31	415.98	0.863	83.22	88.04	10.19	0.91	0.5	11.19
B32	443.58	0.669	12.18	338.89	351.87	0.49	0.16	10.95
B33	423.87	0.192	27.53	287.32	340.78	1.33	0.68	9.26

B34	340.84	0.042	22.83	309.8	129.21	1.1	0.5	10.53
B35	286.1	0.196	35.24	209.36	190.37	0.95	0.66	10.37
B36	392.06	0.92	31.35	12.49	354.86	0.66	0.36	9.88
B37	403.19	0.757	26.51	164.66	359.88	0.71	0.36	10.97
B38	368.78	0.822	38.0	98.02	24.04	0.5	0.08	9.06
B39	438.22	0.402	5.45	184.7	14.41	0.91	0.61	11.71
B40	370.4	0.089	40.27	31.0	268.92	1.12	0.54	7.45
B41	8.97	0.623	41.78	95.22	213.95	0.47	0.06	9.51
B42	13.37	0.26	4.73	265.51	287.48	0.89	0.22	9.69
B43	16.31	0.823	47.49	81.4	80.77	0.63	0.35	5.63
B44	4.19	0.864	27.77	191.37	340.05	0.6	0.24	10.07
B45	29.17	0.651	31.89	348.54	218.22	0.8	0.17	6.54
B46	27.27	0.513	10.42	42.19	15.67	0.31	0.12	10.58
B47	18.81	0.786	52.99	22.58	51.18	0.33	0.16	3.8
B48	16.1	0.442	64.59	223.1	236.32	0.27	0.13	11.3
B49	12.82	0.558	33.82	245.29	98.2	0.89	0.54	8.35
B50	9.63	0.934	25.31	58.19	128.5	0.2	0.12	10.65
B51	138.6	0.808	16.2	151.06	282.75	1.12	0.49	11.91
B52	139.54	0.063	13.69	187.33	50.48	0.79	0.67	9.35
B53	142.07	0.137	40.22	1.59	319.33	0.87	0.58	4.88
B54	81.52	0.343	11.28	77.13	311.25	0.70	0.54	6.82
B55	76.91	0.283	14.58	39.34	321.31	0.80	0.48	7.68
B56	78.5	0.066	9.09	63.02	311.94	1.14	0.51	3.61
B57	169.27	0.573	57.83	256.31	346.48	0.75	0.48	3.96
B58	182.87	0.2	2.66	67.84	347.09	0.68	0.02	4.55
B59	156.81	0.313	20.62	340.37	355.22	0.55	0.26	10.86
B60	110.93	0.182	20.29	196.58	40.96	1.08	0.63	3.45

Table B.1: The orbital parameters, masses, and the time between observations for each of the test binary systems. The leftmost column shows the index used to refer to each system in the text. From left to right, the columns contain the semi-major axes (in au), eccentricities, inclinations (in degrees), orientations (in degrees), mean anomalies (in degrees), the masses of the primary and secondary stars (in solar masses), and the time between observations (in years). All values quoted to 2 d.p. (excluding eccentricity, which is quoted to 3 d.p.). Any values with fewer significant figures are followed by a 0.

No.	a (au)	68% CI	95% CI	e	68% CI	95% CI	i (°)	68% CI	95% CI
B1	54.72	18.41 - 110.44	17.86 - 387.85	0.388	0.279 - 0.79	0.004 - 0.807	20.45	7.14 - 28.04	4.99 - 53.57
B2	54.19	35.59 - 143.36	31.3 - 486.3	0.623	0.13 - 0.665	0.0 - 0.78	41.78	12.17 - 32.55	7.63 - 57.42
B3	18.83	14.27 - 54.34	13.76 - 154.77	0.864	0.692 - 0.905	0.567 - 0.944	27.77	18.37 - 42.44	11.6 - 67.14
B4	189.79	14.49 - 55.86	13.63 - 174.38	0.513	0.0 - 0.509	0.0 - 0.761	10.42	12.16 - 31.19	7.77 - 56.63
B5	107.06	97.92 - 244.75	88.01 - 803.74	0.442	0.0 - 0.465	0.0 - 0.816	64.59	27.15 - 51.46	18.02 - 70.31
B6	82.76	53.86 - 270.19	50.17 - 1068.16	0.558	0.187 - 0.774	0.0 - 0.838	33.82	7.29 - 24.88	4.22 - 51.97
B7	87.46	58.43 - 181.58	44.94 - 593.78	0.02	0.042 - 0.55	0.0 - 0.824	38.93	19.86 - 42.64	12.46 - 64.95
B8	68.73	55.27 - 77.95	39.97 - 77.95	0.955	0.662 - 0.99	0.138 - 0.99	24.3	12.57 - 36.6	6.7 - 50.68
B9	64.6	40.5 - 95.07	36.54 - 296.85	0.235	0.0 - 0.451	0.0 - 0.78	43.6	28.16 - 51.2	18.93 - 68.84
B10	91.27	51.32 - 308.37	50.33 - 1535.83	0.771	0.279 - 0.892	0.007 - 0.896	25.75	3.57 - 17.78	1.85 - 46.86
B11	68.21	58.73 - 151.85	53.15 - 408.13	0.316	0.377 - 0.77	0.264 - 0.919	82.61	48.46 - 72.0	34.37 - 83.74
B12	117.45	99.6 - 429.1	88.07 - 1499.03	0.642	0.165 - 0.73	0.0 - 0.824	46.65	10.87 - 30.31	6.45 - 56.31
B13	183.5	45.91 - 262.92	45.28 - 1213.58	0.682	0.359 - 0.97	0.049 - 0.97	6.7	2.05 - 11.76	1.78 - 42.59
B14	144.64	121.58 - 267.09	110.46 - 843.28	0.091	0.0 - 0.543	0.0 - 0.852	68.92	43.05 - 71.25	30.75 - 83.48
B15	150.02	13.47 - 92.21	13.28 - 340.13	0.04	0.345 - 0.825	0.013 - 0.831	8.9	6.12 - 27.89	4.01 - 52.14
B16	192.23	104.29 - 434.93	90.81 - 1425.94	0.738	0.164 - 0.727	0.0 - 0.82	44.48	11.13 - 30.75	7.08 - 56.82
B17	63.17	47.05 - 95.63	42.29 - 298.44	0.115	0.0 - 0.37	0.0 - 0.757	52.99	35.39 - 60.21	23.84 - 73.85
B18	94.69	38.76 - 246.12	37.96 - 1548.63	0.001	0.331 - 0.962	0.04 - 0.962	9.35	1.76 - 12.36	1.37 - 42.94
B19	70.63	27.86 - 99.2	23.01 - 320.21	0.171	0.096 - 0.628	0.0 - 0.805	26.09	15.27 - 36.27	9.7 - 60.6
B20	74.34	38.48 - 222.93	37.47 - 1025.11	0.693	0.272 - 0.885	0.01 - 0.896	24.38	4.06 - 18.52	2.42 - 47.54
B21	249.98	132.66 - 311.32	117.51 - 1011.47	0.014	0.0 - 0.453	0.0 - 0.815	39.47	29.83 - 54.54	19.73 - 71.76
B22	233.21	101.79 - 299.23	92.34 - 973.81	0.207	0.038 - 0.534	0.0 - 0.809	32.1	21.24 - 44.11	14.07 - 66.06
B23	256.99	112.08 - 229.03	102.85 - 736.41	0.44	0.0 - 0.461	0.0 - 0.819	45.75	40.39 - 68.02	28.26 - 80.66
B24	232.85	38.95 - 324.14	38.95 - 3456.16	0.636	0.456 - 0.99	0.073 - 0.99	1.19	0.14 - 2.79	0.11 - 22.1

B25	322.94	34.44 - 107.23	26.01 - 356.75	0.833	0.366 - 0.828	0.094 - 0.912	20.52	15.9 - 31.86	10.29 - 56.48
B26	319.42	205.54 - 483.57	183.02 - 1464.71	0.56	0.0 - 0.459	0.0 - 0.817	45.68	29.15 - 53.65	19.7 - 71.39
B27	206.5	88.61 - 324.35	75.0 - 1051.73	0.067	0.107 - 0.645	0.0 - 0.81	26.47	14.69 - 35.4	9.37 - 60.1
B28	315.18	27.36 - 264.81	27.36 - 3981.99	0.377	0.602 - 0.99	0.109 - 0.99	0.04	0.0 - 0.39	0.0 - 17.4
B29	383.72	68.28 - 401.46	66.51 - 1945.18	0.355	0.279 - 0.894	0.005 - 0.895	9.86	3.79 - 18.08	2.14 - 46.98
B30	370.29	96.52 - 315.17	76.73 - 1029.02	0.015	0.076 - 0.594	0.0 - 0.811	21.91	17.79 - 39.76	11.33 - 62.85
B31	415.98	260.8 - 440.11	174.47 - 441.15	0.863	0.867 - 0.925	0.861 - 0.968	83.22	36.69 - 69.76	21.22 - 80.85
B32	443.58	38.45 - 177.84	35.33 - 622.26	0.669	0.177 - 0.753	0.0 - 0.821	12.18	8.49 - 26.11	4.85 - 52.47
B33	423.87	126.99 - 325.19	111.93 - 1050.03	0.192	0.001 - 0.469	0.0 - 0.806	27.53	25.42 - 49.2	17.08 - 68.84
B34	340.84	94.35 - 300.42	73.09 - 957.03	0.042	0.079 - 0.585	0.0 - 0.794	22.83	18.52 - 40.49	11.72 - 62.87
B35	286.1	186.68 - 665.76	154.59 - 2179.56	0.196	0.102 - 0.637	0.0 - 0.823	35.24	15.66 - 37.15	10.0 - 61.44
B36	392.06	69.12 - 226.32	45.4 - 382.37	0.92	0.729 - 0.909	0.593 - 0.942	31.35	31.63 - 60.06	20.52 - 73.38
B37	403.19	62.25 - 200.98	57.37 - 645.64	0.757	0.071 - 0.569	0.0 - 0.774	26.51	18.14 - 39.93	11.4 - 62.08
B38	368.78	278.58 - 639.32	235.18 - 1874.93	0.822	0.018 - 0.614	0.0 - 0.874	38.0	43.67 - 72.06	30.1 - 83.86
B39	438.22	108.82 - 724.94	107.38 - 5667.3	0.402	0.375 - 0.989	0.059 - 0.99	5.45	0.93 - 9.28	0.76 - 41.21
B40	370.4	199.03 - 471.56	178.33 - 1565.63	0.089	0.0 - 0.458	0.0 - 0.83	40.27	29.2 - 54.17	19.63 - 72.11
B41	8.97	6.26 - 29.66	6.22 - 97.28	0.623	0.222 - 0.693	0.0 - 0.812	41.78	8.63 - 33.2	5.7 - 58.4
B42	13.37	6.77 - 13.25	6.66 - 40.27	0.26	0.611 - 0.99	0.238 - 0.99	4.73	2.81 - 17.95	2.27 - 47.94
B43	16.31	10.88 - 121.86	10.87 - 662.37	0.823	0.457 - 0.948	0.051 - 0.952	47.49	1.65 - 17.91	1.18 - 46.41
B44	4.19	1.58 - 3.09	1.57 - 8.2	0.864	0.266 - 0.849	0.003 - 0.89	27.77	14.16 - 47.24	0.04 - 67.38
B45	29.17	27.91 - 58.1	23.78 - 153.88	0.651	0.001 - 0.47	0.0 - 0.822	31.89	0.0 - 41.85	0.0 - 71.1
B46	27.27	8.84 - 26.52	8.4 - 87.43	0.513	0.569 - 0.899	0.469 - 0.99	10.42	7.48 - 23.7	3.93 - 56.07
B47	18.81	14.26 - 92.66	14.07 - 466.29	0.786	0.292 - 0.906	0.025 - 0.922	52.99	3.05 - 17.03	1.91 - 46.7
B48	16.1	14.77 - 31.78	13.53 - 98.58	0.442	0.0 - 0.398	0.0 - 0.739	64.59	27.96 - 50.09	18.41 - 67.67
B49	12.82	8.86 - 57.45	8.72 - 201.9	0.558	0.32 - 0.793	0.0 - 0.813	33.82	6.02 - 28.11	4.2 - 54.97
B50	9.63	6.32 - 138.17	6.32 - 1018.66	0.934	0.632 - 0.99	0.119 - 0.99	25.31	0.48 - 14.46	0.26 - 47.43

B51	138.6	98.04 - 662.54	96.76 - 5161.96	0.808	0.372 - 0.989	0.056 - 0.989	16.2	0.95 - 9.46	0.81 - 41.14
B52	139.54	36.22 - 176.82	33.93 - 657.05	0.063	0.144 - 0.74	0.0 - 0.845	13.69	6.52 - 21.88	4.12 - 49.47
B53	142.07	78.1 - 191.61	69.92 - 627.94	0.137	0.0 - 0.459	0.0 - 0.812	40.22	27.62 - 52.0	18.1 - 70.25
B54	81.52	36.02 - 254.92	35.74 - 1600.2	0.343	0.327 - 0.953	0.032 - 0.953	11.28	1.75 - 13.65	1.16 - 44.72
B55	76.91	30.9 - 204.96	30.34 - 955.39	0.283	0.293 - 0.897	0.017 - 0.9	14.58	3.56 - 18.87	2.13 - 48.15
B56	78.5	38.76 - 268.75	37.91 - 2144.28	0.066	0.355 - 0.976	0.059 - 0.99	9.09	1.18 - 11.46	0.76 - 43.9
B57	169.27	80.17 - 183.36	74.2 - 562.16	0.573	0.053 - 0.641	0.0 - 0.863	57.83	43.51 - 71.41	30.63 - 83.32
B58	182.87	51.39 - 319.19	49.95 - 1984.48	0.2	0.43 - 0.99	0.07 - 0.99	2.66	0.59 - 5.48	0.43 - 32.1
B59	156.81	56.55 - 253.14	50.75 - 881.2	0.313	0.165 - 0.737	0.0 - 0.816	20.62	9.0 - 27.26	5.76 - 54.18
B60	110.93	26.66 - 92.04	24.66 - 296.5	0.182	0.0 - 0.506	0.0 - 0.767	20.29	16.25 - 37.18	10.23 - 59.96

Table B.2: The true orbital parameters a, e, and i for each system compared to the 68% and 95% confidence intervals obtained from simulations.

No.	a_{in} (au)	e_{in}	i_{in} (°)	ϕ_{in} (°)	M_{in} (°)	a_{out} (au)	e_{out}	i_{out} (°)	ϕ_{out} (°)	M_{out} (°)	m_1 ($M_\odot$)	m_2 ($M_\odot$)	m_3 ($M_\odot$)	Δt (years)
T1	24.38	0.261	-44.15	316.26	110.34	307.43	0.191	3.48	118.24	9.97	0.98	0.97	0.87	8.26
T2	26.42	0.137	36.2	214.41	262.68	449.44	0.685	-31.34	22.32	23.92	0.65	0.63	0.18	7.07
T3	20.03	0.4	-31.15	138.89	307.4	281.55	0.233	31.07	233.68	352.78	0.99	0.53	0.4	7.45
T4	67.7	0.384	40.36	307.77	155.0	2810.28	0.427	-1.75	349.58	50.2	0.96	0.57	0.34	9.82
T5	24.98	0.503	11.41	271.61	33.09	966.47	0.407	-4.38	354.19	318.89	0.51	0.27	0.09	7.9
T6	92.0	0.022	54.8	88.12	40.19	775.23	0.475	33.16	302.95	353.34	0.92	0.56	0.45	7.22
T7	10.07	0.706	40.65	316.69	251.8	160.68	0.089	-7.93	87.49	241.04	0.99	0.39	0.36	6.25
T8	19.82	0.054	-18.22	164.13	8.32	152.88	0.143	84.31	346.12	255.04	0.63	0.46	0.16	4.96
T9	36.77	0.373	17.16	66.25	71.5	1214.18	0.764	-48.65	300.12	356.45	0.73	0.6	0.31	9.06
T10	22.2	0.857	-60.12	183.17	27.69	739.0	0.295	13.09	44.16	32.93	0.7	0.6	0.47	9.13
T11	13.01	0.223	-20.61	166.92	166.62	184.35	0.144	4.31	275.84	188.02	0.63	0.26	0.18	2.2
T12	47.34	0.301	56.21	1.69	242.18	564.54	0.534	16.24	270.65	344.68	0.75	0.73	0.56	8.02
T13	28.6	0.26	31.7	157.36	226.27	312.79	0.51	-10.43	206.55	0.89	0.66	0.24	0.19	9.43
T14	49.18	0.62	-22.34	98.02	107.9	1340.77	0.551	2.29	338.7	341.47	0.89	0.72	0.62	9.25
T15	105.45	0.535	-37.73	225.74	234.36	2954.16	0.781	14.34	72.77	3.14	0.83	0.74	0.7	9.4
T16	28.33	0.308	-47.24	280.13	16.39	447.56	0.569	27.34	348.93	25.3	0.17	0.1	0.08	9.76
T17	15.39	0.813	26.97	89.04	41.08	326.03	0.022	29.7	215.56	225.04	0.72	0.68	0.24	6.68
T18	98.83	0.831	-34.75	299.51	8.52	3261.11	0.827	10.58	305.59	358.86	0.81	0.36	0.21	8.98
T19	24.51	0.772	-23.51	310.43	277.93	503.89	0.101	-11.0	6.71	272.47	0.68	0.56	0.47	8.67
T20	12.92	0.218	28.93	202.69	77.95	323.87	0.722	-56.96	170.22	21.36	0.6	0.33	0.22	6.54
T21	13.91	0.644	32.63	8.51	146.55	999.72	0.423	-0.52	166.84	331.29	0.75	0.72	0.62	9.9
T22	44.71	0.237	-14.11	46.08	87.49	731.07	0.111	-2.55	190.52	62.5	0.75	0.73	0.16	9.29
T23	28.37	0.16	78.93	113.45	157.48	542.3	0.592	0.06	10.73	320.17	0.82	0.56	0.5	2.89

T24	36.69	0.571	-56.81	163.55	313.1	650.33	0.167	-3.32	209.34	30.31	1.0	0.72	0.62	8.58
T25	52.7	0.388	22.11	192.65	355.45	631.34	0.506	66.86	343.6	2.28	0.95	0.66	0.18	8.9
T26	26.07	0.08	69.43	199.15	40.75	259.49	0.169	37.23	222.24	264.53	0.64	0.61	0.1	8.64
T27	34.14	0.056	39.95	219.98	219.64	198.49	0.153	14.42	20.63	310.22	0.9	0.74	0.29	9.54
T28	96.69	0.493	51.29	120.81	49.63	1410.64	0.552	4.53	275.38	2.37	0.57	0.45	0.24	7.7
T29	19.17	0.215	-48.28	293.0	340.14	210.73	0.406	4.69	307.17	332.14	0.84	0.6	0.36	6.48
T30	10.13	0.604	18.0	351.78	358.7	221.79	0.067	4.66	126.59	125.9	0.87	0.71	0.67	8.91
T31	90.06	0.108	74.23	134.82	311.44	2631.42	0.8	2.72	17.22	7.16	0.98	0.6	0.29	7.76
T32	66.58	0.01	22.88	47.4	48.93	330.66	0.055	-9.77	284.7	333.59	0.36	0.22	0.12	6.47
T33	132.59	0.586	2.17	285.14	334.01	2393.09	0.387	-2.75	268.41	1.46	0.69	0.48	0.25	8.4
T34	14.29	0.336	-20.06	250.5	58.57	323.11	0.291	51.55	73.83	15.08	0.8	0.72	0.24	8.04
T35	45.56	0.554	7.24	256.91	50.28	401.5	0.089	1.99	257.27	27.69	0.59	0.52	0.38	5.15
T36	15.96	0.509	-18.37	108.5	221.76	441.57	0.148	-26.47	328.26	94.9	0.99	0.93	0.13	8.74
T37	13.97	0.827	53.89	329.87	102.3	446.54	0.669	-43.66	241.19	339.11	0.94	0.73	0.63	7.81
T38	73.75	0.253	55.0	331.89	137.14	1883.76	0.091	2.7	78.97	7.94	0.67	0.63	0.3	8.03
T39	20.16	0.891	-42.62	316.58	208.35	2928.27	0.936	-25.89	118.81	359.64	0.31	0.24	0.1	3.19
T40	10.88	0.418	-14.37	99.55	40.17	163.31	0.175	41.63	88.37	10.76	0.79	0.59	0.11	6.3
T41	39.65	0.685	74.94	124.07	183.93	561.59	0.43	23.09	176.49	323.86	0.93	0.62	0.4	6.48
T42	36.82	0.623	-15.53	185.8	44.45	931.13	0.278	-0.88	148.66	94.07	0.67	0.56	0.12	8.52
T43	19.26	0.336	9.46	132.98	270.94	978.81	0.849	54.94	50.65	358.87	0.92	0.78	0.5	3.9
T44	11.32	0.653	38.27	276.45	153.46	386.32	0.62	-4.3	345.3	337.74	0.79	0.77	0.36	5.6
T45	30.31	0.239	-16.32	34.1	201.73	346.54	0.295	-49.61	47.26	45.4	0.79	0.72	0.69	6.54
T46	22.15	0.057	-2.21	274.78	203.93	342.55	0.616	-0.54	307.7	52.53	0.96	0.7	0.69	4.53
T47	49.73	0.619	34.73	183.81	42.48	889.1	0.164	-1.05	276.49	0.21	0.57	0.43	0.33	9.5
T48	32.56	0.908	-42.38	176.07	192.78	1246.48	0.732	54.01	226.4	3.07	0.55	0.4	0.31	8.84
T49	37.76	0.505	-58.6	36.32	286.51	1208.03	0.662	-20.34	234.18	3.85	0.66	0.51	0.24	7.0

T50	26.4	0.693	6.68	299.17	187.38	371.46	0.028	3.97	164.84	299.95	0.71	0.66	0.21	5.76
T51	12.48	0.204	-22.53	212.42	116.67	175.11	0.157	8.32	234.22	273.28	0.56	0.56	0.24	6.92
T52	19.43	0.591	6.14	61.88	15.68	369.72	0.495	-57.52	311.08	348.71	0.86	0.27	0.18	7.45
T53	60.63	0.04	56.34	312.1	234.65	1064.8	0.126	-4.71	197.76	264.48	0.68	0.34	0.23	7.52
T54	15.38	0.338	30.47	14.96	318.97	228.55	0.496	-14.4	164.42	38.89	0.99	0.18	0.18	3.29
T55	16.06	0.402	5.51	68.71	218.03	137.27	0.115	-39.08	99.35	179.8	0.83	0.56	0.11	5.55
T56	55.82	0.52	-0.02	73.79	22.61	2146.54	0.794	-11.52	126.66	356.46	0.65	0.43	0.25	9.88
T57	16.55	0.576	64.88	199.55	278.99	160.44	0.192	-56.37	48.81	9.62	0.81	0.23	0.2	9.17
T58	10.28	0.029	-48.93	262.12	336.51	124.99	0.59	-41.87	249.79	328.44	0.75	0.37	0.25	7.26
T59	49.0	0.009	5.84	49.43	241.16	218.63	0.074	-0.83	206.48	46.51	0.82	0.78	0.3	2.0
T60	24.84	0.628	40.37	218.7	4.92	369.97	0.488	-28.85	84.67	23.49	0.9	0.58	0.54	6.21

Table B.3: The orbital parameters, masses, and the time between observations for each of the test triple systems.

No.	a (au)	68% CI	95% CI	e	68% CI	95% CI	i (°)	68% CI	95% CI
T1	24.38	18.07 - 38.07	15.39 - 65.83	0.261	0.003 - 0.258	0.0 - 0.463	-44.15	26.66 - 43.34	20.72 - 61.72
T2	26.42	14.85 - 29.49	13.43 - 51.17	0.137	0.0 - 0.243	0.0 - 0.471	36.2	30.2 - 47.4	22.95 - 60.7
T3	20.03	15.47 - 30.25	12.78 - 46.17	0.4	0.018 - 0.48	0.004 - 0.805	-31.15	18.34 - 30.68	14.89 - 57.22
T4	67.7	42.38 - 123.27	40.68 - 247.44	0.384	0.147 - 0.586	0.001 - 0.643	40.36	19.37 - 40.79	15.38 - 63.73
T5	24.98	N/A	N/A	0.503	N/A	N/A	11.41	N/A	N/A
T6	92.0	73.94 - 97.99	66.92 - 110.56	0.022	0.005 - 0.236	0.002 - 0.418	54.8	49.28 - 67.74	44.83 - 78.61
T7	10.07	8.62 - 19.98	8.36 - 107.73	0.706	0.48 - 0.802	0.056 - 0.819	40.65	16.71 - 39.85	5.36 - 53.93
T8	19.82	10.19 - 29.72	10.19 - 55.16	0.054	0.368 - 0.835	0.084 - 0.88	-18.22	10.22 - 25.39	10.08 - 55.93
T9	36.77	21.77 - 38.34	21.12 - 56.34	0.373	0.634 - 0.92	0.322 - 0.932	17.16	13.06 - 37.87	11.76 - 62.07
T10	22.2	21.28 - 44.13	19.88 - 74.25	0.857	0.784 - 0.885	0.78 - 0.947	-60.12	31.56 - 62.2	19.94 - 79.69
T11	13.01	9.2 - 18.66	8.12 - 37.81	0.223	0.015 - 0.578	0.0 - 0.828	-20.61	13.13 - 26.3	6.63 - 50.92
T12	47.34	40.23 - 77.35	37.84 - 139.0	0.301	0.027 - 0.364	0.0 - 0.593	56.21	31.67 - 53.36	25.3 - 69.07
T13	28.6	20.35 - 52.17	20.12 - 183.56	0.26	0.262 - 0.719	0.041 - 0.776	31.7	11.94 - 36.07	8.34 - 55.11
T14	49.18	17.86 - 105.23	17.86 - 299.16	0.62	0.517 - 0.876	0.094 - 0.886	-22.34	5.32 - 27.96	4.89 - 56.41
T15	105.45	64.35 - 137.64	62.97 - 256.4	0.535	0.329 - 0.734	0.009 - 0.745	-37.73	22.05 - 48.16	17.51 - 67.07
T16	28.33	15.92 - 26.99	15.19 - 49.89	0.308	0.167 - 0.461	0.1 - 0.655	-47.24	42.64 - 65.41	33.59 - 77.07
T17	15.39	8.96 - 15.93	8.66 - 34.13	0.813	0.437 - 0.733	0.316 - 0.829	26.97	7.67 - 40.58	7.13 - 68.59
T18	98.83	N/A	N/A	0.831	N/A	N/A	-34.75	N/A	N/A
T19	24.51	17.47 - 30.07	17.11 - 51.48	0.772	0.741 - 0.952	0.422 - 0.987	-23.51	10.89 - 42.26	10.33 - 68.17
T20	12.92	7.49 - 13.12	7.4 - 28.93	0.218	0.007 - 0.321	0.002 - 0.68	28.93	20.87 - 47.0	16.05 - 65.05
T21	13.91	16.0 - 25.96	11.82 - 35.55	0.644	0.0 - 0.315	0.0 - 0.715	32.63	0.04 - 29.13	0.04 - 48.49
T22	44.71	27.75 - 60.9	24.82 - 111.69	0.237	0.001 - 0.467	0.003 - 0.802	-14.11	9.15 - 16.36	7.22 - 31.69
T23	28.37	27.98 - 46.65	26.95 - 106.05	0.16	0.001 - 0.256	0.001 - 0.595	78.93	41.92 - 66.89	30.2 - 79.1
T24	36.69	25.58 - 53.74	25.09 - 106.56	0.571	0.434 - 0.65	0.324 - 0.786	-56.81	29.74 - 54.44	26.7 - 74.62

T25	52.7	26.39 - 38.22	17.91 - 54.26	0.388	0.0 - 0.218	0.0 - 0.59	22.11	0.13 - 38.98	0.13 - 69.38
T26	26.07	22.47 - 31.81	21.81 - 57.79	0.08	0.002 - 0.189	0.0 - 0.503	69.43	50.92 - 73.4	41.82 - 83.71
T27	34.14	19.19 - 35.06	17.78 - 54.61	0.056	0.058 - 0.318	0.0 - 0.485	39.95	33.84 - 56.03	29.38 - 73.32
T28	96.69	62.96 - 104.18	59.41 - 212.95	0.493	0.0 - 0.309	0.0 - 0.639	51.29	40.99 - 64.57	31.82 - 76.57
T29	19.17	13.58 - 21.82	13.0 - 41.53	0.215	0.172 - 0.354	0.09 - 0.599	-48.28	37.8 - 58.45	30.0 - 73.15
T30	10.13	9.98 - 15.55	9.95 - 28.86	0.604	0.466 - 0.748	0.278 - 0.798	18.0	0.01 - 9.04	0.01 - 32.42
T31	90.06	79.78 - 132.75	74.98 - 278.94	0.108	0.009 - 0.383	0.0 - 0.71	74.23	50.34 - 72.96	38.12 - 81.06
T32	66.58	17.97 - 42.95	17.16 - 82.37	0.01	0.24 - 0.644	0.011 - 0.632	22.88	22.55 - 48.18	17.47 - 68.97
T33	132.59	47.85 - 135.85	42.44 - 271.96	0.586	0.341 - 0.989	0.062 - 0.986	2.17	1.12 - 3.65	0.88 - 18.49
T34	14.29	8.37 - 17.98	8.16 - 39.21	0.336	0.572 - 0.911	0.081 - 0.922	-20.06	12.67 - 31.7	10.25 - 56.45
T35	45.56	22.51 - 59.12	22.04 - 263.74	0.554	0.285 - 0.951	0.034 - 0.949	7.24	2.56 - 12.34	1.56 - 32.4
T36	15.96	9.12 - 21.82	9.12 - 49.9	0.509	0.661 - 0.919	0.131 - 0.947	-18.37	11.17 - 32.32	8.06 - 57.22
T37	13.97	13.66 - 30.25	13.3 - 56.49	0.827	0.363 - 0.808	0.057 - 0.851	53.89	12.03 - 23.78	9.37 - 47.06
T38	73.75	63.78 - 115.17	56.49 - 213.81	0.253	0.016 - 0.359	0.001 - 0.626	55.0	34.65 - 55.68	27.14 - 70.68
T39	20.16	18.3 - 29.47	17.46 - 36.6	0.891	0.582 - 0.953	0.114 - 0.946	-42.62	12.9 - 36.68	12.4 - 65.16
T40	10.88	4.97 - 13.32	4.97 - 31.76	0.418	0.628 - 0.9	0.209 - 0.953	-14.37	6.08 - 26.5	5.06 - 56.68
T41	39.65	40.66 - 71.54	38.72 - 113.16	0.685	0.343 - 0.681	0.063 - 0.738	74.94	26.84 - 52.26	22.22 - 71.16
T42	36.81	N/A	N/A	0.623	N/A	N/A	-15.53	N/A	N/A
T43	19.26	12.27 - 25.82	11.78 - 38.1	0.336	0.648 - 0.981	0.154 - 0.983	9.46	6.76 - 26.36	6.1 - 56.15
T44	11.32	7.02 - 15.01	6.82 - 28.09	0.653	0.622 - 0.772	0.445 - 0.931	38.27	19.59 - 42.79	15.4 - 66.83
T45	30.31	20.85 - 48.21	18.99 - 73.78	0.239	0.003 - 0.461	0.002 - 0.799	-16.32	10.05 - 17.71	8.95 - 36.92
T46	22.15	N/A	N/A	0.057	N/A	N/A	-2.21	N/A	N/A
T47	49.73	33.39 - 78.23	25.5 - 161.98	0.619	0.286 - 0.728	0.036 - 0.832	34.73	19.75 - 35.71	14.86 - 54.98
T48	32.56	38.26 - 62.26	32.61 - 72.95	0.908	0.488 - 0.962	0.064 - 0.957	-42.38	10.58 - 26.54	9.8 - 53.86
T49	37.76	29.36 - 48.48	26.55 - 66.57	0.505	0.072 - 0.462	0.0 - 0.643	-58.6	36.25 - 57.22	30.54 - 72.33
T50	26.40	N/A	N/A	0.693	N/A	N/A	6.68	N/A	N/A

T51	12.48	8.31 - 18.27	7.89 - 29.89	0.204	0.0 - 0.369	0.0 - 0.755	-22.53	13.43 - 22.89	10.87 - 43.74
T52	19.43	9.71 - 15.56	9.71 - 31.5	0.591	0.375 - 0.62	0.312 - 0.788	6.14	0.05 - 17.91	0.0 - 54.55
T53	60.63	40.29 - 72.33	32.82 - 136.07	0.04	0.0 - 0.377	0.0 - 0.739	56.34	1.77 - 43.33	0.1 - 70.62
T54	15.38	6.48 - 15.95	6.33 - 29.37	0.338	0.03 - 0.437	0.007 - 0.609	30.47	20.26 - 42.52	16.67 - 62.93
T55	16.06	4.35 - 9.36	4.35 - 34.7	0.402	0.315 - 0.76	0.0 - 0.778	5.51	2.85 - 25.81	2.49 - 50.4
T56	55.82	N/A	N/A	0.52	N/A	N/A	-0.02	N/A	N/A
T57	16.55	18.0 - 30.66	16.35 - 38.44	0.576	0.0 - 0.382	0.0 - 0.616	64.88	27.99 - 43.8	26.02 - 64.16
T58	10.28	8.99 - 12.13	8.61 - 18.75	0.029	0.001 - 0.16	0.0 - 0.529	-48.93	31.26 - 56.95	24.25 - 72.84
T59	49.0	10.63 - 35.15	10.21 - 100.03	0.009	0.17 - 0.773	0.016 - 0.914	5.84	4.12 - 13.0	2.68 - 31.42
T60	24.84	13.08 - 32.63	12.56 - 61.05	0.628	0.6 - 0.803	0.58 - 0.891	40.37	32.0 - 62.49	23.26 - 78.19

Table B.4: Confidence intervals for all secondary stars obtained from each of the 60 test simulations. The leftmost column shows the index used to refer to each system in the text. Column 2 shows the true values of the semi-major axis for each system, followed by the 68% and 95% confidence intervals for a in columns 3 and 4 respectively. The eccentricity values and confidence intervals are stated in columns 5, 6, and 7, and this is repeated for inclination in the final three columns. The inclination confidence ranges quoted in columns 9 and 10 represent the positive component of the bimodal inclination PDF, which is mirrored for negative values.

No.	a (au)	68% CI	95% CI	e	68% CI	95% CI	i (°)	68% CI	95% CI
T1	307.43	142.53 - 1134.27	130.05 - 4428.81	0.191	0.037 - 0.518	0.0 - 0.786	3.48	1.13 - 3.63	0.69 - 4.67
T2	449.44	212.02 - 454.11	196.06 - 1223.45	0.685	0.017 - 0.441	0.001 - 0.768	-31.34	32.03 - 52.84	23.17 - 65.7
T3	281.55	142.53 - 270.5	126.41 - 833.42	0.233	0.003 - 0.38	0.001 - 0.787	31.07	29.5 - 42.73	21.52 - 49.26
T4	2810.28	144.5 - 3172.07	144.5 - 11482.51	0.427	0.012 - 0.466	0.001 - 0.775	-1.75	1.03 - 2.87	0.67 - 4.68
T5	966.47	N/A	N/A	0.407	N/A	N/A	-4.38	N/A	N/A
T6	775.23	241.97 - 501.88	221.61 - 2206.3	0.475	0.0 - 0.3	0.0 - 0.77	33.16	31.88 - 54.61	21.56 - 64.02
T7	160.68	94.93 - 1128.88	94.93 - 5380.13	0.089	0.052 - 0.549	0.001 - 0.772	-7.93	1.28 - 6.73	1.2 - 10.2
T8	152.88	144.01 - 330.86	137.41 - 1256.25	0.143	0.001 - 0.452	0.001 - 0.83	84.31	41.67 - 71.16	27.77 - 81.33
T9	1214.18	254.31 - 677.14	254.31 - 2329.24	0.764	0.281 - 0.728	0.201 - 0.918	-48.65	44.28 - 70.29	33.05 - 83.96
T10	739.0	180.62 - 871.68	146.34 - 3321.5	0.295	0.003 - 0.424	0.0 - 0.753	13.09	8.39 - 19.55	5.37 - 26.77
T11	184.35	41.88 - 279.1	41.39 - 1290.86	0.144	0.002 - 0.378	0.0 - 0.739	4.31	2.46 - 6.11	1.49 - 8.15
T12	564.54	233.94 - 1205.7	210.22 - 3627.63	0.534	0.003 - 0.407	0.0 - 0.7	16.24	7.87 - 17.34	5.25 - 21.07
T13	312.79	121.98 - 1221.88	121.98 - 3719.88	0.51	0.0 - 0.407	0.0 - 0.707	-10.43	2.5 - 9.33	2.41 - 13.57
T14	1340.77	89.0 - 1490.46	56.9 - 5597.44	0.551	0.006 - 0.397	0.006 - 0.719	2.29	1.4 - 3.37	0.92 - 5.79
T15	2954.16	325.75 - 1234.34	283.81 - 4280.81	0.781	0.0 - 0.331	0.001 - 0.716	14.34	12.67 - 23.9	8.82 - 29.76
T16	447.56	127.25 - 295.76	113.27 - 1175.51	0.569	0.001 - 0.378	0.0 - 0.781	27.34	29.63 - 52.07	17.08 - 65.5
T17	326.03	129.6 - 304.96	115.35 - 975.94	0.022	0.0 - 0.438	0.0 - 0.762	29.7	25.66 - 45.54	18.95 - 62.4
T18	3261.11	N/A	N/A	0.827	N/A	N/A	10.58	N/A	N/A
T19	503.89	100.86 - 533.75	87.2 - 1769.81	0.101	0.001 - 0.406	0.001 - 0.734	-11.0	8.42 - 17.93	6.6 - 25.15
T20	323.87	319.23 - 842.11	300.95 - 1239.58	0.722	0.652 - 0.826	0.568 - 0.931	-56.96	49.62 - 76.24	27.74 - 84.17
T21	999.72	95.38 - 916.59	85.3 - 4839.42	0.423	0.0 - 0.491	0.0 - 0.777	-0.52	0.28 - 1.1	0.19 - 1.47
T22	731.07	157.46 - 810.67	114.5 - 2614.53	0.111	0.003 - 0.391	0.0 - 0.764	-2.55	2.02 - 4.08	1.28 - 5.41
T23	542.3	99.26 - 2012.21	88.87 - 7019.95	0.592	0.004 - 0.515	0.001 - 0.873	0.06	0.02 - 0.06	0.01 - 0.1
T24	650.33	161.22 - 1078.57	151.06 - 5853.04	0.167	0.0 - 0.405	0.0 - 0.786	-3.32	1.78 - 5.18	1.1 - 6.33

T25	631.34	436.9 - 1036.83	384.34 - 3142.22	0.506	0.445 - 0.806	0.36 - 0.94	66.86	58.69 - 79.21	46.9 - 87.57
T26	259.49	151.28 - 375.38	134.46 - 1180.14	0.169	0.006 - 0.398	0.001 - 0.755	37.23	26.06 - 44.87	17.28 - 58.03
T27	198.49	123.98 - 604.1	113.34 - 2207.16	0.153	0.001 - 0.429	0.0 - 0.776	14.42	6.34 - 15.04	4.23 - 17.84
T28	1410.64	218.05 - 2034.61	218.05 - 5914.73	0.552	0.002 - 0.398	0.001 - 0.694	4.53	2.11 - 5.67	1.7 - 8.1
T29	210.73	67.89 - 326.67	67.89 - 1056.93	0.406	0.018 - 0.404	0.002 - 0.737	4.69	3.19 - 6.56	1.96 - 7.42
T30	221.79	68.53 - 306.61	50.78 - 1040.14	0.067	0.007 - 0.413	0.0 - 0.716	4.66	3.21 - 6.66	2.25 - 8.86
T31	2631.42	294.05 - 2242.33	261.58 - 4322.39	0.8	0.004 - 0.418	0.001 - 0.73	2.72	2.18 - 4.93	1.78 - 7.02
T32	330.66	95.92 - 542.26	85.25 - 1627.94	0.055	0.0 - 0.382	0.0 - 0.713	-9.77	5.31 - 13.23	4.23 - 18.05
T33	2393.09	497.59 - 1677.71	349.87 - 7181.45	0.387	0.001 - 0.408	0.001 - 0.792	-2.75	2.43 - 4.45	1.48 - 5.78
T34	323.11	180.63 - 380.3	176.68 - 1316.13	0.291	0.001 - 0.506	0.0 - 0.856	51.55	44.04 - 73.0	33.73 - 84.96
T35	401.5	142.55 - 2174.11	142.55 - 6032.9	0.089	0.092 - 0.543	0.003 - 0.731	1.99	0.54 - 1.77	0.47 - 2.85
T36	441.57	154.28 - 470.27	140.23 - 1509.59	0.148	0.011 - 0.476	0.007 - 0.778	-26.47	20.49 - 41.84	12.37 - 58.55
T37	446.54	170.49 - 370.64	170.49 - 1433.89	0.669	0.003 - 0.412	0.0 - 0.808	-43.66	29.89 - 50.26	22.69 - 67.8
T38	1883.76	334.21 - 1834.25	145.04 - 6874.01	0.091	0.014 - 0.418	0.001 - 0.763	2.7	2.09 - 4.41	1.5 - 6.36
T39	2928.27	82.27 - 167.68	76.78 - 614.99	0.936	0.0 - 0.31	0.0 - 0.748	-25.89	35.6 - 60.61	25.23 - 71.25
T40	163.31	84.56 - 181.41	74.61 - 592.51	0.175	0.002 - 0.382	0.0 - 0.776	41.63	33.47 - 60.1	23.12 - 73.12
T41	561.59	173.21 - 493.29	156.18 - 1840.18	0.43	0.0 - 0.307	0.0 - 0.716	23.09	19.41 - 34.16	13.83 - 42.32
T42	931.13	N/A	N/A	0.278	N/A	N/A	-0.88	N/A	N/A
T43	978.81	175.17 - 468.35	162.16 - 1422.4	0.849	0.347 - 0.758	0.252 - 0.925	54.94	46.35 - 70.27	37.11 - 80.91
T44	386.32	44.11 - 340.02	43.37 - 1603.0	0.62	0.009 - 0.44	0.005 - 0.769	-4.3	2.81 - 7.83	1.57 - 9.49
T45	346.54	220.41 - 430.02	200.53 - 1645.86	0.295	0.001 - 0.39	0.001 - 0.82	-49.61	37.76 - 63.05	27.53 - 74.89
T46	342.54	N/A	N/A	0.616	N/A	N/A	-0.54	N/A	N/A
T47	889.1	185.94 - 1646.33	123.53 - 6180.94	0.164	0.0 - 0.415	0.0 - 0.733	-1.05	0.45 - 1.37	0.34 - 1.99
T48	1246.48	405.77 - 1138.46	375.42 - 3208.68	0.732	0.504 - 0.839	0.384 - 0.93	54.01	49.69 - 73.07	35.96 - 81.97
T49	1208.03	160.76 - 317.1	141.8 - 955.48	0.662	0.002 - 0.307	0.001 - 0.673	-20.34	30.38 - 46.88	20.91 - 52.71
T50	371.46	N/A	N/A	0.028	N/A	N/A	3.97	N/A	N/A

T51	175.11	91.58 - 247.73	85.02 - 1057.65	0.157	0.004 - 0.414	0.0 - 0.781	8.32	6.29 - 10.49	3.36 - 12.19
T52	369.72	170.34 - 502.27	169.49 - 1501.13	0.495	0.275 - 0.753	0.121 - 0.91	-57.52	42.71 - 70.78	29.27 - 80.62
T53	1064.8	455.03 - 1435.2	345.38 - 4432.84	0.126	0.027 - 0.445	0.0 - 0.748	-4.71	3.44 - 6.33	2.48 - 8.28
T54	228.55	47.14 - 219.22	43.49 - 838.89	0.496	0.012 - 0.417	0.003 - 0.781	-14.4	10.88 - 22.44	8.28 - 31.92
T55	137.27	73.3 - 206.6	68.28 - 737.78	0.115	0.033 - 0.427	0.001 - 0.746	-39.08	25.2 - 46.64	16.54 - 66.7
T56	2146.54	N/A	N/A	0.794	N/A	N/A	-11.52	N/A	N/A
T57	160.44	108.47 - 210.06	97.8 - 760.71	0.192	0.001 - 0.383	0.0 - 0.79	-56.37	45.07 - 74.28	31.16 - 82.06
T58	124.99	63.02 - 127.16	57.63 - 342.54	0.59	0.004 - 0.381	0.001 - 0.737	-41.87	28.26 - 43.92	21.57 - 55.59
T59	218.63	53.42 - 654.95	39.34 - 2568.54	0.074	0.0 - 0.428	0.0 - 0.726	-0.83	0.27 - 0.95	0.2 - 1.46
T60	369.97	166.72 - 411.59	149.71 - 1279.84	0.488	0.001 - 0.42	0.0 - 0.765	-28.85	23.38 - 38.84	13.19 - 47.25

Table B.5: Confidence intervals for all tertiary stars obtained from each of the 60 test simulations. See table B.4.

“It’s a weird feeling, scientific breakthroughs. There’s no Eureka moment. Just a slow, steady progression towards a goal. But man, when you get to that goal, it feels good.”

— Andy Weir, *Project Hail Mary*